2019

Affordances And Control Of A Spine Morphology For Robotic Quadrupedal Locomotion

Jeffrey Duperret
University of Pennsylvania

Affordances And Control Of A Spine Morphology For Robotic Quadrupedal Locomotion

Abstract

How does a robot's body affect what it can do? This thesis explores the question with respect to a body morphology common to biology but rare in contemporary robotics: the presence of a bendable back. In this document, we introduce the Canid and Inu quadrupedal robots designed to test hypotheses related to the presence of a robotic sagittal-plane bending back (which we refer to as a ``spine morphology''). The thesis then describes and quantifies several advantages afforded by this morphological design choice that can be evaluated against its added weight and complexity, and proposes control strategies to both deal with the increase in degrees-of-freedom from the spine morphology and to leverage an increase in agility to reactively navigate irregular terrain. Specifically, we show using the metric of ``specific agility'' that a spine can provides a reservoir of elastic energy storage that can be rapidly converted to kinetic energy, that a spine can augment the effective workspace of the legs without diminishing their force generation capability, and that -- in cases of direct-drive or nearly direct-drive leg actuation -- the spine motors can contribute more work in stance than the same actuator weight used in the legs, but can do so without diminishing the platform's proprioceptive capabilities. To put to use the agility provided by a suitably designed robotic platform, we introduce a formalism to approximate a set of transitional navigational tasks over irregular terrain such as leaping over a gap that lend itself to doubly reactive control synthesis. We also directly address the increased complexity introduced by the spine joint with a modular compositional control framework with nice stability properties that begins to offer insight into the role of spines for steady-state running. A central theme to both the reactive navigation and the modular control frameworks is that analytical tractability is achieved by approximating the modes driving the environmental interactions with constant-acceleration dynamics.

Degree Type

Dissertation

Degree Name

Doctor of Philosophy (PhD)

First Advisor

Daniel E. Koditschek

Subject Categories

Robotics

AFFORDANCES AND CONTROL OF A SPINE MORPHOLOGY FOR ROBOTIC QUADRUPEDAL LOCOMOTION

Jeffrey Duperret

A DISSERTATION

in

Electrical and Systems Engineering

Presented to the Faculties of the University of Pennsylvania in Partial Fulfillment of the Requirements for the Degree of Doctor of Philosophy

2020

Supervisor of Dissertation

Daniel E. Koditschek, Alfred Fitler Moore Professor

Graduate Group Chairperson

Alejandro Ribeiro, Professor of Electrical and Systems Engineering

Dissertation Committee
George Pappas, Professor of Electrical and Systems Engineering
Daniel E. Koditschek, Professor of Electrical and Systems Engineering
Mark Yim, Professor of Mechanical Engineering and Applied Mechanics
Aaron M. Johnson, Professor of Mechanical Engineerings, Carnegie Mellon University

AFFORDANCES AND CONTROL OF A SPINE MORPHOLOGY FOR ROBOTIC QUADRUPEDAL LOCOMOTION

ACKNOWLEDGEMENTS

I would like to acknowledge and thank the sponsors who supported this work. I primarily received funding from the National Science Foundation Graduate Research Fellowship under Grant No. DGE-0822, from the Army Research Office under Grant No. W911NF-17-1-0229, and from the Army Research Laboratory under Cooperative Agreement Number W911NF-10-2-0016.

Thank you to my advisor, Daniel Kodischek, for pushing me to grow as a thinker and for contributing his deep insight into supporting my work. Thanks to my committee members Mark Yim, George Pappas, and Aaron Johnson for their helpful suggestions and putting up with my scheduling inquiries. This work wouldn't have been possible without the community that is Kodlab, and the greater GRASP lab in general. Thank you to all my labmates, I've been so lucky to have you as friends and coworkers from whom I've learned so much. In particular, those who helped me find my footing early on in my Ph.D. deserve special mention. Thanks to Aaron Johnson, Deniz Ilhan, Avik De, Sonia Roberts, and Gavin Kenneally. I feel my education in robotics really came from you guys, through numerous conversations in lab and discussions over pints at Mad Mex. Thanks to Dan Guralnik for the many insightful talks, to Paul Reverdy for invaluable support on navigating the Ph.D. process, and to Diedra Krieger for all her help and time over the years. During my time as a Ph.D. student I had the opportunity to work with some great undergraduate and masters students: Mike Choi, Jenni Herchek, Karena Kai, Mitch Fogelson, Benjamin Bernstein, Benjamin Kramer, and Meghna Gummadi. You are all amazing, many thanks for your hard work that made this thesis possible.

Most of all, I would like to thank all of my family for their love and nurturing support throughout my life, and the opportunities and encouragement they gave me to pursue engineering – especially my parents Mike and Ellen Duperret. In particular, extra special thanks to my wife Liz who supported me immensely through the process and without whom none of this would have been possible. And my cats.

ABSTRACT

AFFORDANCES AND CONTROL OF A SPINE MORPHOLOGY FOR ROBOTIC QUADRUPEDAL LOCOMOTION

Jeffrey Duperret

Daniel E. Koditschek

How does a robot's body affect what it can do? This thesis explores the question with respect to a body morphology common to biology but rare in contemporary robotics: the presence of a bendable back. In this document, we introduce the Canid and Inu quadrupedal robots designed to test hypotheses related to the presence of a robotic sagittal-plane bending back (which we refer to as a "spine morphology"). The thesis then describes and quantifies several advantages afforded by this morphological design choice that can be evaluated against its added weight and complexity, and proposes control strategies to both deal with the increase in degrees-of-freedom from the spine morphology and to leverage an increase in agility to reactively navigate irregular terrain. Specifically, we show using the metric of "specific agility" that a spine can provides a reservoir of elastic energy storage that can be rapidly converted to kinetic energy, that a spine can augment the effective workspace of the legs without diminishing their force generation capability, and that – in cases of direct-drive or nearly direct-drive leg actuation – the spine motors can contribute more work in stance than the same actuator weight used in the legs, but can do so without diminishing the platform's proprioceptive capabilities. To put to use the agility provided by a suitably designed robotic platform, we introduce a formalism to approximate a set of transitional navigational tasks over irregular terrain such as leaping over a gap that lend itself to doubly reactive control synthesis. We also directly address the increased complexity introduced by the spine joint with a modular compositional control framework with nice stability properties that begins to offer insight into the role of spines for steady-state running. A central theme to both the reactive navigation and the modular control frameworks is that analytical tractability is achieved by approximating the modes driving the environmental interactions with constant-acceleration dynamics.

Contents

List of Tables

List of Figures

CHAPTER 1

Introduction

Legged robots capable of rapid, efficient performance in any way comparable to that of their biological counterparts – especially over uneven, broken, or unstable terrain that is inaccessible to wheeled or tracked vehicles – would radically benefit applications ranging from search-and-rescue operations to the transportation of goods and services. Yet decades of work on legged platforms [228] has thus far largely yielded designs that attach legs to single rigid-bodies, despite the abundance of morphological diversity in biology such as tails and spines that contribute to locomotion prowess. In particular, locomotion using a flexible trunk is poorly understood in robotics despite its fundamental role in biological legged locomotion [87]. Throughout this thesis we use "trunk", "core", and "spine" equivalently to refer to actuated degrees of freedom that connect the front and rear legs; actuated degrees of freedom that are proximal to (rather than distal from) the mass center. A better understanding of robotic core actuation – particularly for quadrupedal running and transitional maneuvers where core actuation is commonly used in biology – is needed to quantify its advantages and disadvantages for designers.

1.1. Contributions and organization

The remainder of Chapter 1 outlines the contributions and organization of the thesis and provides relevant background information, specifically on the role of spines for locomotion and an introduction to modeling legged locomotion for the purposes of control.

Chapter 2 presents an overview of the Canid and Inu research platforms which form the experimental foundation of the subsequent chapters. Both are quadrupedal robots equipped with a parallel elastic-actuated spine that bends in the sagittal plane. To the best of the authors' knowledge, they remain (at the time of writing) the only power-autonomous

sagittal-bending spined quadrupeds that have been documented in the academic literature performing dynamic locomotion tasks. Canid (Chapter 2.1) – created from the RHex robot [103] and containing identical motors and electronics to it – provides a platform for morphological comparison with its predecessor. We describe lessons learned using this machine that motivated the creation of the Inu platform (Chapter 2.2), which has a similar spine mechanism to Canid but adds a degree of freedom to each leg.

Chapter 3 discusses the role of a spine morphology for achieving agile transitional (non-steady-state) maneuvers. The metric of specific agility is introduced (Chapter 3.1), and is used to quantify three affordances provided by a spine morphology for transitional behaviors: the ability to rapidly convert stored elastic energy to kinetic energy (Chapter 3.1), the ability to augment the leg's volumetric workspace without diminishing their force generation capabilities (Chapter 3.2), and – when using direct-drive legs – the ability to generate more work in stance than could be done using the same actuator weight instead in the legs, making it more than worth its added weight in terms of work production all without diminishing the platforms proprioceptive capabilities (Chapter 3.3). We then consider how one might apply a suitably designed agile platform for transitional maneuvers, a concept still poorly understood in the field. We introduce a formalism to approximate a set of transitional navigation tasks over irregular terrain, such as gap leaping, involving constant-acceleration interactions with the environment that lends itself to doubly reactive control synthesis along with a natural and intuitive Lyapunov function (Chapter 3.4).

Chapter 4 provides analytical insight into sagittal-plane bounding with a locked back, the beginnings of a formalism we believe can be applied to bounding with an unlocked spine (we leverage the locked-back analysis for insight into spined running in Chapter 5.4). This formalism is modular and – like in Chapter 3.4 – utilizes constant-acceleration dynamics that drive environmental interaction to obtain analytical tractability. A hybrid dynamical systems model of locked-back sagittal bounding is introduced (Chapter 4.2), followed by an analysis of a hybrid periodic orbit (Chapter 4.3) and a discussion of its stability (Chapters

4.4, 4.8). The controller is then demonstrated on the Inu platform using a locked back (Chapter 4.5).

Chapter 5 introduces the beginnings of steady-state running utilizing the spine. We introduce a simplified model containing a spine joint (Chapter 5.1) and demonstrate a correspondence between experimental data of Inu running with an unlocked spine – to our knowledge, the first such documentation of power-autonomous spined bounding in the literature – with a controlled simulation of the simplified model (Chapters 5.2 and 5.3). The relationship between the experimental work bounding with a spine and the locked-back formal analysis of Chapter 4 is then discussed (Chapter 5.4).

Chapter 6 provides concluding remarks, discusses possible future work, and considers the implications of the contributions of this thesis.

1.2. Background

1.2.1. Morphological affordances

Morphology influences behavior and performance [7, 116] as it is a mechanism to take advantages of the complex relationship between a physical agent and its environment. By morphology, we mean an agent's structure [137] (its body), including any measurable aspects of its physiology [13]. This complex relationship between body, environment, and performance is expressed by Gibson's notion of an affordance [95]. "The affordances of the environment are what it offers the animal, what it provides or furnishes...It implies the complementarity of the animal and the environment." [95, p. 127], or – more succinctly – they are an opportunity for action [107, p. 290], [181, p. 1]. We are most familiar with the usage of legs as a morphology to traverse our environment, however nature is full of examples of creative ways of using body morphology to move [71]: different numbers of legs [91], or the use of tails [145], fins, and wings to name a few [7]. Such benefits can be energetic, related to stability, or many other performance metrics that influence fitness [7].

In biology, clever usage of body-environment interaction can offer enormous benefits, the oft-used example of the albatross being one of the most impressive: soaring on the ocean's atmospheric shear layer close to the water's surface reduces metabolic cost-of-transport so much for these birds that – remarkably – flying is not the primary energy expenditure when foraging over vast distances [17]. Well studied examples of affordance utilization include geckos' ability to leverage the quantum dynamics phenomenon of van der Waals forces in their feet to exhibit impressive climbing ability [21,22], and cockroaches' encoding of running and obstacle navigation control into the mechanical aspects of their bodies [117, 203].[1]

As robotic locomotion is likewise a synergy of morphology and environment, the literature on animal morphological affordances contains some general principles useful to roboticists: Natural physical dynamics must be contended with or leveraged – despite the fact they are often complex and emergent [161], indeed as Marc Raibert (whose seminal work [175] arguably launched the careful study of dynamical legged machines) has been quoted: the central control authority "can only make 'suggestions' which are reconciled with the physics of the system and the task" [51, p. 556]. Environments can constitute energy landscapes as related to movement [200]. Computation (and even cognition itself [221] which is thought by some to perhaps require "grounded" embodiment [24]) may be offloaded from an agent to its body and environment [135], providing analog computation of sorts that can result in "unexpected simplifications of the control problem" [52, p. 12812] and "opportunities for neural control" [51, p. 553], for example affording "cheap and efficient tricks for generating situation-appropriate action on the fly" [221, p. 628].[2] But robotic morphological design is a difficult, largely unsolved problem, and one should be careful to apply the principles underlying biomechanism success towards bioinspiration rather than descending into

[1] Cockroaches have been measured running fast enough through obstacle fields and perturbations that the time it takes for a full brain-neural computation "loop" to be effected can be much longer than the observed perturbation correction [178], and even "fast" reflexes can take half of a stance duration to begin their effect [203].

[2] This may seem abstract to many readers and is worth clarifying with an example many are familiar with: catching a ball. It's been observed that baseball players run to the correct location on the field so as to catch a ball not by doing calculus in their heads to estimate where the ball will land, but instead with the simple rule of running such that the ball stays at the same spot in their field of view [157].

blind biomimicry as: "the relationship between morphology and performance can be nonlinear, context-dependent, and sometimes surprising...small changes in morphology or simple changes in size can lead to novel functions, while in other cases changes in form can occur without performance consequence" [137, p. 501], and because biological and synthetic materials are often vastly different.[3]

Legged morphologies are of particular interest to robot designers as they afford movement over irregular, discontinuous terrain; they not beholden to the presence of infrastructure (as typical to wheels) nor uncluttered open space (as typical to quad-rotors). The affordances of robotic legs in various environments is a research field in its own right [181] and is beginning to indicate complex and nuanced interactions;[4] of particular interest to us is the understanding that the properties of a legged robot's body proximal to the mass-center – meaning the morphology not including the (necessarily distal) legs or other appendages that directly interact with the ground – appear to greatly influence environmental interaction. For example, Karl Murphy famously observed that a quadrupedal robot will naturally bound in a stable fashion with a mass distribution close (which he quantified) to the mass center when the legs simply kick downwards in stance, providing a robust behavior without necessitating subtle control [175, p. 193], a properties which also appears to have a biological correspondence [168]. Legged robotics is still in its nascent beginnings – locomotion prowess even approaching the albatross is clearly still science fiction – and we cannot ignore the powerful principles demonstrated by morphological affordances in biology.

[3]For example: simplified models of muscle dynamics [106] resembling that of electromagnetic motor actuation [19] hold only in tightly controlled conditions of a small regime of muscle operation [219], and the "framing" costs of adding additional muscle to an agent appear vastly superior to that of adding additional motors [197, 219]. Not to mention that animals use their muscles in a wide variety of roles beyond what is traditionally considered "actuation" in robotics [71].

[4]An early result of this was the creation of passive dynamic walking machines [154]. These machines convert gravitational energy into kinetic energy to walk down slight inclines without the use of motors [54], and their study has led to robots able to walk ultra-marathons with only small reserve of onboard power [32].

1.2.2. The role of spines for legged locomotion

Core actuation in biology

Muscular spine morphologies have a long evolutionary history in quadrupeds [128, 184], as evolutionary evidence suggests that core actuation is the primordial engine of much of terrestrial locomotion [189]. Animal tetrapods have a 400 million year history [174] of which only very little was spent developing "emancipated" therian legs [86]. Instead, vertebrate legs had a long prelude in which they appeared as struts and the body was primarily actuated by strong, segmented, undulatory trunks responsible for propulsion as animals emerged from the sea [87].

Animals today still derive locomotion prowess from their ancestral prime mover. It is generally accepted that many quadrupedal mammals obtain their highest locomotion speeds through a bounding or galloping gait [111] during which spine bending is often observed [93, 156]. For example, the cheetah – considered the fastest running mammal on earth – and the greyhound, both with similar lean musculoskeletal structures, make extensive use their spine during high speed running [30, 34, 104]. In these animals, the flexion excitation of the spine systematically coordinated with the swing of the legs provide kinematic advantages in increased stride length [105], flight leg-swing acceleration [93, 104, 156], and (when accelerating at higher speeds [220]) power production [217].

The biological literature on sagittal[5] core actuation offers many careful studies regarding its low-level mechanics [12, 47, 82, 85, 88, 92, 101, 102, 126, 172, 186, 188–191, 217] (see [112] for additional references) and its proposed role as a mechanical energy storage in gaits [4, 6, 33]. These suggest that the core can: directly contribute to propulsion and produce useful mechanical work both in running and leaping [112], increase mammalian leg retraction velocity, increase running speed through an increase in stride length (in small therian mammals, the

[5] Transverse and horizontal-plane spine bending have been studied carefully in the literature (ex: [28, 45, 179]), although such work is outside the scope of this thesis. There is also a large literature on the sagittal role of spines in primate brachiation and upright postures that doesn't fit in the thesis' focus.

spine has been observed contributing up to half of the stance length [85, 188, 191]), reduce metabolic cost-of-transport up to half via elastic energy storage (primarily through strain energy stored in back tendon, but the elasticity of vertebrae play a role as well [156]), regulate body stiffness [180], and reduce the vertical oscillation amplitude of the mass-center. Spine morphologies appear in diverse ranges of stiffnesses and range of motion [101, 102]. They are hypothesized to have other roles perhaps not pertinent to contemporary robotics such as allowing animals to curl up to allow for better heat retention (especially in smaller mammals with larger surface-area to volume ratios) [101] and to drive oscillations in chest cavity volume so as to assist with respiration (in the process phase-locking breathing and stride frequency in quadrupeds) [41, 42, 225].

Core actuation in robotics

Probably the very first flexible-spined bounding robot was the boom-supported "Planar Quadruped" developed in Raibert's Leg Lab [142], which achieved speeds of up to ∼70 cm/s in a ∼90 cm long body powered by off-board hydraulic actuators. Subsequent research has focused on the role of bioinspired gaits in flexibly spined legged platforms. For example, ELIRO-II incorporates a two degree-of-freedom spine to promote study of salamander walking gait control [134, 165]. Salamander locomotion has also inspired the development of central pattern generators (CPGs) and reflex controllers for multi-locomotor gaits such as swimming, crawling, and walking [11, 43, 115], as well as purely leg-driven flexible spined gaits [205]. Other more mammalian bioinspiration for quadrupedal robots with articulated spinal mechanical joints include GEO-II [143, 144] and BISAM [29], used to develop and explore CPG controllers. The pneumatically actuated robots [209, 226] were used for gait studies, and [129] was an interesting purely passive, gravity drive spined quadruped that bounded downhill. In contrast to our focus on robot energetics in this work, none of these rigid-link spinal-joint mechanisms are designed for operation in regimes of high kinetic energy: aside from the purely passive [129] they do not incorporate mechanisms for recycling energy absorbed into the articulated trunk from locomotive contact with the environment,

and appear limited to operation in a quasi-static regime.

After decades of work on higher-energy rigid-body legged platforms [228], robotics researchers have begun to demonstrate [1] and document [49, 89] designs for spine-actuated quadrupedal runners intended for locomotion at faster speeds. Experimental results have suggested increased running speed [133] using off-board power and gait transition stability [209], however power-autonomous empirical results are notably absent in the literature and even some mechanical designs seem to be accompanied only by simulation data [89]. Dynamical machines using spines in the horizontal and transverse planes exist [187], but as far as the author is aware, there have not been any instances of empirical power-autonomous dynamic locomotion utilizing a sagittal-plane bending spine with the notable exception of Boston Dynamics' Wildcat: a hydraulically actuated quadrupedal robot – utilizing a combustion engine to power its hydraulic compressor – which was demonstrated in 2013 running up to speeds of 8.9 m/s and (as far as we know) had an actuated spine joint [1]. It is not documented in the academic literature and there is little publicly available information regarding the spine design, the extent it was used, or how the designers believed it benefited the platform. Nevertheless, the robot's performance is quite remarkable even compared to platforms today in 2019.

There is also a sizable literature on simulating robotic core actuation, largely focusing on steady-state running gaits. Simulation studies of reduced-order models suggest that core actuation and compliance can provide increased speed, stability, and apex height while running [61, 171, 223, 227]. Self-stabilizing gaits and decreased energetic cost of transport have been found with purely passive core compliance [46], yet verifying these models on power-autonomous physical machines remains open.

1.2.3. Models for controlling legged locomotion

Legged locomotion involves the making and breaking of contact between a body and its environment. Discontinuous contact is necessitated by the fact that legs have finite reach and

must recirculate, but this allows for locomotion over intermittent footholds which gives legs an advantage in highly unstructured environments over more continuous forms of contact such as wheels. Oftentimes – but certainly not always – legged environmental interaction is dominated by reaction forces generated at the environmental contact points, and can be approximated by assuming the leg is a simple kinematic chain connecting a rigid body (representing the robot or animal) to a point stationary in space (representing the environmental contact point).

Newtonian physics lends itself to describing legged locomotion using this formulation, particularly the field of mechanics [16,97] and – more specific to robotics in particular – theories of rigid body manipulation [159] (which directly applies to locomotion through the idea of self-manipulation [124] being dual to that of manipulation). Mechanics models of legged locomotion considered in this text are assumed to be deterministic and take the form of ordinary differential equations [14]. This allows us to apply the wealth of tools from dynamical systems theory [100] (and its foundations in differential topology [141]) to analyze legged locomotion physics models [2, 5] and make formal statements about model behavior [109]. Frequently these statements take the form of asymptotic behavior (are a set of initial conditions guaranteed to eventually do the "intended" task while avoiding "bad" regions) and robustness (do nearby initial conditions or even "nearby" model formulations [15, ch. 3] themselves behave in similar ways).

However, the intrinsically discontinuous nature of legged locomotion due to making and breaking ground contact complicates this formalism, as a single set of differential equations is typically insufficient to describe different permutations of leg-ground interaction. Hybrid dynamical systems theory [23] is a popular tool to deal with this complexity, where multiple instances of continuous dynamics describe the model. The instances of continuous dynamics can have regions (called guards) that – when reached – initiate a transition (called a reset) to another instance of continuous dynamics. Usually these guards and resets occur when a leg touches down or lifts off. In this work we use the notation of [122, Section 3] to represent

hybrid dynamical systems. Results in hybrid dynamical systems are more difficult to come by, however they can allow for sufficiently expressive behavior so as to model many of the salient features of legged locomotion.

Transitional vs. steady-state tasks

Many tasks in legged robotics can broadly be classified as either steady-state or transitional. Steady-state tasks are repetitive, often cyclic tasks such as walking and running that can be encoded by some asymptotic behavior. What we call transitional (often called transient or non-steady-state) tasks are those that can't be described by a repetitive asymptotic behavior.

Roboticists are becoming increasingly successful at both implementing [1, 114, 196] and analyzing [67] dynamic steady-state legged robotic tasks such as running. Underlying this success is the mathematical understanding that many useful steady-state behaviors can be encoded as stable limit cycles of the controlled hybrid dynamics of the system. The dynamical systems literature [100] has given engineers a wealth of strategies for encoding and controlling the asymptotic properties of such systems – for example, to recast the problem of generating stable locomotion as manipulating the Jacobian of an appropriate Poincaré map of the system to have eigenvalues with magnitude less than unity at a designated fixed point. We believe this understanding has played a large role in the past decades' slow trickle of dynamical legged robots growing to a stream of academic [228] and commercial [1] advances yielding an emerging set of design and control principles sufficient for steady-state locomotion [11, 98, 109, 135, 166, 196, 204].

In contrast, tasks such as leaping, turning, and dodging [40, 70, 72, 125, 145, 210] have no well-agreed upon mathematical description that lends itself to synthesis. These tasks – which we refer to as *transitional* and intuitively think of as exhibiting agility – are inherently not steady-state but represent, nevertheless, a canonical motivating setting for legged locomotion, for example in operation over unstructured or irregular terrain such as leaping from

foothold to foothold in rubble during disaster response. The inherently transient nature of these maneuvers does not seem well-suited to straightforward encoding via asymptotic dynamical properties and seems to call for alternative formulations.

Several techniques exist in the literature for achieving transitional tasks in hybrid systems, albeit for limited classes of legged models. Implicit model predictive control [140, 152] has been used to great effect, for example, by recourse to quadratic programming [164] over a finite horizon for leaping over obstacles. Such methods recompute a solution at every step even in a static environment and are generally sensitive to their cost functions, which often are constrained to take an artificial form due to the optimization methods available and may not readily express the designer's underlying intent or handle gracefully the inherent nonlinearity of a given problem. Exciting work in sum-of-squares verification [149, 206] allows reactive local controllers via Lyapunov functions but thus far appear to be fragile in the face of model uncertainty as they can incur vanishingly small basins of attraction and it remains to be demonstrated that actuator saturation – perhaps the predominant constraint in legged locomotion – can be elegantly incorporated. Reactive techniques taking the form of sequential composition [44] such as [18, 57] can be very robust and incorporate actuator constraints, however methods are typically conservative and often require the by-hand deployment of local controllers in the environment instead of in an automated, *doubly-reactive* fashion. Classical sequential composition techniques also provide guarantees over an infinite time horizon, which can be overly restrictive for transitional tasks that may be as quick in duration as a single stride. The reachability literature's notion of maximal controlled invariant sets – the largest subset of state space for which a control input exists to achieve a safety specification – and the corresponding least restrictive safe controller – the set of all controls that make this set invariant – offer an interesting approach to achieving transitional tasks in hybrid systems [147] and can be thought of as computing the set of all reactive control solutions, however in general computation of these sets is NP-hard [55].

Compositional methods

The task of making formal statements about a legged locomotion task – be it steady-state or transitional – quickly becomes one of choosing a model sufficiently simple to yield a tractable analysis while complex enough to express the desired behavior. This is because the initial value problem in differential equations cannot be explicitly solved for except in the most trivial of circumstances, relegating designers to making "qualitative" (but still quite useful) statements about their models of the likes of quantifying asymptotic behavior, instead of explicitly describing exactly how the model will evolve. But even qualitative statements require sufficiently simple models to meaningfully apply the tools that hybrid dynamical systems theory currently provides.

Various techniques have been developed to deal with this complexity, for example the idea of templates and anchors [90]. Classically, a template-anchor relationship is one between two models (one being the template and the other the anchor) of differing complexity, specifically in which the template is an attracting invariant sub-manifold of the anchor. This allows the roboticist to design behaviors in the reduced template space and need only anchor the dynamics of the robot body to the template to inherit the template's stability properties, for example: [185]. This way of understanding complexity has also proven fruitful in the field of biology – due to both the necessity of making sense of complicated phenomenon and the inherently many-to-one mapping from form to function [207, 212, 213]. Roboticists and biologists have jointly "discovered" several canonical templates which appear to describe salient features of many modalities of locomotion such as the spring-loaded inverted pendulum (SLIP) [10, 37, 94, 194, 195], illustrating how work in this multi-disciplinary field can contribute to understanding both robotics and biology [60, 215]. The fields have also began to organize notions of composition beyond hierarchical template-anchor relationships; particularly sequential compositions [44, 58] and parallel compositions [67, 68]. These are further discussed in Chapter 4, which introduces the use of cascade compositions to models of quadrupedal running.

CHAPTER 2

Overview of the Canid and Inu research platforms

This section provides the reader with an overview of the Canid and Inu spined quadrupedal research platforms used in this document. We also offer lessons learned from our experience in designing and using the robots in experiments. At the time of publication – to the best of the authors' knowledge – they remain the only power-autonomous sagittal-plane-bending spined quadrupeds that have been documented in the academic literature performing dynamic locomotion tasks.[6]

2.1. Canid

The Canid robot was the first legged platform built with a spine morphology at the University of Pennsylvania's Kodlab. Using the same motors and electronics as the XRHex-Lite (XRL) robot, it was created to test comparative morphological hypotheses related to spined locomotion with respect to the RHex family of robots, as well as to demonstrate the ubiquity of the RHex "laboratory on legs" architecture [103]. The robot – shown in Figure 1 with its predecessor XRL – consists of a front and a rear body segment with RHex-style C-shaped legs driven by fourbar linkages, as well as a cable-driven spine. The front and rear body segments house the electronics and motors while the spine holds the two batteries (not depicted in Figure 1) between adjacent vertebrae. A table of metrics for the robot is given in Table 2.2.

Canid was created in collaboration between the U.S. Army Research Laboratory (ARL) and the University of Pennsylvania under support from the Robotics Collaborative Technology

[6]Boston Dynamics' Wildcat is a hydraulically actuated quadrupedal robot from 2013 that ran up to speeds of 8.9 m/s and – as far as we know – had an actuated spine joint [1]. It is not documented in the academic literature and there is little publicly available information regarding the spine design, the extent it was used, or how the designers believed it benefited the platform. Nevertheless, the robot's performance is quite remarkable compared to platforms even today in 2019.

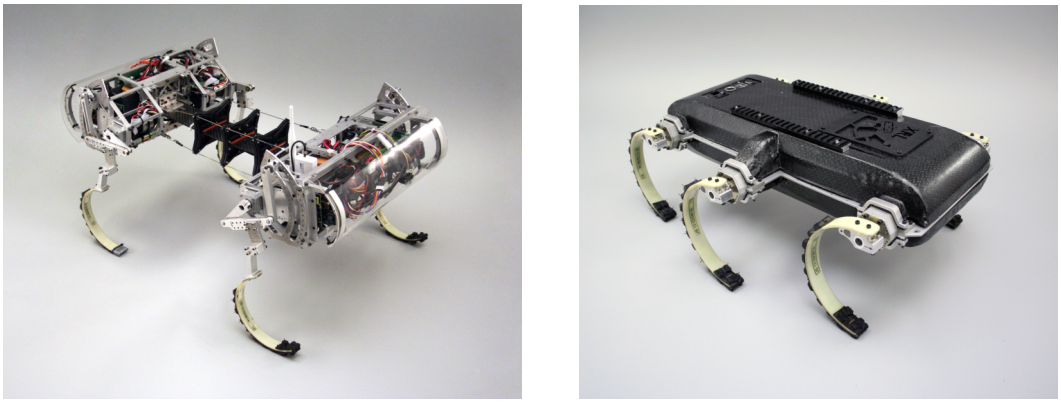

Figure 1: The Canid research platform (left) and its predecessor, the XRL robot (right).

Alliance (R-CTA). The machine was designed and built by Clark Haynes and Ryan Knopf while they were at the University of Pennsylvania, as well as by Jason Pusey at ARL. They also began the first behavioral experiments beginning to tune isolated leaps as documented in [103]. Jeff Duperret began working on the project as Clark and Ryan were leaving in 2012 and was responsible for behavior and gait generation – still in collaboration with ARL's Jason Pusey – as well as the in-house fabrication and characterization of the fiberglass leaf springs used for the spine [173].

Canid's spine consists of a rectangular fiberglass leaf spring which is actuated in parallel by a cable system driven antagonistically by two geared motors (which are identical to the leg motors) that pitch the spine up and down with one actuated degree of freedom. One motor in the rear body segment pitches the spine upwards while the other motor in the front body segment pitches the spine downwards. Care must be taken in the robot's control code to ensure that the spine motors do not fight each other; one always lets slack out as the other takes slack in. Vertebrae connect the fiberglass leaf spring and cables to constrain the bending curvature. Different fiberglass leaf springs of varying thickness can be inserted into the spine, allowing the user to use differing spine compliances as required by the experiments. The leaf springs are well-approximated as Hooke's law springs over their regime of operations, an example of which is depicted in Figure 2. The rectangular geometry of the fiberglass leaf spring prevents Canid's front and rear body segments from

yawing with respect to each other, however nothing directly prevents one body segment from rolling with respect to another. We found that this mode of movement wasn't a problem with bounding gaits where the left and right legs act in unison. During these gaits it seems that the natural damping in the system was enough to prevent this mode from being excited and leading to instability.

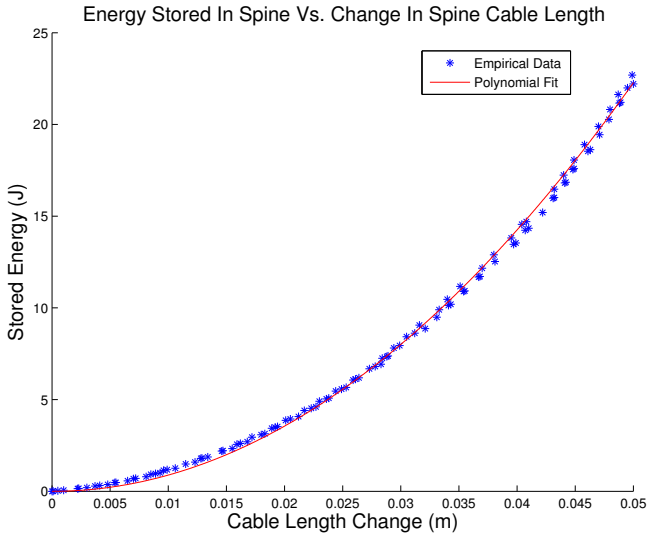

Figure 2: Energetic characterization of a Canid spine typical of those used in the leaping experiments described in Chapter 3.1. The results indicate that the spine elastic energy storage is well-described by a Hooke's law quadratic polynomial fit.

Canid was able to bound forwards in a halting manner that did not maintain significant kinetic energy between strides [173], as well as catapult itself forwards in a bounding leap utilizing stored elastic potential energy in the spine in parallel with spine-motor actuation. These isolated leaps greatly outperform its RHex predecessors in terms of leaping distance and energetics [74], and are described more in-depth in Chapter 3.1.

The biggest limitation to achieving steady-state gaits and transitional maneuvers in a variety of environments on Canid was the fixed leg trajectories imposed by the fourbar mechanism as depicted in Figure 3. The mechanism was introduced to give the robot user a way of selecting an appropriate leg trajectory for a task while maintaining a relatively constant motor shaft speed, a feature not necessary on the ancestral RHex robot because the presence

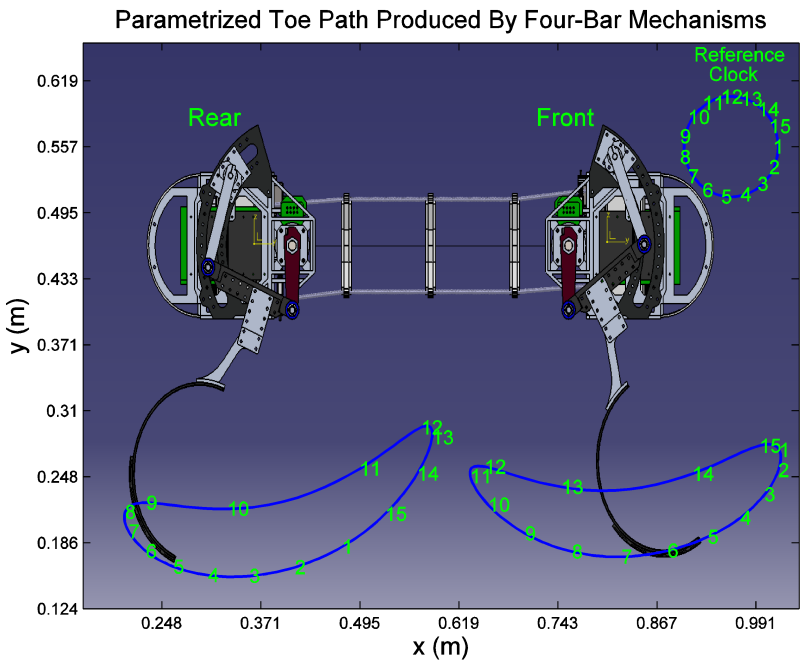

Figure 3: Toe path trajectory imposed by Canid's fourbar kinematics, which can be modified between experiments to achieve various shapes. The reference clock in the upper right gives a correspondence between the angle of the dark-red crank-shaft at the motor's gearbox output and the toe position.

of more legs obviated the need for large sweeping leg trajectories. The inability on Canid to vary the leg trajectory shape at "execution-time" of a behavior caused several problems that motivated the creation of the Inu robot. One primary function of a robot's legs is to generate frictional and normal forces at the "toes"[7] so as to apply a wrench on the mass center, thus the legs' ability to vary this wrench as part of a feedback loop is critical. Canid's one degree-of-freedom legs made it very difficult to regulate both the generated frictional and normal forces at the same time, resulting in seemingly needing the halting nature of its bounding gait as a strategy to correct disturbances for which Canid lacked the control affordance to actively cancel out. The lack of control authority in varying the ground-reaction force also made it very difficult to stay within the friction cone during leaps. We tried giving Canid "claws" to greatly increase its coefficient of friction, which worked well on neoprene mats in a lab environment. But when Canid was attempting leaps across drainage

[7]We refer to the point of leg-ground contact as the "toe" in this work.

gaps at the Fort Indiantown Gap Army Post, it was unable to use the same trajectories without slipping. This experience made clear the need for additional degrees-of-freedom in the legs when conducting agile quadrupedal maneuvers.

2.2. Inu

The Inu robot – successor to the Canid robot – was created primarily to address the need for a spined quadrupedal platform having more than one actuated degree of freedom in its legs, so as to better utilize the spine mechanism. Inu's two degree-of-freedom (2-DOF) legs do not utilize springs and instead rely on high bandwidth and proprioceptive capabilities of its direct-drive [19] leg motors to achieve artificial compliance and high-fidelity ground-contact sensing [132,196]. Its spine is functionally similar to Canid's but has some features that make it lighter and easier to use as described below. Inu also departs from the RHex electronics architecture and instead uses custom lab electronics similar to that of the Minitaur robot. A more detailed comparison of the Inu and Canid platforms is given in Table 2.2.

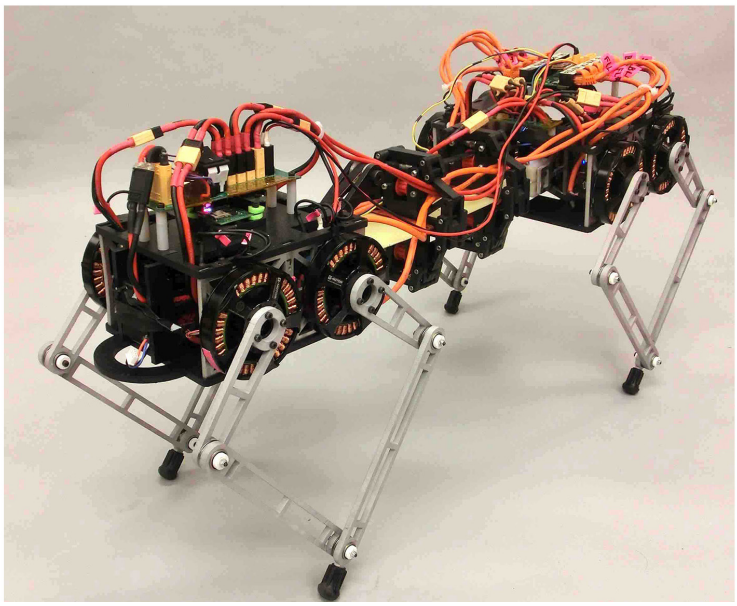

Figure 4: The Inu robot.

Inu's legs are similar to that of the Minitaur platform [132] in that the linkage configuration

is a parallelly actuated five-bar, however – different from Minitaur – Inu's leg linkage has the motors placed in a co-planar fashion rather than co-radially. This increased the mechanical simplicity of mounting the motors to the robot body and decreased the width of the robot at the expense of reducing the workspace volume of the leg linkage. The bottom row of Chapter 3.2's Figure 10 depicts both the workspace of Inu's legs as well as the averaged squared singular values of the leg linkage's forward kinematic Jacobian over the workspace. Most of the lost workspace occurs above the robot, which is very useful to have if the robot flips over on its back because it can allow the robot to run symmetrically upside-down, however behaviors like this were outside the mandate of the Inu research platform.

We found that Inu's 2-DOF direct-drive legs function much better than Canid's geared 1-DOF legs for achieving steady-state gaits, as was expected. However, they lack the force affordance to generate as powerful of leaps as Canid could. While the spine is able to compensate some for this, as described in Chapter 3.3, the platform would still be able to leap further if the legs were geared. But this would would come at the cost of reduced proprioceptive capabilities and would make investigating the role of a spine morphology for steady-state gaits – where the ability to easily detect ground contact is a great virtue – more difficult.

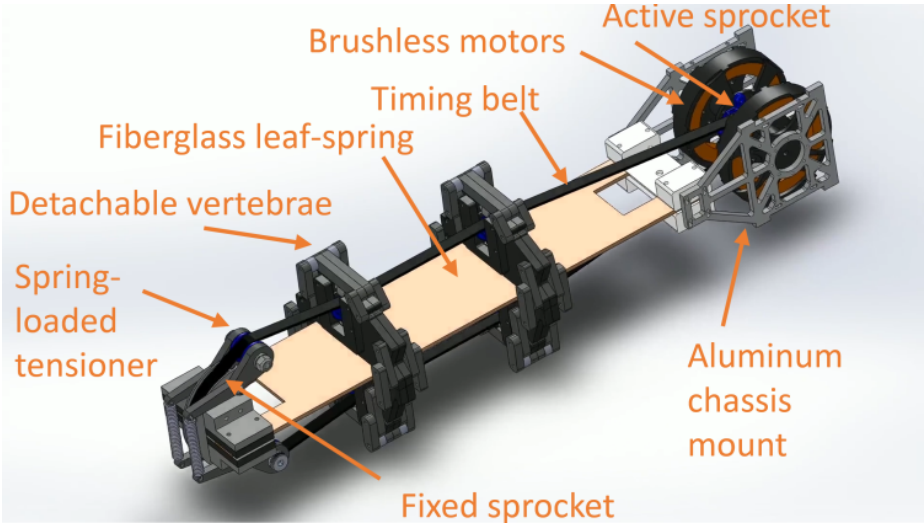

Figure 5: Annotated rendering of Inu's spine mechanism.

Inu's spine was designed based on lessons learned from the Canid robot, although functionally it is quite similar to Canid's. The mechanism was made significantly lighter by removing many steel and aluminum components, and the cable system was replaced by a belt-drive system which we found easier to work with. Perhaps most significantly, Inu's two spine motors together act in parallel on the same sprocket shaft to drive the belt, so that during extension or contraction the spine is always using both motors to do useful work. The system is designed so that when the motors pull on the belt from one direction, they in doing so let out a sufficient amount of slack in the other direction so as not to impede bending. Two motors were used to provide the spine module the same available power as each leg module. The final major difference was that latches were installed on the vertebrae for easy removal. This greatly decreased the time required to swap out fiberglass leaf springs as compared to in Canid, where each vertebrae needed to be disassembled by removing all of its bolts to change a spine spring.

	Canid	Inu
Body weight (w/ batteries)	11.3 kg	6.8 kg
Body length	78 cm	70 cm
Spine leaf-spring length/width	44.0 cm / 7.6 cm	34.0 cm / 7.6 cm
Hip-to-hip length	47 cm	47 cm
Maximum hip-height	29 cm	33 cm
Total number of motors	6	8
Motors per leg	1	2
Motors in spine	2	2
Motor type	Maxon EC-45, 50 W	Tiger Motor U8-16, 100 kv
Leg motor gearing	28:1 Maxon planetary gearbox	None
Batteries	2 5-cell Thunderpower TP2250-5SP30 batteries	1 4-cell Thunderpower TP6400-4SRP80 battery
Nominal bus voltage	37V	14.8V
Sensing	Motor shaft encoders, IMUs on front and rear body segments	Motor shaft encoders, IMUs on front and rear body segments
Inertial measurement unit (IMU)	3DM-GX3-35 MicroStrain	InvenSense MPU6000

Table 1: Metrics comparing the Canid and Inu robots.

CHAPTER 3

Spines and transitional behaviors

Chapters 3.1, 3.2, and 3.3 describe and quantify affordances that can be provided by a spine morphology for transitional maneuvers. To assist in making statements of comparative morphology in these sections, we introduce the metric of specific agility in Chapter 3.1. Chapter 3.1 discusses elastic energy release in the spine, Chapter 3.2 deals with how the spine can augment the leg's workspace, and Chapter 3.3 goes over benefits of adding actuation proximal to the mass center (via the spine) rather than distal from it (via the legs) on a machine with direct-drive legs. Finally, we end on the topic of what can be done with a machine possessing significant agility; in Chapter 3.4 we offer the beginnings of a computationally tractable method for executing doubly reactive transitional maneuvers to navigate irregular terrain. This marks the first instance in this document of obtaining analytical simplicity by having environmental interaction be driven by dynamics approximated by constant acceleration, a theme that will be further explored in Chapter 4.

3.1. Specific agility and spine elastic energy storage

3.1.1. The metric of specific agility

We are still in the early stages of understanding how to characterize legged agility. In this passage we propose a measure for nimble legged transitions that help organize a suite of experiments designed to test hypotheses about the comparative benefits of specific morphological features [74]. Following the tradition of the more mature aircraft [162], aquatic [216], and wheeled [53] vehicle literatures (wherein variously dimensioned agility and maneuverability measures are introduced for different purposes and at different operating points), we explore the utility of a dimensional measure (m^2/s^2) that at the very least proves useful for comparing legged leaps from rest of different machines. Given its (rough) invariance across

animal leaping maneuvers, this measure may also have relevance for probing biological energetics. Most immediately, we aim to apply insights provided by the empirical support or refutation of our stated hypotheses toward the design of more agile machines.

Notwithstanding the many informative and inspiring studies of legged animal performance, e.g. [26, 27, 121, 158, 167, 183, 214], we have not been able to find any previous formalization of the notion of legged agility suitable for comparing robots of different morphologies and different sizes over different tasks. Perhaps the most common measure for acceleration and leaping used in the legged biology literature is specific power (watts per kilogram taken over a gait cycle of leg power output relative to leg muscle mass or body mass) [155, 182, 183, 220] but it is not scale invariant as we observe in Chapter 3.5. Specific work has been proposed as a measure for legged leaping with respect to muscle mass [183], and this seems closest to the body-mass normalized measure we will introduce shortly. In contrast, characterizing directional aspects of agility performance seems trickier. Animal turning maneuvers have been studied in robotics [110] as well as biology [120] yielding a variety of useful associated performance measures such as turning radius at speed, leg effectiveness, linear maneuverability number [119], and usage of braking/acceleration forces [118]. But it is not clear to us how to generalize such measures for reasons we will discuss below as well.

Many intuitive measures for a legged platform involving, say, jumping height or the magnitude of linear acceleration, are equivalent to a change in kinetic and gravitational potential energy during the stance phase of locomotion. Thus, we focus our proposed measure on the change in what we term the *extrinsic body energy*, the sum of the mass center's kinetic and gravitational potential energy, relative to the natural unit over which a legged platform can adjust it, a single, isolated stance. We use the qualifier "extrinsic" to distinguish this notion from the body energy introduced in [173] that is sensitive to the state of a platform's internal mechanical springs. Catapult-like elastic energy storage used to augment muscle power in leaping from rest has been shown to occur in animals across widely different scales [20, 27] and, intuitively, we feel such use of initially stored spring energy should not count against

the agility of a transition. We also avoid the notion of "stride" which connotes a regularity of stance and swing that may not prevail in sudden legged maneuvers characterized by combinatorial sequences of leg contacts [125]. Instead, we construe "stance" as the dimensionless event characterized by some number of legs in ground contact, punctuated either by a prior or subsequent aerial phase (or both).

Thus we find it useful to introduce a working notion of *specific agility* during stance in terms of the mass-normalized change in extrinsic body energy:

$$\alpha := \frac{\Delta W}{m} / \textit{stance event}, \tag{3.1}$$

where ΔW is the extrinsic body energy (the sum of the mass center's kinetic and gravitational potential energy) at the end of stance minus the extrinsic body energy at the start stance, and m is the mass of the agent. The SI units of α are $(\mathrm{m/s})^2$ and can be interpreted as mass-specific work in the equivalent units of (J/kg). Note that steady-state motions such as running or hopping that can be approximated with Hamiltonian systems will have negligible agility according to our metric in accordance with biological observations that these motions require significantly less muscle power output as compared to leaping accelerations [155, 183].

As we have tried to suggest in our brief survey of the extensive literature, and seems most carefully summarized in [216], it does not appear straightforward to find a single dimensionless group capable of capturing all relevant aspects of maneuverability and agility. We tolerate the lack of a dimensionless measure in our quantification of agility because mass-specific work seems to be the fundamental quantity of interest — at least for changes in velocity magnitude. For example, measuring work done on the body during stance is sensitive to accelerations along a velocity vector fixed in the inertial frame and takes into account the operating point, capturing the greater energetic cost of accelerating a given amount at higher relative to lower speeds (such energetic costs are consistent with

biological observations of animal accelerating and braking [220]). However, it does not reward purely directional changes even though, intuitively, rapid turns ought to represent a similarly important concomitant of any comprehensive "agility" measure. Any attempt to reconcile nimble turning with energetic expressions of performance must address the fact that fixed rate circular motion entails no work since the direction of motion is orthogonal to the force.

The proposed measure (3.1) does appear to confer some scale invariance. In biology, this is predicted by arguments found in [192] and empirical observations of vertical jumping height known as Borelli's law [65]. This "law" is demonstrated in animals across eight orders of magnitude mass variation which are shown to have vertical jumping heights (proportional to specific agility if air resistance is neglected) within a factor of three — ranging from around 20 to 60 cm or a specific agility of around 2 to 6 m^2/s^2. Similar arguments about the scale invariance of this measure with electromagnetic actuators in a robotic leg are detailed in Chapter 3.5.

Spine elastic energy release

The first benefit potentially afforded by a spine morphology (assuming a suitable design implementation) that we discuss is the rapid release of stored elastic energy that the spine can contribute to forward leaping energetics. We show from comparative empirical observation a case where the usage of parallel actuation to guide this spine elastic energy release for forward leaping is an energetically better usage of actuator weight than actuating additional legs.

We use the metric of specific agility to compare the performance of Canid [173] and XRL [103] – two comparably powered but morphologically different robots that are shown in Figure 6 – in the open-loop leaping-from-rest task, a transitional behavior of near ubiquitous value, e.g. in gap crossing or rapid preparation [44] of high energy steady-state gait basins [94]. We use this comparison to examine the relevant benefit of distal versus core actuation

as the quadrupedal Canid uses two motors to actuate its spine while the hexapedal XRL uses these two motors to actuate a pair of additional legs. This comparison seems particularly apt because of the close relationship between the two machines described in [103]: both robots have the same electronics, use similar motors and gearing, and are capable of comparable (respecting speed and specific resistance) steady-state locomotion as partially documented in [173]. Disregarding the spine, the platforms differ primarily in their mass — Canid weighs 11.3 kg while XRL weights 7.3 kg — and leg actuation as Canid's four hip actuators drive their C-legs through a four-bar linkage while XRL directly actuates its six C-legs. It is worth noting the enabling role the specific agility measure plays in allowing this comparison that requires somehow normalizing for the very different actuation strategies used by these two nominally similar machines during forward leaping. Canid only uses three of its six motors to generate work (actuating its rear two legs and the top spine cables), while XRL uses four of its six motors (two are not used since they contribute little to leaping [125]).

We pause to briefly introduce the concept of endurance. The operational utility of an agile motion will generally depend on the number of times n it can be performed in succession – which we term *endurance*. Given resource constraints present in executing a movement, we expect endurance to decrease with increasing specific agility. For example a robot that heats its motors to its thermal limits in a single leap cannot immediately perform the same leap on the next step; it must wait until its motors cool before completing the action again, giving it an n of one. A robot capable of performing an agile motion an infinite number of times (unlikely with current technology given limited energy storage) would have an n of ∞. Although "stance event" was introduced as taking integer values, we find it convenient to recast the measure as taking (extended) real values. Thus we will consider the ordered real pair (α, n) when evaluating agile motions in an experimental setting. Further details regarding the calculation of endurance are given in [74].

Canid leapt 11 times under a motion capture system,[8] including five times across an 85

[8] Vicon motion capture data is used to back out the kinetic and potential energy of the robots. Neglecting air resistance, the apex specific extrinsic body energy minus the starting specific extrinsic body energy gives

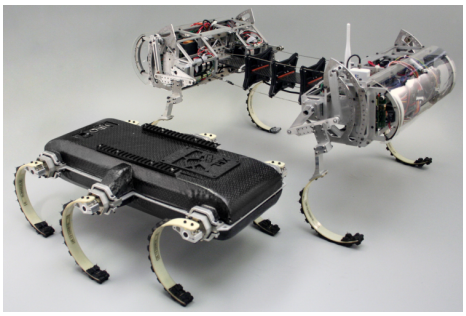

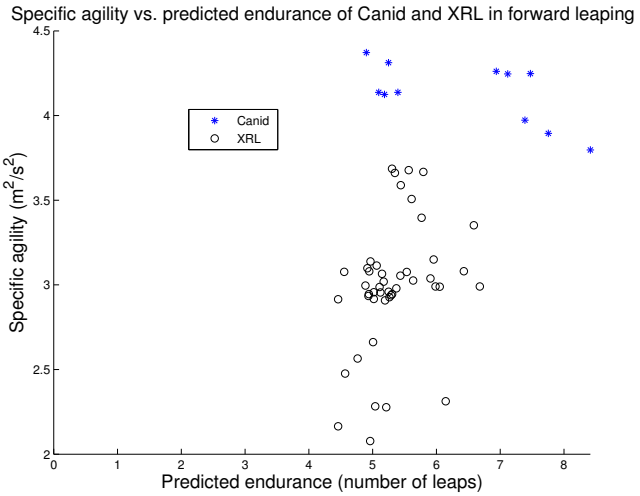

Figure 6: The Canid (left image, upper right) and XRL (left image, bottom left) robots. Their specific agility vs. predicted endurance during forward leaping is shown on the right. The methods used for calculating these quantities are explained in Footnote 8.

cm gap which is close to the observed limit of its repeatable leaping ability from standstill (leaps over gaps up to 1 m across have been achieved however not in a repeatable fashion). XRL leaping data was taken from [123] during which parameters for quadrupedal forward leaping were systematically varied to search for various high extrinsic body energy forward leaps. The best XRL forward leap crossed a 50 cm gap, which is likely very close to the limit of its leaping ability from standstill.

The resulting specific agility and endurance for each Canid and XRL leap is shown in Figure 6. Canid has a better maximum observed specific agility than XRL at a comparable endurance, despite using one fewer actuator. Although it is likely that we could tune both machines to perform incrementally better, such adjustments would likely further advantage Canid, since this was the very first leaping experiments with Canid whereas XRL leaping has already benefited from extensive past study and tuning [123]. These results indicate that at least one of the salient morphological differences between Canid and XRL confers upon Canid a significant agility advantage, particularly in light of its reduced (one fewer)

a very close approximation to the specific agility (3.1) of the leap. The method used to calculate endurance is given in [74].

number of actuators used during liftoff.

Additional experiments summarized in Figure 7 were conducted on Canid to quantify the relative agility benefit conferred by Canid's parallel elastic actuated spine (rather than its four-bar leg transmission) while leaping. Forward leaping data was collected on Canid using five different spine stiffnesses varying from rigid to negligible stiffness. Zero agility is recorded in the case where the robot was unable to achieve an aerial phase due to insufficient spine power. For each spine stiffness, Canid was run multiple times while systematically varying its spine motor current limit from 15 A to 0 A in increments of 5 A — always from the same initial condition for every run (except for the rigid case) characterized by a spine preloaded to the same angular displacement prior to its release with lowered current limit reset at the onset of leaping. While successively more compliant spines afford the possibility of successively greater spine pre-loading by a given actuator, we chose to fix the pre-loading angle because: (1) this avoids the confounding effects of varied initial posture (and attendant variations in control strategy); and (2) the spine motors are capable of breaking the elastic fiberglass plate and it is not yet clear at which point plastic deformation begins. The spine stiffness is approximated by empirical data fit to a torsional Hooke's law spring as discussed in Chapter 2. Current limits above 15 A are tenable in principle for our actuators, but do not result in substantially different results in any of these cases because the rapidly extending spine quickly brings them into the no-load regime.

The results in Figure 7 indicate that — all else being equal — replacing a rigid back with a sufficiently powered spine mechanism (either through releasing initially stored elastic energy or through actuation) can provide a significant morphological advantage for forward leaping agility. We can directly account for energy initially stored in the elastic spine contributing to leaping kinetic energy, as the $k = 1.82$ Nm/rad spine with no actuation outperforms the fully actuated negligible stiffness $k = 0.14$ Nm/rad spine as well as the rigid spine (both of which initially store a negligible amount of initial elastic energy). Also, the monotonic average increase in agility with increased spine actuation power indicates that the spine motors

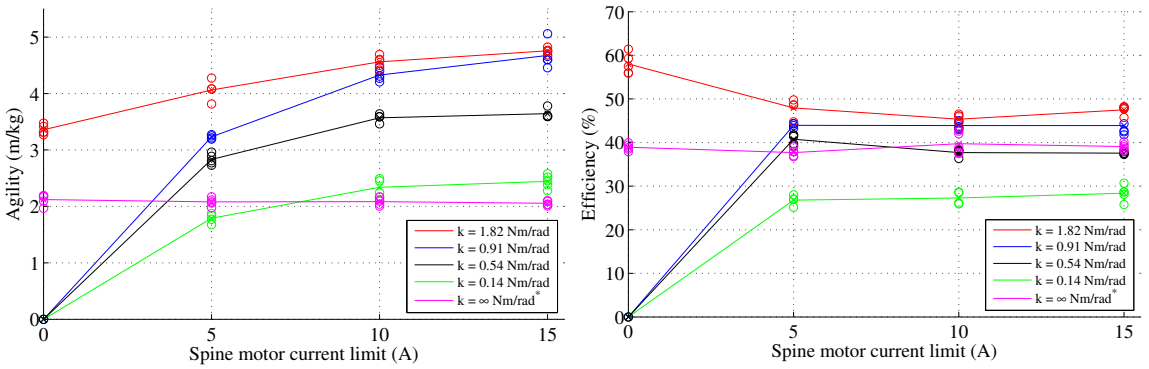

Figure 7: (Left) Canid leaping agility with a variety of spine stiffnesses and spine motor current limits. A total of 80 runs are shown. Canid was allowed to pre-load its spine to the same angular displacement in every run (except for the rigid case) before setting the lower spine current limit and leaping. Zero agility is recorded in the case where the robot was unable to achieve an aerial phase due to insufficient spine power.
(Right) Energetic efficiency of the experiments shown in Figure 7. Energetic efficiency was calculated by dividing the total change in extrinsic body energy during the leap by the combined mechanical energy output of the motors (comprising of Canid's two rear leg motors and the spine motor actuating the top spine cables). This motor energy output is calculated at the output shaft before the gearbox and thus doesn't directly take into account gearbox or transmission inefficiencies.
*The k = ∞ case is approximated and was not empirically measured for fear of damaging the spine. Rigidity was achieved by locking the spine mechanism with minimal added mass.

are directly contributing to forward leaping agility irrespective of spine elastic stiffness — except for of course in the rigid case. The greatest observed forward leaping performance was achieved with the k = 0.91 Nm/rad and k = 1.82 Nm/rad spines using the highest spine actuator current limits, averaging a specific agility of 4.7 m^2/s^2. This is likely because the nature of parallel elastic-actuations allows the release of the elastic energy stored in the spine to augment the spine motor power during the leap, supporting our claim that using parallel elastic spine actuation outperforms both a purely actuated and purely elastic spine in forward leaping. However if efficiency is deemed more important than raw agility then the performance using the unactuated k = 1.82 Nm/rad spine shown in Figure 7 demonstrates that a sufficiently stiff spine, if properly pre-loaded in stance (either by motors or by a prior maneuver) may offer almost similar agility with considerably greater efficiency. Further details regarding the analysis of these experiments are given in [74].

We note that sufficiently-powered core actuation substantially increases rear leg loading in forward leaping. Specifically, the more than two-fold increase in average specific agility between the rigid back (2.1 m^2/s^2) and the best spined runs (4.8 m^2/s^2) must have been accompanied by a more than two-fold increase in average rear leg forces given the nearly constant stance duration during the runs. Canid avoids torque-saturating the rear leg motors with spine forces by operating the rear legs near their kinematic singularity when the spine is doing work. Similar consideration of rear-leg kinematics is advised in general if a spine is added to a legged machine, a concept explored more carefully when using direct-drive legs in Chapter 3.3.

In summary, leaping experiments suggest that a significant specific agility benefit is conferred by adding a four-bar and a parallel elastic actuated spine [173] to the base XRL robot at no cost to endurance. Canid uses fewer actuators to leap significantly further. Further investigation into characterizing the isolated benefit of the spine concluded that — all else being equal — replacing a rigid back with a sufficiently powered spine mechanism (either through releasing initially stored elastic energy or through actuation) can provide a significant morphological advantage for forward leaping agility. There was a measurable individual specific agility contribution from both spine actuation and releasing stored elastic energy in the spine. Furthermore, a parallel-elastic actuated spine confers a larger specific agility benefit to forward leaping than does a purely actuated or purely passive spine.

3.2. Volumetric workspace augmentation

For legged robots operating in unstructured environments, workspace volume and force generation are competing, scarce resources. In this section we demonstrate that introducing core actuation (i.e., proximal to rather than distal from the mass center) increases the legs' effective workspace volume without decreasing their force generation capabilities, in some respects circumventing this trade-off [80]. These effects are analytically quantifiable up to modest assumptions, and are demonstrated empirically on the Inu robot perching on an isolated foothold – an archetypal feature of unstructured terrain expected in disaster scenarios,

on which contemporary quadrupedal robots typically are incapable of self-manipulation.

It is desirable for the limb kinematics to produce high forces for given motor torques. Increasing force generation by decreasing lever arm length, however, trades away workspace size. Larger workspaces are highly beneficial in unstructured environments; they afford better access to intermittent footholds and improved body self-manipulation over a wider range of postures. A small workspace runs the risk of the robot becoming high-centered and losing balance on smaller footholds. We explicitly show the trade-off between leg force generation and workspace volume confronting the designer by considering a simple scaling of a nominal leg linkage design by a scaling factor λ, assuming a fully actuated leg interacting with the ground through a point contact. Let the forward kinematic map of the nominal leg linkage with a point toe and origin at the hip be given by $f : Q \to \mathbb{R}^n$, where $q \in Q$ denotes the actuated joint positions. Consider a uniform scaling transformation applied to this linkage, scaling the length of all vectors by a factor of $\lambda \in \mathbb{R}^+$, and let $f_\lambda(q) := \lambda f(q)$ denote the forward kinematic map of the scaled linkage. The nominal leg linkage has a workspace volume given by $V := \int_{f(Q)} \Omega$, where Ω indicates the standard volume form on $\mathbb{R}^n$ [159]. The forces F generated at the toe from motor torques τ is then given by $F(q) := Df^{-T}(q)\tau$ assuming the leg linkage is not at singularity, where $Df := \frac{\partial f}{\partial q}$. Denoting the workspace volume of the scaled linkage by $V_\lambda := \int_{f_\lambda(Q)} \Omega$ and the forces generated at the toe by $F_\lambda(q) := Df_\lambda^{-T}(q)\tau$, we have that

$$\begin{aligned} V_\lambda &= \int_{\lambda f(Q)} \Omega = \int ... \int_{\lambda f(Q)} dx_1 ... dx_n = \int ... \int_{f(Q)} \lambda dy_1 ... \lambda dy_n \\ &= \lambda^n \int ... \int_{f(Q)} dy_1 ... dy_n = \lambda^n V \end{aligned}$$

and

$$F_\lambda(q) = (\lambda Df(q))^{-T}\tau = \frac{1}{\lambda} Df^{-T}(q)\tau = \frac{1}{\lambda} F(q),$$

so that increasing scale has the dual effect of decreasing end effector force magnitude for a

given motor torque vector while increasing workspace volume.[9]

To quantify the effect of the spine on the legs, we use a typical quadrupedal model – depicted in Figure 8(a) – as a rigid body with common distances between the hips and mass center [164, 170]. Following [46, 61, 89, 171], we add core actuation to this model by introducing an actuated revolute joint to the body, depicted in Figure 8(b) (note that alternative formulations exist, such as [227]).

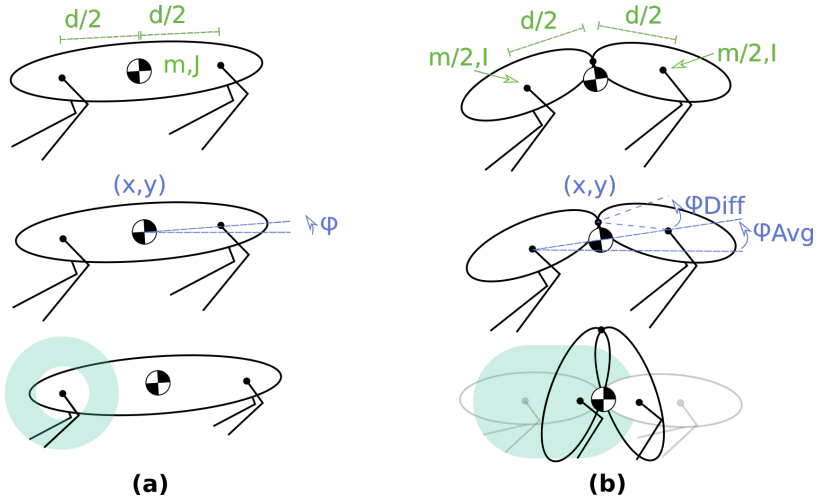

Figure 8: (a) Simplified sagittal-plane three-degree-of-freedom model of a rigid body quadrupedal platform. (b) Simplified sagittal-plane four-degree-of-freedom model of a spined quadrupedal platform possessing an actuated revolute joint proximal to the mass center. The models have a simple parametrization (mass, moment of inertia, and body segment length) shown in green, and their degrees of freedom (mass center position, average body pitch, and – for the spined model – the difference between the pitch of the front and rear) are in blue. Spine bending augments the nominal leg workspace (depicted in teal for a nominal annulus leg workspace) and provides an additional source of actuation to do useful work on the mass center. The core can be geared without affecting the direct-drive leg transparency, as discussed in Chapter 3.3.

Core actuation allows the body to move the leg hip with respect to the mass center, thereby augmenting the leg workspace volume. Consider the simplified case of an annulus leg workspace with inner radius r_1 and outer radius r_2. The volume of the workspace is given

[9] An established metric for evaluating the ability of a direct-drive limb to generate forces is thermal cost of force (for a normalized motor constant) given by the mean of the squared singular values of the forward kinematic Jacobian [19, page 48], [132]. As shown in the analysis above, in general smaller singular values are achievable by decreasing the length of lever arms in the (possibly parallel) kinematic chain to gain a greater mechanical advantage.

by $V = \pi(r_2^2 - r_1^2)$. Assuming core bending can translate the center of this annulus a distance $\bar{d}$ with respect to the mass center and that $\bar{d} \geq r_1$, the augmented workspace provided by core actuation is $\bar{V} = \pi r_2^2 + 2r_2\bar{d}$, a volume increase of $2r_2\bar{d} + \pi r_1^2$. This is depicted in teal in Figure 8.

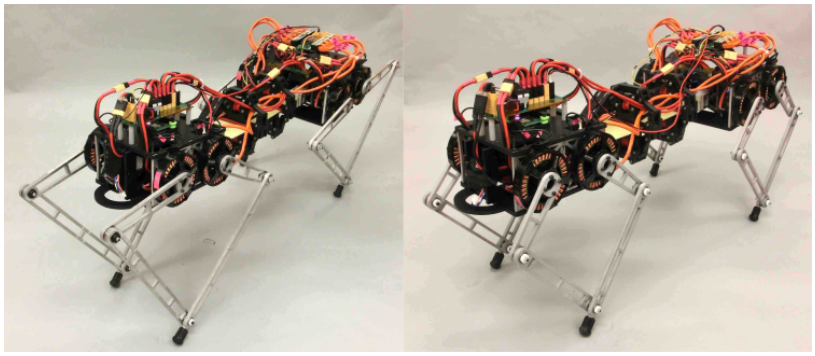

Figure 9: A version of Inu with longer legs (left) is compared with a version with shorter legs (right) in leaping from an isolated foothold, as well as from level ground in experiments described in Chapter 3.3.

To empirically illustrate the sensitivity to workspace size when operating on isolated footholds, Inu executed leaps off of a 20 cm-tall, 9 cm-wide perch as depicted in Figure 11. These leaps were performed with the longer legs shown in Figure 9 without spine bending to illustrate task performance without workspace constraints, and with shorter legs to introduce workspace constraints. Spine bending was then used with the shorter legs shown in Figure 9 to evaluate if the workspace benefit provided by the spine yielded a significant performance advantage. Each leaping configuration (long legs without spine bending, short legs without spine bending, and short legs with spine bending) was run 6 times using a feed-forward control strategy. As this experiment didn't not focus on the energetic contribution of this parallel compliance, a thin fiberglass plate storing minimal elastic energy was used. Further experimental details are available in [80].

The leg kinematics used in the experiments were chosen as follows. The ratio between the lengths of the distal and proximal link, shown in Figure 10, was found in numerical study to approximately maximize vertical leaping height over a range of scaling factors. The scaling

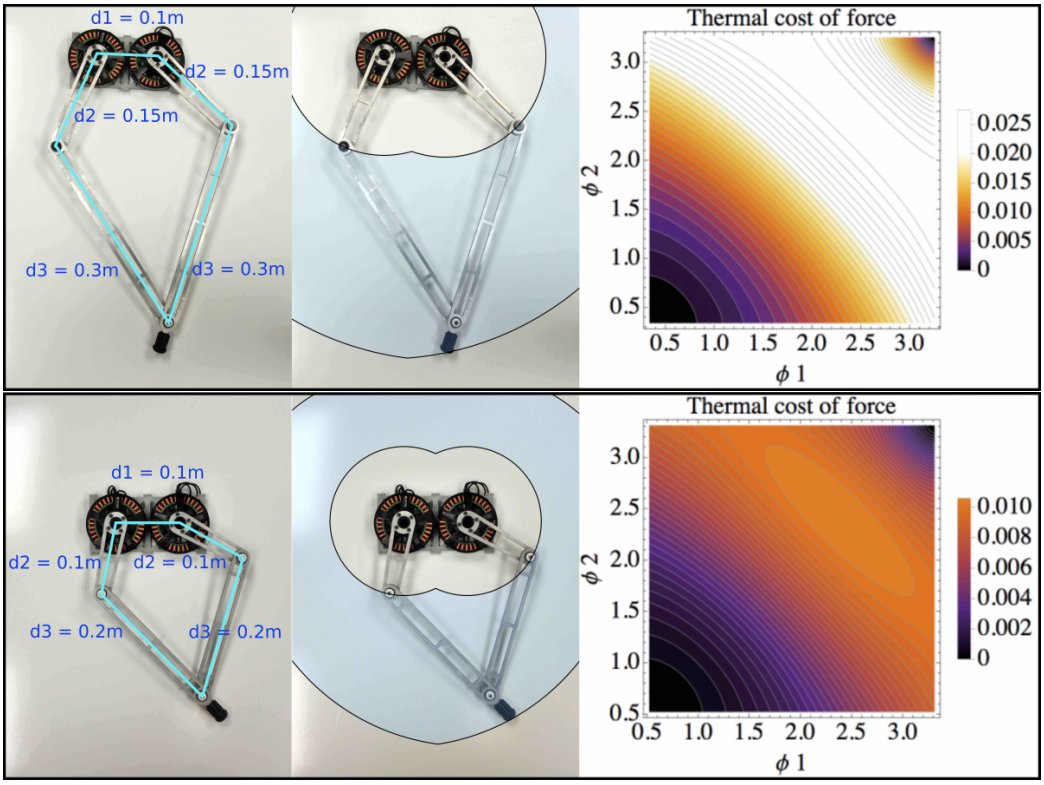

Figure 10: The leg kinematics (left) are shown for two different sets of linkage lengths used in the experiments of Chapters 3.2 and 3.3. The longer legs have a larger workspace (middle) while the shorter legs are able to generate higher forces for a fixed motor torque (right), as indicated by the smaller average of the squared singular values of the forward kinematic Jacobian for given motor shaft angles ϕ_1, ϕ_2, or equivalently, thermal cost of force [19, page 48] for a normalized motor constant.

factor of the distal and proximal links for the shorter legs was chosen near the smallest that allowed for balancing on the isolated foothold (specifically, to yield a minimal but non-empty intersection of the front and rear leg workspaces without core bending, allowing both legs to "grasp" the same point), and for the longer legs was chosen to be 1.5 times the shorter legs—a large enough increase to reasonably expect a significant performance difference compared to the shorter legs while keeping the extended leg length less than the hip-to-hip length as we were wary of avoiding excessive pitching when accelerating from rest caused by long legs [220].

Balancing on and leaping from a 20 cm-tall, 9 cm-wide foothold was successful using the longer legs of Figure 10 without core bending. With shorter legs and without core bend-

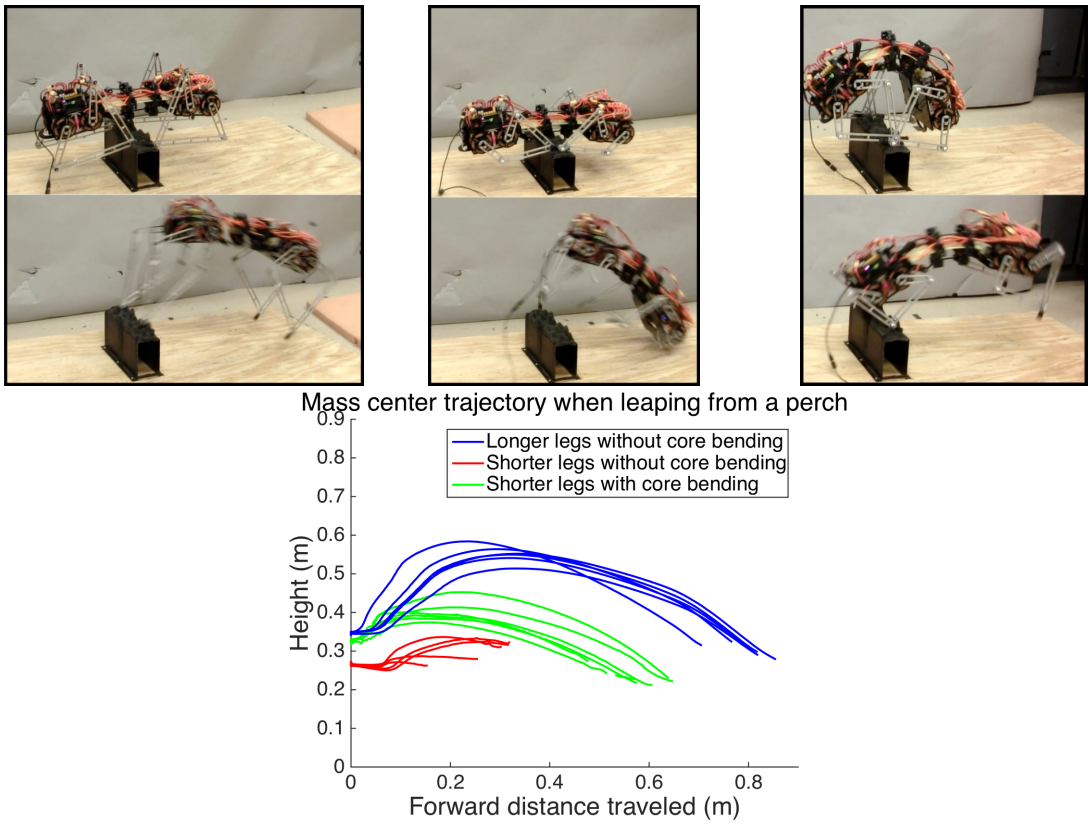

Figure 11: Leaping off a 9 cm-wide isolated foothold succeeded without core bending using longer legs (top-left, bottom blue), failed without core bending using shorter legs (top-center, bottom red), and succeeded with core bending using shorter legs (top-right, bottom green). These qualitative results suggest that core bending provides a benefit to the robot's kinematic workspace, allowing a successful leap using shorter legs than would be possible without core bending.

ing, the robot balanced on the foothold despite all four legs being near the edge of their workspace, but attempts at leaping failed. Specifically, the front legs were unable to push backwards during the leap, and any forward motion of the body moved the foothold out of the front legs' workspace. The result was that the robot cantilevered on the back legs and pitched downwards, causing the front body segment to impact the ground. On the other hand, with shorter legs and with core bending the robot successfully leaped, aided by the increased workspace volume provided by the spine bending. The mass center trajectories during the leaps are plotted in Figure 11. The robot achieved an average horizontal leap distance of 0.80 m using the long legs without the spine and 0.59 m using the short legs

with the spine. We attribute this difference to several contributing factors. First, the longer legs provide a larger kinematic extension than the shorter legs, which directly increases the distance they push the mass center. Second, the previous analysis indicates that the spine successfully augments the workspace but the longer legs still provide a greater contribution to accomplish the workspace-sensitive task. Finally, we still do not fully understand how to apply the entire energetic contribution of the spine to the mass center using hand-tuned leaps – a difficulty that is only compounded when leaping from a perch.

The results of the experiments in leaping from a small isolated foothold qualitatively indicate that the core is able to increase the legs' workspace with respect to the mass center to accomplish a useful task. This benefit allows for the leap to be completed using shorter legs capable of generating higher forces—as indicated by the singular values of Figure 10—than if no spine was used. Analytically quantifying the increased workspace conferred by the spine is confounded by the complex workspace geometry of the legs and their lack of rotational symmetry. We can estimate this increase, however, by making the approximation $d_1 = 0$ for the leg kinematics shown in Figure 10 such that the linkage becomes the annulus analyzed in Figure 8 with an inner radius $r_1 = d_3 - d_2$ and outer radius $r_2 = d_3 + d_2$. Under this approximation, the longer leg linkage represents a scaling of the shorter leg linkage by a scaling factor of 1.5. The spine can move one hip a distance $\bar{d} = 10$ cm with respect to the center of mass, satisfying $\bar{d} \geq r_1$ for the shorter legs. Thus, the volume for the shorter-legs-without-spine configuration is 0.25 m^2, for the shorter-legs-plus-spine configuration is 0.34 m^2, and for the longer legs is 0.57 m^2. The perching experiments show that—while the volumetric benefit provided by the spine is not greater than that provided by the longer legs—this approximately 36% increase in workspace volume provided by the core allows successful self-manipulation on the perch. We believe that improved balance and leap performance on isolated footholds is just one example of many possible uses of core actuation in unstructured terrain.

3.3. Proximal vs distal work production with direct-drive legs

The usage of back-drivable direct-drive leg actuators (as on Inu) provides proprioception [132, 196], however this typically comes at the expense of stance work generation. Here we show how the addition of a spine to an otherwise direct-drive platform can be more than worth its added weight from a purely work-generation standpoint without diminishing the leg's proprioceptive capabilities [80].

Geared core actuation allows otherwise direct-drive machines to augment their inherently limited ability to exert large sustained forces on the environment. Since the gearing is proximal rather than distal to the mass center, it does not diminish the leg linkages transparency that allow sensing of environmental forces. For sufficiently high-powered operation, however, core actuation requires the legs to operate in a non-transparent region of their workspace near singularity as large forces generated on the ground by the core must be transmitted through the torque-limited legs to be usefully applied to the mass center. As commented on in Chapter 3.1, this phenomenon can occur even with substantial gearing in the legs. Explicitly, if F_{core} is the force generated by the core on a point contact with the ground through a static leg linkage, the leg motors must apply the torque $Df^T(q)F_{\text{core}}$, where $Df(q)$ is the Jacobian of the leg's forward kinematic chain and q are the leg motor-shaft positions. For sufficiently large force magnitudes this necessitates operating the legs near singularity, where a small singular value of $Df(q)$ magnifies a component of the limited motor torque so the force generated at the core can transmit through the toe. This is a low-transparency regime of operation for the leg because external forces transferred to the motor are diminished along the direction corresponding to the small singular value of the linkage Jacobian. The robot, then, is able to operate in real-time in the continuum between two modes of operation: a low-force, high-transparency mode where the motors are capable of high-bandwidth environmental sensing, and a high-force, low-transparency mode where the geared core is able to perform significant work on the mass center.

To demonstrate this effect, Inu was recorded leaping on flat ground using the shorter leg configuration of Chapter 3.2 both with and without spine bending. The energetic results are shown in in Figure 12, calculated from the extrinsic body energy of the robot.

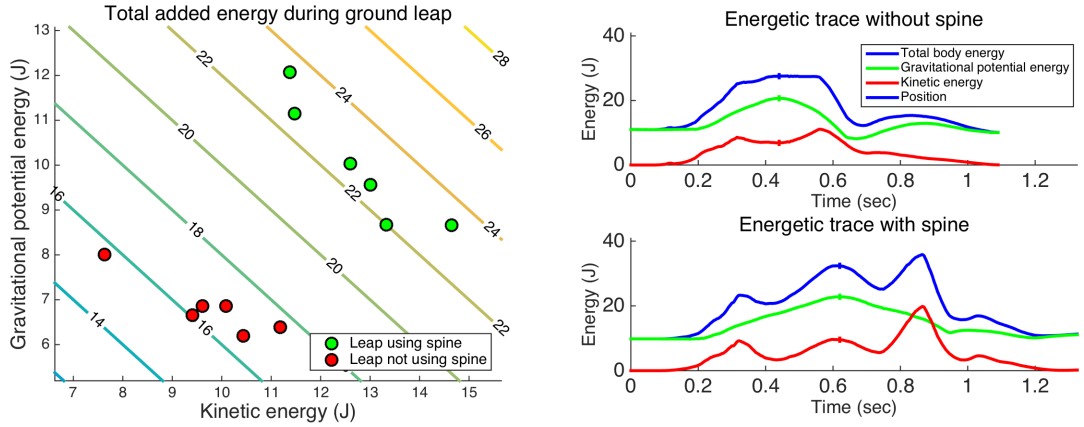

Figure 12: Leaping from the ground with and without spine bending using an otherwise identical feed-forward control scheme shows that the spine motors add on average 5.7 J to the body energy [80] (discounting the 0.5 J stored in initial spine elastic potential energy). The body energy added is calculated by subtracting the energy at the leap height apex—indicated by a vertical tick in the sample energetic traces shown in the right figure—from the starting energy. These results show the spine motors add a disproportionate amount of work (36% more) during the leap on a per-motor basis as compared with the leg motors due to their gearing.

Leaping aided by spine bending added an average of 22.8 ± 0.5 J to the body (an average of 22.3 J when discounting the elastic potential energy separately measured to be stored in the spine's fiberglass plate bending) and leaping with an identical strategy but without bending the spine added an average of 16.6 ± 0.7 J to the body, 6.2 J less than with spine bending. After discounting the elastic potential energy stored in the spine, we attribute the 34% increase in energy when using the spine to the spine motors, since they are the only other source of work available.

The 34% increase in body energy provided by the spine motors during the ground leaping experiments show that the spine motors add a disproportionate amount of work during the leap on a per-motor basis as compared with the leg motors. By commanding the spine motors to do useful work during the leap, the number of work-producing motors increased

by 25% from 8 to 10. If the spine motors had the same energetic effect as an average leg motor, then one could reasonably assume a 25% increase in leaping body energy by using the spine.[10] Instead, by increasing the body energy by 34%, each spine motor did 36% more work on the mass center than the average leg motor did. This is made possible by the spine gearing which allows the spine motors to rotate through a much greater angular displacement than the leg motors (2.6π radians in the spine versus an average less than π radians in the legs) while maintaining a similar torque.[11]

Under ideal conditions, the spine could likely perform much better. Theoretically, if the leg motors were used to their full potential at their low-speed torque-limited regime of operation they would each do $\pi\tau$ Joules of work in a leap or stride, assuming operation at a torque limit of τ over an angular displacement of π radians. With 8 leg motors used on a quadrupedal machine this gives $8\pi\tau$ Joules of available work. Adding 2 spine motors capable of a conservative angular displacement of 2.5π radians in the same low-speed torque-limited regime of operation would then increase the total maximum available work in a leap to $13\pi\tau$, a 62.5% increase in body energy in which each spine motor does 2.5 times more work on the mass center than a leg motor. Our spine experiments saw only slightly more than half of this theoretical increase in body energy, indicating that further efforts toward improving the leaping controllers would be required in order to fully exploit the potential energetic benefits of core actuation.

[10] This assumes that all the leg motors operate at near constant torque, which is often a reasonable assumption for direct-drive legged-robot motors given their typical low-speed, torque-limited regime of operation. In these experiments, the motor torque is limited by the power electronics's 43 A maximum current output, so a U8-16 motor being driven at 12 V hits the speed-torque curve and becomes power-limited when rotating faster than 42 rad/sec. The maximum angular velocity observed on the leg motors was less than 30 rad/sec, so the leg motors never leave their low-speed torque-limited regime of operation.

[11] Unlike the legs, the spine motors see speeds as high as 62 rad/sec and thus transition from being torque-limited by the power electronics to being limited by the speed-torque curve. At such high speeds, the maximum torque output is 76% of the maximum leg torque output. Increasing the voltage driving the motors would diminish this torque loss. These experiments used a 3-cell battery, and were the motivation for switching to a 4-cell battery for the experiments in later chapters.

3.4. Doubly-reactive planning of short time-horizon transitional maneuvers

Once a designer has created an agile machine, it is only natural to want to put it to use. This section offers the beginnings of how one might utilize an agile machine to transitionally navigate unstructured terrain. We show that we can approximate a simplified class of legged transitional tasks such as leaping over a gap in a way that lends itself to doubly reactive control synthesis. Our empirical implementation of the framework includes a situation where the reactive control scheme correctly identifies the need to back up to gain a running start so as to clear a gap, demonstrating that seemingly high-level behavioral autonomy can be embedded into a low-level reactive control scheme [77].

In contrast to the transitional methods introduced in Chapter 1.2.3, in the following we explore application of the reachability ideas presented in [31] and the sizable literature it generated ([153,176,177] to name a few) that construct controllers for discrete-time systems to reach some target set in a minimum number of steps, a framework that intersects the similarly longstanding tradition of pre-image backchaining in the LMT literature [83, 146, 151] as well as explicit model predictive control [3, 25]. Particularly, we directly employ the techniques of [131] which gives the complete class of minimum-time feedback laws to reach a target set, a modified formulation of which is presented in Theorem 1, computing the least restrictive safe controller to accomplish the control task [147], made computationally tractable through linear dynamics with polytopic constraints. To our knowledge, such techniques have not heretofore been used for reactive control on legged robots.

We connect this theory to legged locomotion by proposing a formal definition of a class of transitional tasks that we term a *discrete navigation problem*, which consists of controlling the state of a discrete-time control system to reach a goal set while in the interim avoiding a set of obstacle states. Here the passage from the continuous hybrid dynamics of a physical plant to the discrete-time system is achieved through the imposition of a suitable stance

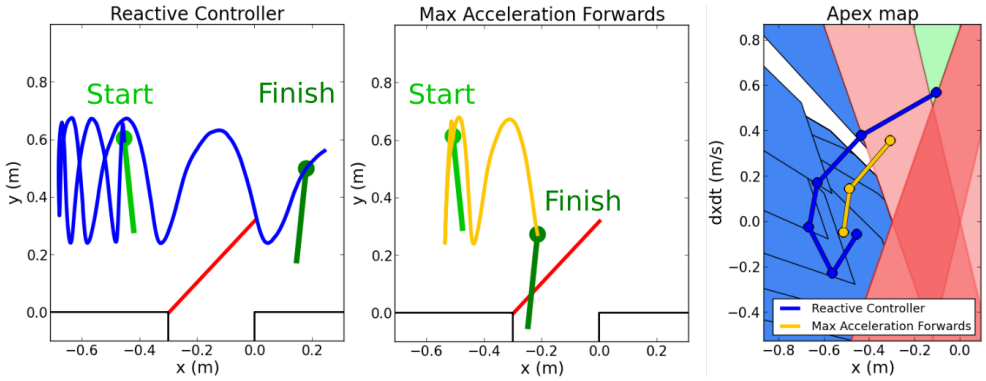

Figure 13: Empirical data from two experiments using the hopper introduced in Figure 15 to perform a leap across a gap obstacle subject to a continuous-time within-stance controller that enforces the linear stance map described in Chapter 3.4.4. The first experiment – left – uses our new scheme to suggest a degree of behavioral autonomy by forcing the robot to back up so as to get a sufficient running start to clear the gap. The second experiment – middle – demonstrates that simply applying a maximum forwards acceleration is not sufficient to cross the gap. Our algorithm generates a hopping controller guaranteeing that the abstract representation of the mass center will leap over but not cross through the the red line segment - a coarse approximate obstacle set derived from the actual terrain (depicted in black in the two plots on the left). The apex states of both experiments – right – are plotted on top of the goal set of apices that will cross the gap (green), the obstacle set of apices will fall into the gap (red), and the set of apex states that can reach the goal in k steps for some integer $k > 0$ (light blue) as introduced in Chapter 3.4.2, while the remaining white set will enter the obstacle regardless of the applied control input and can be considered "as good as lost." These sets are explicitly constructed in Chapter 3.4.3 and [76]. The k-step goal-reachable blue sets "funnel" into the goal set and illustrate that reversing to get a longer running start to clear the gap is required from the robot's starting state.

map via an appropriate continuous-time within-stance controller. Our main contribution is summarized in Figure 13. We empirically demonstrate the efficacy of the control relation given in Theorem 1 implemented on a physical hopping robot affixed to a boom (controlled in continuous time in stance to exhibit a linear stance map) for the encoding and execution of a reactive leap over an obstacle. We formulate this task as a discrete navigation problem such that — if a task solution exists — application of Theorem 1 is necessary and sufficient for its solution in a minimum number of steps. The real-time deployment of this reactive control relation is completely automated, however our understanding of how to effectively compute it is limited to affine control systems with polyhedral obstacles, goal sets, and

control constraints.

3.4.1. Discrete navigation problems

We begin by defining a *discrete navigation problem*, an abstract notion of a transitional task. Consider a discrete-time control system $\mathbf{q}_{n+1} = f(\mathbf{q}_n, \mathbf{u}_n)$, where $\mathbf{q}_n \in \mathbf{q} \subset \mathbb{R}^m$, $\mathbf{u}_n \in \mathscr{U} \subset \mathbb{R}^p$, and the continuous map $f : \mathscr{D} \times \mathscr{U} \to \mathscr{D}$ is a homeomorphism of $\mathscr{D}$ for each fixed value of the second argument. We are interested in the task of controlling the state of such system to reach a nonempty goal set $\mathscr{G} \subset \mathscr{D}$ while in the interim avoiding a set of obstacle states $\mathscr{O} \subset \mathscr{D}$ where $\mathscr{O} \cap \mathscr{G} = \emptyset$. We call this task a *discrete navigation problem* since it is the discrete-time analogue of a continuous-time navigation problem where the state needs to reach (but not necessarily stay in) the goal set.

To give the reader some intuition for how this task differs from a more traditional task encoded with a limit-set goal – using an example well beyond the scope of this chapter's experiments – consider a running leap to grab a vine or tree branch extending over a deep gorge so as to swing over it, where we separate the running leap to the vine from the brachiation task of grasping and swinging from it. The goal state of the running leap might be designated as requiring an apex state of ballistic flight to be within reaching distance of the vine while the obstacle would be the gorge. This task differs from encoding limit sets in that there is no notion of continuing the task indefinitely to reduce error (as missing the vine goal set over the gorge would be catastrophic) or even remaining in the goal set for an arbitrary amount of time. Instead, the behavior of the modeled dynamics is irrelevant (in the encoding) after the goal is reached. In our example the forward flow would enter the gorge obstacle after task is finished, however phenomena outside the scope of the model take over. The vine is grasped and used to brachiate across the chasm. The brachiation itself could be considered a discrete navigation problem which could be composed with its predecessor.

To provide a framework for deriving a controller for this task we mathematically represent

the discrete navigation problem as executing (if it exists) a *K-step navigation plan* starting from $\mathbf{q} \in \mathscr{D}, \mathbf{q} \notin \mathscr{O} \cup \mathscr{G}$ for some unspecified $K \in \mathbb{N}^+$ [12]. We define a K-step navigation plan ($K \in \mathbb{N}^+$) from $\mathbf{q}_0 \in \mathscr{D}, \mathbf{q}_0 \notin \mathscr{O} \cup \mathscr{G}$ as the ordered pair $(\hat{\mathbf{q}}, \hat{\mathbf{u}})$ where $\hat{\mathbf{u}}$ is the length K control sequence $\hat{\mathbf{u}} = \{\mathbf{u}_0, \mathbf{u}_1, ..., \mathbf{u}_{K-1}\}, \mathbf{u}_i \in \mathscr{U}$ such that the length $(K+1)$ sequence of states $\hat{\mathbf{q}} = \{\mathbf{q}_0, \mathbf{q}_1, ..., \mathbf{q}_K\}$ given by the execution of the control sequence $\hat{\mathbf{u}}$ via $\mathbf{q}_{i+1} = f(f(...f(\mathbf{q}_0, \mathbf{u}_0), \mathbf{u}_1), ..., \mathbf{u}_i)$ has the properties (which we term *admissible* in the sequel) $\mathbf{q}_i \notin \mathscr{O} \cup \mathscr{G}$ for $i \in \{0, ..., K-1\}$ and $\mathbf{q}_K \in \mathscr{G}$.

We additionally introduce the notion of a *candidate K-step navigation plan* to assist in the later proofs, which we define as the ordered pair $(\hat{\mathbf{q}}, \hat{\mathbf{u}})$ that satisfies all the requirements of a K-step navigation plan except for possibly admissibility. Once admissibility of a candidate K-step navigation plan has been verified, it is a K-step navigation plan and we say that it is a *solution* to the discrete navigation problem, where by definition a candidate K-step navigation plan completes the discrete navigation task (is a solution) if and only if it is admissible.

3.4.2. Reactive control for discrete navigation tasks

As shown below, there exists a reactive control relation (given in Theorem 1) that – if a solution to the task exists – is necessary and sufficient to solve a discrete navigation problem. Proofs of Proposition 1, Corollary 1, and Theorem 1 are provided in [76].

We inductively define the set of all states $\mathscr{R}_k$ for which a control action exists that first completes the discrete navigation problem in k iterations as

$$\mathscr{R}_{k+1} := f^{-1}(\mathscr{R}_k, \mathscr{U}) \setminus (\mathscr{O} \cup \mathscr{G}), \quad \mathscr{R}_0 := \mathscr{G},$$

where we define $f^{-1}(\mathscr{S}, \mathscr{V}) := \{\mathbf{q} \in \mathscr{D} | f(\mathbf{q}, \bar{\mathbf{u}}) = \bar{\mathbf{q}}, \bar{\mathbf{q}} \in \mathscr{S}, \bar{\mathbf{u}} \in \mathscr{V}\}$ on sets $\mathscr{S} \subset \mathscr{D}, \mathscr{V} \subset \mathscr{U}$, noting that the set $\mathscr{R} = \bigcup_k \mathscr{R}_k$ gives the set of all states which are able to complete the discrete navigation problem.

[12] $\mathbb{N}^+$ denotes the positive integers.

Proposition 1. *A candidate K-step navigation plan $(\hat{\mathbf{q}}, \hat{\mathbf{u}}) = (\{\mathbf{q}_0, ..., \mathbf{q}_K\}, \{\mathbf{u}_0, ..., \mathbf{u}_{K-1}\})$ is admissible if and only if for every $i \in \{0, ..., K-1\}$ it holds that $\mathbf{q}_i \in \mathscr{R}_{K-i}$ and $f(\mathbf{q}_i, \mathbf{u}_i) \in \mathscr{R}_{K-(i+1)}$ (proof given in [76, Section 1]).*

Define the index set $\mathscr{I}_{\mathbf{q}}$ as $\mathscr{I}_{\mathbf{q}} := \{i \in \mathbb{N}^+ | \mathbf{q} \in \mathscr{R}_i\}$.

Corollary 1. *There exists an admissible K-step navigation plan from $\mathbf{q}$ if and only if $K \in \mathscr{I}_{\mathbf{q}}$. If a solution to the discrete navigation problem exists, the minimum number of steps that it can be completed in from $\mathbf{q}$ is $\min(\mathscr{I}_{\mathbf{q}})$ (proof given in [76, Section 1]).*

We note that the sets $P_i = \{\mathbf{q} \in \mathscr{R} | i = \min(\mathscr{I}_{\mathbf{q}})\}$ for $i = 1, 2, ...$, together with $P_0 = \mathscr{R}_0$ form a partition of $\mathscr{R}$, where $\mathbf{q} \in P_i$ implies that an i-step solution from $\mathbf{q}$ exists and that i is the minimum number of steps that the navigation task can be solved in.

For ease of notation define $\mathscr{U}_{\mathbf{q},k} := \{\mathbf{u} \in \mathscr{U} | f(\mathbf{q}, \mathbf{u}) \in \mathscr{R}_{k-1}\}, k \in \mathbb{N}^+$.

Theorem 1. *If a solution to the discrete navigation problem exists, then the discrete navigation problem is solved in the minimum number of possible steps if and only if the following reactive control relation is observed at every step:*

$$\mathbf{u} \in \begin{cases} \mathscr{U}_{\mathbf{q},\min(\mathscr{I}_{\mathbf{q}})} & \mathscr{I}_{\mathbf{q}} \neq \emptyset, \\ \mathscr{U} & \textit{else}, \end{cases} \tag{3.2}$$

where $\mathbf{q}$ is the state at any given iteration and $\mathbf{u}$ is the chosen control action at that iteration (proof given in [76, Section 1]).

Solving the discrete navigation problem with this strategy has the practical utility that it is reactive. It reduces the problem of forming a full navigation plan – which might need to be re-planned in the case of state disturbance or uncertainty – to that of only choosing the next step from wherever the current state is.

In general there is no known method for computing $\mathscr{R}_k$, without which computing the control relation is infeasible and the user is relegated to techniques such as computing

conservative approximations of these sets [83]. Even if computing a single $\mathscr{R}_k$ set is possible for a particular problem, the set of relevant $\mathscr{R}_k$'s might have infinite cardinality in which case the algorithm is not guaranteed to terminate.

However, specific cases can admit readily computable $\mathscr{R}_k$ sets and there are situations in which the cardinality of the set of all relevant $\mathscr{R}_k$ sets is finite. We show in [76, Section 2.2] a $\mathscr{R}_k$ computation method for a linear form of the system dynamics with polyhedral control constraints which is directly generalizable to affine system dynamics. Regarding the cardinality problem, if the region of operation $\mathscr{D}$ is compact (for example, if the state space is restricted to be a closed set sufficiently local to the robot) then there are problems where – for a sufficiently large K – the set $\bigcup_{i=0}^{K} \mathscr{R}_i$ has the property that for any $j \in \mathbb{N}$, $\mathscr{R}_j \subset \bigcup_{i=0}^{K} \mathscr{R}_i$, allowing the computation to terminate. Even if $\mathscr{D}$ is not compact, in some applications the user is only interested in solutions that complete the task within a maximum number of steps K (for example, if the task must be performed quickly) in which case specifying a maximum K guarantees termination. Since transitional maneuvers are typically local to a robot and must be performed quickly we could in theory adopt either of these methods but for simplicity we choose to specify a maximum K in our implementation described in Chapter 3.4.4.

3.4.3. Leaping Over an Obstacle With a Legged Hopper: Formulation as a Transitional Discrete Navigation Problem

Here we present our method for applying the control relation of Theorem 1 to the generation of autonomous leaping behavior in a simple sagittal-plane legged hopping model. It entails the interaction of three distinct abstracted representations of the task, the environment, and the robot. The terrain height and robot template [90] dynamics representative of the physical machine are described in what we term the *sagittal-hopper model*. We make a local approximation of the sagittal-hopper model called the *local ballistic-approach (LBA) approximation* that gives a physically useful criterion for leaping over an obstacle in a way that is agnostic to the particular stance dynamics at the expense of making solutions slightly

conservative and allowing a small but well-characterized (and rarely encountered) class of low-speed obstacle collisions as described more carefully in the third paragraph of this section's *Local Ballistic-Approach Approximation*. From this approximation we form the *task space* that forms the basis of a discrete navigation problem suitable for the application of the control relation in Theorem 1 and consists of the set of ballistic flight apex states – subsets of which form goal and obstacle sets – along with a control apex map. The control relation of Theorem 1 is explicitly calculated in [76, Equation 3] to complete the leap in the task space under the simplified dynamics presented in this section. We use these calculations as the basis for the physical experiments depicted in Figure 3.4.4.

Note that in this section we will write all set boundaries as closed to avoid the cumbersome notation of keeping track of which set boundaries are open and closed.

Sagittal-hopper model

Consider a reduced-order point-mass sagittal-plane hopper tasked with leaping over (without falling in or impacting) a simple obstacle such as a gap, wall, or ledge from relatively flat ground. Denote the location of the hopper mass center by $\mathbf{x} = (x, y)$, where x is forward position and y is vertical height. The robot locomotes over ground represented by some terrain height function $h(x) : \mathbb{R} \to \mathbb{R}$. Suppose that the hopper's template dynamics together with the terrain height function h admit an apex map $\mathbf{q}_{n+1} = f(\mathbf{q}_n, \mathbf{u}_n)$, $f : \mathbb{R}^3 \times \mathscr{U} \to \mathbb{R}^3$ mapping the apex state $\mathbf{q}_n = (x_n, y_n, \dot{x}_n) \in \mathbb{R}^3$ at the n-th step to the $(n+1)$-th step according to the control vector $\mathbf{u}_n \in \mathscr{U} \subset \mathbb{R}^m$ chosen at step n, where $\mathbf{u}_n$ is representative of some member of a parametrized family of continuous stance-controllers.

We assume a single obstacle that is some user-specified or pre-sensed feature in the height function which is encoded with $p \in \mathbb{N}^+$ closed connected line-segments which the robot should leap over but not cross through. These line segments are individually denoted $\mathscr{L}(\mathbf{x}_{i,O1}, \mathbf{x}_{i,O2})$ in (x, y) space with endpoints $\mathbf{x}_{i,O1} = (x_{i,O1}, y_{i,O1})$ and $\mathbf{x}_{i,O2} = (x_{i,O2}, y_{i,O2})$, where $i \in \{1, ..., p\}$ and by convention we assume $\mathbf{x}_{i,O1} < \mathbf{x}_{i,O2}$ lexicographically. In future

work we hope to incorporate multiple obstacles but expect interesting issues such as deadlock to arise where in certain states avoiding one obstacle would make another unavoidable. We specify which direction the hopper is to cross the obstacle by the variable σ, where $\sigma = 1$ if the hopper is tasked with traversing the obstacle forwards in x and $\sigma = -1$ if the hopper is tasked with traversing the obstacle backwards in x. Without loss of generality, we assume the hopper is initialized on the proper side of the obstacle so as to cross it in the direction determined by σ.

Local Ballistic-Approach (LBA) Approximation

Passage from the sagittal-hopper model to the task space is achieved through an approximation called the *local ballistic-approach (LBA) approximation.* The LBA approximation uses only the ballistic apex map f and obstacle line segments $\mathscr{L}(\mathbf{x}_{i,O1}, \mathbf{x}_{i,O2})$, ignoring the terrain height and continuous hybrid dynamics except for their effect on the apex map. In place of the actual continuous dynamics we associate with each ballistic apex state q (with position (x_q, y_q) and forward velocity $\dot{x}_q$) the parametrized set of configurations in the (x, y) plane over which the apex evolves under the influence of solely gravity's acceleration g as given by $\phi_\alpha(q) \equiv \phi(q, \alpha) = (x + \dot{x}\alpha,\ y - \frac{g}{2}\alpha^2)^T$ where $\phi : \mathbb{R}^3 \times \mathbb{R} \to \mathbb{R}^2$. Such an evolution gives rise to an orbit $\mathscr{M}(q) := \{(x, y) \in \mathbb{R}^2 | (x, y)^T = \phi_\alpha(q), \alpha \in \mathbb{R}\}$. We write the orbit as a function of x via $y = f_q(x) = y_q - \frac{g}{2}\left(\frac{x - x_q}{\dot{x}_q}\right)^2$ or as a function of y for $y \leq y_q$ via the components $x = g_q^-(y) = x_q - \dot{x}_q\sqrt{\frac{2}{g}(y_q - y)}$ and $x = g_q^+(y) = x_q + \dot{x}_q\sqrt{\frac{2}{g}(y_q - y)}$, where g_q^- corresponds to the time leading up to apex and g_q^+ to the time subsequent to apex.

In this approximation we deem apex states whose ballistic evolutions pass over the obstacle line segments in the correct direction as determined by σ as completing the task and ballistic evolutions that pass through any of the obstacle line segments as immediately failing the task. More precisely, we define the set of apex states q completing the task as those with $sign(\dot{x}) = \sigma$ whose hypograph of f_q contains the line segment endpoints of $\mathscr{L}(\mathbf{x}_{i,O1}, \mathbf{x}_{i,O2})$ for all $i \in \{1, ..., p\}$. We define the set of apex states q immediately failing the task by those

having the property that, for some $i \in \{1, ..., p\}$, the hypograph of g_q^- or g_q^+ contains one endpoint of $\mathscr{L}(\mathbf{x}_{i,O1}, \mathbf{x}_{i,O2})$ and the the epigraph of the same function contains the other endpoint. In this abstracted representation of the environment there is no accounting for stance interactions with the obstacle. Settings requiring perfect safety guarantees could only tolerate this simplification at the expense of dilating the obstacle diameter by the hopper's maximal shank length - a badly conservative excess. Instead, we adjoin to the set of "failing" apex states all those whose (if $\sigma = 1$) hypograph of g_q^- contain any of the obstacle endpoints or (if $\sigma = -1$) epigraph of g_q^- contain any of the obstacle endpoints so as to not let the state begin stance before the obstacle in x and end stance after the obstacle in x. These sets are graphically shown in Figure 14.

The reason for making the LBA approximation is because it provides a convenient method of approximating task success or failure from the ballistic apex state in a way that is agnostic to both the continuous stance dynamics and local characteristics of the terrain height function h. This generality comes at the price of (a) labeling some trajectories which complete the task in the sagittal-hopper model as failing in the LBA approximation, and (b) labeling some trajectories which fail the task in the sagittal-hopper model as not failing in the LBA approximation. Specifically, solutions in the sagittal-hopper model with ballistic apex q which complete the task but which transition from stance to flight directly above an obstacle line segment can be labeled in the LBA approximation as failing the task if $\mathscr{M}(q)$ intersects the line segment despite the state never doing so in the sagittal-hopper model. Additionally, trajectories in the sagittal-hopper model which pass through an obstacle line segment a nonzero even number of times in stance will be not counted as immediately failing the task in the LBA approximation. We expect such violations to be at low kinetic energies because they require a direction reversal[13] close to the obstacle and so we assume the robot structure can tolerate such collisions. In simulation we have observed such violations when the robot is initialized very close to and slowly moving towards an

[13] We believe that one of the fundamental constraints of legged robot technology is limited actuation power, implying a limited affordance to change kinetic energy over the course of a stride.

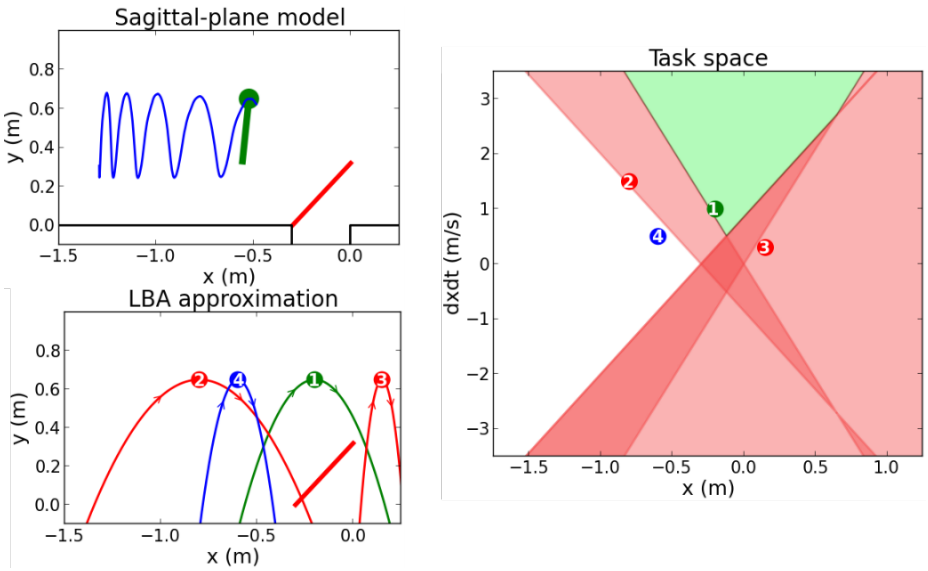

Figure 14: Illustration of the problem setup given in Chapter 3.4.3. The sagittal-plane model in the upper left includes the terrain height (black) and the user-encoded or pre-sensed obstacle (red) that the mass center (green dot) should leap over in some pre-specified direction but not pass through. Here the line segment was user-specified to span the horizontal width of the physical obstacle and to vertically extend beyond the physical obstacle by the length of the hopper's leg so as to allow room for the hopper's leg to clear the physical obstacle in flight. Note that the obstacle can include multiple line segments to better "contour" the obstacle but a single line segment is used in this work for simplicity. Notional robot trajectories are given in blue. The local ballistic-approach (LBA) approximation of the sagittal-plane model in the lower left provides a convenient method of approximating task success or failure from only the ballistic apex state and obstacle line segments, associating with each ballistic apex state the parametrized set of configurations over which the apex evolves solely under the influence of gravity. The task space slice on the right shows the goal set (green) of apex states whose LBA evolution passes over the obstacle line segment and the obstacle set (red) of apex states whose LBA evolution parabola either passes through the obstacle line segment or is past the obstacle. For example, the apex state 1 passes over the obstacle in the LBA approximation so it is in the goal set. The apex state 2 will hit the obstacle in the LBA approximation so is in the obstacle set. The apex state 3 has already passed the obstacle so it is also in the obstacle set. The apex state 4 is before the obstacle and will neither pass over nor through the obstacle in the LBA approximation and therefore isn't in the goal or obstacle set.

obstacle. Thus this formulation is best suited for use in uncluttered environments where the obstacles are not extremely close to each other so that after navigating one obstacle the robot will not initialize itself adjacent to the next obstacle.

Task Space

The task space is composed of the set of ballistic apex states – which evolve according to the dynamics of the control apex map f – together with a goal set and obstacle set. For simplicity in this work we restrict the set of apex heights under consideration to be those that are higher than the obstacle height, i.e. $y > max(y_{i,O1}, y_{i,O2}) \forall i \in \{1, ..., p\}$, so that g_q^- and g_q^+ are well-defined (if the robot starts below this threshold height we assume it is able to safely leap to above this threshold on the next leap). Let the goal set $\mathscr{G}$ be the set of apex states which complete the leaping task according to the LBA approximation and similarly let the obstacle set $\mathscr{O}$ be the set of apex states which immediately fail the leaping task. Explicitly, they are given by:[14]

$$\mathscr{G} = \left\{ (x, \dot{x}, y) \in \mathbb{R}^3 | \forall i \in \{1, ..., p\} : \begin{bmatrix} 1 & \sigma\sqrt{\frac{2}{g}(y - y_{i,O1})} \\ -1 & \sigma\sqrt{\frac{2}{g}(y - y_{i,O1})} \\ 1 & \sigma\sqrt{\frac{2}{g}(y - y_{i,O2})} \\ -1 & \sigma\sqrt{\frac{2}{g}(y - y_{i,O2})} \end{bmatrix} \begin{bmatrix} x \\ \dot{x} \end{bmatrix} > \begin{bmatrix} x_{i,O1} \\ -x_{i,O1} \\ x_{i,O2} \\ -x_{i,O2} \end{bmatrix} \right\},$$

and

$$\mathscr{O}_i = \Big\{ (x, \dot{x}, y) \in \mathbb{R}^3 |$$
$$\left(\begin{bmatrix} 1 & \sqrt{\frac{2}{g}(y - y_{i,O1})} \\ -1 & -\sqrt{\frac{2}{g}(y - y_{i,O2})} \end{bmatrix} \begin{bmatrix} x \\ \dot{x} \end{bmatrix} \geq \begin{bmatrix} x_{i,O1} \\ -x_{i,O2} \end{bmatrix} \right) \vee \left(\begin{bmatrix} -1 & -\sqrt{\frac{2}{g}(y - y_{i,O1})} \\ 1 & \sqrt{\frac{2}{g}(y - y_{i,O2})} \end{bmatrix} \begin{bmatrix} x \\ \dot{x} \end{bmatrix} \geq \begin{bmatrix} -x_{i,O1} \\ x_{i,O2} \end{bmatrix} \right) \vee$$
$$\left(\begin{bmatrix} -1 & \sqrt{\frac{2}{g}(y - y_{i,O1})} \\ 1 & -\sqrt{\frac{2}{g}(y - y_{i,O2})} \end{bmatrix} \begin{bmatrix} x \\ \dot{x} \end{bmatrix} \geq \begin{bmatrix} -x_{i,O1} \\ x_{i,O2} \end{bmatrix} \right) \vee \left(\begin{bmatrix} 1 & -\sqrt{\frac{2}{g}(y - y_{i,O1})} \\ -1 & \sqrt{\frac{2}{g}(y - y_{i,O2})} \end{bmatrix} \begin{bmatrix} x \\ \dot{x} \end{bmatrix} \geq \begin{bmatrix} x_{i,O1} \\ -x_{i,O2} \end{bmatrix} \right) \vee$$
$$\left(\begin{bmatrix} \sigma & -\sigma\sqrt{\frac{2}{g}(y - y_{i,O1})} \end{bmatrix} \begin{bmatrix} x \\ \dot{x} \end{bmatrix} \geq \sigma x_{i,O1} \right) \vee \left(\begin{bmatrix} \sigma & -\sigma\sqrt{\frac{2}{g}(y - y_{i,O2})} \end{bmatrix} \begin{bmatrix} x \\ \dot{x} \end{bmatrix} \geq \sigma x_{i,O2} \right) \Big\},$$

where $\mathscr{O} = \cup_{i=1}^{p} \mathscr{O}_i$, and where $\sigma = 1$ if the obstacle is to be traversed forwards in x and $\sigma = -1$ if the obstacle is to be traversed backwards in x. We note that for a constant y, $\mathscr{G}$ and $\mathscr{O}_i$ become polyhedra, a fact we use in the following section. When holding y

[14] These sets are calculated by solving the inequalities resulting from the hypograph/epigraph of f_q, g_q^-, or g_q^- containing obstacle line segment endpoints, as explained in this section's *Local Ballistic-Approach (LBA) Approximation*.

constant, the goal set is described by four halfspace constraints for a given obstacle line segment. The first two halfspace constraints of the goal set require that $\mathscr{M}(q)$ pass over $\mathbf{x}_{i,O1}$ while the second two require that $\mathscr{M}(q)$ pass over $\mathbf{x}_{i,O2}$. The obstacle set is described by six polyhedra for a fixed y. The first four obstacle set polyhedra correspond to $\phi_\alpha(q)$ intersecting $\mathscr{L}(\mathbf{x}_{i,O1}, \mathbf{x}_{i,O2})$. There are four to account for the cases of intersections through either direction of $\mathscr{L}(\mathbf{x}_{i,O1}, \mathbf{x}_{i,O2})$ and for intersecting with positive or negative values of α in $\phi_\alpha(q)$. The point 2 in Figure 14 gives an example of such a case. The last two polyhedra encode states whose evolution $\phi_\alpha(q)$ with negative α pass under either of the obstacle endpoints to account for all apex states that have already passed the obstacle. The point 3 in Figure 14 gives an example of such a case.

Restriction to Linear Apex Map and Polyhedra Goal and Obstacles in Sagittal-Hopper Model

We restrict our attention to a linear form of the apex map f predicated on the desire for iterated dynamics simple enough for analysis but complex enough to give physically relevant sagittal-plane behavior. To achieve such a map, we prescribe our point-mass hopper model a constant stance time u_T during which we apply an average horizontal stance acceleration $u_{\ddot{x}}$ on the mass center – where $u_{\ddot{x}}$ is constrained to a closed interval containing zero – and some vertical force to achieve the (artificially imposed) constant ballistic flight apex height $y_n = y$. For simplicity we require that the beginning of stance occur when the point mass drops below a height of y_{TD} and that the hopper lift off from stance into flight at this height as well. While these assumptions (mainly the assumption of a constant apex height) severely restricts the behavior of the template, they still yield a reduced-order model capable of relevant sagittal plane behaviors such as hopping over gaps and onto ledges from a running start. These restrictions also endow the apex map with a linear form, making it suitable for the linear programming computations given in [76, Section 2]. We hope in future work to investigate restricted dynamics with more expressive behaviors that are also simple enough to be used with a similar algorithm.

Let $\mathbf{u} = u_{\ddot{x}} \in \mathscr{U} = [u_{\ddot{x},min}, u_{\ddot{x},max}] \subset \mathbb{R}$. We treat the constant apex height y and constant touchdown/liftoff height y_{TD} as parameters, along with the vertical acceleration due to gravity g. The linear controlled apex map $\mathbf{q}_{n+1} = f(\mathbf{q}_n, \mathbf{u}_n)$ of such a system is given by:

$$
\begin{aligned}
x_{n+1} &= x_n + u_T \dot{x}_n + (2\dot{x}_n + u_{\ddot{x},n} u_T) \sqrt{\frac{2}{g}(y - y_{TD})} + \left(\frac{u_T^2}{2}\right) u_{\ddot{x},n}, \\
y_{n+1} &= y \\
\dot{x}_{n+1} &= \dot{x}_n + u_{\ddot{x},n} u_T,
\end{aligned}
\tag{3.3}
$$

While many continuous stance dynamics could satisfy such an apex map, they can be as simple as applying a constant horizontal force and piecewise constant vertical force in stance for a time duration u_T to satisfy the desired forwards acceleration and vertical apex height.

3.4.4. Experimental results

A series of running leap experiments using a robotic hopper on a boom were performed to demonstrate the utility of the control relation given in Theorem 1 under the linear dynamics assumption at the end of Chapter 3.4.3.

The hopper, shown in Figure 15, consists of a two degree-of-freedom 3.2 kg leg fixed to a circular boom, constrained to allow translation but not rotation in the sagittal plane. The hopper leg is a parallel five-bar mechanism [132] actuated by two T-Motor U10-Plus 80 KV motors[15] using Ghost Robotics motor controllers.[16] An STM-32 F303VC micro-controller[17] performs the control algorithm and sends commands to the motor controllers at 1 kHz.[18] The only sensors used by the machine are encoders at the motor shafts to sense the leg kinematics and two encoders on the boom that sense the polar angle of the boom (used to calculate forward distance in the sagittal plane) as well as the azimuth angle of the boom (used to calculate the vertical height in the sagittal plane). No sensing of the obstacle is

[15] http://store-en.tmotor.com/goods.php?id=362

[16] https://www.ghostrobotics.io/

[17] http://www.st.com/en/microcontrollers/stm32-32-bit-arm-cortex-mcus.html?querycriteria=productId=SC1169

[18] The computations of [76] are not constrained to a 1 kHz update rate and are only computed once per stride.

necessary as its location is preprogrammed into the algorithm, although future work will involve its sensing. An off-board 4-cell lithium polymer battery was used to power the hopper.

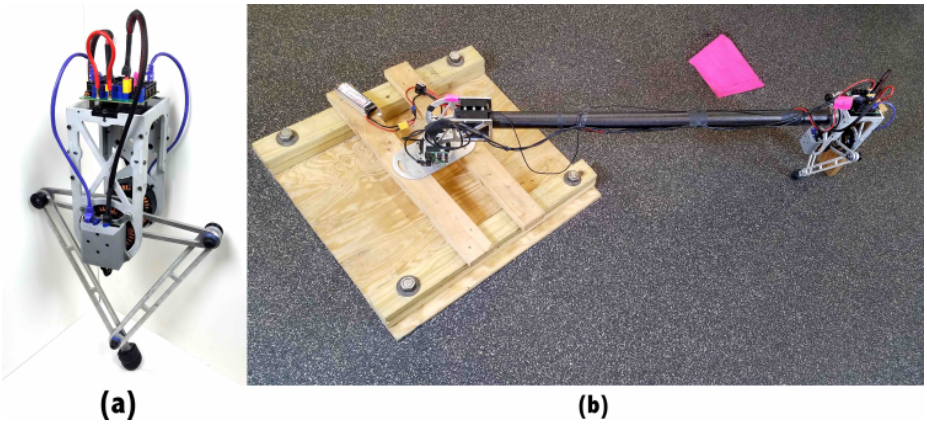

Figure 15: The legged hopper (a) is used to empirically demonstrate the utility of the control relation given in Theorem 1 on a microcontroller to perform a leaping maneuver with a running start. The fully actuated two degree-of-freedom legs allow the command of arbitrary-direction sagittal-plane stance forces so as to anchor the linear apex map template model given in (3.3) for use in the experiments. The experimental setup (b) shows the hopper constrained to the sagittal plane by a boom in front of the gap obstacle consisting of pink tape.

The template dynamics given in (3.3) were achieved in stance by applying a constant feed-forward horizontal force $u_{\ddot{x}}$, a feed-forward piecewise constant vertical force to achieve the desired deadbeat apex height y, and limiting the stance duration time to u_T. Simple proportional derivative control was used as feedback to track the stance trajectory expected from the feed-forward signals. This anchoring [90] was achieved by mapping force commands to torque commands through the inverse transpose of the kinematic Jacobian, and saturating the infinity norm of the required torque according to the motor's torque limits. A singularity-avoidance controller that applies increasing amounts of torque as the leg approaches a singular configuration guarantees that the leg won't travel through a kinematic singularity during stance. We demonstrate the efficacy of this anchoring on the hopper at low speeds in Figure 16 and high speeds in Figure 17, although we save an in-depth description and experimental statistical analysis for future work on the more interesting case

of a free-running untethered robot.

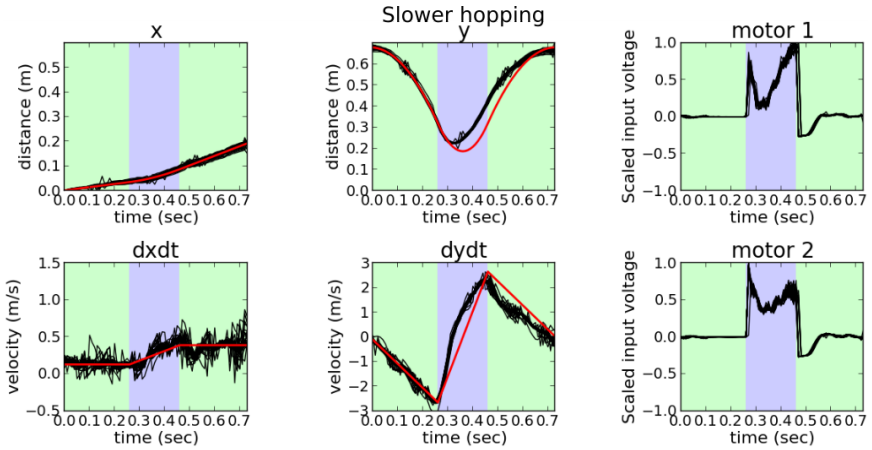

Figure 16: Boom encoder readings and motor commands (black) from 30 runs of experiments of lower-speed hopper strides, superimposed with the desired trajectory of the robot (red), show that at slower speeds the linear apex-map template of (3.3) is approximately achieved – as indicated by the correspondence of the desired and actual trajectories at the apex events occurring at times 0 and 0.7 seconds. However, work remains to improve the in-stance anchoring as indicated by the y-trace in which a variety of undesired phenomena are evident as discussed in Chapter 3.4.4. Note that the blue background indicates stance while the green background indicates ballistic flight. The data has been shifted in x so that every run starts from $x = 0$ as well as in time so that detected stance onset occurs simultaneously in every run.

Figure 16 shows 30 instances of anchoring a low-speed stride on the hopper. The correspondence of the desired and actual trajectories at the apex events indicate that the linear apex-map template of (3.3) is approximately achieved, however work remains to improve the in-stance anchoring as indicated by the the y-trace in which a variety of undesired phenomena are evident. We believe that the larger-than-expected vertical acceleration early in stance is due to the effect of a singularity avoidance controller activating as the leg approaches the edge of its workspace. We are also unclear exactly as to why the correct apex is achieved despite liftoff occurring at too great a height but suspect that some friction-like effect from the boom is responsible. For now we allow these effects to roughly cancel each other out but they deserve a more careful treatment in future work when we implement this controller on an untethered robot unhindered by the dynamics of the boom.

Figure 17 shows 28 runs of attempting to anchor a higher-speed stride on the hopper,

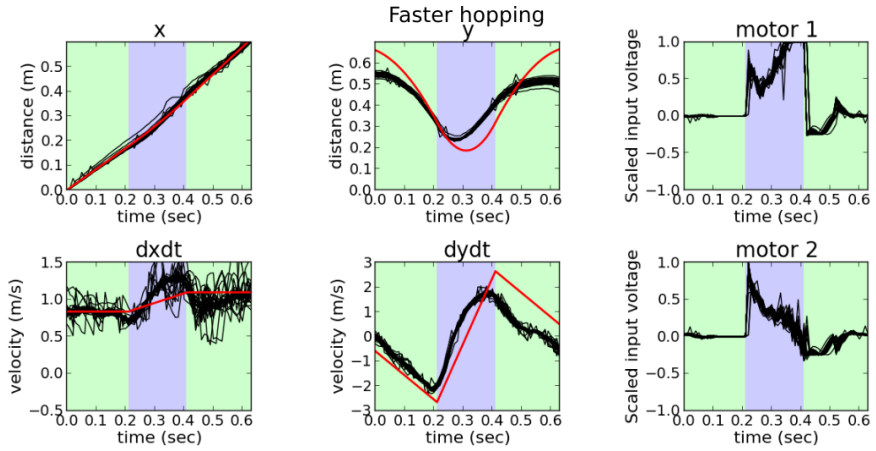

Figure 17: Boom encoder readings and motor-commands (black) from 28 runs of experiments of higher-speed hopper strides, superimposed with the desired trajectory of the robot (red), show that at higher speeds the hopper is unable to anchor the linear apex-map template of (3.3). This appears to be due to the fact that at higher speeds the kinematic configuration of the leg is such that, in the second half of stance, one of the two motors is saturated and the other one is doing almost no work as shown in the motor plots on the right as discussed in Chapter 3.4.4. Note that at these higher speeds the boom dynamics become more pronounced; ringing oscillations are evident in both the forward and vertical velocity traces later in the stride.

demonstrating that at higher speeds the hopper is unable to anchor the linear apex-map template of (3.3). This appears to be due to the fact that at higher speeds the kinematic configuration of the leg is such that in the second half of stance one of the two motors is saturated and the other one is doing almost no work, as shown in the motor plots on the right. This manifests itself in a sharp drop-off in vertical velocity in the second half of stance so that the hopper is unable to generate enough liftoff velocity to attain the commanded apex height, indicating that the implementation of this algorithm on an untethered robot would benefit from a leg configuration that more evenly shares the burden of the motor affordance while running, bearing in mind that the requirement that the motor-leg kinematics be designed to support this class of templates will likely decrease the performance of some other task.

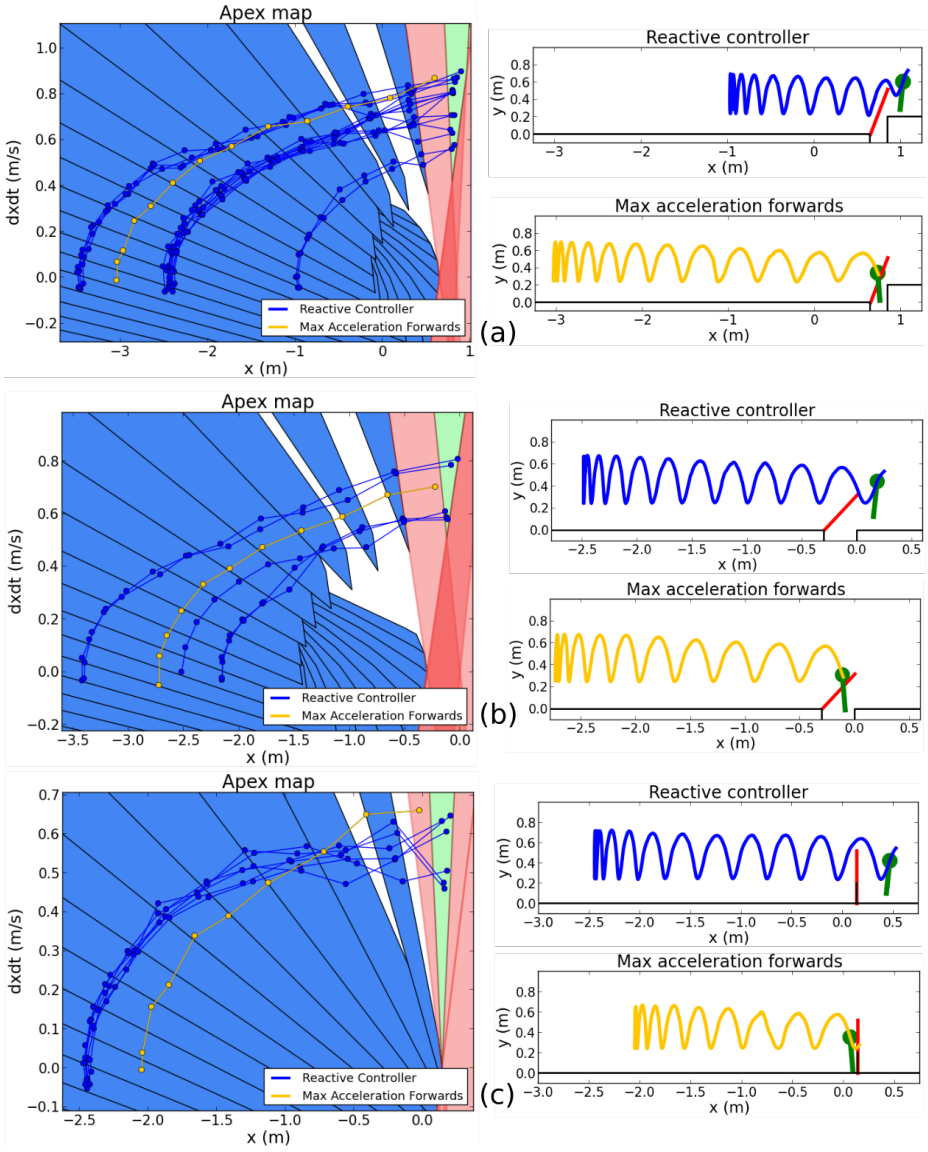

Figure 18: Experimental results of the robotic hopper introduced in Figure 15 using the control relation of Theorem 1 to reactively leap over various obstacles from a running start. Row (a) depicts 15 instances of the hopper leaping onto a ledge immediately preceded by a gap from various initial conditions, (b) depicts 6 instances of leaping over a simple gap obstacle, and (c) depicts 5 instances of leaping over a hurdle obstacle. The right column of the figure shows the sagittal-plane representation of the environment with the terrain depicted in black and an example controlled robot trajectory from the experiments in blue, smoothed to filter out measurement noise. The yellow trajectory demonstrates failure when the robot simply accelerates at maximum. The red line segment is the encoded obstacle to be avoided by the mass-center. This line segment was user-specified to span the horizontal width of the physical obstacle and to vertically extend beyond the physical obstacle by the length of the hopper's leg so as to allow room for the hopper's leg to clear the physical

obstacle in flight. Future work will seek to automate this obstacle detection process from sensor data such as LiDAR readings. The left column of the figure shows the apex-state representation of the leaping task where the robot's apex trajectory is depicted by dark blue dots sequentially connected by dark blue lines. The set of apex states which result in immediately passing through the obstacle as-per the approximations of Chapter 3.4.3 are shown in red and comprise the obstacle set $\mathscr{O}$, while the set of apex states which pass over the obstacle are shown in green and comprise the goal set $\mathscr{G}$. The lighter blue sets represent the set of states $\mathscr{R}_k$ which can reach the goal in k steps and which "funnel" into $\mathscr{G}$, while the remaining white area is the set of apex states which flow into $\mathscr{O}$ regardless of the applied control input.

We implement the algorithm on-board the robot by computing the $\mathscr{R}_k$ sets up to a k of 20 when the robot initializes and then using the estimated apex state to calculate the control relation $\mathscr{U}_{\mathbf{q},\min(\mathscr{I}_{\mathbf{q}})}$ via [76, Equation 3] once per stride. The hopper then chooses the forward acceleration $u_{\ddot{x}}$ that is both consistent with the control relation and maximizes the distance of the next apex state to the boundary of the relevant $\mathscr{R}_k$ set containing it, achieving a degree of robustness in an informal sense that is elaborated on in [76, Section 3] . The obstacle location (represented by features in the black line-segment terrain in the right-hand-side column of Figure 3.4.4) is known a-priori to the control algorithm and encoded in the sagittal-hopper model using a single line segment (represented by the red line segments in the right-hand-side column of Figure 3.4.4), which is user-specified to span the horizontal width of the physical obstacle and to vertically extend beyond the physical obstacle by the length of the hopper's leg so as to allow room for the hopper's leg to clear the physical obstacle in flight. Future work will seek to automate this obstacle detection process from sensor data such as LiDAR readings.

Three experiments were performed to demonstrate the applicability of Theorem 1 to a physical machine using embedded hardware. In the first, the hopper is commanded to repeatedly leap over a ledge with a gap in front of it from various initial conditions to demonstrate repeatability. In the second and third, the hopper was commanded to cross other types of obstacles (a hurdle and a simple gap) to showcase a few of the different

obstacle types that can be traversed and give a sense of their corresponding sets $\mathscr{G}$ and $\mathscr{O}$. In each case the hopping apex height y was set to 0.65 m, the touchdown and liftoff height y_{TD} was set to 0.32 m, the stance time u_T was set to 200 ms, and the forward acceleration was limited to the modest $u_{\ddot{x},max} = -u_{\ddot{x},min} = 0.5$ m/s^2 due actuator saturation constraints.

The results of the experiments are shown in Figure 3.4.4. Figure 3.4.4(a) depicts 15 runs of the hopper leaping onto a ledge immediately preceded by a gap, and demonstrates that the task can be repeatedly completed from various initial conditions. Figure 3.4.4(b) depicts 5 runs of the hopper leaping over a simple gap obstacle, and Figure 3.4.4(c) depicts 6 runs of the hopper leaping over a hurdle obstacle. The variation in apex trajectories from similar initial conditions indicates our anchoring scheme of the linear apex dynamics given in (3.3) remains to be improved (as depicted in Figures 16 and 17), however the task is still completed.

An additional experiment is shown in Figure 13 which demonstrates a degree of behavioral autonomy which this reactive control relation can provide. In this set of experiments the maximum acceleration was set to $u_{\ddot{x},max} = -u_{\ddot{x},min} = 1.0$ m/s^2. The robot is initialized too close to a gap to directly leap over it and – when using the proposed control scheme – reverses to gain enough of a running start to clear the gap. Without this direction reversal (when simply accelerating forwards at $u_{\ddot{x},max}$) the robot is observed falling into the gap.

Conclusions and Future Work

We propose the notion of a discrete navigation problem – consisting of controlling the state of a discrete-time control system to reach a goal set while in the interim avoiding a set of obstacle states – to approximate a class of tasks useful for legged robotic applications such as leaping. We demonstrated the efficacy of the control relation given in Theorem 1, which is (assuming a task solution exists) necessary and sufficient to solve a discrete navigation problem in a minimum number of steps, on a physical hopping robot affixed to a boom to reactively leap over an obstacle with a running start, controlling the continuous stance

dynamics to exhibit a linear stance map.

Future work should focus on implementing this algorithm on a pronking quadruped robot autonomously sensing obstacles with LiDAR. We also plan to apply this algorithm to multiple sequential obstacles in an "obstacle course"-like environment which we expect will raise interesting issues such as avoiding deadlock. Finally, we hope to be able to make formal claims on forming various control laws from the proposed control relation as it relates to criteria such as robustness and aggressiveness now that we have an exact representation of the solution space of discrete navigation problems as opposed to a conservative representation of it.

3.5. Appendix to Chapter 3: Energy and Power Density for Legged EM Actuators

Assuming that EM motors produce a magnetic field of uniform density, the motor creates force by having this field interact with permanent magnets. This interaction occurs over some area (the air gap) and so is proportional to l^2, where l is the characteristic length. Assuming that the motor does work by rotating through a fixed angle, the transformed displacement through a leg of arbitrary geometry will scale according to l. The energy produced by the motor (the work done) is therefore proportional to l^3, so for constant density, specific energy is scale invariant.

Power density scaling is originally presented in [192] pages 176-181, but will be reworked below with more detailed scaling analysis. Assuming energy density is mass-invariant in an actuator, the power density scaling will be considered for a hopping task. Neglecting air resistance the apex height will be constant, and so it follows that the liftoff velocity, v_f, will also be constant. Assuming the system starts crouched at rest, the leg must go through a fixed extension, l, and accelerate the body to v_f. Assuming constant acceleration, a, $v_f = at$ and $l = \frac{1}{2}at^2$ where t is the time the system is in contact with the ground. Substituting for a, $l = \frac{1}{2}v_f t$. Since v_f is constant, t scales according to l. Given constant energy density,

power density then scales according to l^{-1}. This means that for specific energy to remain performance limiting, specific power must scale according to l^{-1}. We note that this is in sharp contrast to [148] where specific power scales according to $l^{0.5}$ in support of maintaining dynamic similarity with respect to the pendulous motion of a swinging body characteristic of certain animal climbers [96].

CHAPTER 4

Bounding with a locked back

The utility of bounding in the sagittal-plane with a spine must be compared to bounding in the sagittal-plane with a locked back, a behavior for which there remains a dearth of formal results. This chapter presents a controlled reduced-order hybrid dynamical system with a limit cycle that has well-understood stability properties and that well-approximates locked-backed bounding in the sagittal plane with physical hardware. This chapter begins with a background on cascade compositions and hybrid transition control in Chapter 4.1. Chapter 4.2 introduces a simplified hybrid dynamical systems model (4.3) representing a bounding quadruped, with a rigid-bar body and massless legs that exert ground-reaction forces at the toes. Ground reaction force laws and hybrid transition behaviors are specified that make the dynamics a cascaded composition of two hybrid dynamical system modules. Simplifying assumptions (shown in Chapter 4.3 to be approximately valid) give these modules trivial dynamics. Chapter 4.3 formulates a stride map for a bounding gait, and factors it into a more easily analyzable half-stride map. A fixed point representing a hybrid periodic orbit is found, and its properties are examined. Chapter 4.4 formulates control on the hybrid transitions to make the aforementioned periodic orbit an attracting limit cycle. Control weights are chosen so that the stride map representing the orbit is infinitesimally deadbeat. Chapter 4.5 details the empirical instantiation of the controlled model on the Inu robot. Experimental results indicate reasonably close correspondence to the theoretically predicted behavior of the simplified model. Chapter 4.6 provides a brief discussion about the ideas in the chapter, and Chapter 4.7 provides concluding remarks. Proofs and a full stability analysis are given in the appendices. A table of symbols is provided in Tables 2 and 3. The modular nature of this approach leads us to believe that it can be used to assist in

describing running with a spine, the beginnings of which are done in Chapter 5.4.[19]

4.1. Background

Legged robots exhibit increasingly successful steady-state [1, 114] and transitional [1, 164, 208] behaviors, yet they remain scarce in real-world applications. One challenge impeding their widespread adoption is the difficulty of developing parametrized families of controllers that work over identifiable ranges of body and environmental parameters. Today's most successful gait control methods for high degree of freedom legged machines generally appeal to numerical optimization [62, 113, 138], yielding increasingly impressive controls for specific mechanisms at specific operating conditions in specific environments. Achieving stable gait controllers with functional dependence on task and environment parameters that specify the operating characteristics of useful legged machines is fundamentally hard, owing to the non-integrability of their high dimensional nonlinear hybrid dynamics. Prior results of this nature are rare even for three degree-of-freedom mechanisms [8, 50, 66]. The authors are not aware of any complete stability result for three or higher degree-of-freedom models of quadrupedal locomotion (where the various appendages do not connect to the body at a common point in the simplified model).

This paper presents a parametrized family of controllers that stabilize a hybrid dynamical systems model of quadrupedal bounding arising from a simple three degree-of-freedom sagittal plane representation of a legged robot. The stability guarantees extend over a specified range of variations in body mass, length, and moment of inertia that dictate the achievable range of commanded forward running speeds and thereby, in turn, the full set of controller parameters. These formal results arise from key approximations and a controller structure that exploits them to afford a decomposition of the full model into the cascade of a two degree-of-freedom in-place bounding component forward-coupled to drive a one degree-of-freedom fore-aft component. This model and the resulting controller are simple in the sense

[19] This chapter has been submitted for publication. An extended version of the submission is available in technical report form as [78].

that they encode ground-reaction force laws resulting in trivial continuous body dynamics and they achieve the family of asymptotically stable limit cycles representing the desired steady state gait using proportional control on the hybrid transitions. Nevertheless, the model is sufficiently faithful and the controller is sufficiently robust as to permit empirical implementation over many repeated trials (accumulating hundreds of body lengths) on a physical robot, Inu [80].

4.1.1. Cascade Compositions

The use of simplified models for the control of legged running has a rich history of empirical [9, 163, 175] and analytical [169, 204, 218] success. We are particularly interested in modular approaches that can offer an analytically tractable path to formal results, as they decouple the stability problem into a composition of lower-dimensional subproblems. For example, "parallel composition" – approximation in terms of modules operating simultaneously in isolation – was pioneered with great success empirically by Raibert [175], and has been formally redeveloped in recent years for bipedal [66], quadrupedal [67], and more general [68] legged systems. While empirically very effective, this recent formal analysis of legged parallel composition uses the framework of hybrid dynamical averaging [69] requiring not only that the neglected "crosstalk" between modules be sufficiently small but that potentially deleterious components (that cannot be averaged away) be identified and compensated by feedback.

In this paper, we introduce a cascade composition (4.1) to control quadrupedal bounding, which – in contrast to parallel compositions – allows for arbitrarily large feed-forward signals from one module to another cascaded module. From the analytical perspective, the cascade also achieves an eigenvalue separation property in the stride-map Jacobian that guarantees local stability of coupled modules so long as they are stable in isolation, providing a separation of concerns to the designer. Cascade compositions have long been used to reduce the complexity of adding dimensionality both in continuous-time systems [202, 211] and iterated maps [139]. However – to the best of our knowledge – their formal consideration

for simplified models of dynamic quadrupedal locomotion has only been used to "extract" away fast actuator dynamics [39] or for similar situations with multiple timescales [127] that reduce to feed-forward cascades in Fenichel normal form [81].

We say an iterated map $P : \mathbb{R}^n \times \mathbb{R}^m \to \mathbb{R}^n \times \mathbb{R}^m$ is a *cascade composition* if it is of the form:

$$P(x, y) = \begin{pmatrix} P_1(x) \\ P_2(x, y) \end{pmatrix}, \tag{4.1}$$

where $x \in \mathbb{R}^n$, $y \in \mathbb{R}^m$, $P_1 : \mathbb{R}^n \to \mathbb{R}^n$, $P_2 : \mathbb{R}^n \times \mathbb{R}^m \to \mathbb{R}^m$. Such a system has the block-triangular Jacobian:

$$DP = \begin{pmatrix} D_x P_1 & 0 \\ D_x P_2 & D_y P_2 \end{pmatrix}, \tag{4.2}$$

in which the eigenvalues of DP consist of the eigenvalues of the smaller $(n \times n)$ matrix $D_x P_1$ and $(m \times m)$ matrix $D_y P_2$. The task of showing that the spectral radius of DP has modulus less than unity for a linearized stability analysis then reduces to establishing the same property individually for the smaller constituent matrices, $D_x P_1$ and $D_y P_2$, generally a much easier task.

4.1.2. Controlling on Hybrid Transitions

The long practiced tradition of achieving control through shaping a hybrid dynamical system's guards and resets (the hybrid transitions) has been used since the earliest days of empirically successful dynamical robots when Raibert used the fact that a robot leg's angle in flight could be freely set to affect touchdown conditions and thereby control forward running speed [175] (inspiring many similarly conceived subsequent speed controllers [67, 169, 193]). This insight was generalized by Seyfarth [198], initiating a "swing-leg retraction" literature (e.g. [108, 130]) that occasioned two fundamental observations that bear on our work. First, minimally sensed stabilization is not only achievable (demonstrated numerically [199] and

analytically [94]) by control on hybrid transitions, but can afford deadbeat performance[20] as well with only a bit more sensing. Specifically, as shown numerically [222] and analytically [59], proper feed-forward servoing of sagittal leg angle in flight affords control over the apex height with no sensing required other than the detection of the apex and touchdown events, even when running over uneven terrain. Second, the implicit function theorem provides sufficient conditions for the existence of deadbeat control given a sufficiently expressive input vector using full state feedback [48]. Studies in humans [38] and birds [35, 63, 64] document some combination of feed-forward and feedback hybrid transition control strategies during biological running, further motivating their study for roboticists.

Previous results on hybrid transition control (particularly the deadbeat literature) are limited in several ways. The majority of results are limited to simulation and the recent preliminary experimental work in this area [150, 224] suggest performance is very sensitive to state estimation error or perhaps model parametric uncertainty, conceivably limiting the application of deadbeat results to robots in controlled environments such as motion capture feedback systems. Even methods requiring no sensing aside from the detection of apex suffer from the fact that the apex event is difficult to precisely detect in practice without motion capture data.

Noting that previous work controlling hybrid transitions in legged locomotion has been limited to varying the flight leg angle, we take inspiration from Blickhan's studies indicating that humans vary both their leg angle and leg length in flight to affect touchdown conditions [99, 160] and expand consideration of hybrid transition control to vary flight leg angle and length. We also allow our hybrid transition controller to affect liftoff conditions. In these ways, we more fully leverage the affordance inherently provided by making and breaking contact in sagittal running. Moreover, aiming for greater robustness and avoiding the need to detect the apex event, we forgo deadbeat control for a linearized version of it and also use a combination of feed-forward and feedback control – only using feedback on states that

[20] Here, deadbeat control refers to a strategy resulting in exact correction to perturbations in a finite (typically minimum) number of steps [48].

can be accurately measured on-board the robot.

Symbol	Description
$\mathcal{H} := (\mathcal{J}, \mathcal{T}, \mathcal{D}, \mathcal{F}, \mathcal{G}, \mathcal{R})$	Hybrid system (4.3), (4.5), (4.6), (4.13), (4.17), (4.18)
$\mathrm{F}, \mathrm{D}, \mathrm{R}$	Hybrid modes (4.4)
$D_i, G_{i,j}, R_{i,j}, F_i$	Mode domains (4.7), guards (4.17), (4.24), resets (4.19), (4.29) and vector fields (4.14)
t	Time
y, φ, τ	Mass-center height, body pitch, mode timer (4.10), Figure 19
$x,\ x^f,\ x^r$	Mass-center and front/rear toe horizontal positions (4.11), Figure 19
$\Delta x^f = x^f - x,\ \Delta x^r = x^r - x$	Front and rear horizontal leg-splay distance (4.11), (4.12), measured from the mass-center
$\boldsymbol{x}_i := (\boldsymbol{x}_i^{I\,T}, \boldsymbol{x}_i^{H\,T})^T$	State (4.9) in mode i, with in-place (4.10) and horizontal (4.11) components
$\boldsymbol{x}^I := (\boldsymbol{q}^I, \dot{\boldsymbol{q}}^I, \tau)^T, \quad \boldsymbol{q}^I := (y, \varphi)^T$	In-place state, configuration (4.10)
$m,\ I,\ g,\ d$	Physical model parameters (Figure 19)
$\Delta x^{\mathrm{Avg}},\ a,\ l_0$	Pseudo-physical parameters related to control parameters (4.22), (4.23), (4.25), (also Figure 19)
$G^I_{i,j}$	In-place components of the guard set (4.24), (4.25)
$y^{f_{hip}}(\boldsymbol{x}^I), y^{r_{hip}}(\boldsymbol{x}^I), \dot{y}^{f_{hip}}(\boldsymbol{x}^I), \dot{y}^{r_{hip}}(\boldsymbol{x}^I)$	Front/rear hip heights and velocity maps (4.28)
$g_{TD}(\boldsymbol{x}^I_{\mathrm{F}}),\ g_{LO}(\boldsymbol{x}^I_{\mathrm{D}})$	Guard "control" functions for touchdown, liftoff events (4.25), (4.57)
$\boldsymbol{k}^I = ({\boldsymbol{k}^I}_{\mathrm{F}}^{\,T}, {\boldsymbol{k}^I}_{\mathrm{D}}^{\,T})^T$	In-place guard control weights (4.25)
$y^{f_{hip}}_{i0}(\boldsymbol{x}^I), y^{r_{hip}}_{i0}(\boldsymbol{x}^I)$	Front and rear initial hip height in mode i (4.58)
$b,\ b^I,\ b^H$	"Bounding" symmetry map (4.40), with in-place (4.26) and horizontal (4.32) components
$\mathcal{L}_f V(x) := \frac{\partial}{\partial x} V(x) \cdot f(x)$	Lie derivative (4.27) of scalar field V along vector field f at point x
$R^I_{i,j}, R^H_{i,j}$	In-place (4.30), horizontal (4.31) reset function components
$r_{\mathrm{F,D}}(\boldsymbol{x}^H_{\mathrm{F}}),\ r_{\mathrm{D,R}}(\boldsymbol{x}^H_{\mathrm{D}})$	Reset "control" functions (4.31), (4.62)
$\boldsymbol{k}^H := (k^H_{\mathrm{F}}, k^H_{\mathrm{D},1}, k^H_{\mathrm{D},2})^T \in \mathbb{R}^3$	Reset control weights (4.63)

Table 2: Main symbols, part I used in this work with reference to their equations of introduction

Symbol	Description
Δx^{Nom}	Nominal touchdown leg splay for front leg (4.31)
$\bar{y}$	Mass-center constant-height approximation value (Approximation 1)
$u_y \in (\frac{g}{2}, g), \quad u_{xi}(\boldsymbol{x})$	Vertical (4.16), (4.20), (4.33), horizontal (4.16), (4.21) (mass-specific) force from each hip
$\phi_i^t(\boldsymbol{x}^I), \quad \hat{\phi}_i^t(\boldsymbol{x}^H)$	In-place (4.34), horizontal (4.35) mode-i flow
$\boldsymbol{c}_i$	(y, φ) simplified acceleration vector for mode i (4.34)
$C_{\text{F}},\ C_{\text{D}},\ C_{\text{R}}$	Matrix components used in the description of $\hat{\phi}_i^t(\boldsymbol{x}^H)$ (4.35)
$\Phi_{i,j},\ \Phi_{i,j}^I,\ \Phi_{i,j}^H$	Mode map (4.37) from mode i to j, with in-place, horizontal components (4.38)
$T_{i,j}^I(\boldsymbol{x}^I)$	Mode i time-to-impact map (4.39) with guard $G_{i,j}^I$
$\widetilde{D}_i := \widetilde{D}_i^I \times \widetilde{D}_i^H$	Reduced domain for stride map with horizontal, in-place components (4.41)
$\widetilde{\boldsymbol{x}} := (\widetilde{\boldsymbol{x}}^{I^T}, \widetilde{\boldsymbol{x}}^{H^T})^T$	Reduced (stride map) state with in-place and horizontal components (4.42)
$\Pi(\boldsymbol{x}), \Sigma(\widetilde{\boldsymbol{x}})$	Projection and lift maps (4.43)
$\Pi^I(\boldsymbol{x}^I),\ \Sigma^I(\widetilde{\boldsymbol{x}}^I),\ \Pi^H(\boldsymbol{x}^H),\ \Sigma^H(\widetilde{\boldsymbol{x}}^H)$	In-place, horizontal projection and lift maps (4.43)
S, H	Stride (4.44) and "flipped" half-stride (4.46) maps
$\widetilde{\widetilde{\boldsymbol{x}}} = (\widetilde{\widetilde{\boldsymbol{x}}}^{I^T}, \widetilde{\widetilde{\boldsymbol{x}}}^{H^T})^T \in \widetilde{D}_{\text{F}}$	Fixed point of H (4.47)
$\bar{\Delta x}^f, \bar{\Delta x}^r$	Leg splay components of $\widetilde{\widetilde{\boldsymbol{x}}}^H$ (4.49)
$\bar{T}_{\text{Stance}},\ \delta\bar{x}_{\text{Stance}}$	Total hip stance duration (4.53) and leg sweep distance (4.54) on the hybrid periodic orbit associated with $\widetilde{\widetilde{\boldsymbol{x}}}^H$
$\bar{\boldsymbol{x}} = \Sigma(\widetilde{\widetilde{\boldsymbol{x}}}) \in D_{\text{F}}$	Lift of $\widetilde{\widetilde{\boldsymbol{x}}}$ (4.59)
$\bar{T}_{i,j}, \bar{\boldsymbol{x}}_{i0,j}^I$	Mode i's duration (4.51) and initial state (4.60) as it evolves into mode j under the hybrid execution from $\bar{\boldsymbol{x}}^I$
$V^I, \Lambda^I, A^I,\ \boldsymbol{d}^I,\ R^I,\ T^I$	Matrices/vectors used in Lemma 2 (4.77), (4.78)
$\widetilde{b}^I, D\widetilde{\Phi}_{i,j}^I$	Simplified factors of H's in-place component (4.72)
$\widetilde{\boldsymbol{k}}_{\text{F}}^I, \widetilde{\boldsymbol{k}}_{\text{D}}^I$	Change of variables for ${\boldsymbol{k}^I}_{\text{F}}$, ${\boldsymbol{k}^I}_{\text{D}}$ (4.73)
$A^H,\ \boldsymbol{d}^H,\ R^H := (\boldsymbol{d}^H,\ A^H\boldsymbol{d}^H)$	Matrices/vectors used in Lemma 3 (4.84)

Table 3: Main symbols, part II used in this work with reference to their equations of introduction

4.1.3. Outline

Chapter 4.2 introduces a simplified hybrid dynamical systems model (4.3) representing a bounding quadruped, with a rigid-bar body and massless legs that exert ground-reaction

forces at the toes. Ground reaction force laws and hybrid transition behaviors are specified that make the dynamics a cascaded composition of two hybrid dynamical system modules. Simplifying assumptions (shown in Chapter 4.3 to be approximately valid) give these modules trivial dynamics. Chapter 4.3 formulates a stride map for a bounding gait, and factors it into a more easily analyzable half-stride map. A fixed point representing a hybrid periodic orbit is found in Proposition 2, and its properties are examined. Chapter 4.4 formulates control on the hybrid transitions to make the aforementioned periodic orbit an attracting limit cycle. Control weights are chosen in Proposition 3 so that the stride map representing the orbit is infinitesimally deadbeat. Chapter 4.5 details the empirical instantiation of the controlled model on the Inu robot. Experimental results indicate reasonably close correspondence to the theoretically predicted behavior of the simplified model. Chapter 4.6 provides a brief discussion about the ideas in the paper, and Chapter 4.7 provides concluding remarks. Proofs and lemmas are given in the appendices. A table of symbols is provided in Tables 2 and 3.

4.2. Model

This section introduces the simplified model shown in Figure 19 of a quadrupedal robot bounding in the sagittal-plane. The model consists of a rigid bar representing a robot body with massless legs protruding from the hips that are able to generate ground-reaction forces at the toes. This basic model has been used to describe sagittal quadrupeds since Raibert's work [175, p. 139], typically using torques and radial forces generated at the hips (equivalent to ours through a change of coordinates). It has been used more recently with commanded Cartesian ground-reaction forces to model both steady-state and transitional empirical behaviors [163, 164]. The model should approximately represent the sagittal dynamics of physical bounding robots with mass-center roughly halfway between their hips, as long as the leg inertia is sufficiently less than that of the body so as to satisfy the massless leg approximation.

Chapter 4.2.1 gives the model's hybrid dynamical system description for a non-aerial bound

(because of the actuator limits described in Chapter 4.5.1) as depicted in Figure 20. Chapter 4.2.2 constrains the ground-reaction force laws (4.20), (4.21), and hybrid transitions (4.24), (4.29) to enact a cascade composition. Chapter 4.2.3 introduces dynamical simplifications in the form of Approximations 2, 1, and (4.33) that – together with the previous modeling choices – give the cascaded system the trivial dynamics depicted in Figure 21. These modeling and control choices yield simple closed form expressions for the flow on the hybrid modes (4.34), (4.35), that in turn allow a closed form expression for the targeted bounding limit cycles in Chapter 4.3 and a tractable stability analysis in Chapter 4.4.

4.2.1. Hybrid Dynamical System Description

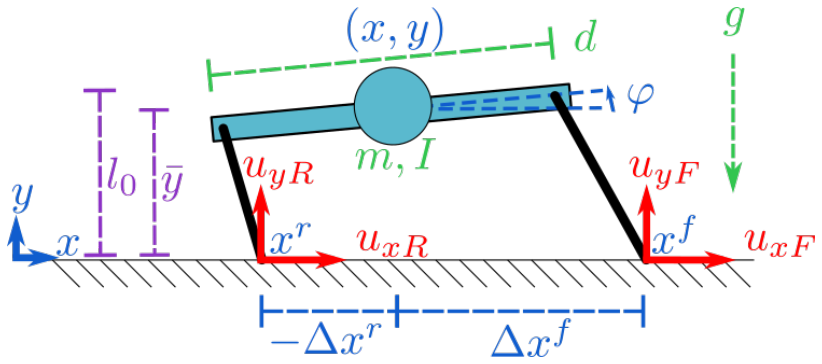

Figure 19: The simplified massless-leg representation of a quadrupedal robot bounding in the sagittal-plane. The model's configuration is shown in blue and is given by the body's location in $SE(2)$ with mass-center position (x, y) and body-pitch φ, as well as the horizontal location of the front and rear toes encoded either by their toe positions x^i or splay-distance Δx^i from the mass-center, $i \in \{f, r\}$. The physical parameters shown in green are the body's mass m and moment-of-inertia I about its mass-center, the body length d, and gravity's acceleration g. Each leg in contact with the ground imparts a vertical (u_y) and horizontal (u_x) mass-specific ground-reaction force law at each toe shown in red. Purple values relate to control parameters. The value l_0 is a nominal vertical leg length at the touchdown and liftoff events (used as a control parameter in (4.25)). In Approximation 1 we introduce $\bar{y}$ as a representing the approximately-constant mass-center stance height under a suitable choice of ground-reaction force control laws.

Following the convention of [122], we define the hybrid system $\mathcal{H}$ representing the sagittal-plane massless-leg robot model depicted in Figures 19 and 20 as the tuple:

$$\mathcal{H} := (\mathcal{J}, \mathcal{T}, \mathcal{D}, \mathcal{F}, \mathcal{G}, \mathcal{R}). \tag{4.3}$$

The set:

$$\mathcal{J} := \{\mathrm{F}, \mathrm{D}, \mathrm{R}\} \tag{4.4}$$

represents the hybrid modes corresponding to front single-support F, double-support D, and rear single-support R, respectively. No flight mode is given due to the actuator constraints of the Inu robot as explained in Chapter 4.5.1, but a similar analysis is possible replacing the double support phase with a flight phase.

The allowed hybrid transitions are given by:

$$\mathcal{T} := \{(\mathrm{F}, \mathrm{D}), (\mathrm{D}, \mathrm{R}), (\mathrm{R}, \mathrm{D}), (\mathrm{D}, \mathrm{F})\}. \tag{4.5}$$

The set of continuous domains is given by:

$$\mathcal{D} := \sqcup_{i \in \mathcal{J}} D_i, \tag{4.6}$$

where – to aid with the decoupling introduced in Chapter 4.2.2 – we decompose each continuous domain into the product:

$$D_i := D_i^I \times D_i^H, \tag{4.7}$$

of "in-place" and "horizontal" respective state components that will form the basis for a cascaded composition (4.1), where:

$$D_i^I := T(\mathbb{R} \times \mathbb{S}) \times \mathbb{R}, \qquad D_i^H := T(\mathbb{R}) \times \mathbb{R}^2, \tag{4.8}$$

with state:

$$\boldsymbol{x}_i = \begin{pmatrix} \boldsymbol{x}_i^I \\ \boldsymbol{x}_i^H \end{pmatrix}, \tag{4.9}$$

where $\boldsymbol{x}_i^I$ represents the "in-place" state components relating to vertical and pitching mo-

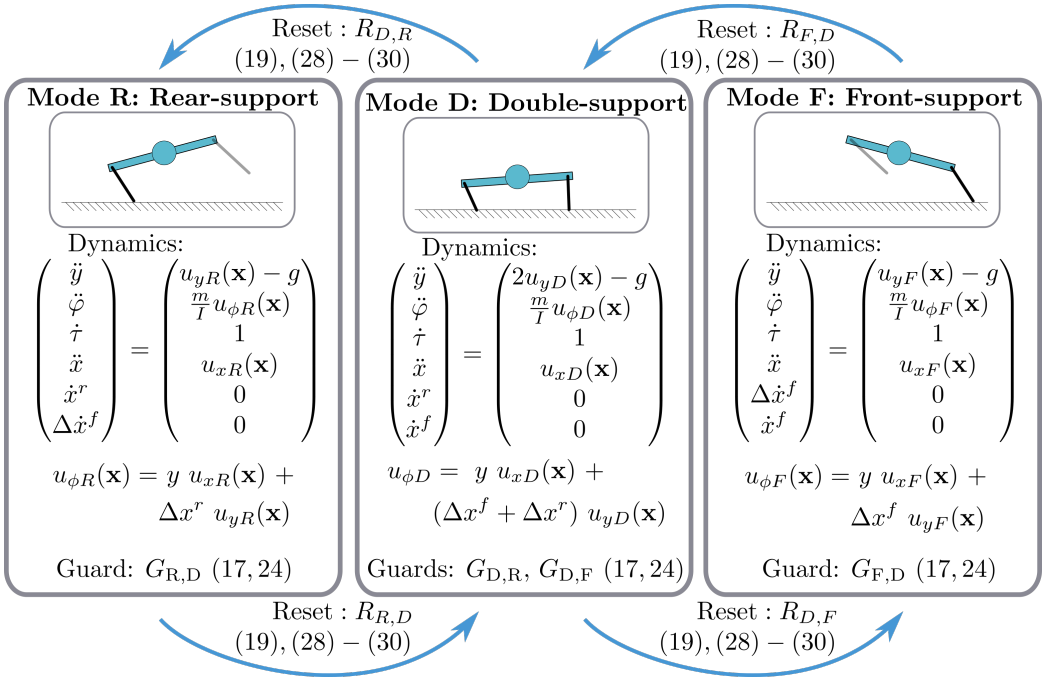

Figure 20: The hybrid dynamical system (4.3) representing the model shown in Figure 19 with state $\boldsymbol{x}_i = ({\boldsymbol{x}^I}^T, {\boldsymbol{x}_i^H}^T)^T$. The state component $\boldsymbol{x}^I$ (4.10) gives the state related to the mass center's vertical height and pitch states, as well as mode timers; while $\boldsymbol{x}_i^H$ (4.11) gives the mass center's horizontal position and velocity, as well as the horizontal toe positions. The guards $G_{i,j}$ and resets $R_{i,j}$ are introduced in (4.17) and (4.19), respectively, and further specified in (4.24)-(4.25) and (4.29)-(4.31) to decouple the hybrid transitions as shown in Figure 21. Approximation 1 and the choice of force laws (4.21), (4.33) decouple the continuous dynamics as shown in Figure 21. There is no flight phase due to actuator limitations when running at speed on the physical machine as described in Chapter 4.5.1, however accounting for an aerial mode instead of double support would yield a system for which a similar control strategy as described in Chapter 4.4 could be applied. Note that the horizontal toe locations indicated by Δx^i and x^i, $i \in \{f, r\}$ – unchanged by the continuous dynamics – are set by the resets as control inputs.

tions, and $\boldsymbol{x}_i^H$ represents the "horizontal" state components relating to horizontal motions.

We will drop mode subscripts when appropriate.

The in-place state $\boldsymbol{x}^I$ is given by:

$$\boldsymbol{x}^I := \begin{pmatrix} \boldsymbol{q}^I \\ \dot{\boldsymbol{q}}^I \\ \tau \end{pmatrix}, \ \boldsymbol{q}^I := \begin{pmatrix} y \\ \varphi \end{pmatrix}, \tag{4.10}$$

representing the configuration and velocity of the mass center's height y and body pitch φ as depicted in Figure 19, as well as the integrated mode duration τ – appended to the state so we can use mode duration as a state variable in the guard events (4.25), (4.57). Intuitively these components represent the state of the robot when it is bounding in-place.

The horizontal state $\boldsymbol{x}_i^H$ in mode $i \in \mathcal{J}$ is given by:

$$\boldsymbol{x}_{\mathrm{F}}^H = \begin{pmatrix} x \\ \dot{x} \\ \Delta x^r \\ x^f \end{pmatrix}, \quad \boldsymbol{x}_{\mathrm{D}}^H = \begin{pmatrix} x \\ \dot{x} \\ x^r \\ x^f \end{pmatrix}, \quad \boldsymbol{x}_{\mathrm{R}}^H = \begin{pmatrix} x \\ \dot{x} \\ x^r \\ \Delta x^f \end{pmatrix}, \tag{4.11}$$

where – as depicted in Figure 19 – x and $\dot{x}$ respectively represent the mass center's horizontal position and velocity, x^f and x^r respectively represent the front and rear foot position, and Δx^f and Δx^r respectively represent the relative distance of the front and rear toe to the mass center according to:

$$\Delta x^f = x^f - x, \quad \Delta x^r = x^r - x. \tag{4.12}$$

The reason for switching between the Δx^i and x^i state representations is simply mathematical convenience as it allows us to represent the continuous evolution of the foot with a zero vector field in (4.14) (although the behavior on the hybrid resets is more complicated), where in stance a hip's toe position x^i does not move and in flight a hip's toe position relative to its mass center Δx^i does not change.

The continuous dynamics of the system are shown in Figure 20. To represent them as first-order vector fields, we define the hybrid vector field:

$$\mathcal{F} : \mathcal{D} \to T\mathcal{D} \tag{4.13}$$

that restricts to the vector fields $F_i := \mathcal{F}|_{D_i}$ for each $i \in \mathcal{J}$ such that:

$$F_i(\boldsymbol{x}) := \begin{pmatrix} \dot{\boldsymbol{q}}^I \\ u_{y_i}(\boldsymbol{x}) - g \\ \frac{m}{I} u_{\varphi_i}(\boldsymbol{x}) \\ 1 \\ \dot{x} \\ u_{xi}(\boldsymbol{x}) \\ 0 \\ 0 \end{pmatrix}, \tag{4.14}$$

where:

$$\begin{aligned} u_{\varphi \mathrm{F}}(\boldsymbol{x}) &= y\ u_{x\mathrm{F}}(\boldsymbol{x}) + \Delta x^f\ u_{y\mathrm{F}}(\boldsymbol{x}), \\ u_{\varphi \mathrm{R}}(\boldsymbol{x}) &= y\ u_{x\mathrm{R}}(\boldsymbol{x}) + \Delta x^r\ u_{y\mathrm{R}}(\boldsymbol{x}), \\ u_{\varphi \mathrm{D}}(\boldsymbol{x}) &= y\ u_{x\mathrm{D}}(\boldsymbol{x}) + (\Delta x^f + \Delta x^r)\ u_{y\mathrm{D}}(\boldsymbol{x}). \end{aligned} \tag{4.15}$$

In Chapter 4.2.3, $u_{y_i}(\boldsymbol{x})$ and $u_{\varphi_i}(\boldsymbol{x})$ will be set to be constant throughout each of the stance modes. Until then, we use the more general functional form to illustrate in Chapter 4.2.2 that we can achieve a cascaded composition without requiring constant values.

For simplicity, we identify $\bar{y}$ with the value of fixed point's height component of (4.15) via the following approximation. This, along with (the to be introduced) Approximation 2 and (4.33), will allow an explicit representation of a relevant hybrid periodic orbit derived in Chapter 4.3:

Approximation 1. *In the pitching acceleration components* (4.15)*, we take the stance height terms* y *to be the constant* $\bar{y} \in \mathbb{R}^+$.

Approximation 1 has the effect of replacing y with $\bar{y}$ in the horizontal force law (4.21). This assumption is approximately valid in the experiments of Chapter 4.5 as shown by the

nearly-constant height in Figures 26 and 27. Further implications of this assumption are discussed in Chapter 4.3.3.

The set of physical parameters is the body length d, gravity's acceleration g, the body mass m, and moment of inertia I (also we later introduce Δx^{Avg} (4.22), a (4.23), and l_0 (4.25) as pseudo-physical parameters chosen by the user for the controller that are strongly influenced by the physical parameters), and the vertical and horizontal (mass-specific) force laws are respectively:

$$\begin{aligned} u_{y_i} &: D_i \to (\frac{g}{2}, g), \\ u_{xi} &: D_i \to \mathbb{R}, \end{aligned} \tag{4.16}$$

which we later set in (4.21), (4.33). The interval bounds on the codomain of $u_{y_i}(\cdot)$ is artificially imposed both to take into account the actuator constraints of Chapter 4.5.1 and to give the range of vertical forces over which the hybrid periodic orbit result described in Proposition 2 holds. Note that $u_{x\text{D}}(\boldsymbol{x})$ is the sum of the double-support force components from each leg, how this force burden is distributed to the legs is an implementation detail (e.g., adjusted in case of reduced traction detected at one or another toe). The experiments of Chapter 4.5 used an even distribution.

The collection of guards is:

$$\mathcal{G} := \sqcup_{(i,j)\in\mathcal{T}} G_{i,j}, \tag{4.17}$$

where $G_{i,j} \subset D_i$ for each $(i,j) \in \mathcal{T}$. We assume that the robot's hip is able to retract its legs in stance to force a flight event and similarly protract its legs in flight to influence the timing of a stance event, according to intersection with a guard set. The guards are considered part of the controller and are further specified in (4.24), (4.25) and in Chapter 4.4.1.

Finally, the hybrid reset map is given by:

$$\mathcal{R} : \mathcal{G} \to \mathcal{D}, \tag{4.18}$$

which restricts to:

$$\begin{aligned} R_{i,j} &:= \mathcal{R}|_{G_{i,j}} \\ R_{i,j} &: G_{i,j} \to D_j, \end{aligned} \tag{4.19}$$

for each $(i, j) \in \mathcal{T}$. The resets – considered part of the controller and specified in (4.29) and Chapter 4.4.2 – move the horizontal state of the toes instantaneously in flight (taking advantage of the assumption of massless legs) and reset the mode timer component τ to zero. To avoid physically unrealistic situations, we require that the resets give all other states continuous motion across hybrid transitions as these states have associated mass.

4.2.2. Cascaded Composition

We impose a cascaded composition (Chapter 4.1.1) with the following choice of force laws and hybrid transitions. We first decouple the horizontal state from the in-place continuous dynamics by choice of horizontal and vertical force laws, giving the in-place acceleration components $\boldsymbol{c}_i(\cdot)$ the form $\boldsymbol{c}_i(\boldsymbol{x}) = \boldsymbol{c}_i(\boldsymbol{x}^I)\ \forall i \in \mathcal{J}$. To do so, we specify the vertical force law to be only a function of in-place state:

$$u_{y_i}(\boldsymbol{x}) = u_{y_i}(\boldsymbol{x}^I), \quad \forall i \in \mathcal{J} \tag{4.20}$$

(which will be set to the constant $u_{y_i}(\boldsymbol{x}^I) = u_y$ in Chapter 4.2.3), and let the horizontal force law be given by:[21]

$$\begin{aligned} u_{x\mathrm{F}}(\boldsymbol{x}) &= \frac{u_y(\boldsymbol{x}^I)}{\bar{y}}\big(\quad \Delta x^{\mathrm{Avg}} - \Delta x^f\big), \\ u_{x\mathrm{D}}(\boldsymbol{x}) &= -\frac{u_{y\mathrm{D}}(\boldsymbol{x}^I)}{\bar{y}}\big(\quad \Delta x^f + \Delta x^r\big), \\ u_{x\mathrm{R}}(\boldsymbol{x}) &= \frac{u_{y\mathrm{R}}(\boldsymbol{x}^I)}{\bar{y}}\big(-\Delta x^{\mathrm{Avg}} - \Delta x^r\big), \end{aligned} \tag{4.21}$$

which makes the pitch dynamics act as if the only torque on the body were from a vertically applied $u_{y_i}(\boldsymbol{x}^I)$ associated with a leg splay of:

$$\Delta x^{\mathrm{Avg}} \in \mathbb{R}. \tag{4.22}$$

We choose to set Δx^{Avg} to equal $\frac{d}{2}$, representing pitch dynamics that mimic the toes being directly below the hips – a choice that maximizes the platform's achievable running speed as discussed in Chapter 4.3.5. In principle any Δx^{Avg} could be chosen, and so for generality we don't fix Δx^{Avg} in our mathematical results. The resulting pitch dynamics from the force law (4.21) are:

$$\ddot{\varphi}_{\mathrm{F}} = \frac{2u_{y\mathrm{F}}(\boldsymbol{x}^I)}{da}, \quad \ddot{\varphi}_{\mathrm{D}} = 0, \quad \ddot{\varphi}_{\mathrm{R}} = -\frac{2u_{y\mathrm{R}}(\boldsymbol{x}^I)}{da}$$

(which in Chapter 4.2.3 become the constants $\ddot{\varphi}_{\mathrm{F}} = \frac{2u_y}{da}$, $\ddot{\varphi}_{\mathrm{D}} = 0$, $\ddot{\varphi}_{\mathrm{R}} = -\frac{2u_y}{da}$ with the choice $u_{y_i}(\boldsymbol{x}^I) = u_y$), where:

$$a := \frac{I}{m\frac{d}{2}\Delta x^{\mathrm{Avg}}} \tag{4.23}$$

is a dimensionless generalized Murphy number [175, p. 193] induced by the leg splay Δx^{Avg} and body parameters.[22]

[21] The smallest value of y is physically bounded by the kinematics to be far from zero so the quotient in (4.21) would never create a problem.

[22] We define our generalized Murphy number as $a := \frac{I}{m\frac{d}{2}\Delta x^{\mathrm{Avg}}}$, where I is the body's moment of inertia, d is the body length, and m is the body mass. When the leg splay distance Δx^{Avg} goes to $\frac{d}{2}$, then our definition agrees with Raibert's presentation of the Murphy number, which he represented by the symbol j.

We next decouple the horizontal state from the in-place hybrid transitions. To do so, we first let only the in-place state components determine the guard intersections:

$$G_{i,j} := \{\boldsymbol{x} \in D_i \mid \boldsymbol{x}^I \in G^I_{i,j}\}. \tag{4.24}$$

If instead we allowed the horizontal state to enter into the form of the guards, then the horizontal flow could influence the mode transitions via the time-to-guard-impact map and thereby affect the the in-place state components, violating the feedforward dependence we are constructing.

Specifically, we define the mode guard set $G^I_{i,j}$ as when a hip's height $y^{j_{hip}} : D^I \to \mathbb{R},\ j \in \{f, r\}$ is moving in the correct direction for a mode change and is equal to some value $l_0 \in \mathbb{R}^+$ plus the value of a control function $g(\boldsymbol{x}^I) : D^I \to \mathbb{R}$ as given by:

$$\begin{aligned}
G^I_{\mathrm{F,D}} &:= \{\boldsymbol{x}^I \in {D^I}_{\mathrm{F}} \mid y^{r_{hip}}(\boldsymbol{x}^I) = l_0 + g_{TD}(\boldsymbol{x}^I) \\
&\qquad\qquad \wedge\ \dot{y}^{r_{hip}}(\boldsymbol{x}^I) < 0\}, \\
G^I_{\mathrm{D,R}} &:= \{\boldsymbol{x}^I \in {D^I}_{\mathrm{D}} \mid y^{f_{hip}}(\boldsymbol{x}^I) = l_0 + g_{LO}(\boldsymbol{x}^I) \\
&\qquad\qquad \wedge\ \dot{y}^{f_{hip}}(\boldsymbol{x}^I) > 0\}, \\
G^I_{\mathrm{R,D}} &:= \{\boldsymbol{x}^I \in {D^I}_{\mathrm{R}} \mid b^I(\boldsymbol{x}^I) \in G^I_{\mathrm{F,D}}\}, \\
G^I_{\mathrm{D,F}} &:= \{\boldsymbol{x}^I \in {D^I}_{\mathrm{D}} \mid b^I(\boldsymbol{x}^I) \in G^I_{\mathrm{D,R}}\},
\end{aligned} \tag{4.25}$$

where the guard $G^I_{\mathrm{F,D}}$ represents the rear leg's touchdown event that initiates double support, $G^I_{\mathrm{D,R}}$ represents the front leg's liftoff event that initiates rear stance, $G^I_{\mathrm{R,D}}$ represents the front leg's touchdown event that initiates double-support, and $G^I_{\mathrm{D,F}}$ represents the rear leg's liftoff event that initiates front stance.

In (4.25), the function $b^I : D^I \to D^I$ is an involutory symmetry map intended to enforce a

"Murphy found that when $j < 1$ the attitude of the body can be passively stabilized in a bounding gait. When $j > 1$, stabilization is not so easily obtained" [175, p. 193]. We use a generalized version of Murphy's result because we feel that accounting for a toe not being directly under the hips when bounding in-place is important, as the user may want to use an arbitrary leg splay. See Figure 24 for a visual depiction of the Murphy number as it relates to this paper's simplified model.

symmetric bound:

$$b^I(\boldsymbol{x}^I) := (y, -\varphi, \dot{y}, -\dot{\varphi}, \tau)^T, \tag{4.26}$$

and the functions g_{LO}, g_{TD} represent the control functions used to modify the touchdown or liftoff hip height from the nominal value of l_0 as a function of state so as to achieve the desired gait. The control functions are chosen in (4.57) of Chapter 4.4.1, but for now we require that they go to zero when the state lies on the desired gait and that:

$$\mathcal{L}_{F_{\mathrm{F}}^I}\, g_{TD} \geq 0, \quad \mathcal{L}_{F_{\mathrm{D}}^I}\, g_{LO} \leq 0, \tag{4.27}$$

so that the hip-height at which touchdown occurs is never decreasing in time during flight and the hip-height at which liftoff occurs is never increasing in time during stance – conditions that will be used in the proof of Proposition 2 to guarantee the existence of a specific hybrid periodic orbit. Here F_{F}^I and F_{D}^I represent the in-place components of the vector field (4.14) in modes F and D, respectively. The value l_0 represents the leg length at touchdown and liftoff on the hybrid limit cycle and should be chosen to be sufficiently far from the workspace singularity as to have room to implement g_{LO}, g_{TD} to stabilize the gait.

Approximation 2. *We use a small-angle approximation on the robot pitch for purposes of checking guard intersections.*

Thus, in the representation of the guards in (4.25), we take the hip heights to be:

$$\begin{aligned} y^{r_{hip}}(\boldsymbol{x}^I) &:= y - \frac{d}{2}\varphi, & y^{f_{hip}}(\boldsymbol{x}^I) &:= y + \frac{d}{2}\varphi, \\ \dot{y}^{r_{hip}}(\boldsymbol{x}^I) &:= \dot{y} - \frac{d}{2}\dot{\varphi}, & \dot{y}^{f_{hip}}(\boldsymbol{x}^I) &:= \dot{y} + \frac{d}{2}\dot{\varphi}. \end{aligned} \tag{4.28}$$

We expect this to be reasonably valid at lower levels of pitching such as those observed in the experiments of Chapter 4.5, but expect its validity will deteriorate if limiting behavior with high pitch is commanded.

Finally, we give the resets $R_{i,j}$ the cascaded form (4.1):

$$R_{i,j}(\boldsymbol{x}^I, \boldsymbol{x}^H) = \begin{pmatrix} R^I_{i,j}(\boldsymbol{x}^I) \\ R^H_{i,j}(\boldsymbol{x}^I, \boldsymbol{x}^H) \end{pmatrix}. \tag{4.29}$$

There is relatively little choice in how to reset the state components since they are largely physically determined, however we are free to reset the mode timers τ as they are non-physical and to reset the horizontal toe positions in flight.

Specifically, we define the in-place resets as:

$$\begin{aligned} R^I_{i,j} : G^I_{i,j} &\to D^I_j \\ (\boldsymbol{q}^I \dot{\boldsymbol{q}}^I, \tau) &\mapsto (\boldsymbol{q}^I \dot{\boldsymbol{q}}^I, 0) \end{aligned} \tag{4.30}$$

for each $(i,j) \in \mathcal{T}^I$, where $R^I_{i,j} \equiv R^I$ simply zeros the timer component of the state. The horizontal resets represent the affordance to stabilize the horizontal components of the model for a bounding gait, in the same manner as the guards for the in-place state components. In placing the foot horizontally ahead or behind of a nominal touchdown configuration according to some control function, they function much like Raibert's neutral

point controller [175]. They are defined as:

$$R^H_{\mathrm{F,D}} : \begin{pmatrix} x \\ \dot{x} \\ \Delta x^r \\ x^f \end{pmatrix} \mapsto \begin{pmatrix} x \\ \dot{x} \\ x + \Delta x^r + r_{\mathrm{F,D}}(\boldsymbol{x}^H_{\mathrm{F}}) \\ x^f \end{pmatrix}, \tag{4.31}$$

$$R^H_{\mathrm{R,D}}(\boldsymbol{x}^H_{\mathrm{R}}) = b^H \circ R^H_{\mathrm{F,D}} \circ b^H(\boldsymbol{x}^H_{\mathrm{R}}),$$

$$R^H_{\mathrm{D,R}} : \begin{pmatrix} x \\ \dot{x} \\ x^r \\ x^f \end{pmatrix} \mapsto \begin{pmatrix} x \\ \dot{x} \\ x^r \\ \Delta x^{\mathrm{Nom}} + r_{\mathrm{D,R}}(\boldsymbol{x}^H_{\mathrm{D}}) \end{pmatrix},$$

$$R^H_{\mathrm{D,F}}(\boldsymbol{x}^H_{\mathrm{D}}) = b^H \circ R^H_{\mathrm{D,R}} \circ b^H(\boldsymbol{x}^H_{\mathrm{D}}),$$

where:

$$b^H : \mathbb{R}^4 \to \mathbb{R}^4 \tag{4.32}$$

$$: \begin{pmatrix} x_1 \\ x_2 \\ x_3 \\ x_4 \end{pmatrix} \mapsto \begin{pmatrix} x_1 \\ x_2 \\ x_4 - 2\Delta x^{\mathrm{Avg}} \\ x_3 + 2\Delta x^{\mathrm{Avg}} \end{pmatrix}$$

is an involutory symmetry map intended to enforce a symmetric bound. The control functions $r_{\mathrm{F,D}}(\boldsymbol{x}^H_{\mathrm{F}}), r_{\mathrm{D,R}}(\boldsymbol{x}^H_{\mathrm{D}})$ (chosen in (4.62) of Chapter 4.4.2) modify the horizontal foot placement in flight prior to touchdown, and – like g_{LO}, g_{TD} – we require that they go to zero when the state lies on the desired gait. The constant value $\Delta x^{\mathrm{Nom}} \in \mathbb{R}$ (chosen in (4.50) of Chapter 4.3.3) represents a nominal touchdown leg splay magnitude.

Having removed all influence of the horizontal state from the in-place hybrid dynamics, we have endowed a feed-forward structure in which the in-place state alone determines the

in-place hybrid execution and which feeds forward into the horizontal dynamics, making any suitably chosen Poincaré map for the system have the cascaded architecture (4.1).

4.2.3. Dynamical Simplification

To further simplify the dynamics, we choose the (mass-specific) vertical force component generated at each foot to be the constant u_y:

$$u_{y_i}(\boldsymbol{x}^I) = u_y \quad \forall i \in \mathcal{J}, \tag{4.33}$$

giving the in-place state components a mode-i flow $\phi_i^t(\boldsymbol{x}^I)$ of the form:

$$\phi_i^t(\boldsymbol{x}^I) = \begin{pmatrix} I & tI & 0 \\ 0 & I & 0 \\ 0 & 0 & 1 \end{pmatrix} \boldsymbol{x}^I + \begin{pmatrix} \frac{t^2}{2}\boldsymbol{c}_i \\ t\boldsymbol{c}_i \\ t \end{pmatrix}, \tag{4.34}$$

$$\boldsymbol{c}_{\mathrm{F}} = \begin{pmatrix} u_y - g \\ \frac{2u_y}{da} \end{pmatrix}, \ \boldsymbol{c}_{\mathrm{D}} = \begin{pmatrix} 2u_y - g \\ 0 \end{pmatrix}, \ \boldsymbol{c}_{\mathrm{R}} = \begin{pmatrix} u_y - g \\ -\frac{2u_y}{da} \end{pmatrix}.$$

Approximations 1, 2 and (4.33) result in the simplified cascaded dynamics depicted in Figure 21. In particular, the choice of a constant vertical force gives rise to affine horizontal continuous dynamics with mass-center forwards acceleration given by:

$$\begin{aligned} \text{Mode F:} \quad \ddot{x} &= \frac{u_y}{\bar{y}}\big(\ \Delta x^{\mathrm{Avg}} - \Delta x^f\big), \\ \text{Mode D:} \quad \ddot{x} &= -\frac{u_y}{\bar{y}}\big(\ \Delta x^f + \Delta x^r\big), \\ \text{Mode R:} \quad \ddot{x} &= \frac{u_y}{\bar{y}}\big(-\Delta x^{\mathrm{Avg}} - \Delta x^r\big), \end{aligned}$$

and the corresponding mode-i horizontal-component flow $\hat{\phi}_i^t(\boldsymbol{x}_i^H)$ of the form:

$$\hat{\phi}_{\mathrm{F}}^t(\boldsymbol{x}_{\mathrm{F}}^H) = \tag{4.35}$$
$$\begin{pmatrix} e^{C_{\mathrm{F}}t}\begin{pmatrix} x \\ \dot{x} \end{pmatrix} + \left(e^{C_{\mathrm{F}}t} - I\right) {C_{\mathrm{F}}}^{-1} \begin{pmatrix} 0 \\ \frac{u_y}{\bar{y}}\left(\Delta x^{\mathrm{Avg}} - x^f\right) \end{pmatrix} \\ \Delta x^r \\ x^f \end{pmatrix},$$
$$\hat{\phi}_{\mathrm{D}}^t(\boldsymbol{x}_{\mathrm{D}}^H) =$$
$$\begin{pmatrix} e^{C_{\mathrm{D}}t}\begin{pmatrix} x \\ \dot{x} \end{pmatrix} + \left(e^{C_{\mathrm{D}}t} - I\right) C_{\mathrm{D}}^{-1} \begin{pmatrix} 0 \\ -\frac{u_y}{\bar{y}}\left(x^r + x^f\right) \end{pmatrix} \\ x^r \\ x^f \end{pmatrix},$$
$$\hat{\phi}_{\mathrm{R}}^t(\boldsymbol{x}_{\mathrm{R}}^H) =$$
$$\begin{pmatrix} e^{C_{\mathrm{R}}t}\begin{pmatrix} x \\ \dot{x} \end{pmatrix} + \left(e^{C_{\mathrm{R}}t} - I\right) C_{\mathrm{R}}^{-1} \begin{pmatrix} 0 \\ \frac{u_y}{\bar{y}}\left(-\Delta x^{\mathrm{Avg}} - x^r\right) \end{pmatrix} \\ x^r \\ \Delta x^f \end{pmatrix},$$

where:

$$C_{\mathrm{F}} = \begin{pmatrix} 0 & 1 \\ \frac{u_y}{\bar{y}} & 0 \end{pmatrix} \quad C_{\mathrm{D}} = \begin{pmatrix} 0 & 1 \\ \frac{2u_y}{\bar{y}} & 0 \end{pmatrix} \quad C_{\mathrm{R}} = \begin{pmatrix} 0 & 1 \\ \frac{u_y}{\bar{y}} & 0 \end{pmatrix}. \tag{4.36}$$

4.3. Hybrid periodic orbit

The explicit flow representation (4.34), (4.35) – combined with guards (4.25) and resets (4.31) – yields expressions for the mode maps (4.37) (derived from the implicit function expressing time to the guard), which are composed in Chapters 4.3.1 and 4.3.2 to form

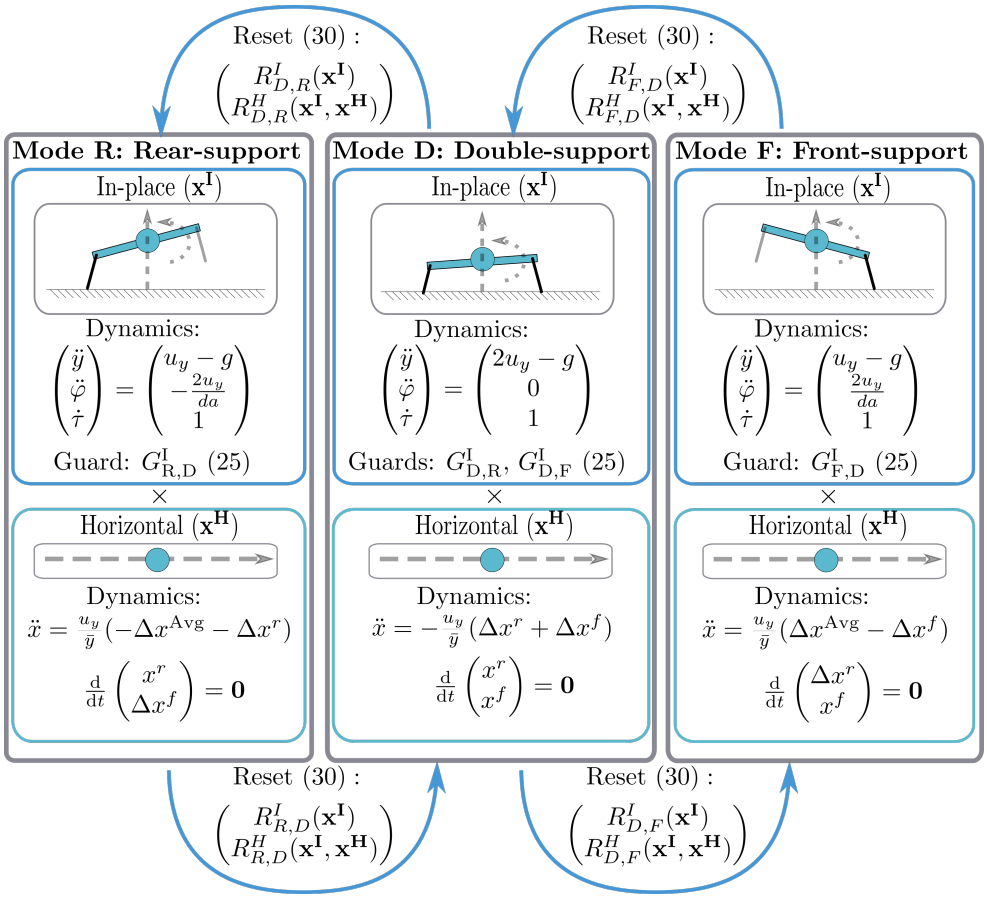

Figure 21: Cascaded hybrid dynamics achieved through the choice of force laws and hybrid guards and resets. The choice of force laws (4.20), (4.21) decouple the continuous dynamics of the hybrid system (4.3) into the cross product of "in-place" and "horizontal" vector fields representing the behavior of the "in-place" vertical and pitching states $\boldsymbol{x}^I$ as well as the "horizontal" fore-aft mass-center and toe position states $\boldsymbol{x}^H$. The isolated continuous dynamics – along with the hybrid guards being purely dependent on the in-place states (4.24) and the hybrid reset maps having cascaded form (4.29) – endows a feed-forward relationship between the in-place states and horizontal states in which a linearized stability analysis of a hybrid periodic orbit's Poincaré map Jacobian has the separation of eigenvalues property indicated by (4.2), allowing for a more tractable analysis. A stable limit cycle is achieved by controlling on the hybrid guards and the resets via (4.25), (4.30), and (4.31). In the vertical states, this is accomplished on the guards by vertically retracting the leg in stance to transition to flight and similarly by protracting the leg in flight to affect the onset of stance. In the horizontal states, this is accomplished on the resets by placing the toe position horizontally in flight in a similar fashion to Raibert's neutral point algorithm [175].

a stride map for the model. We take advantage of symmetry to derive a simpler half-stride Poincaré map, and in Chapter 4.3.3 express a closed-form fixed point (Proposition

2) representing a hybrid periodic orbit. With the form of the hybrid periodic orbit in mind, Chapter 4.3.4 revisits the validity of Approximation 1 (assuming a constant mass-center height in the pitch dynamics), Chapter 4.3.5 discusses a forward-running speed limit associated with the kinematic limitations of a physical machine, and Chapter 4.3.6 discusses the actuator cost to enforce the cascaded decoupling of Chapter 4.2.2.

4.3.1. Choice of Poincaré Section

We now introduce a symmetry that expresses the dynamics of the mode F and its transition into the mode D as a mirror image of mode R and its corresponding transition to D. By restricting attention to only symmetric bounds, this observation affords a factorization of the resulting Poincaré map modeling a stride cycle as comprising a pair of successive half-strides. These considerations in turn motivate our choice of a Poincaré section (with coordinates denoted by a $\sim$ superscript) at the image of the guards under the hybrid reset map of the paired half-strides corresponding to the event of the timer for one being reset to initiate the timer of the next.

Each hybrid mode has an associated map taking a starting state to its value along the forward flow intersecting a guard. For convenience we pre-compose this with the appropriate reset map, so that the hybrid mode-reset composition – which we refer to as the *mode map* and denote by $\Phi_{i,j}$ – maps a starting state in mode i to the reset of where the forward flow intersects the guard $G_{i,j}$. Specifically:

$$\begin{aligned}\Phi_{i,j} : \begin{pmatrix} U^I_{i,j} \\ \\ D^H_i \end{pmatrix} \subset D_i \to D_j, \ (i,j) \in \mathcal{T}, \\ \begin{pmatrix} \boldsymbol{x}^I \\ \boldsymbol{x}^H \end{pmatrix} \mapsto \begin{pmatrix} R^I \circ \phi_i^{T^I_{i,j}(\boldsymbol{x}^I)}(\boldsymbol{x}^I) \\ R^H_i \circ \hat{\phi}_i^{T^I_{i,j}(\boldsymbol{x}^I)}(\boldsymbol{x}^H) \end{pmatrix},\end{aligned} \tag{4.37}$$

(recalling the forms of the resets R^I (4.30), R^H_i (4.31), the in-place flow ϕ_i (4.34), and the

horizontal flow $\hat{\phi}_i$ (4.35)) where we denote the separate components of $\Phi_{i,j}$ as:

$$\Phi_{i,j}(\boldsymbol{x}^I, \boldsymbol{x}^H) = \begin{pmatrix} \Phi^I_{i,j}(\boldsymbol{x}^I) \\ \Phi^H_{i,j}(\boldsymbol{x}^I, \boldsymbol{x}^H) \end{pmatrix}, \tag{4.38}$$

and where:

$$\begin{aligned} T^I_{i,j} : U^I_{i,j} &\to \mathbb{R}^+ \\ \boldsymbol{x}^I &\mapsto \min\{t \in \mathbb{R}^+ | \phi^t_i(\boldsymbol{x}^I) \in G^I_{i,j}\} \end{aligned} \tag{4.39}$$

denotes the implicit time-to-impact map of the flow with the guard. Here $U^I_{i,j}$ represents the largest subset of D^I_i over which $T^I_{i,j}(\cdot)$ is defined and over which the forward flow does not first intersect another guard. We show in the proof of Proposition 2 the existence of points $\bar{\boldsymbol{x}}^I_{\mathrm{F0,D}} \in U^I_{\mathrm{F,D}}$, $\bar{\boldsymbol{x}}^I_{\mathrm{D0,R}} \in U^I_{\mathrm{D,R}}$, $b^I(\bar{\boldsymbol{x}}^I_{\mathrm{F0,D}}) \in U^I_{\mathrm{R,D}}$, and $b^I(\bar{\boldsymbol{x}}^I_{\mathrm{D0,R}}) \in U^I_{\mathrm{D,F}}$, hence the sets $U^I_{i,j}$ are non-empty.

Define the involutory "bounding" symmetry map:

$$\begin{aligned} b : \quad D \quad &\to \quad D \\ \begin{pmatrix} \boldsymbol{x}^I \\ \boldsymbol{x}^H \end{pmatrix} &\mapsto \begin{pmatrix} b^I(\boldsymbol{x}^I) \\ b^H(\boldsymbol{x}^H) \end{pmatrix}, \end{aligned} \tag{4.40}$$

where b^I is given by (4.26) and b^H is given by (4.32). The map b induces a flow conjugacy between F_{F} and F_{R}, as well on flows in F_{D}. This, together with the guard symmetry (4.25) and reset symmetry (4.31), results in b inducing a topological conjugacy between $\Phi_{\mathrm{F,D}}$ and $\Phi_{\mathrm{R,D}}$, as well as between $\Phi_{\mathrm{D,R}}$ and $\Phi_{\mathrm{D,F}}$.

Define the reduced domains $\widetilde{D}_i$ to equal to the domain D_i without mode-timer τ or forward position x components, so as to be of use in defining a stride map whose Poincaré section has the property $\tau = 0$ and does not contain a x component so as to permit stride map

fixed points at speed. Specifically, let:

$$\begin{aligned} \widetilde{D}_i &:= \widetilde{D}_i^I \times \widetilde{D}_i^H, \quad i \in \mathcal{J}, \\ \widetilde{D}_i^I &:= T(\mathbb{R} \times \mathbb{S}), \quad \widetilde{D}_i^H := \mathbb{R}^3 \end{aligned} \tag{4.41}$$

(where we sometimes drop the mode subscripts when appropriate), and the reduced state $\widetilde{\boldsymbol{x}} \in \widetilde{D}$ as:

$$\widetilde{\boldsymbol{x}} := \begin{pmatrix} \widetilde{\boldsymbol{x}}^I \\ \widetilde{\boldsymbol{x}}^H \end{pmatrix}, \quad \widetilde{\boldsymbol{x}}^I \in \widetilde{D}^I, \quad \widetilde{\boldsymbol{x}}^H \in \widetilde{D}^H. \tag{4.42}$$

Specifically, passage between $\widetilde{D}$ and D occurs according to the projection $\Pi : D \to \widetilde{D}$ and lift $\Sigma : \widetilde{D} \to D$ maps:

$$\begin{aligned} \Pi(\boldsymbol{x}) &:= \begin{pmatrix} \Pi^I(\boldsymbol{x}^I) \\ \Pi^H(\boldsymbol{x}^H) \end{pmatrix}, \\ \Pi^I(\boldsymbol{x}^I) &:= \begin{pmatrix} \boldsymbol{q}^I \\ \dot{\boldsymbol{q}}^I \end{pmatrix}, \quad \Pi^H : \begin{pmatrix} x_1 \\ x_2 \\ x_3 \\ x_4 \end{pmatrix} \mapsto \begin{pmatrix} x_2 \\ x_3 \\ x_4 - x_1 \end{pmatrix}, \\ \Sigma(\boldsymbol{x}) &:= \begin{pmatrix} \Sigma^I(\widetilde{\boldsymbol{x}}^I) \\ \Sigma^H(\widetilde{\boldsymbol{x}}^H) \end{pmatrix}, \\ \Sigma^I(\widetilde{\boldsymbol{x}}^I) &:= \begin{pmatrix} \boldsymbol{q}^I \\ \dot{\boldsymbol{q}}^I \\ 0 \end{pmatrix}, \quad \Sigma^H : \begin{pmatrix} x_1 \\ x_2 \\ x_3 \end{pmatrix} \mapsto \begin{pmatrix} 0 \\ x_1 \\ x_2 \\ x_3 \end{pmatrix}. \end{aligned} \tag{4.43}$$

4.3.2. Stride map

We are interested in the asymptotic behavior of a bounding gait with a periodic hybrid mode sequence $(\mathrm{F}, \mathrm{D}, \mathrm{R}, \mathrm{D}, ...)$. To this end, define the stride map S:

$$S : \begin{pmatrix} \widetilde{V}^I \\ \widetilde{D}^H \end{pmatrix} \subset \widetilde{D} \to \widetilde{D}, \tag{4.44}$$
$$\widetilde{\boldsymbol{x}} \mapsto \Pi \circ \Phi_{\mathrm{D,F}} \circ \Phi_{\mathrm{R,D}} \circ \Phi_{\mathrm{D,R}} \circ \Phi_{\mathrm{F,D}} \circ \Sigma,$$

local to some fixed point in the interior of the domain, where $\widetilde{V}^I \subset \Pi^I(U^I_{\mathrm{F,D}})$ is the largest subset of $\Pi^I(U^I_{\mathrm{F}})$ over which S^I is defined. We show in the proof of Proposition 2 the existence of such a fixed point of S^I, so $\widetilde{V}^I$ is not empty.

To simplify the analysis, we use the fact that the stride map factors according to:

$$\begin{aligned} S =& \Pi \circ \Phi_{\mathrm{D,F}} \circ \Phi_{\mathrm{R,D}} \circ \Phi_{\mathrm{D,R}} \circ \Phi_{\mathrm{F,D}} \circ \Sigma \\ =& \Pi \circ (b^H \circ \Phi_{\mathrm{D,R}} \circ b^H) \circ (b^H \circ \Phi_{\mathrm{F,D}} \circ b^H) \circ \\ & \Phi_{\mathrm{D,R}} \circ \Phi_{\mathrm{F,D}} \circ \Sigma \\ =& \Pi \circ b^H \circ \Phi_{\mathrm{D,R}} \circ \Phi_{\mathrm{F,D}} \circ b^H \circ \Phi_{\mathrm{D,R}} \circ \Phi_{\mathrm{F,D}} \circ \Sigma \\ =& \Pi \circ b^H \circ \Phi_{\mathrm{D,R}} \circ \Phi_{\mathrm{F,D}} \circ (\Sigma \circ \Pi) \circ b^H \circ \\ & \Phi_{\mathrm{D,R}} \circ \Phi_{\mathrm{F,D}} \circ \Sigma \\ =& (\Pi \circ b^H \circ \Phi_{\mathrm{D,R}} \circ \Phi_{\mathrm{F,D}} \circ \Sigma) \circ \\ & (\Pi \circ b^H \circ \Phi_{\mathrm{D,R}} \circ \Phi_{\mathrm{F,D}} \circ \Sigma) \\ =& H^2, \end{aligned} \tag{4.45}$$

where $H : \begin{pmatrix} \widetilde{V}^I \\ \widetilde{D}^H \end{pmatrix} \to \widetilde{D}$ such that:

$$H := \Pi \circ b \circ \Phi_{\mathrm{D,R}} \circ \Phi_{\mathrm{F,D}} \circ \Sigma \tag{4.46}$$

represents a "flipped" (by b) half-stride of the stride map.

4.3.3. Stride Map Fixed Point

A stable fixed point of H is a stable fixed point of S, so we reduce our attention to the asymptotic behavior of H which is simpler. We note that we are interested in a symmetric bound so any fixed points of S that we are discarding by virtue of not being fixed points of H via the symmetry b are not symmetric.

Proposition 2. *The maps H and S have a fixed point at:*

$$\widetilde{\bar{\boldsymbol{x}}} := \begin{pmatrix} \widetilde{\bar{\boldsymbol{x}}}^I \\ \widetilde{\bar{\boldsymbol{x}}}^H \end{pmatrix}, \quad \widetilde{\bar{\boldsymbol{x}}}^I := \begin{pmatrix} \bar{y} \\ \bar{\varphi} \\ \dot{\bar{y}} \\ \dot{\bar{\varphi}} \end{pmatrix}, \quad \widetilde{\bar{\boldsymbol{x}}}^H := \begin{pmatrix} \dot{\bar{x}} \\ \bar{\Delta x}^r \\ \bar{\Delta x}^f \end{pmatrix}, \tag{4.47}$$

where:

$$\begin{pmatrix} \bar{y} \\ \bar{\varphi} \\ \dot{\bar{y}} \\ \dot{\bar{\varphi}} \end{pmatrix} = \begin{pmatrix} l_0 - \frac{u_y(g-u_y)}{4a(2u_y-g)} \bar{T}^2_{\mathrm{F,D}} \\ -\frac{u_y(g-u_y)}{2ad(2u_y-g)} \bar{T}^2_{\mathrm{F,D}} \\ \frac{g-u_y}{2} \bar{T}_{\mathrm{F,D}} \\ -\frac{u_y}{ad} \bar{T}_{\mathrm{F,D}} \end{pmatrix}, \tag{4.48}$$

and:

$$\bar{\Delta x}^f = \frac{\begin{pmatrix} 0 & 1 \end{pmatrix} \left(e^{C_{\mathrm{F}} \bar{T}_{\mathrm{F,D}}} - I \right) \begin{pmatrix} \Delta x^{Avg} \\ \dot{\bar{x}} \end{pmatrix}}{\begin{pmatrix} 0 & 1 \end{pmatrix} \left(e^{C_{\mathrm{F}} \bar{T}_{\mathrm{F,D}}} - I \right) \begin{pmatrix} 1 \\ 0 \end{pmatrix}}, \tag{4.49}$$

$$\bar{\Delta x}^r = \bar{\Delta x}^f - 2\Delta x^{Avg} + \begin{pmatrix} 1 & 0 \end{pmatrix} \left(e^{C_{\mathrm{D}} \bar{T}_{\mathrm{D,R}}} + I \right)^{-1} \left(e^{C_{\mathrm{D}} \bar{T}_{\mathrm{D,R}}} - I \right) \left(e^{C_{\mathrm{F}} \bar{T}_{\mathrm{F,D}}} + I \right) \begin{pmatrix} \Delta x^{Avg} - \bar{\Delta x}^f \\ \dot{\bar{x}} \end{pmatrix},$$

where (recall (4.36)) $C_{\mathrm{F}} = \begin{pmatrix} 0 & 1 \\ \frac{u_y}{\bar{y}} & 0 \end{pmatrix}$ *and* $C_{\mathrm{D}} = \begin{pmatrix} 0 & 1 \\ \frac{2u_y}{\bar{y}} & 0 \end{pmatrix}$.

The fixed point $\widetilde{\boldsymbol{x}}^H$ *is parametrized by the physical parameters of the system, the duration* $\bar{T}_{\mathrm{F,D}} \in \mathbb{R}^+$ *of the periodic orbit's evolution in mode* F *(equal to its duration in mode* R*), and the forward speed component* $\dot{\bar{x}}$ *of the fixed point. The term* Δx^{Nom} *in (4.31) is given by:*

$$\Delta x^{\mathrm{Nom}} = \Delta \bar{x}^r + 2\Delta x^{Avg}, \tag{4.50}$$

and the terms $\Delta \bar{x}^r{}_{\mathrm{D}}$, $\Delta \bar{x}^f{}_{\mathrm{D}}$ *– defined in (4.49) and used in (4.62) – have the property that:*

$$\Delta \bar{x}^r{}_{\mathrm{D}} = \Delta \bar{x}^f - 2\Delta x^{Avg},$$
$$\Delta \bar{x}^f{}_{\mathrm{D}} = -\Delta \bar{x}^r.$$

Additionally, the duration $\bar{T}_{\mathrm{D,R}} = \bar{T}_{\mathrm{D,F}}$ *of the periodic orbit's evolution in mode* D *is equal to:*

$$\bar{T}_{\mathrm{D,R}} = \bar{T}_{\mathrm{F,D}} \frac{g - u_y}{2u_y - g}. \tag{4.51}$$

Proof. See Chapter 4.10. □

The form of the fixed point does not give much insight into the nature of the resulting orbit and how parameter choices (particularly u_y and $\bar{T}_{\mathrm{F,D}}$) affect it. As such, we give the minimum and maximum state variable values along the orbit associated with $\widetilde{\boldsymbol{x}}$ in Table 4. Recall that $u_y \in (\frac{g}{2}, g)$ (4.16) and $\bar{T}_{\mathrm{F,D}} \in \mathbb{R}^+$, where the interval constraint on u_y guarantees a physically realistic double support phase on the hybrid periodic orbit to capture the actuator constraints of Chapter 4.5.1. Additionally, the mass center height varies by a value of:

$$\frac{\bar{T}_{\mathrm{F,D}}^2}{8} \frac{g - u_y}{2u_y - g} u_y \tag{4.52}$$

along the orbit.

State	Min value along orbit	Max value along orbit
y	$l_0 + \frac{1}{8}\bar{T}_{\mathrm{F,D}}^2 \frac{g-u_y}{2u_y-g}(\zeta - u_y)$	$l_0 + \frac{1}{8}\bar{T}_{\mathrm{F,D}}^2 \frac{g-u_y}{2u_y-g}\zeta$
	$\zeta = 2u_y(1-a^{-1}) - g$	
φ	$-\frac{gu_y\bar{T}_{\mathrm{F,D}}^2}{4ad(2u_y-g)}$,	$\frac{gu_y\bar{T}_{\mathrm{F,D}}^2}{4ad(2u_y-g)}$
$\dot{y}$	$-\frac{g-u_y}{2}\bar{T}_{\mathrm{F,D}}$,	$\frac{g-u_y}{2}\bar{T}_{\mathrm{F,D}}$
$\dot{\varphi}$	$-\frac{u_y}{ad}\bar{T}_{\mathrm{F,D}}$,	$\frac{u_y}{ad}\bar{T}_{\mathrm{F,D}}$
$\lvert\dot{x}\rvert$	$\sqrt{\dot{\bar{x}}^2 - \xi}$,	$\lvert\dot{\bar{x}}\rvert$
	$\xi = \frac{u_y}{\bar{y}} \cdot \max\left\{(\Delta x^{\mathrm{Avg}} - \Delta\bar{x}^f)^2,\ \frac{1}{2}(\Delta x^{\mathrm{Nom}} - \Delta\bar{x}^f)^2\right\}$	
Δx^r	$-\Delta x^{\mathrm{Nom}}$,	$-(2\Delta x^{\mathrm{Avg}} - \Delta x^{\mathrm{Nom}})$
Δx^f	$2\Delta x^{\mathrm{Avg}} - \Delta x^{\mathrm{Nom}}$,	Δx^{Nom}

Table 4: Minimum and maximum state values along the hybrid periodic orbit
Minimum and maximum state values along the hybrid periodic orbit associated with the fixed point $\widetilde{\bar{\boldsymbol{x}}}$ (defined in Proposition 2) of H (4.46) as determined by the parameters and "user-specified" selection of $u_y \in (\frac{g}{2}, g)$ (4.16), $\bar{T}_{\mathrm{F,D}} \in \mathbb{R}^+$, and $\dot{\bar{x}} \in \mathbb{R}$. In practice $\dot{\bar{x}}$ is not truly a free variable, as a speed limit (approximated by (4.55)) exists by virtue of a machine's inherently limited leg workspace constraining the maximum achievable leg sweep distance. Both legs sweep a distance of $\delta\bar{x}_{\mathrm{Stance}} = |2(\Delta x^{\mathrm{Nom}} - \Delta x^{\mathrm{Avg}})|$ during their stance phases, a complicated expression (due to the form of Δx^{Nom} (4.50)) for which an approximation is proposed in (4.54). Figure 22 shows the hybrid periodic orbit trajectory when using the parameters of Table 5, illustrating where in the mode sequence the minima and maxima occur.

The "user-specified" terms in the form of the hybrid periodic orbit (the terms not determined by the physical robot parameters) are u_y, $\bar{T}_{\mathrm{F,D}}$, and $\dot{\bar{x}}$. The (mass-specific) applied vertical force at the toe u_y can be thought of as analogous to a spring constant: increasing u_y decreases vertical height and pitch oscillations,[23] as well as total hip stance time (by

[23]The reason that increasing the stance force u_y decreases height y and pitch φ variations of the orbit is because total stance time (4.53) is reduced by an increase in u_y, giving the system configuration less time to change in stance. While the variations in y and φ decrease with increasing u_y, total energy of the orbit increases.

decreasing the double-support time $\bar{T}_{\mathrm{D,R}}$ (4.51)), where the total hip's stance time $\bar{T}_{\mathrm{Stance}}$ is equal to:

$$\bar{T}_{\mathrm{Stance}} := \bar{T}_{\mathrm{F,D}} + 2\bar{T}_{\mathrm{D,R}} \;=\; \bar{T}_{\mathrm{F,D}} \left(\frac{g}{2u_y - g} \right). \tag{4.53}$$

The value of $\bar{T}_{\mathrm{F,D}}$ directly sets the single-support stance duration (equal to a hip's flight duration) and can be thought of as the dominant determiner of a hip's total stance time $\bar{T}_{\mathrm{Stance}}$ in cases with shorter double support $\bar{T}_{\mathrm{D,R}}$.[24] Larger values of $\bar{T}_{\mathrm{F,D}}$ increase vertical height and pitch oscillations. Smaller values of $\bar{T}_{\mathrm{F,D}}$ leaves less time for the leg to reset its position in flight, and sufficiently small values will be prohibitive for the actuators. The value of $\dot{\bar{x}}$ sets the desired speed at mode transitions.

4.3.4. Constant Stance Height Approximation

With an explicit representation for the hybrid periodic orbit's mass-center height variation (4.52) in hand, we revisit Approximation 1's usage of a constant stance height in the pitching acceleration components of the dynamics (4.15). Approximation 1 will hold on the hybrid periodic orbit for height variation values of (4.52) that are small compared to the height of the robot.

For Inu using the experimental parameters of $u_y = 8.5$ m/s^2 and $\bar{T}_{\mathrm{F,D}} = 0.15$ seconds as indicated in Table 5, the height variation of the mass-center along the desired limit cycle is equal to a deviation of 4 mm, thus the height is only expected to change 1% from its nominal value of 0.21 meters during the periodic orbit, which begins to approach the noise floor on our sensors and is thus more than sufficient for a constant approximation assumption. This is illustrated in the experimental traces of Inu running in Figures 26 and 27, where the mass-center height is approximately constant both in the experimental data and in the desired limit cycle.

More generally, the validity of this approximation is strongly dependent on the duration of

[24] Our regime of operation involves a short double support time $\bar{T}_{\mathrm{D,R}}$, however the double support time would be longer for very low vertical forces approaching just barely supporting the weight of the robot. In this case a change of variables to total support time might be more insightful.

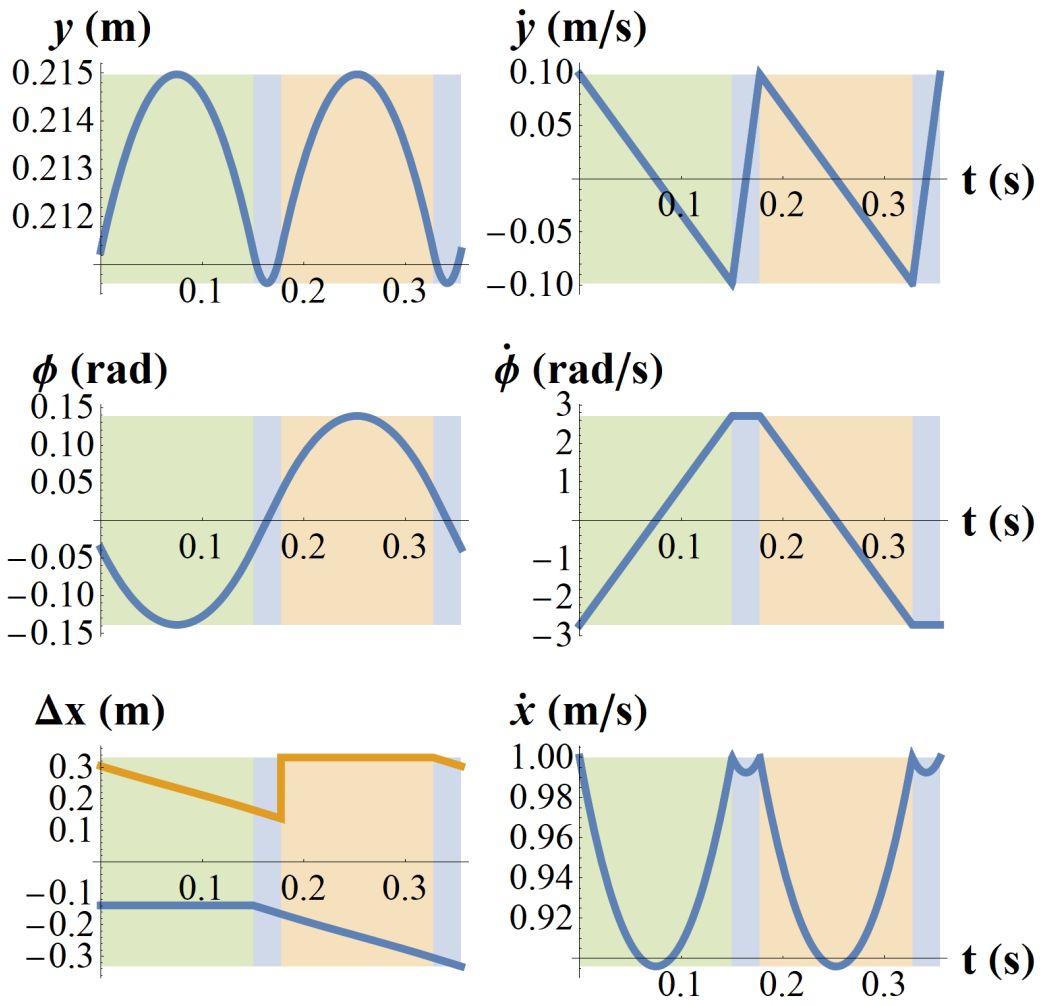

Figure 22: Traces of the hybrid periodic orbit over a full stride using the parameters of Table 5 at a commanded speed of 1 m/s. The background color indicates the mode (4.4). Green is F, blue is D, and yellow is R. In the Δx graph, the blue trace gives Δx^r while the orange trace gives Δx^f (4.12). Notice that deviations in body height y and forward speed $\dot{x}$ are quite small, indicating a valid Approximation 1 as discussed in Chapter 4.3.4 and a small value of ξ from Table 4.

the hip's stance but – for the following reasons – we expect it to hold for a large class of machines. In terms of the duration of the hip's stance (equal to 205 ms on Inu with the parameters of Table 5), the mass-center's height deviation is equal to:

$$\frac{1}{8}\frac{\bar{T}^2_{\text{Stance}}}{g^2}u_y(g-u_y)(2u_y-g),$$

which is maximized by u_y when $u_y = \frac{g}{6}(3+\sqrt{3}) \approx 0.79g$, resulting in a mass-center height deviation of $\frac{g\bar{T}^2_{\text{Stance}}}{48\sqrt{3}}$. Stance durations of approximately 300 ms or less – where 300 ms is a relatively long stance duration for robots of Inu's mass scale – result in mass-center height deviations of 1 cm or less – a small value compared to Inu's nominal mass-center height 0.21 meters while running. In biology, the duration of stance has a strong scale dependence: it generally increases with body mass and animals up to the size of horses have been documented having stance times of 300 ms or less [84].[25] If the same results were to hold on robots, even when using our antagonistic value of u_y we would expect that larger robots would satisfy Approximation 1 and that smaller robots (with much shorter stance times) would have an even smaller height deviation for their size.[26] Of course, one could design a robot with an artificially long stance duration to break the validity of Approximation 1 but this would result in a severely speed-limited robot as discussed in Chapter 4.3.5.

4.3.5. Speed Limit

The inherently limited workspace of a leg's kinematic linkage induces a speed limit to running [136]. In our case, the leg linkage workspace must accommodate the maximum and minimum values of the leg splays Δx^r and Δx^f in Table 4 to physically instantiate the periodic orbit associated with the fixed point $\widetilde{\boldsymbol{x}}$. This results in a horizontal leg-sweep distance of $\delta\bar{x}_{\text{Stance}} = |2(\Delta x^{\text{Nom}} - \Delta x^{\text{Avg}})|$, where recall Δx^{Nom} is speed dependent (4.50). The sweep distance has a complicated form in terms of the model parameters as Δx^{Nom} involves the complicated expression $\Delta\bar{x}^r$ (4.49), however we can understand the dominant terms using a simple approximation.

Approximate the average forward speed in stance by $\dot{\bar{x}}$, which is valid given a small value of the term ξ in Table 4 relative to $\dot{\bar{x}}^2$ (this applies to Inu as indicated by the small speed

[25] In the study, ground contact time was found to be generally proportional to $M^{0.19\pm0.06}$ for animals with body mass M.

[26] One would also need to reconsider the use of this approximation when using a much more energetic gait that has a flight phase, but of course this would assume a difference hybrid mode sequence than is considered in this work.

deviations in both the hybrid periodic orbit in Figure 22 and the robot's instantiation of those orbits in Figures 26, 27). Then the mass center's (and thus the hip's) horizontal sweep distance in stance $\delta\bar{x}_{\text{Stance}}$ is:

$$\begin{aligned}\delta\bar{x}_{\text{Stance}} &\approx \dot{\bar{x}}(\bar{T}_{\text{F,D}} + 2\bar{T}_{\text{D,R}}) \\ &= \dot{\bar{x}}\bar{T}_{\text{F,D}}\left(\frac{g}{2u_y - g}\right) \\ &\overset{(4.53)}{=} \dot{\bar{x}}\bar{T}_{\text{Stance}}.\end{aligned} \tag{4.54}$$

A robot with a horizontal leg-stroke distance that is kinematically limited to $\delta x^{\text{Max}}_{\text{Stance}}$ and with a stance time $\bar{T}_{\text{Stance}}$ (limited from below by a value of u_y achievable by the actuators) would physically be able to instantiate an orbit with a maximum running speed magnitude $\dot{\bar{x}}^{\text{Max}}$ of:

$$\dot{\bar{x}}^{\text{Max}} \approx \frac{\delta x^{\text{Max}}_{\text{Stance}}}{\bar{T}_{\text{Stance}}} = \delta x^{\text{Max}}_{\text{Stance}} \frac{2u_y - g}{g\bar{T}_{\text{F,D}}}, \tag{4.55}$$

a value of 1.6 m/s for Inu as explained in Chapter 4.5.1.

We now revisit our decision in Chapter 4.2.2 to set Δx^{Avg} to equal $\frac{d}{2}$ so as to maximize forward running speed. The horizontal interval that the legs sweep when operating on the periodic orbit is centered at a distance of Δx^{Avg} from the mass center as calculated from Table 4. Coarsely assume that the leg linkage workspace permits an interval of horizontal reach centered at the hip. The horizontal leg-sweep interval must be contained in the leg workspace interval for a physically realizable gait. The maximum speed that can be physically realized occurs when the horizontal leg-sweep interval and leg workspace interval are identical, which requires that they be centered at the same point, which requires Δx^{Avg} equal $\frac{d}{2}$.

4.3.6. Cost of Enforcing a Cascade

Proposition 2 allows us to revisit the cost of enforcing the cascade composition of Chapter 4.2.2 with the horizontal force law (4.21) along the hybrid periodic orbit. Very often in robotics, a disadvantage of canceling the natural system dynamics with control is that it requires significant actuation affordance. However – as we argue below – at lower speeds the horizontal forces needed to achieve this dynamic decoupling are quite small; they are only a fraction of the applied constant vertical force.

We quantify this by considering the maximum horizontal leg force magnitude encountered during a stride on the periodic orbit. This maximum value is obtained when the horizontal length from the toe to the mass-center is furthest from Δx^{Avg} (4.21). When operating on the hybrid periodic orbit, recall that the leg sweeps an interval of length $\delta\bar{x}_{\text{Stance}}$ centered at a distance Δx^{Avg} from the mass center (Chapter 4.3.5), thus reaching out a maximum distance of $\frac{1}{2}\delta\bar{x}_{\text{Stance}}$ from the centered distance of Δx^{Avg} and giving the horizontal force the maximum stance magnitude:[27]

$$|u_{x\text{Max}}| = \frac{1}{2}|\delta\bar{x}_{\text{Stance}}|\frac{u_y}{\bar{y}}.$$

Putting this in terms of forward running speed using the approximation (4.54) gives:

$$|u_{x\text{Max}}| \approx \frac{1}{2}|\dot{\bar{x}}|\bar{T}_{\text{Stance}}\frac{u_y}{\bar{y}}. \tag{4.56}$$

This force would be briefly equal to the applied specific vertical force u_y in stance at an average stance speed of $\dot{\bar{x}} = \frac{2\bar{y}}{\bar{T}_{\text{Stance}}}$. Using a duration of hip-stance of $\bar{T}_{\text{Stance}} = 0.2$ seconds and an average mass-center stance height of 0.21 meters (Inu's experimental parameters derived from Table 5) results in a speed of 2.1 m/s where the maximum horizontal and vertical

[27] The given maximum horizontal force is really a conservative upper bound, as it corresponds to the double-support mode and a sensible user would not program both the front and rear legs to generate opposing internal forces of this magnitude, rather they could achieve the same total horizontal force on the body with much smaller horizontal toe forces to decrease internal forces. The user's choice of front/rear force distribution in double support is elaborated on near the end of Chapter 4.2.1

forces are briefly equal. Inu is kinematically limited to a running speed of approximately 1.6 m/s, so the platform cannot approach the high-cost-of-cascade-enforcement regime. On a quadruped not kinematically limited, higher speeds than $\dot{\bar{x}} = \frac{2\bar{y}}{\bar{T}_{\text{Stance}}}$ require that the toes reach sufficiently in front of or behind the hips to the point of causing the horizontal cascade-enforcement force to briefly eclipse the vertical at the beginning and end of stance. In these cases we can consider the cascade enforcement to be "expensive" for the actuators. A shorter stance duration (4.53) would mitigate this cost, achieving this through reducing $\bar{T}_{\text{F,D}}$ would increase the actuator cost of reseting the leg's position in flight, and achieving this through increasing u_y would also tax the actuators.

The approximate cost of enforcing the cascade is linear in speed (4.56), going to zero when bounding in-place. Thus at low speeds and small horizontal forces we believe that the natural dynamics are themselves "almost" a feedforward cascade of the in-place module with the horizontal bead-on-a-wire dynamics, and that our choice of a horizontal force law represents only a slight "nudge" to the dynamics so as to complete this decoupling (Figure 21) and provide us with a tractable stability analysis.

4.4. Controller

Control of the system to achieve a symmetric bound occurs on the hybrid guards and resets. Recall from Chapter 4.2.2 that cascading the dynamics naturally places the in-place control gains in the guards and the horizontal control gains in the resets. A summary of our control strategy is as follows.

The in-place controllers perform feedback on the mode timers and hip heights, as time and kinematic configuration are the most accurately measured aspects of the state as discussed in Chapter 4.6.1. Instead of controlling on the continuous value of the hip heights, we only control on their value at the start of the mode. This has the practical benefit of providing hip-height measurements for the controller even when the hip is in flight (having measured its value at liftoff), as well as the algebraic benefit of simplifying the stability calculations

in Chapter 4.4.3 as the hip-height values being controlled on don't change over the course of a mode. The fact that six easily measurable quantities exist per half-stride (two modes, each with one timer and two hip-height measurements) results in six control gains. Four of the gains are used to place the four poles of the stride map corresponding to the four in-place components (recall that the presence of the timer coordinate in the dynamics gives four in-place Poincaré map components, not three), and the remaining two gains are used to optimize for other performance criteria.

The reset controllers perform feedback on the system's forward speed and the two toe positions. This gives three gains (rather than six, as the controllers can only set the horizontal toe position in flight and not in stance) to place the three poles of the stride map corresponding to the three horizontal components (recall that one component corresponds to forward speed and the other two correspond to the horizontal toe locations). In principle the horizontal controller could be chosen to take in additional inputs and thereby allow the user to optimize for other performance criteria, for example the in-place mode timers and hip heights, however we found that performance was reasonable without needing to introduce additional feedback paths.

Chapter 4.4.1 specifies the controller on the guards, which stabilizes the in-place state components. Chapter 4.4.2 specifies the controller on the resets, which stabilizes the horizontal state components. Chapter 4.4.3 presents the central stability result of the paper. Specifically, we present a choice of control weights that makes the Poincaré map Jacobian evaluated at the fixed point nilpotent (Proposition 3), making the closed-loop dynamics infinitesimally deadbeat.

4.4.1. Hybrid Guard Control

Recall that hybrid guards intersections (4.24), (4.25) require the appropriate hip height equal some nominal value l_0 plus some (to-be-specified) state-dependent guard control function $g_{LO}, g_{TD} : D^I \to \mathbb{R}$. Recall from above, we choose to use guard controllers that are

functions of the mode timers and hip-heights – giving six control gains as shown below in (4.57) – as mode time and kinematic configuration (hip height) are the most accurately measured aspects of the in-place state by our robot as discussed in Chapter 4.6.1. Specifically, we use guard control functions of the following form:

$$g_{TD}(\boldsymbol{x}^I) := {\boldsymbol{k}^I}_{\mathrm{F}}{}^T \begin{pmatrix} {y^{r_{hip}}}_{\mathrm{F0}}(\boldsymbol{x}^I) - y^{r_{hip}}(\bar{\boldsymbol{x}}^I_{\mathrm{F0,D}}) \\ {y^{f_{hip}}}_{\mathrm{F0}}(\boldsymbol{x}^I) - y^{f_{hip}}(\bar{\boldsymbol{x}}^I_{\mathrm{F0,D}}) \\ \tau - \bar{T}_{\mathrm{F,D}} \end{pmatrix}, \tag{4.57}$$

$$g_{LO}(\boldsymbol{x}^I) := {\boldsymbol{k}^I}_{\mathrm{D}}{}^T \begin{pmatrix} {y^{r_{hip}}}_{\mathrm{D0}}(\boldsymbol{x}^I) - y^{r_{hip}}(\bar{\boldsymbol{x}}^I_{\mathrm{D0,R}}) \\ {y^{f_{hip}}}_{\mathrm{D0}}(\boldsymbol{x}^I) - y^{f_{hip}}(\bar{\boldsymbol{x}}^I_{\mathrm{D0,R}}) \\ \tau - \bar{T}_{\mathrm{D,R}} \end{pmatrix},$$

where the vectors ${\boldsymbol{k}^I}_{\mathrm{F}}, {\boldsymbol{k}^I}_{\mathrm{D}} \in \mathbb{R}^3$ represent control weights, $y^{f_{hip}}$, $y^{r_{hip}} : D^I \to \mathbb{R}$ give the front and rear hip heights (4.28), and the functions ${y^{r_{hip}}}_{i0}, {y^{f_{hip}}}_{i0} : D^I_i \to \mathbb{R}, i \in \mathcal{J}^I$ give the mode's initial hip heights (according to the hip heights that occurred when $\tau = 0$) via:

$$\begin{aligned} {y^{r_{hip}}}_{i0}(\boldsymbol{x}^I) &:= y^{r_{hip}} \circ \phi_i^{-\tau}(\boldsymbol{x}^I), \\ {y^{f_{hip}}}_{i0}(\boldsymbol{x}^I) &:= y^{f_{hip}} \circ \phi_i^{-\tau}(\boldsymbol{x}^I). \end{aligned} \tag{4.58}$$

The values of $\bar{\boldsymbol{x}}^I_{i0,j}$ in (4.57) are set as follows and represent "target" states for the controller to track, we choose them so that the control functions vanish by design along the hybrid orbit associated with a privileged fixed point of H. Denote the lift (4.43) of the stride map fixed point $\widetilde{\bar{\boldsymbol{x}}}$ in Proposition 2 from $\widetilde{D}$ to D_{F} by:

$$\bar{\boldsymbol{x}} = \begin{pmatrix} \bar{\boldsymbol{x}}^I \\ \bar{\boldsymbol{x}}^H \end{pmatrix} := \Sigma(\widetilde{\bar{\boldsymbol{x}}}), \tag{4.59}$$

and set $\bar{\boldsymbol{x}}^I_{i0,j}$ in (4.57) to equal the in-place component of the state of the hybrid execution

initialized at $\bar{\boldsymbol{x}}$ as it periodically enters mode i before entering mode j according to:

$$\bar{\boldsymbol{x}}^I_{\mathrm{F0,D}} := \bar{\boldsymbol{x}}^I, \quad \bar{\boldsymbol{x}}^I_{\mathrm{D0,R}} := \Phi^I_{\mathrm{F,D}}(\bar{\boldsymbol{x}}^I). \tag{4.60}$$

Finally, let $\bar{T}_{\mathrm{F,D}}$ and $\bar{T}_{\mathrm{D,R}}$ in (4.57) agree with the durations of the hybrid trajectory in modes F and D, respectively.

Let ${k^I}_{\mathrm{F}i}$ and ${k^I}_{\mathrm{D}i}$ denote the i'th components of control parameter vectors ${\boldsymbol{k}^I}_{\mathrm{F}}$ and ${\boldsymbol{k}^I}_{\mathrm{D}}$, respectively. We impose the requirement that:

$${k^I}_{\mathrm{F3}} \geq 0, \quad {k^I}_{\mathrm{D3}} \leq 0, \tag{4.61}$$

so that the hip-height necessary for touchdown is not decreasing in time and the hip-height necessary for liftoff is not increasing in time, satisfying (4.27).

Intuitively, the guard control functions (4.57) act as proportional controllers and modify the nominal touchdown or liftoff hip heights according to a weighted sum of errors between scalar-valued functions of the state and constant "target" values. These scalar-valued functions consist of the hip height values at the start of the mode execution (calculated by back-flowing the state until the component τ coincides with 0 and examining the hip heights at that time instance, and physically implemented by measuring the state variables at the start of the mode) and the current mode duration according to τ. The "target" states were chosen to force the control functions to zero at the hybrid transitions along the privileged periodic orbit of Proposition 2, by setting them to equal the state along the orbit when the evolution initially enters mode i as it evolves to mode j. The control weights ${\boldsymbol{k}^I}_{\mathrm{F}}, {\boldsymbol{k}^I}_{\mathrm{D}}$ will be chosen in Chapter 4.4.3 and Chapter 4.8 to make the periodic hybrid trajectory associated with $\widetilde{\bar{\boldsymbol{x}}}$ a stable hybrid limit cycle.

4.4.2. Hybrid Reset Control

Recall that the in-place components of the hybrid resets simply zero the mode timer variable τ, while the horizontal components of the reset place the foot horizontally in flight from a nominal value according to control functions $r_{\mathrm{F,D}}, r_{\mathrm{D,R}} : D^H \to \mathbb{R}$ (4.31). We choose reset control functions of the following form:

$$r_{\mathrm{F,D}}(\boldsymbol{x}_{\mathrm{F}}^H) := k_{\mathrm{F}}^H \left(\dot{x} - \dot{\bar{x}}\right), \tag{4.62}$$

$$r_{\mathrm{D,R}}(\boldsymbol{x}_{\mathrm{D}}^H) := \begin{pmatrix} k_{\mathrm{D},1}^H, & k_{\mathrm{D},2}^H \end{pmatrix} \begin{pmatrix} \Delta x^r - \Delta\bar{x}^r{}_{\mathrm{D}} \\ \Delta x^f - \Delta\bar{x}^f{}_{\mathrm{D}} \end{pmatrix},$$

where:

$$\boldsymbol{k}^H := \begin{pmatrix} k_{\mathrm{F}}^H & k_{\mathrm{D},1}^H & k_{\mathrm{D},2}^H \end{pmatrix}^T \in \mathbb{R}^3, \tag{4.63}$$

are control weight constants that will be chosen to stabilize the horizontal components of the gait in Chapter 4.4.3 and Chapter 4.8. The values of $\dot{\bar{x}}, \Delta\bar{x}^r{}_{\mathrm{D}}, \Delta\bar{x}^f{}_{\mathrm{D}} \in \mathbb{R}$ are equal to the values in Proposition 2 so that the control functions vanish along the privileged fixed point of the stride map (on the periodic orbit's intersection with $G_{\mathrm{D,R}}$, $\Delta\bar{x}^r{}_{\mathrm{D}}$ equals $(x^r - x)$ and $\Delta\bar{x}^f{}_{\mathrm{D}}$ equals $(x^f - x)$).

Intuitively, the reset control functions (4.62) act as proportional controllers – much like the guard control functions – to correctly place the foot horizontally in flight so as to control the horizontal state components. Note that the reset $R_{\mathrm{F,D}}^H$ takes place at the touchdown event, at which time the toe cannot move horizontally without undesirable slipping. Thus, in the physical implementation of $R_{\mathrm{F,D}}^H$ one should apply the control function $r_{\mathrm{F,D}}(\boldsymbol{x}_{\mathrm{F}}^H)$ continuously in flight (as in [59]) so that when touchdown does occur the toe is in the correct position to satisfy $R_{\mathrm{F,D}}^H$.

4.4.3. Controller Stability Analysis

In the half-stride map H (4.46), the horizontal states have no influence on the in-place components of H, giving the map the cascade form:

$$H(\widetilde{\boldsymbol{x}}) = \begin{pmatrix} H^I(\widetilde{\boldsymbol{x}}^I) \\ H^H(\widetilde{\boldsymbol{x}}^I, \widetilde{\boldsymbol{x}}^H) \end{pmatrix}, \tag{4.64}$$

and endowing a block-diagonal Jacobian (4.2) whose structure we will now take advantage of. The Jacobian of H is given by:

$$DH = D\Pi \cdot Db \cdot D\Phi_{\mathrm{D,R}} \cdot D\Phi_{\mathrm{F,D}} \cdot D\Sigma, \tag{4.65}$$

where:

$$D\Pi = \begin{pmatrix} D\Pi^I & 0 \\ 0 & D\Pi^H \end{pmatrix}, \quad Db = \begin{pmatrix} Db^I & 0 \\ 0 & Db^H \end{pmatrix},$$
$$D\Sigma = \begin{pmatrix} D\Sigma^I & 0 \\ 0 & D\Sigma^H \end{pmatrix},$$

with in-place components:

$$D\Pi^I = \begin{pmatrix} I & 0 & 0 \\ 0 & I & 0 \end{pmatrix}, \quad Db^I = \begin{pmatrix} 1 & 0 & 0 & 0 & 0 \\ 0 & -1 & 0 & 0 & 0 \\ 0 & 0 & 1 & 0 & 0 \\ 0 & 0 & 0 & -1 & 0 \\ 0 & 0 & 0 & 0 & 1 \end{pmatrix}, \tag{4.66}$$
$$D\Sigma^I = \begin{pmatrix} I & 0 \\ 0 & I \\ 0 & 0 \end{pmatrix},$$

and horizontal components:

$$D\Pi^H = \begin{pmatrix} 0 & 1 & 0 & 0 \\ 0 & 0 & 1 & 0 \\ -1 & 0 & 0 & 1 \end{pmatrix}, \quad Db^H = \begin{pmatrix} 1 & 0 & 0 & 0 \\ 0 & 1 & 0 & 0 \\ 0 & 0 & 0 & 1 \\ 0 & 0 & 1 & 0 \end{pmatrix},$$

$$D\Sigma^H = \begin{pmatrix} 0 & 0 & 0 \\ 1 & 0 & 0 \\ 0 & 1 & 0 \\ 0 & 0 & 1 \end{pmatrix}.$$

The mode-map Jacobians have the form:

$$D\Phi_{i,j}\Big|_{\boldsymbol{x}} = \begin{pmatrix} D_{\boldsymbol{x}^I}\Phi^I_{i,j} & 0 \\ D_{\boldsymbol{x}^I}\Phi^H_{i,j} & D_{\boldsymbol{x}^H}\Phi^H_{i,j} \end{pmatrix}\Big|_{\boldsymbol{x}},$$

where $D_{\boldsymbol{x}^I}\Phi^I_{i,j} \equiv D\Phi^I_{i,j}$ is given by (recalling the structure of the flow (4.34) and reset (4.30)):

$$D\Phi^I_{i,j} = \begin{pmatrix} I & T_{i,j}(\boldsymbol{x}^I{}_i)I & 0 \\ 0 & I & 0 \\ 0 & 0 & 0 \end{pmatrix} + \begin{pmatrix} \dot{\boldsymbol{q}} + \boldsymbol{c}_i T_{i,j}(\boldsymbol{x}^I_i) \\ \boldsymbol{c}_i \\ 0 \end{pmatrix} \frac{\partial T_{i,j}}{\partial \boldsymbol{x}^I}, \tag{4.67}$$

and where $\Phi^H_{i,j}(\boldsymbol{x}) = R^H_{i,j} \circ \hat{\phi}_i^{T^I_{i,j}(\boldsymbol{x}^I)}(\boldsymbol{x}^H)$ (4.37), with resets $R^H_{i,j}$ (4.31), (4.62), and horizontal flow $\hat{\phi}^t_i$ (4.35). Note that all the factors of DH are lower block-triangular.

The half-stride map Jacobian $DH\big|_{\tilde{\tilde{\boldsymbol{x}}}}$ has the form:

$$DH\big|_{\tilde{\tilde{\boldsymbol{x}}}} = \begin{pmatrix} D_{\tilde{\boldsymbol{x}}^I}H^I & 0 \\ D_{\tilde{\boldsymbol{x}}^I}H^H & D_{\tilde{\boldsymbol{x}}^H}H^H \end{pmatrix}\Big|_{\tilde{\tilde{\boldsymbol{x}}}}, \tag{4.68}$$

indicating the eigenvalue separation property discussed in Chapters 4.1.1. Four of the

eigenvalues are determined from $D_{\tilde{\bar{\boldsymbol{x}}}^I} H^I\big|_{\tilde{\bar{\boldsymbol{x}}}} \equiv DH^I\big|_{\tilde{\bar{\boldsymbol{x}}}^I}$, given by:

$$DH^I\Big|_{\tilde{\bar{\boldsymbol{x}}}^I} = D\Pi^I \cdot Db^I \cdot D\Phi^I_{\mathrm{D,R}}\Big|_{\Phi^I_{\mathrm{F,D}}(\bar{\boldsymbol{x}}^I)} \cdot D\Phi^I_{\mathrm{F,D}}\Big|_{\bar{\boldsymbol{x}}^I} \cdot D\Sigma^I, \tag{4.69}$$

where $\Phi^I_{\mathrm{F,D}}(\bar{\boldsymbol{x}}^I)$ simplifies to $\begin{pmatrix} \bar{y}, & \bar{\varphi}, & -\dot{\bar{y}}, & -\dot{\bar{\varphi}}, & 0 \end{pmatrix}^T$. The remaining three eigenvalues are from $D_{\tilde{\bar{\boldsymbol{x}}}^H} H^H\big|_{\tilde{\bar{\boldsymbol{x}}}} \equiv D_{\tilde{\bar{\boldsymbol{x}}}^H} H^H\big|_{\tilde{\bar{\boldsymbol{x}}}^I}$, which has the form:

$$\begin{aligned} D_{\tilde{\bar{\boldsymbol{x}}}^H} H^H\big|_{\tilde{\bar{\boldsymbol{x}}}^I} =& D\Pi^H \cdot Db^H \cdot D_{\boldsymbol{x}^H} R^H_{\mathrm{D,R}} \cdot D_{\boldsymbol{x}^H} \hat{\phi}_{\mathrm{D}}^{\bar{T}_{\mathrm{D,R}}} \cdot \\ & D_{\boldsymbol{x}^H} R^H_{\mathrm{F,D}} \cdot D_{\boldsymbol{x}^H} \hat{\phi}_{\mathrm{F}}^{\bar{T}_{\mathrm{F,D}}} \cdot D\Sigma^H, \end{aligned} \tag{4.70}$$

where:

$$D_{\boldsymbol{x}^H} \hat{\phi}_{\mathrm{F}}^{\bar{T}_{\mathrm{F,D}}} = \begin{pmatrix} e^{C_{\mathrm{F}} \bar{T}_{\mathrm{F,D}}} & (e^{C_{\mathrm{F}} \bar{T}_{\mathrm{F,D}}} - I) \begin{pmatrix} 0 & -1 \\ 0 & 0 \end{pmatrix} \\ 0 & I \end{pmatrix},$$

$$D_{\boldsymbol{x}^H} \hat{\phi}_{\mathrm{D}}^{\bar{T}_{\mathrm{D,R}}} = \begin{pmatrix} e^{C_{\mathrm{D}} \bar{T}_{\mathrm{D,R}}} & \frac{1}{2}(e^{C_{\mathrm{D}} \bar{T}_{\mathrm{D,R}}} - I) \begin{pmatrix} -1 & -1 \\ 0 & 0 \end{pmatrix} \\ 0 & I \end{pmatrix},$$

$$D_{\boldsymbol{x}^H} R^H_{\mathrm{F,D}} = \begin{pmatrix} I & 0 \\ \begin{pmatrix} 1 & k^H_{\mathrm{F}} \\ 0 & 0 \end{pmatrix} & I \end{pmatrix},$$

$$D_{\boldsymbol{x}^H} R^H_{\mathrm{D,R}} = \begin{pmatrix} I & 0 \\ \begin{pmatrix} 0 & 0 \\ -(k^H_{\mathrm{D},1} + k^H_{\mathrm{D},2}) & 0 \end{pmatrix} & \begin{pmatrix} 1 & 0 \\ k^H_{\mathrm{D},1} & k^H_{\mathrm{D},2} \end{pmatrix} \end{pmatrix},$$

and C_{F} and C_{D} are given in (4.36).

We can further simplify the Jacobian block $DH^I\Big|_{\tilde{\bar{\boldsymbol{x}}}^I}$. By multiplying the values of Π^I, Σ^I

through, (4.69) simplifies to:

$$DH^I\Big|_{\widetilde{\widetilde{\boldsymbol{x}}}^I} = D\widetilde{b}^I \cdot D\widetilde{\Phi}^I_{\mathrm{D,R}}\Big|_{\Phi^I_{\mathrm{F,D}}(\bar{\boldsymbol{x}}^I)} \cdot D\widetilde{\Phi}^I_{\mathrm{F,D}}\Big|_{\bar{\boldsymbol{x}}^I}, \tag{4.71}$$

where:

$$D\widetilde{\Phi}^I_{i,j} = \begin{pmatrix} I & T_{i,j}(\boldsymbol{x}^I{}_i)I \\ 0 & I \end{pmatrix} + \begin{pmatrix} \dot{\boldsymbol{q}} + \boldsymbol{c}_i T_{i,j}(\boldsymbol{x}^I_i) \\ \boldsymbol{c}_i \end{pmatrix} \frac{\partial T_{i,j}}{\partial \widetilde{\boldsymbol{x}}^I}, \tag{4.72}$$

$$D\widetilde{b}^I = \begin{pmatrix} 1 & 0 & 0 & 0 \\ 0 & -1 & 0 & 0 \\ 0 & 0 & 1 & 0 \\ 0 & 0 & 0 & -1 \end{pmatrix},$$

and – as specified in (4.71) – the points of evaluation for the terms $\frac{\partial T_{i,j}}{\partial \widetilde{\boldsymbol{x}}^I}$ all have in common that $\tau = 0$. The form of $\frac{\partial T_{i,j}}{\partial \widetilde{\boldsymbol{x}}^I}$ is given in Lemma 1.

We now have explicit expressions for all terms in the iterated map Jacobian DH (4.65) and can begin analysis of the map's local stability at $\widetilde{\widetilde{\boldsymbol{x}}}$. It remains to choose weights $\boldsymbol{k}^I{}_{\mathrm{F}}, \boldsymbol{k}^I{}_{\mathrm{D}}$ in the hybrid guards (4.25), (4.57) and weights $\boldsymbol{k}^H$ (4.63) in the hybrid resets (4.31), (4.62) such that the spectral radius of $DH\big|_{\widetilde{\widetilde{\boldsymbol{x}}}}$ (4.68) is less than unity.

Given the unwieldy form of the Jury stability criteria for fourth-order polynomials we instead opt to obtain an *infinitesimally deadbeat solution*, by which we mean that all the eigenvalues of the Jacobian of the iterated map evaluated at the fixed point are equal to zero.

Proposition 3. *For any operating point* $\widetilde{\widetilde{\boldsymbol{x}}}$ (4.47)*, there exists a choice of gains* $\boldsymbol{k}^I{}_{\mathrm{F}}$, $\boldsymbol{k}^I{}_{\mathrm{D}}$ (4.57)*, and* $\boldsymbol{k}^H$ (4.63) *that – conjectured on the conditions* (4.82) *– make the associated Poincaré map Jacobian* $DH\big|_{\widetilde{\widetilde{\boldsymbol{x}}}}$ (4.68) *nilpotent, endowing the operating point with infinitesimal deadbeat stability.*

Proof. The $D_{\widetilde{\boldsymbol{x}}^I} H^I$ component of $DH\big|_{\widetilde{\widetilde{\boldsymbol{x}}}}$ in (4.68) is made nilpotent through the choice of gains ${\boldsymbol{k}^I}_{\mathrm{F}}$ and ${\boldsymbol{k}^I}_{\mathrm{D}}$ given in Lemma 2 (via the change of coordinates (4.74)), assuming the invertibility of the matrix (4.79) which we conjecture to be generically invertible.[28] The $D_{\widetilde{\boldsymbol{x}}^H} H^H$ component of $DH\big|_{\widetilde{\widetilde{\boldsymbol{x}}}}$ is made nilpotent through the choice of gains $\boldsymbol{k}^H$ given in Lemma 3.

The eigenvalues of the block-triangular $DH\big|_{\widetilde{\widetilde{\boldsymbol{x}}}}$ are given by the union of the eigenvalues of the diagonal blocks $D_{\widetilde{\boldsymbol{x}}^I} H^I$ and $D_{\widetilde{\boldsymbol{x}}^H} H^H$. These diagonal blocks are nilpotent, and so $DH\big|_{\widetilde{\widetilde{\boldsymbol{x}}}}$ is nilpotent.

□

The procedure for choosing gains for infinitesimal deadbeat stability is algorithmic in the sense that the gain choices for $\boldsymbol{k}^H$ and ${\boldsymbol{k}^I}_{\mathrm{F}}$ are explicitly given by equations (4.80) (via the change of coordinates (4.74)) and (4.83), respectively; and equation (4.76) constrains ${\boldsymbol{k}^I}_{\mathrm{D}}$ to a hypersurface (a hyperplane constraint in the coordinates of (4.73)).

There still exists some freedom in choosing the control parameters as only a hypersurface constraint on the three-dimensional ${\boldsymbol{k}^I}_{\mathrm{D}}$ is required for infinitesimal deadbeat stability (nine control gains were used to place seven poles). We chose the remaining control parameters according to the procedure given in Chapter 4.9. We found that selecting control parameters ${\boldsymbol{k}^I}_{\mathrm{D}}$ with parametric robustness and transients in mind was important; naively selecting values during the experiments resulted in poor performance. The numerical values chosen are shown in Table 5.

Slices of the numerically-derived basin of attraction for the in-place components of the control scheme are depicted in Figure 23, using parameters given in Table 5 and enforcing the desired hybrid mode sequence. An enforced hybrid mode sequence is a conservative assumption compared to physical implementation on our robot where transient hybrid mode sequences are perfectly acceptable, and so we suspect that the actual basin of attraction

[28] We numerically verified invertibility of (4.79) when using the values from Table 5.

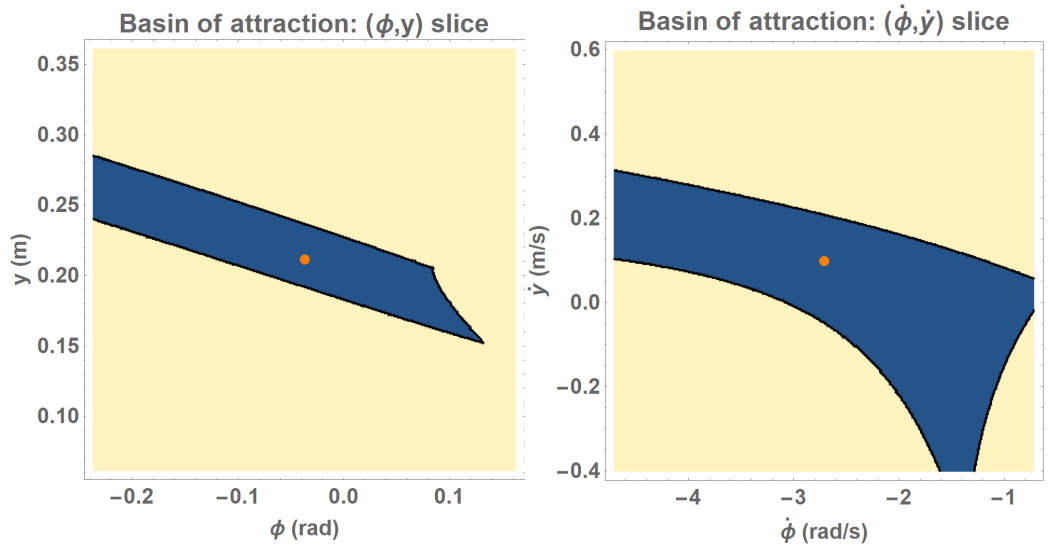

Figure 23: Two slices of the numerically-computed basin of attraction when the hybrid mode sequence is enforced, using parameters given in Table 5 (left - in the (φ, y) plane, right - in the $(\dot{\varphi}, \dot{y})$ plane). The blue region indicates the basin, and the center orange dot corresponds with the fixed point $\bar{\boldsymbol{x}}^I$ of the map H^I. The enforcement of the hybrid mode sequence is a very conservative assumption for real-world implementation, as the ability to move through transient hybrid mode sequences is an inherent affordance of legs that provides robustness and motivates their use on machines.

without enforcing the hybrid mode sequence is larger.

The robustness of the in-place components of the control scheme to parametric uncertainty is indicated in Figure 24. While we can measure the majority of the physical parameters of the robot quite well, we have a difficult time accurately measuring the body's moment of inertia which is folded into the generalized Murphy number a, as well as the stance specific vertical force u_y. Here, we show the spectral radius of the Jacobian of H^I when the "true" parameter values are varied from the parameter values used by the controller, evaluated at the fixed point that results from this parameter perturbation. The results of Figure 24 show that the controller will only destabilize when our error in estimating these two parameters is very large.

The basin of attraction for the horizontal components of the controller is global, as the iterated dynamics H^H are affine in $\widetilde{\boldsymbol{x}}^H$. Of course, because H^H is also a function of $\widetilde{\boldsymbol{x}}^I$,

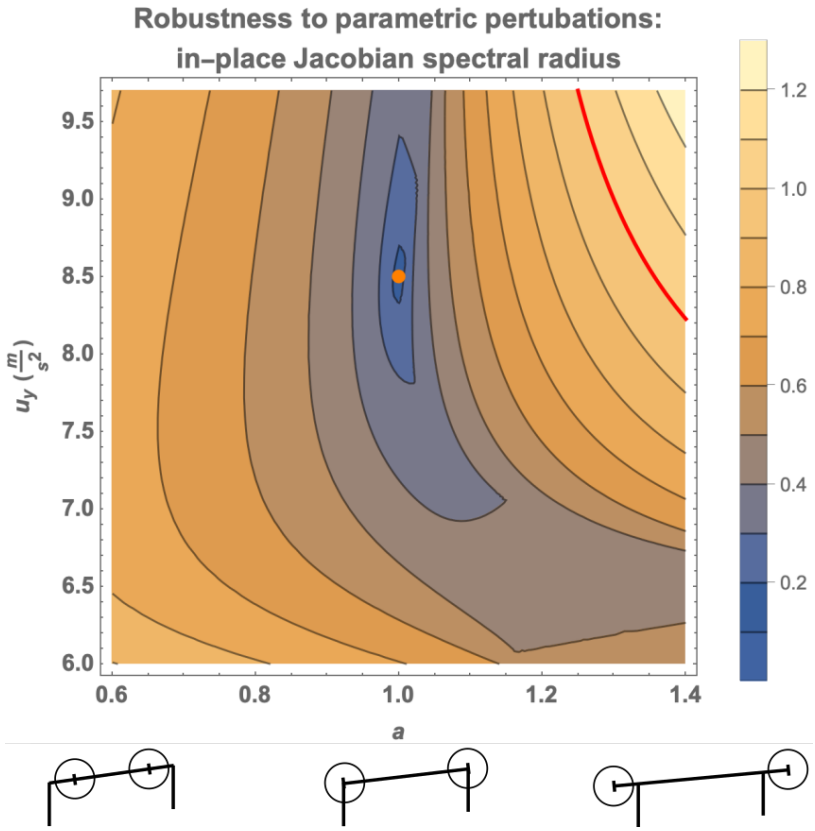

Figure 24: Robustness of deadbeat solution to perturbations in the parameters u_y and the unitless a, as indicated by the value of the spectral radius of the Jacobian of H^I when the true parameter values are varied from the parameter values used by the controller, evaluated at the fixed point that results from this parameter perturbation. This analysis uses the numerical parameter values given in Table 5. To give the reader an intuition on the range of a displayed, below the graph are cartoon representations of the robot for a generalized Murphy value a of 0.6, 1.0, and 1.4, assuming all the robot mass is equally distributed at two point masses along the robot. The controller becomes unstable when the spectral radius exceeds unity, indicated by the red line. The parameters a and u_y are the two parameters which are difficult to measure on the physical robot. The large distance from the unperturbed case (indicated by the orange dot) to the onset of destabilizing perturbations (indicated by the red line) suggests a large degree of robustness to uncertainty in these parameters.

convergence in $\widetilde{\boldsymbol{x}}^H$ is only guaranteed by our local stability analysis once $\widetilde{\boldsymbol{x}}^I$ approaches its limiting value. We can think of the dynamics of the combined system H as containing an attracting invariant sub-manifold given by $\widetilde{\boldsymbol{x}}^I = \widetilde{\widetilde{\boldsymbol{x}}}^I$, on which the dynamics globally attract to $\widetilde{\boldsymbol{x}}^H = \widetilde{\widetilde{\boldsymbol{x}}}^H$.

We see from Figure 25 that the horizontal control scheme has a reasonable degree of robustness to parametric variation. Unlike the in-place control scheme, the horizontal does not have any free control parameters to optimize performance metrics other than for achieving infinitesimal deadbeat stability. Thus this control scheme is hostage to whatever transients emerges as a result of the deadbeat control law Lemma 3, although we didn't observe large transients in the experiments of Chapter 4.5. If we had, we could increase the number of state variables and control coefficients appearing in the input of the control functions (4.62) – for example, by introducing in-place state components – and then perform an optimization similar to the in-place control scheme to limit transients, however this would come at the cost of added feedback paths along which noise and the negative effects of measurement uncertainty would grow.

4.5. Empirical Demonstration of Controller

This section documents the implementation of the controller of Chapter 4.4 on the Inu robot. Chapter 4.5.1 describes the experimental setup and Chapter 4.5.2 gives the experimental results.

4.5.1. Setup

We demonstrate the controller of Chapter 4.4 implemented on the Inu robot [80], a direct-drive quadruped that has an articulated spine (held rigid in these experiments). While the experiments of this paper do not utilize Inu's flexible spine, we hope in future work to cascade another module (that encapsulates an added degree of freedom representing a bendable back) to the modeling composition and thus chose this robotic platform for continuity with future work.

The robot's lack of gearing in the legs necessitates operating the actuators far from their operating point of maximum power (although the lack of gearing provides benefits such as proprioceptive ground contact detection [132, 196]), which manifests itself in actuator saturation preventing the platform from achieving an aerial phase when running at faster

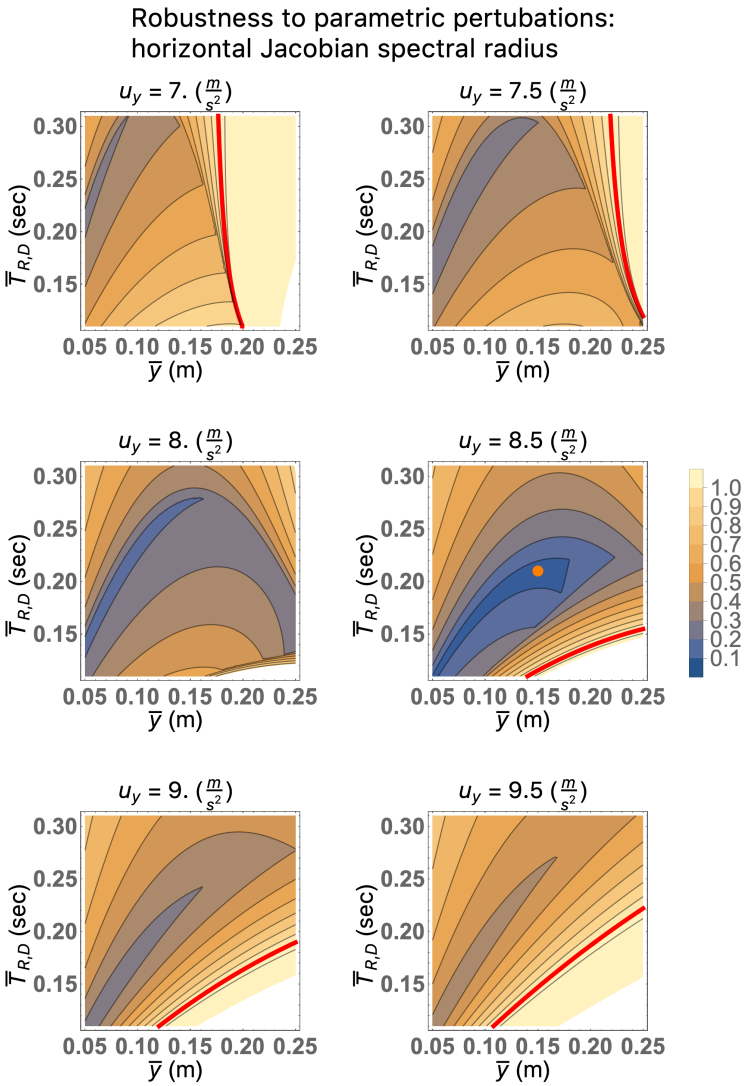

Figure 25: Slices of the Jacobian spectral radius of H^H evaluated at the appropriate fixed point with parametric perturbations in the parameters $\bar{y}$, $\bar{T}_{\mathrm{F,D}}$, and u_y – the only parameters entering into the Jacobian. This analysis uses numerical parameter values given in Table 5 as the unperturbed values. Here the control is being done using the unperturbed parameters, showing the robustness of the control scheme to parametric uncertainty. The distance from the orange dot in the middle-right plot (representing the unperturbed parameter values) to the red line (indicating slices of the edge of stability) demonstrates that the controller can withstand sizable perturbations in parameter space before going unstable.

speeds. We decided to forgo an aerial phase at slower speeds as well – hence the choice of hybrid modes (4.4) – to demonstrate consistent behavior across all feasible running speeds, and chose commanded vertically applied force and mode durations (u_y and $\bar{T}_{\mathrm{F,D}}$ in Table

5) according to what the actuators could achieve at higher speeds.

Inu's parametric correspondence with the simplified model is given in Table 5. While most of the simplified model parameters are easily measurable to a high degree of accuracy, calculating the robot's moment of inertia about its mass center (and hence its generalized Murphy number a) and the mass-specific vertically applied force u_y are more difficult. Our lab does not have the equipment to accurately measure these two parameters, however Figure 24 indicates a wide basin of stability to combined perturbations of these parameters and so we do not expect to see instability arise from our lack of good measurement capability.

Numerical parameters		
Physical and pseudo-physical parameters	d	$0.47m$
	l_0	$0.22m$
	a	1
	Δx^{Avg}	$\frac{d}{2}$
	$\bar{y}$	$0.21m$
	g	$9.81\frac{m}{s^2}$
Fixed-point parameters	u_y	$8.5\frac{m}{s^2}$
	$\bar{T}_{\text{F,D}}$	$0.15s$
	$\dot{\bar{x}}$	Varies by experiment
Control weights	${\boldsymbol{k}^I}_{\text{F}}$	$(0.5443,\ -0.0815,\ 0.2990)^T$
	${\boldsymbol{k}^I}_{\text{D}}$	$(0.4267,\ 0,\ -0.3139)^T$
	$\boldsymbol{k}^H$	$(0.2065, -0.1262, 0)^T$

Table 5: Parameter values used in experiments
Numerical reduced-order model and control parameters used in the experiments as well as in the calculations of Figures 22, 23, 24, and 25.

The robot is kinematically limited to a horizontal leg stroke distance of 32 cm when using a nominal touchdown height of 22 cm. Since the hip's stance time along the limit cycle (4.54) is equal to 20 ms, we have (as discussed in Chapter 4.3.5) that the forward running speed is theoretically limited to approximately 1.6 m/s.

Inu executed a bounding run at several speeds to demonstrate the viability of the controller

on physical hardware, using only its onboard MPU-6000 IMU[29] and motor encoders for sensing. A Vicon motion capture system[30] was used to log experimental kinematic data of Inu's mass-center and body-pitch trajectories and compare them with the predicted periodic orbits of the reduced-order model. The raw (unfiltered) trajectory data from motion capture is provided. In an effort to demonstrate the behavior of the in-place dynamics $H^I(\widetilde{\boldsymbol{x}}^I)$ (4.64) in isolation, we first ran the robot without implementing the horizontal reset speed controller – instead using a simple PD loop to dampen out horizontal movement. In a second set of experiments, we used the full controller to test the behavior at speeds up to the theoretical limit.

4.5.2. Results

The results of the experiments are summarized in Figures 26 and 27. The in-place controller was run on Inu over the course of approximately 30 strides as shown in Figure 26, demonstrating a good empirical correspondence between the robot and the predicted orbit of the in-place controller. The full controller's implementation in Figure 27 shows a reasonable agreement with the desired limit cycle at lower speeds, although the addition of the forward speed controller introduces more noise into the orbits as compared with the in-place controller. The predicted behavior was reliably repeatable over dozens of trials at many horizontal speed set points, $\dot{\bar{x}}$, in the range allowed by (4.55). At higher speeds, we see the orbit of the pitch degree of freedom inconsistently sag during negative pitch values corresponding to when the front is in stance. This is due to the motors of the front body segment saturating when running at speed, the front is slightly inertially disadvantaged compared to the rear due to the battery weight being carried by the front. Inu can still run without falling when approaching the speed limit imposed by Inu's kinematics, however the legs are commanded to lift off prematurely when they near their kinematic singularity as shown in Figure 28 which results in inconsistent trajectories.

[29] https://www.invensense.com/wp-content/uploads/2015/02/MPU-6000-Datasheet1.pdf
[30] https://www.vicon.com/

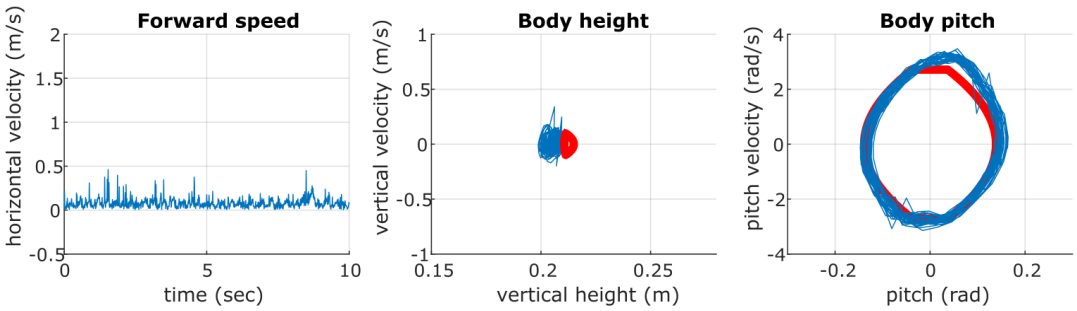

Figure 26: The in-place component of the controller implemented on the Inu robot shows a good correspondence between the actual (blue) and analytically predicted (red) behavior of the robot over approximately 30 strides (10 seconds) of motion capture data. Here the horizontal toe position is maintained through the use of a simple PD controller with relatively high-magnitude derivative term to dampen out fore-aft oscillations.

Inu is able to run up to its theoretical kinematic running speed of 1.6 m/s, but Figure 28 demonstrates that Inu is at the limit of its available workspace at this speed. The robot wasn't able to exceed speeds higher than this, and commanding it to do so resulted in the legs hitting their kinematic singularity earlier in stance. This resulted in the robot stumbling, the onset of which lowered the running speed substantially. To run faster, either longer legs would be needed to increase the workspace (which would require greater motor torques via the increased lever arm) or a shorter stance duration would be required through increasing the applied vertical stance force. Both are precluded by Inu's inherently torque-limited actuation. In future work we will investigate the addition of a spine morphology to provide this added workspace without detracting from the hips torque generation affordance.

4.6. Discussion

4.6.1. Infinitesimally deadbeat nature of our result

Our stability result is not one that is deadbeat, but rather infinitesimally deadbeat by achieving a nilpotent stride map Jacobian at the fixed point. As such, local convergence to the fixed point is not in a finite number of steps but rather super-exponential due to the vanishing of linear terms in the Taylor approximation of the k-th iterate of the stride map

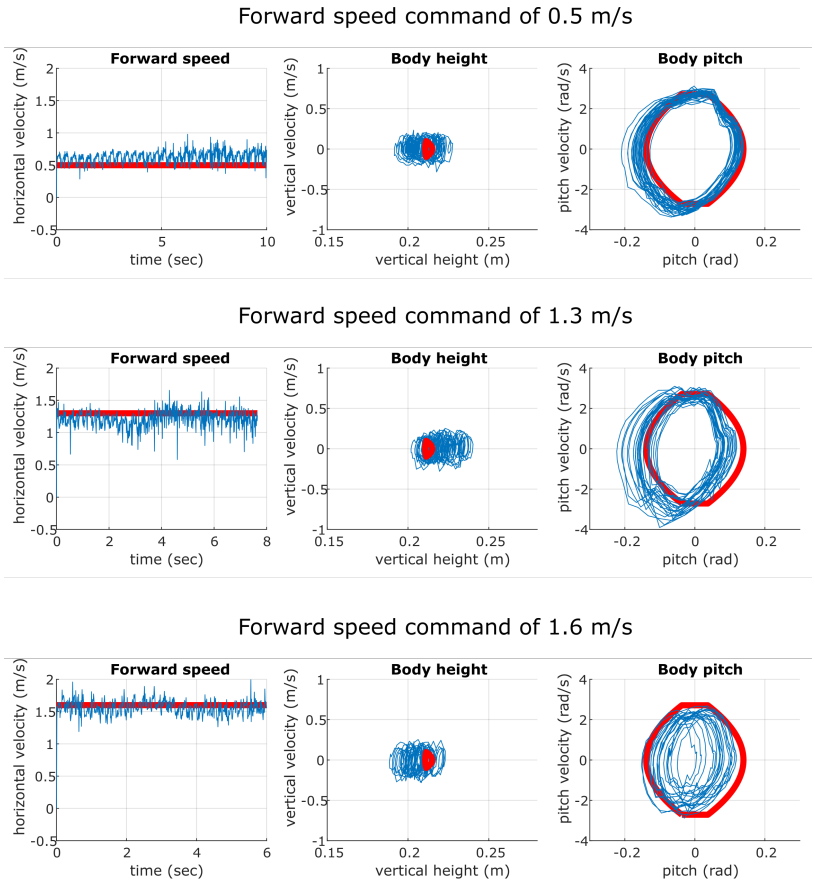

Figure 27: Depicted are the actual (blue) and desired (red) orbits and trajectories under motion capture using the full controller of Chapter 4.4 on the Inu robot over various running speeds up to Inu's kinematic speed limit (as discussed in Chapters 4.3.5 and 4.5.1). We see a reasonable agreement with the desired limit cycle at lower speeds (top), although the addition of the forward speed controller introduces more noise into the orbits as compared with the isolated in-place controller shown in Figure 26. At higher speeds (middle) we see the orbit of the pitch degree of freedom inconsistently sag during negative pitch values corresponding to when the front is in stance. This is due to the motors of the front body segment saturating when running at speed, the front is slightly inertially disadvantaged compared to the rear due to the battery weight being carried by the front. Approaching the speed limit imposed by Inu's kinematics (bottom), Inu can still run without falling, however the legs are commanded to lift off prematurely when they near their kinematic singularity as shown in Figure 28 which results in inconsistent trajectories. The lower time durations of the faster experiments are the result of the robot running faster through the motion capture area.

at the fixed point for some $k \in \mathbb{N}$. We believe that finite step convergence often comes with the price of an increased control burden that – as suggested by the current general lack of

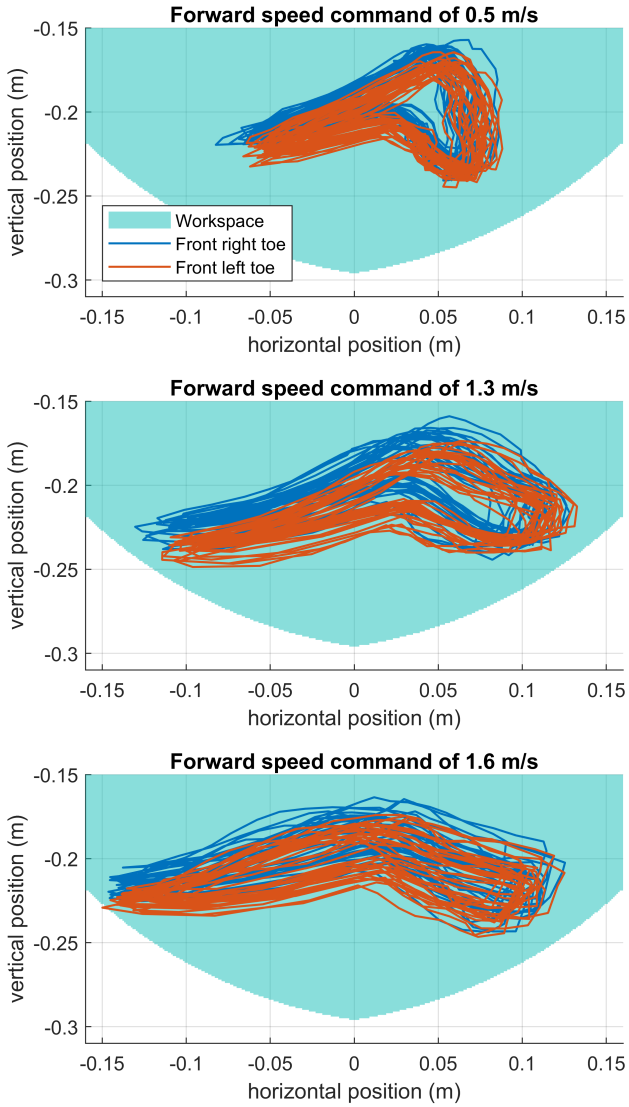

Figure 28: Toe kinematic trajectories for the front legs in the local hip frame show that at running speeds of 1.6 m/s, the leg linkage is going close to singularity. This represents a constraint on maximum running speed, as the leg runs out of workspace to sweep the leg backwards in stance. Faster running with the control strategy of Chapter 4.2 could be achieved by either using longer legs to increase the workspace or by achieving shorter stance durations through increasing the applied vertical stance force. In future work we will investigate the addition of a spine morphology to provide this added workspace without detracting from the hip's torque generation affordance.

deadbeat results "in the wild" without utilizing motion capture – is poorly conditioned to state/parameter uncertainty.

Specifically, a k-step deadbeat control law requires the cancellation of all nonlinear terms in the Taylor series of a system's k-times composed Poincaré map local to the fixed point. Regarding state uncertainty, the canceling of the combined effect of these nonlinear terms can be worse-conditioned to errors in state measurement than only canceling the linear terms (sometimes much worse). We avoided the possibility of this ill-conditioning by both choosing not to cancel the nonlinear terms and by designing feedback paths in our control law to only use states that we felt we can accurately measure: time, kinematic configurations, and forward speed (which changes relatively slowly) – thus eschewing the common method of detecting a hip's apex event in flight as it is typically backed out of the hip's vertical liftoff velocity, which we have difficulty measuring in stance due to its quickly changing nature. We are wary of using these feedback paths for deadbeat stability as state measurement error inherent to operation in the physical world is still present in states that we can "accurately" measure, and an ill-conditioned canceling of dynamics can still magnify their adverse effects to result in a controller with poor empirical performance. Regarding parametric uncertainty, deadbeat control amounts to inverse dynamics and it is known that cancellation of inertial terms can lead to poor parametric robustness. Rather, the empirical performance depicted in Figures 26, 27 demonstrates a reasonable degree of robustness to state measurement error inherent to operation in the physical world and Figures 24, 25 indicate a reasonable degree of parametric robustness.

4.6.2. Controlling on the hybrid transitions

In controlling on the guards and resets, we are utilizing a natural affordance provided by the use of legs. The control affordance provided by hybrid transitions is important because it is in some sense independent of actuator power constraints: on one hand, we achieve arbitrarily good pole placement with only modest control gains (Table 5); while on the other, our specification of desired hybrid periodic orbit (Proposition 2, Chapter 4.3.3) depends strongly on actuator performance but is almost entirely devoid of controller specification (Chapter 4.4). As we attempt to make more precise below, we believe that

controlling on the hybrid transitions frees scarce actuator power resources from the task of shaping the continuous dynamics into the proper "funnel" [56] required for stability, allowing their application to go instead to accessing dynamical regimes of higher energy operation. Settings rich in hybrid interactions are ripe for this style of control, and as such the intrinsic necessity of making and breaking contact that accompanies legged robots is an opportunity for exploiting the natural hybrid nature of the dynamics to achieve stability.

The costs inherent to our control formulation are twofold. First, the actuator cost is equal to the enforcement of the (piecewise) Hamiltonian dynamics through generating conservative potential field force laws at the toes. In the vertical this is a constant force (4.20), in the horizontal the force is affine with respect to leg horizontal toe position (4.21). Due to the simple and transparent nature of these force laws (constant and affine), a user can easily evaluate if they are prohibitively costly at any point in the workspace and – as long as transients in state are not bad – shouldn't expect that operation near the hybrid periodic orbit would be suddenly costly for the actuators. The fact that the Inu robot used in the experiments is inherently force-limited (Chapter 4.5.1) yet can tolerate using the force laws even as perturbations are corrected suggest the cost associated with it are not prohibitive.

Second, our hybrid transition control scheme consists of displacing the toe from some nominal location using proportional control. Practically, the toes can only tolerate so much displacement from the controllers (legs being limited in workspace, or perhaps needing to avoid a corner of the workspace with unfavorable actuator performance) which we relate to the tolerable state-error as follows. If one puts interval constraints on the values that a control function g_{TD}, g_{LO}, $r_{\mathrm{F,D}}$, or $r_{\mathrm{D,R}}$ (4.57), (4.62) may take, this is equivalent to being able to – on the hybrid transitions – tolerate perturbations from the periodic orbit that satisfy two halfspace constraints (whose hyperplanes are parallel and offset). For example,

specifying that $r_{\mathrm{D,R}} \in (\delta r_{\mathrm{MIN}}, \delta r_{\mathrm{MAX}})$ in (4.62) is equivalent to the requirement that:

$$\delta r_{\mathrm{MIN}} < \boldsymbol{k}_{\mathrm{D}}^{HT} \begin{pmatrix} \Delta x^r - \bar{\Delta x^r}_{\mathrm{D}} \\ \Delta x^f - \bar{\Delta x^f}_{\mathrm{D}} \end{pmatrix} < \delta r_{\mathrm{MAX}},$$

allowing the user to quantify the state-errors tolerable by the leg mechanisms.

4.6.3. Cascade compositions as attracting invariant submanifolds

Stable fixed points of cascaded iterated maps necessarily have an attracting invariant submanifold. Let D_1 and D_2 be (respectively) n and m-dimensional differentiable manifolds, and suppose the iterated map $P : D_1 \times D_2 \to D_1 \times D_2$ has the form:

$$P(x, y) = \begin{pmatrix} P_1(x) \\ P_2(x, y) \end{pmatrix},$$

and stable fixed point $(\bar{x}, \bar{y})$. Then $\bar{x} \times D_2$ is an invariant submanifold, and is attracting due to $\bar{x}$ being attracting in P_1. In our system, the attracting invariant submanifold is given by the horizontal dynamics along the in-place limit cycle. It is interesting to note that in the language of templates and anchors [90], traditionally the dynamics on the attracting invariant submanifold – called the template dynamics – drive the hybrid transitions, while in our case it is the dynamics that collapse to the attracting invariant submanifold – called the anchor dynamics – that do so.

4.7. Conclusion

This paper considered the problem of stabilizing a three mechanical degree-of-freedom simplified model of quadrupedal bounding in the sagittal plane. By using the continuous stance forces to effect simple continuous dynamics and a cascade dynamical decoupling giving a useful eigenvalue separation condition in the stride map Jacobian, we analytically showed local stability by controlling on the guards and resets to obtain an "infinitesimal" deadbeat re-

sult. The model, while simple, well-approximates physical robot experiments implementing the running controller. Aside from the contribution of the running controller, we hope this paper motivates further progress in analytical stability results of three degree-of-freedom (and higher) legged locomotion models – a currently underdeveloped literature that has the potential to greatly enhance the empirical performance of legged machines.

4.8. Appendix to Chapter 4: Controller Stability Lemmas

This appendix contains results related to the choice of control gains in Proposition 3 guaranteeing infinitesimal deadbeat stability of the half-stride map H (4.46) at the operating point (4.47). Lemma 1 gives the explicit form of the time-to-impact map Jacobians $\frac{\partial T_{\mathrm{F,D}}}{\partial \widetilde{\boldsymbol{x}}^I}\Big|_{\tau=0}$ and $\frac{\partial T_{\mathrm{D,R}}}{\partial \widetilde{\boldsymbol{x}}^I}\Big|_{\tau=0}$. The control weight change-of-coordinates (4.73) is given to assist in expressing the deadbeat gain expressions, which are presented in Lemmas 2 and 3 below.

Lemma 1. *The relevant Jacobians of the time-to-guard-impact functions in* (4.72) *are given by:*

$$\frac{\partial T_{\mathrm{F,D}}}{\partial \widetilde{\boldsymbol{x}}^I}\Big|_{\tau=0} = \frac{1}{k^I_{\mathrm{F},3} - s_{\mathrm{F}}} \begin{pmatrix} 1 - k^I_{\mathrm{F},1} - k^I_{\mathrm{F},2} \\ (-1 + k^I_{\mathrm{F},1} - k^I_{\mathrm{F},2})\frac{d}{2} \\ \bar{T}_{\mathrm{F,D}} \\ -\frac{d}{2}\bar{T}_{\mathrm{F,D}} \end{pmatrix}^T,$$

$$s_{\mathrm{F}} = \dot{y} - \frac{d}{2}\dot{\varphi} + \Big((1 - a^{-1})u_y - g\Big)\bar{T}_{\mathrm{F,D}},$$

$$\frac{\partial T_{\mathrm{D,R}}}{\partial \widetilde{\boldsymbol{x}}^I}\Big|_{\tau=0} = \frac{1}{k^I_{\mathrm{D},3} - s_{\mathrm{D}}} \begin{pmatrix} 1 - k^I_{\mathrm{D},1} - k^I_{\mathrm{D},2} \\ (1 + k^I_{\mathrm{D},1} - k^I_{\mathrm{D},2})\frac{d}{2} \\ \bar{T}_{\mathrm{D,R}} \\ \frac{d}{2}\bar{T}_{\mathrm{D,R}} \end{pmatrix}^T,$$

$$s_{\mathrm{D}} = \dot{y} + \frac{d}{2}\dot{\varphi} + (2u_y - g)\bar{T}_{\mathrm{D,R}}.$$

Proof. See Chapter 4.11. □

We introduce the following coordinate change to simplify the form of the time-to-guard-impact Jacobians above. Let:

$$\widetilde{\boldsymbol{k}}^I_{\mathrm{F}} = \begin{pmatrix} \widetilde{k}^I_{\mathrm{F},1} \\ \widetilde{k}^I_{\mathrm{F},2} \\ \widetilde{k}^I_{\mathrm{F},3} \end{pmatrix} = \frac{1}{k^I_{\mathrm{F},3} - s_{\mathrm{F}}} \begin{pmatrix} 1 - k^I_{\mathrm{F},1} - k^I_{\mathrm{F},2} \\ (-1 + k^I_{\mathrm{F},1} - k^I_{\mathrm{F},2})\frac{d}{2} \\ \bar{T}_{\mathrm{F,D}} \end{pmatrix}, \tag{4.73}$$

$$\widetilde{\boldsymbol{k}}^I_{\mathrm{D}} = \begin{pmatrix} \widetilde{k}^I_{\mathrm{D},1} \\ \widetilde{k}^I_{\mathrm{D},2} \\ \widetilde{k}^I_{\mathrm{D},3} \end{pmatrix} = \frac{1}{k^I_{\mathrm{D},3} - s_{\mathrm{D}}} \begin{pmatrix} 1 - k^I_{\mathrm{D},1} - k^I_{\mathrm{D},2} \\ (1 + k^I_{\mathrm{D},1} - k^I_{\mathrm{D},2})\frac{d}{2} \\ \bar{T}_{\mathrm{D,R}} \end{pmatrix},$$

such that:

$$\frac{\partial T_{\mathrm{F,D}}}{\partial \widetilde{\boldsymbol{x}}^I}\Big|_{\tau=0} = \widetilde{\boldsymbol{k}}_{\mathrm{F}}{}^{I\,T} M^I_{\mathrm{F}}, \quad M^I_{\mathrm{F}} = \begin{pmatrix} 1 & 0 & 0 & 0 \\ 0 & 1 & 0 & 0 \\ 0 & 0 & 1 & -\frac{d}{2} \end{pmatrix},$$

$$\frac{\partial T_{\mathrm{D,R}}}{\partial \widetilde{\boldsymbol{x}}^I}\Big|_{\tau=0} = \widetilde{\boldsymbol{k}}_{\mathrm{D}}{}^{I\,T} M^I_{\mathrm{D}}, \quad M^I_{\mathrm{D}} = \begin{pmatrix} 1 & 0 & 0 & 0 \\ 0 & 1 & 0 & 0 \\ 0 & 0 & 1 & \frac{d}{2} \end{pmatrix}.$$

This transformation is invertible via:

$$\boldsymbol{k}^I{}_{\mathrm{F}} = \frac{\bar{T}_{\mathrm{F,D}}}{d\ \widetilde{k}^I_{\mathrm{F},3}} \begin{pmatrix} -\frac{d}{2} & 1 & 0 \\ -\frac{d}{2} & -1 & 0 \\ 0 & 0 & 0 \end{pmatrix} \widetilde{\boldsymbol{k}}^I_{\mathrm{F}} + \begin{pmatrix} 1 \\ 0 \\ s_{\mathrm{F}} + \frac{\bar{T}_{\mathrm{F,D}}}{\widetilde{k}^I_{\mathrm{F},3}} \end{pmatrix}, \tag{4.74}$$

$$\boldsymbol{k}^I{}_{\mathrm{D}} = \frac{\bar{T}_{\mathrm{D,R}}}{d\ \widetilde{k}^I_{\mathrm{D},3}} \begin{pmatrix} -\frac{d}{2} & 1 & 0 \\ -\frac{d}{2} & -1 & 0 \\ 0 & 0 & 0 \end{pmatrix} \widetilde{\boldsymbol{k}}^I_{\mathrm{D}} + \begin{pmatrix} 0 \\ 1 \\ s_{\mathrm{D}} + \frac{\bar{T}_{\mathrm{D,R}}}{\widetilde{k}^I_{\mathrm{D},3}} \end{pmatrix},$$

where:

$$\widetilde{k}^I_{\mathrm{F},3} \neq 0, \quad \widetilde{k}^I_{\mathrm{D},3} \neq 0. \tag{4.75}$$

Lemma 2. *The following choice of* $\widetilde{\boldsymbol{k}}_{\mathrm{F}}^{I}$ *and* $\widetilde{\boldsymbol{k}}_{\mathrm{D}}^{I}$ *make* $DH^{I}\Big|_{\widetilde{\bar{\boldsymbol{x}}}^{I}}$ *nilpotent assuming the conditions given in* (4.82) *can be satisfied. Choose* $\widetilde{\boldsymbol{k}}_{\mathrm{D}}^{I}$ *such that:*

$$\widetilde{\boldsymbol{k}}_{\mathrm{D}}{}^{I^{T}}\begin{pmatrix} -\dot{\bar{y}} \\ -\dot{\bar{\varphi}} \\ 2u_y - g \end{pmatrix} = -1, \tag{4.76}$$

which zeros one eigenvalue of $D\widetilde{\Phi}^{I}_{\mathrm{D,R}}\Big|_{\Phi^{I}_{\mathrm{F,D}}(\bar{\boldsymbol{x}}^{I})}$ *and hence of* $DH^{I}\Big|_{\widetilde{\bar{\boldsymbol{x}}}^{I}}$*. Denote the resulting Jordan decomposition of* $D\widetilde{\Phi}^{I}_{\mathrm{D,R}}\Big|_{\Phi^{I}_{\mathrm{F,D}}(\bar{\boldsymbol{x}}^{I})}$ *by:*

$$D\widetilde{\Phi}^{I}_{\mathrm{D,R}}\Big|_{\Phi^{I}_{\mathrm{F,D}}(\bar{\boldsymbol{x}}^{I})} = V^{I}\Lambda^{I}V^{I^{-1}}, \tag{4.77}$$

where the zero eigenvalue is placed in the upper-left element of Λ^{I} *and the explicit form of* V^{I} *and* Λ^{I} *is given in* (4.94) *of Chapter 4.12. Let:*

$$A^{I} = T^{I}\Lambda^{I}V^{I^{-1}}\begin{pmatrix} I & I\bar{T}_{\mathrm{F,D}} \\ 0 & I \end{pmatrix} D\widetilde{b}^{I}V^{I}T^{I^{T}}, \tag{4.78}$$

$$\boldsymbol{d}^{I} = T^{I}\Lambda^{I}V^{I^{-1}}\begin{pmatrix} -\dot{\bar{y}} \\ -\dot{\bar{\varphi}} \\ u_y - g \\ -\frac{2u_y}{da} \end{pmatrix},$$

$$T^{I} = \begin{pmatrix} 0 & 1 & 0 & 0 \\ 0 & 0 & 1 & 0 \\ 0 & 0 & 0 & 1 \end{pmatrix},$$

and:

$$R^{I} = \begin{pmatrix} \boldsymbol{d}^{I} & A^{I}\boldsymbol{d}^{I} & A^{I^{2}}\boldsymbol{d}^{I} \end{pmatrix}. \tag{4.79}$$

Then choose:

$$\widetilde{\boldsymbol{k}}_{\mathrm{F}}^{I} = -\begin{pmatrix} 0 & 0 & 1 \end{pmatrix} R^{I^{-1}} A^{I^{3}} \left(M_{\mathrm{F}}^{I} D \widetilde{b}^{I} V^{I} T^{I^{T}} \right)^{-1}. \tag{4.80}$$

Along with the hyperplane constraint (4.76)*, we require that the choice of* $\widetilde{\boldsymbol{k}}_{\mathrm{D}}^{I}$ *satisfy:*

$$\begin{aligned} &\widetilde{k}_{\mathrm{D},1}^{I} \neq 0, -\frac{1}{2\dot{\tilde{y}}}, \quad \widetilde{k}_{\mathrm{D},2}^{I} \neq \frac{d}{2}\widetilde{k}_{\mathrm{D},1}^{I}, \quad \widetilde{k}_{\mathrm{D},3}^{I} \neq 0, \\ &\widetilde{\boldsymbol{k}}_{\mathrm{D}}{}^{I^{T}} \begin{pmatrix} \dot{\tilde{y}} \\ -\dot{\tilde{\varphi}} \\ 2u_y - g \end{pmatrix} \neq -1, \\ &\det(R^{I}) \neq 0, \\ &\widetilde{k}_{\mathrm{F},3}^{I} \neq 0, \textit{ (dependent on } \widetilde{\boldsymbol{k}}_{\mathrm{D}}^{I} \textit{ via (4.80))}, \end{aligned} \tag{4.81}$$

according to (4.75)*,* (4.80)*,* (4.95)*,* (4.97) *and to guarantee the invertibility of* R^{I} (4.96)*. We leave as a conjecture that the constraints:*

$$\det(R^{I}) \neq 0, \quad \widetilde{k}_{\mathrm{F},3}^{I} \neq 0 \tag{4.82}$$

from (4.81) *don't produce an empty set of feasible choices for* $\widetilde{\boldsymbol{k}}_{\mathrm{D}}^{I}$*.*

Proof. See Chapter 4.12. □

We numerically verified (4.81) when using the values from Table 5.

Lemma 3. *The following choice of* $\boldsymbol{k}^{H} = (k_{\mathrm{F}}^{H}, k_{\mathrm{D},1}^{H}, k_{\mathrm{D},2}^{H})^{T}$ *makes* $D_{\widetilde{\boldsymbol{x}}^{H}} H^{H}\big|_{\widetilde{\boldsymbol{x}}^{I}}$ *nilpotent.*

Let:

$$\begin{aligned}\begin{pmatrix} k_{\mathrm{F}}^{H} \\ k_{\mathrm{D},1}^{H} \end{pmatrix} &= \begin{pmatrix} \cosh\left(\bar{T}_{\mathrm{F,D}}\sqrt{\frac{u_y}{\bar{y}}}\right) & 0 \\ -\sqrt{\frac{u_y}{\bar{y}}}\sinh\left(\bar{T}_{\mathrm{F,D}}\sqrt{\frac{u_y}{\bar{y}}}\right) & 1 \end{pmatrix}^{-1} \\ &\quad \left\{ \begin{pmatrix} \tilde{k}_{\mathrm{F}}^{H} \\ \tilde{k}_{\mathrm{D},1}^{H} \end{pmatrix} - \begin{pmatrix} \sqrt{\frac{\bar{y}}{u_y}}\sinh\left(\bar{T}_{\mathrm{F,D}}\sqrt{\frac{u_y}{\bar{y}}}\right) \\ 1-\cosh\left(\bar{T}_{\mathrm{F,D}}\sqrt{\frac{u_y}{\bar{y}}}\right) \end{pmatrix} \right\}, \\ k_{\mathrm{D},2}^{H} &= 0,\end{aligned} \tag{4.83}$$

where:

$$\begin{pmatrix} \tilde{k}_{\mathrm{F}}^{H} \\ \tilde{k}_{\mathrm{D},1}^{H} \end{pmatrix} = -\left(R^{H^{-1}}A^{H^{2}}\right)^{T}\begin{pmatrix} 0 \\ 1 \end{pmatrix},$$

and:

$$\begin{aligned} R^{H} &= \begin{pmatrix} \boldsymbol{d}^{H} & A^{H}\boldsymbol{d}^{H} \end{pmatrix}, \\ A^{H} &= \begin{pmatrix} 0 & 1 \\ -1 & 0 \end{pmatrix} e^{C_{\mathrm{D}}\bar{T}_{\mathrm{D,R}}}\left\{ e^{C_{\mathrm{F}}\bar{T}_{\mathrm{F,D}}}\begin{pmatrix} 0 & -1 \\ 1 & 0 \end{pmatrix} + \begin{pmatrix} 0 & \frac{1}{2} \\ 0 & 0 \end{pmatrix} \right\} \\ &\quad - \begin{pmatrix} 0 & 0 \\ 0 & \frac{1}{2} \end{pmatrix}, \\ \boldsymbol{d}^{H} &= \begin{pmatrix} 0 & 1 \\ -1 & 0 \end{pmatrix} e^{C_{\mathrm{D}}\bar{T}_{\mathrm{D,R}}}\begin{pmatrix} -\frac{1}{2} \\ 0 \end{pmatrix} + \begin{pmatrix} 0 \\ \frac{1}{2} \end{pmatrix}. \end{aligned} \tag{4.84}$$

Proof. See Chapter 4.13. □

4.9. Appendix to Chapter 4: Control gain selection procedure

The choice of control gains (4.76), (4.80), (4.83) that grants the system infinitesimal deadbeat stability fully constrains $\boldsymbol{k}^H$ and ${\boldsymbol{k}^I}_{\mathrm{F}}$, and constrains ${\boldsymbol{k}^I}_{\mathrm{D}}$ to a hypersurface. We chose where to place ${\boldsymbol{k}^I}_{\mathrm{D}}$ on this hypersurface as follows.

We chose to fix $k^I_{\mathrm{D},3}$ as a function of $k^I_{\mathrm{D},1}$ and $k^I_{\mathrm{D},2}$ via (4.76), explicitly:

$$k^I_{\mathrm{D},3} = \frac{-1 + \dot{\tilde{y}} k^I_{\mathrm{D},1} + \dot{\tilde{\varphi}} k^I_{\mathrm{D},2}}{2u_y - g}.$$

We then chose to set the value of $k^I_{\mathrm{D},2}$ to zero, severing a feedback path in (4.57) that corresponds to the hip's usage of its own vertical height measurement in determining liftoff height. Setting $k^I_{\mathrm{D},2}$ to zero was observed in the experiment to improve performance, likely this feedback path made the controller very sensitive to the sagging of the front body segment due to actuator saturation when running at faster speeds (depicted in Figure 27).

We chose $k^I_{\mathrm{D},1}$ using the following constrained optimization problem in an effort to reduce transients and control gain magnitudes, and to increase parametric robustness:

$$\begin{aligned}
\min_{k^I_{\mathrm{D},1}} \quad & c_1 ||\boldsymbol{k}^I||^2 + c_2 \left|\left| DH^I|_{\tilde{\boldsymbol{x}}^I} \right|\right|_F^2 + c_3 \left|\left| \frac{\partial}{\partial \widehat{\boldsymbol{k}^I}} \boldsymbol{p}(\widehat{\boldsymbol{k}^I}) \right|\right|_F^2 \\
\text{s.t.} \quad & k^I_{\mathrm{D},2} = 0 \\
& k^I_{\mathrm{D},3} = \frac{-1 + \dot{\tilde{y}} k^I_{\mathrm{D},1} + \dot{\tilde{\varphi}} k^I_{\mathrm{D},2}}{2u_y - g} \\
& \boldsymbol{k}^I = \begin{pmatrix} {\boldsymbol{k}^I}_{\mathrm{F}} \\ {\boldsymbol{k}^I}_{\mathrm{D}} \end{pmatrix} \\
& \widehat{\boldsymbol{k}^I} = \begin{pmatrix} {\boldsymbol{k}^I}^T & g & d & a & l_0 & u_y & \bar{T}_{\mathrm{F,D}} \end{pmatrix}^T,
\end{aligned}$$

additionally subject to the constraints (4.76), (4.80), (4.83) granting infinitesimal deadbeat

stability, and where $\boldsymbol{p}(\widehat{\boldsymbol{k}^I})$ equals the coefficient vector for the characteristic polynomial of $DH^I\Big|_{\widetilde{\widetilde{\boldsymbol{x}}}^I}$. The terms associated with c_1 are intended to keep the control inputs relatively small, the terms associated with c_2 are intended to reduce transients, and the terms associated with c_3 are intended to increase robustness to parametric uncertainty and measurement errors in applying control. We used $c_1 = 500$, $c_2 = 1.1$, $c_3 = 1.5$ and numerically verified that the resulting control weights satisfied (4.81). The numerical values chosen are shown in Table 5.

4.10. Appendix to Chapter 4: Fixed point calculations

The following proof of Proposition 2 is given in two parts. The first derives the form of the fixed point $\widetilde{\widetilde{\boldsymbol{x}}}^I$ for the map $H^I(\cdot)$. The second derives the form of the fixed point $\widetilde{\widetilde{\boldsymbol{x}}}^H$ for the map $H^H(\widetilde{\widetilde{\boldsymbol{x}}}^I, \cdot) \equiv H^H|_{\widetilde{\widetilde{\boldsymbol{x}}}^I}(\cdot)$.

Proof of Proposition 2, part 1

Proof. Consider the in-place component of the "flipped" half-stride map (4.46) given by:

$$H^I = \Pi^I \circ b^I \circ \Phi^I_{\mathrm{D,R}} \circ \Phi^I_{\mathrm{F,D}} \circ \Sigma^I.$$

Recall that the maps Π^I (4.43), b^I (4.26), and Σ^I (4.43), in H^I are simple linear maps while the mode maps $\Phi^I_{i,j}$ (4.38) in H^I have the form $\Phi^I_{i,j}(\boldsymbol{x}^I) = R^I \circ \phi_i^{T^I_{i,j}(\boldsymbol{x}^I)}(\boldsymbol{x}^I)$, where $\phi^t_i(\boldsymbol{x}^I)$ is the continuous flow (4.34), $R^I : (\boldsymbol{q}^I, \dot{\boldsymbol{q}}^I, \tau) \mapsto (\boldsymbol{q}^I, \dot{\boldsymbol{q}}^I, 0)$, and $T^I_{i,j}$ (4.39) is the implicit time-to-guard-impact map given by $T^I_{i,j}(\boldsymbol{x}^I) = \min\{t \in \mathbb{R}^+ | \phi^t_i(\boldsymbol{x}^I) \in G^I_{i,j}\}$.

We wish to show that:

$$\widetilde{\widetilde{\boldsymbol{x}}}^I = \begin{pmatrix} l_0 - \frac{a^{-1}u_y(g-u_y)}{4(2u_y-g)}\bar{T}^2_{\mathrm{F,D}} \\ -\frac{a^{-1}u_y(g-u_y)}{2d(2u_y-g)}\bar{T}^2_{\mathrm{F,D}} \\ \frac{g-u_y}{2}\bar{T}_{\mathrm{F,D}} \\ -\frac{a^{-1}u_y}{d}\bar{T}_{\mathrm{F,D}} \end{pmatrix}$$

is a fixed point of H^I and additionally that the hybrid execution from this fixed point spends a duration in mode D equal to:

$$\bar{T}_{\mathrm{D,R}} = \bar{T}_{\mathrm{F,D}} \frac{g - u_y}{2u_y - g}.$$

One could simply solve $H^I(\widetilde{\widetilde{\boldsymbol{x}}}^I) = \widetilde{\widetilde{\boldsymbol{x}}}^I$ algebraically to obtain this result, however this entails explicitly expressing the time-to-impact maps which have a complicated form involving roots of quadratic equations. Instead, it is much cleaner to first take the duration constants $\bar{T}_{\mathrm{F,D}}$ and $\bar{T}_{\mathrm{D,R}}$ as surrogates for the time-to-guard-impact maps and algebraically solve for the fixed point, then secondly verify that the resulting $\bar{T}_{\mathrm{F,D}}$ and $\bar{T}_{\mathrm{D,R}}$ agree with the values of time-to-guard-impact maps.

We first solve the equations:

$$\begin{aligned} \widetilde{\widetilde{\boldsymbol{x}}}^I &= \Pi^I \circ b^I \circ R^I \circ \phi_{\mathrm{D}}^{\bar{T}_{\mathrm{D,R}}} \circ R^I \circ \phi_{\mathrm{F}}^{\bar{T}_{\mathrm{F,D}}} \circ \Sigma^I(\widetilde{\widetilde{\boldsymbol{x}}}^I), \\ l_0 &= y^{r_{hip}} \circ \phi_{\mathrm{F}}^{\bar{T}_{\mathrm{F,D}}} \circ \Sigma^I(\widetilde{\widetilde{\boldsymbol{x}}}^I), \end{aligned} \tag{4.85}$$

which have the expanded form:

$$\begin{aligned} \begin{pmatrix} \bar{\boldsymbol{q}}^I \\ \dot{\bar{\boldsymbol{q}}}^I \end{pmatrix} &= \begin{pmatrix} \tilde{I} & 0 \\ 0 & \tilde{I} \end{pmatrix} \Bigg\{ \begin{pmatrix} \frac{\bar{T}_{\mathrm{D,R}}^2}{2} \boldsymbol{c}_{\mathrm{D}} \\ \bar{T}_{\mathrm{D,R}} \boldsymbol{c}_{\mathrm{D}} \end{pmatrix} + \begin{pmatrix} I & \bar{T}_{\mathrm{D,R}} I \\ 0 & I \end{pmatrix} \\ &\qquad \Bigg[\begin{pmatrix} I & \bar{T}_{\mathrm{F,D}} I \\ 0 & I \end{pmatrix} \begin{pmatrix} \bar{\boldsymbol{q}}^I \\ \dot{\bar{\boldsymbol{q}}}^I \end{pmatrix} + \begin{pmatrix} \frac{\bar{T}_{\mathrm{F,D}}^2}{2} \boldsymbol{c}_{\mathrm{F}} \\ \bar{T}_{\mathrm{F,D}} \boldsymbol{c}_{\mathrm{F}} \end{pmatrix} \Bigg] \Bigg\}, \\ l_0 &= \begin{pmatrix} 1 \\ -\frac{d}{2} \end{pmatrix}^T \left(\bar{\boldsymbol{q}}^I + \bar{T}_{\mathrm{F,D}} \dot{\bar{\boldsymbol{q}}}^I + \frac{\bar{T}_{\mathrm{F,D}}^2}{2} \boldsymbol{c}_{\mathrm{F}} \right), \end{aligned} \tag{4.86}$$

for state $\widetilde{\widetilde{\boldsymbol{x}}}^I = \begin{pmatrix} \bar{\boldsymbol{q}}^I \\ \dot{\bar{\boldsymbol{q}}}^I \end{pmatrix} \in \widetilde{D}_{\mathrm{F}}^I$ and $\bar{T}_{\mathrm{D,R}} \in \mathbb{R}^+$. Here $\tilde{I} = \begin{pmatrix} 1 & 0 \\ 0 & -1 \end{pmatrix}$ and both (4.85) and (4.86) represents the requirement that – starting from $\Sigma^I(\widetilde{\widetilde{\boldsymbol{x}}}^I)$ – the flow in F at time $\bar{T}_{\mathrm{F,D}}$ satisfies

the first predicate of the definition of $G^I_{\mathrm{F,D}}$ (4.25). Solving these equations yields:

$$\widetilde{\bar{\boldsymbol{x}}}^I = \begin{pmatrix} l_0 - \frac{a^{-1}u_y(g-u_y)}{4(2u_y-g)}\bar{T}^2_{\mathrm{F,D}} \\ -\frac{a^{-1}u_y(g-u_y)}{2d(2u_y-g)}\bar{T}^2_{\mathrm{F,D}} \\ \frac{g-u_y}{2}\bar{T}_{\mathrm{F,D}} \\ -\frac{a^{-1}u_y}{d}\bar{T}_{\mathrm{F,D}} \end{pmatrix},$$
$$\bar{T}_{\mathrm{D,R}} = \bar{T}_{\mathrm{F,D}}\frac{g-u_y}{2u_y-g},$$

where we will require that:

$$\bar{T}_{\mathrm{D,R}} \in \mathbb{R}^+, \tag{4.87}$$

so as to satisfy the domain requirement in (4.39). Notice that $\frac{g-u_y}{2u_y-g} > 0$ in the expression for $\bar{T}_{\mathrm{D,R}}$ as $g \in \mathbb{R}^+$ and $u_y \in (\frac{g}{2}, g)$ as specified in (4.16).

The fact that the above computation, which involves the roots of quadratic equations, has a clean solution is due to the highly symmetric nature of the hybrid trajectory associated with the fixed point. Specifically, the configuration variables along this trajectory in each mode – in the case where they undergo a nonzero acceleration – end where they begin, so that the quadratic formula associated with solving the event time simplifies to a simple rational function. For example, the form of (4.86) is simplified by the fact that $(1, -\frac{d}{2})\bar{\boldsymbol{q}}^I = l_0$, which reduces (4.86) to:

$$\bar{T}_{\mathrm{F,D}}\begin{pmatrix} 1 \\ -\frac{d}{2} \end{pmatrix}^T \dot{\bar{\boldsymbol{q}}}^I + \frac{\bar{T}^2_{\mathrm{F,D}}}{2}\begin{pmatrix} 1 \\ -\frac{d}{2} \end{pmatrix}^T \boldsymbol{c}_{\mathrm{F}} = 0,$$

which then, because $\bar{T}_{\mathrm{F,D}} > 0$, further reduces to:

$$\begin{pmatrix} 1 \\ -\frac{d}{2} \end{pmatrix}^T \dot{\bar{\boldsymbol{q}}}^I + \frac{\bar{T}_{\mathrm{F,D}}}{2}\begin{pmatrix} 1 \\ -\frac{d}{2} \end{pmatrix}^T \boldsymbol{c}_{\mathrm{F}} = 0,$$

which does not possess any quadratic terms.

It remains to show that that the mode duration constants $\bar{T}_{\mathrm{F,D}}$ and $\bar{T}_{\mathrm{D,R}}$ agree with the value of time-to-guard-impact maps, specifically that:

$$\begin{aligned}
\bar{T}_{\mathrm{F,D}} &= T^I_{\mathrm{F,D}}\Big|_{\Sigma^I(\widetilde{\widetilde{\boldsymbol{x}}}^I)} \\
&= \min\{t \in \mathbb{R}^+ | \phi^t_{\mathrm{F}} \circ \Sigma^I(\widetilde{\widetilde{\boldsymbol{x}}}^I) \in G^I_{\mathrm{F,D}}\}, \\
\bar{T}_{\mathrm{D,R}} &= T^I_{\mathrm{D,R}}\Big|_{\Phi^I_{\mathrm{F,D}} \circ \Sigma^I(\widetilde{\widetilde{\boldsymbol{x}}}^I)} \\
&= \min\{t \in \mathbb{R}^+ | \phi^t_{\mathrm{D}} \circ \Phi^I_{\mathrm{F,D}} \circ \Sigma^I(\widetilde{\widetilde{\boldsymbol{x}}}^I) \in G^I_{\mathrm{D,R}}\},
\end{aligned}$$

where the relevant guards (4.25) are:

$$\begin{aligned}
G^I_{\mathrm{F,D}} := \{\boldsymbol{x}^I \in {D^I}_{\mathrm{F}} \mid y^{r_{hip}}(\boldsymbol{x}^I) &= l_0 + g_{TD}(\boldsymbol{x}^I) \\
&\wedge\ \dot{y}^{r_{hip}}(\boldsymbol{x}^I) < 0\}, \\
G^I_{\mathrm{D,R}} := \{\boldsymbol{x}^I \in {D^I}_{\mathrm{D}} \mid y^{f_{hip}}(\boldsymbol{x}^I) &= l_0 + g_{LO}(\boldsymbol{x}^I) \\
&\wedge\ \dot{y}^{f_{hip}}(\boldsymbol{x}^I) > 0\},
\end{aligned}$$

recalling that the functions g_{LO}, g_{TD} are required to vanish on the hybrid periodic orbit's guard intersection.

We first concentrate on $T^I_{\mathrm{F,D}}\Big|_{\Sigma^I(\widetilde{\widetilde{\boldsymbol{x}}}^I)}$. The flow through mode F given by $\phi^t_{\mathrm{F}} \circ \Sigma^I(\widetilde{\widetilde{\boldsymbol{x}}}^I)$ intersects the guard $G^I_{\mathrm{F,D}}$ when:

$$y^{r_{hip}}\Big|_{\phi^t_{\mathrm{F}} \circ \Sigma^I(\widetilde{\widetilde{\boldsymbol{x}}}^I)} = l_0 + g_{TD}\Big|_{\phi^t_{\mathrm{F}} \circ \Sigma^I(\widetilde{\widetilde{\boldsymbol{x}}}^I)} \ \wedge\ \dot{y}^{r_{hip}}\Big|_{\phi^t_{\mathrm{F}} \circ \Sigma^I(\widetilde{\widetilde{\boldsymbol{x}}}^I)} < 0. \tag{4.88}$$

The terms in (4.88) evaluated at time $\bar{T}_{\mathrm{F,D}}$ are:

$$
\begin{aligned}
g_{TD}\Big|_{\phi_{\mathrm{F}}^{\bar{T}_{\mathrm{F,D}}}\circ\Sigma^I(\widetilde{\boldsymbol{x}}^I)} &= 0,\\
y^{r_{hip}}\Big|_{\phi_{\mathrm{F}}^{\bar{T}_{\mathrm{F,D}}}\circ\Sigma^I(\widetilde{\boldsymbol{x}}^I)} &= y^{r_{hip}}\left(\begin{pmatrix} l_0 - \frac{a^{-1}u_y(g-u_y)}{4(2u_y-g)}\bar{T}_{\mathrm{F,D}}^2 \\ -\frac{a^{-1}u_y(g-u_y)}{2d(2u_y-g)}\bar{T}_{\mathrm{F,D}}^2 \\ -\frac{g-u_y}{2}\bar{T}_{\mathrm{F,D}} \\ \frac{a^{-1}u_y}{d}\bar{T}_{\mathrm{F,D}} \\ \bar{T}_{\mathrm{F,D}} \end{pmatrix}\right),\\
&= l_0,\\
\dot{y}^{r_{hip}}\Big|_{\phi_{\mathrm{F}}^{\bar{T}_{\mathrm{F,D}}}\circ\Sigma^I(\widetilde{\boldsymbol{x}}^I)} &= \dot{y}^{r_{hip}}\left(\begin{pmatrix} l_0 - \frac{a^{-1}u_y(g-u_y)}{4(2u_y-g)}\bar{T}_{\mathrm{F,D}}^2 \\ -\frac{a^{-1}u_y(g-u_y)}{2d(2u_y-g)}\bar{T}_{\mathrm{F,D}}^2 \\ -\frac{g-u_y}{2}\bar{T}_{\mathrm{F,D}} \\ \frac{a^{-1}u_y}{d}\bar{T}_{\mathrm{F,D}} \\ \bar{T}_{\mathrm{F,D}} \end{pmatrix}\right)\\
&= -\frac{\bar{T}_{\mathrm{F,D}}}{2}\big(g + (a^{-1}-1)u_y\big) < 0,
\end{aligned}
$$

and so the predicates of (4.88) are satisfied and $\phi_{\mathrm{F}}^{\bar{T}_{\mathrm{F,D}}} \circ \Sigma^I(\widetilde{\boldsymbol{x}}^I) \in G^I_{\mathrm{F,D}}$.

We still must show that $\bar{T}_{\mathrm{F,D}}$ is the *minimum* positive value of time t at which this predicate is satisfied. It is helpful to note that the rear hip has constant negative-acceleration dynamics, and thus $y^{r_{hip}} \circ \phi_{\mathrm{F}}^t \circ \Sigma^I(\widetilde{\boldsymbol{x}}^I)$ has the graph of a downwards-facing parabola. At both times $t = 0$ and $t = \bar{T}_{\mathrm{F,D}}$, we have that $y^{r_{hip}} \circ \phi_{\mathrm{F}}^t \circ \Sigma^I(\widetilde{\boldsymbol{x}}^I) = l_0$, and so (because a parabola can intersect a line no more than two times) at no other time may the predicate $y^{r_{hip}} \circ \phi_{\mathrm{F}}^t\big|_{\Sigma^I(\widetilde{\boldsymbol{x}}^I)} = l_0$ be true. The parabola is downwards-facing, hence on the time interval $(0, \bar{T}_{\mathrm{F,D}})$ the rear hip height is greater than l_0 in value. Since we require that the Lie derivative of g_{TD} along the vector field not be decreasing (4.27), we have – on the time interval

$(0, \bar{T}_{\mathrm{F,D}})$ – that $g_{TD}\Big|_{\phi^t_{\mathrm{F}} \circ \Sigma^I(\widetilde{\widetilde{\boldsymbol{x}}}^I)} \leq 0$. Then:

$$y^{r_{hip}}\Big|_{\phi^t_{\mathrm{F}} \circ \Sigma^I(\widetilde{\widetilde{\boldsymbol{x}}}^I)} > l_0 + g_{TD}\Big|_{\phi^t_{\mathrm{F}} \circ \Sigma^I(\widetilde{\widetilde{\boldsymbol{x}}}^I)}, \quad t \in (0, \bar{T}_{\mathrm{F,D}}), \tag{4.89}$$

and so $\phi^t_{\mathrm{F}} \circ \Sigma^I(\widetilde{\widetilde{\boldsymbol{x}}}^I) \notin G^I_{\mathrm{F,D}}$ for $t \in (0, \bar{T}_{\mathrm{F,D}})$. Thus $T^I_{\mathrm{D,R}}$ is indeed the minimum positive time at which the guard predicate is satisfied, allowing us to conclude that:

$$\bar{T}_{\mathrm{F,D}} = T^I_{\mathrm{F,D}}\Big|_{\Sigma^I(\widetilde{\widetilde{\boldsymbol{x}}}^I)}.$$

By similar reasoning (omitted for brevity) one can show that:

$$\bar{T}_{\mathrm{D,R}} = T^I_{\mathrm{D,R}}\Big|_{\Phi^I_{\mathrm{F,D}} \circ \Sigma^I(\widetilde{\widetilde{\boldsymbol{x}}}^I)},$$

allowing us to conclude that: $\widetilde{\widetilde{\boldsymbol{x}}}^I = H^I(\widetilde{\boldsymbol{x}}^I)$ and $\bar{T}_{\mathrm{D,R}}$ is the time-duration spent in mode D of the hybrid execution from $\bar{\boldsymbol{x}}^I$. Additionally, $\widetilde{\widetilde{\boldsymbol{x}}}^I$ is a fixed point of S^I since $S^I = H^I \circ H^I$. □

Proof of Proposition 2, part 2

Proof. We wish to solve for the fixed point of H, parametrized by its velocity component $\dot{x}$ as well as the model's physical parameters and the in-place model's fixed point parametrization. Recall that H (4.46) has the form:

$$H = \Pi \circ b \circ \Phi_{\mathrm{D,R}} \circ \Phi_{\mathrm{F,D}} \circ \Sigma, \tag{4.90}$$

where Π, b, and Σ are simple linear maps (4.43), (4.40), (4.32), while the mode maps $\Phi_{\mathrm{D,R}}$ and $\Phi_{\mathrm{F,D}}$ are given by (4.37). In the form of the mode maps, the horizontal flows are given by (4.35) and the horizontal resets are given by (4.31), recalling that the otherwise unspecified control functions $r_{\mathrm{F,D}}, r_{\mathrm{D,R}}$ in the resets are required to vanish on the hybrid periodic orbit's guard intersections.

The map H has the structure:

$$H(\widetilde{\boldsymbol{x}}) = \begin{pmatrix} H^I(\widetilde{\boldsymbol{x}}^I) \\ H^H(\widetilde{\boldsymbol{x}}^I, \widetilde{\boldsymbol{x}}^H) \end{pmatrix}, \quad \widetilde{\boldsymbol{x}} = \begin{pmatrix} \widetilde{\boldsymbol{x}}^I \\ \widetilde{\boldsymbol{x}}^H \end{pmatrix},$$

where, by the previous proof, H^I has the fixed point $\widetilde{\widetilde{\boldsymbol{x}}}^I$ (4.48). It remains to find a fixed point $\widetilde{\widetilde{\boldsymbol{x}}}^H = (\dot{\bar{x}}, \Delta\bar{x}^r, \Delta\bar{x}^f)^T$ such that:

$$\widetilde{\widetilde{\boldsymbol{x}}}^H = H^H(\widetilde{\widetilde{\boldsymbol{x}}}^I, \widetilde{\widetilde{\boldsymbol{x}}}^H) = H^H\big|_{\widetilde{\widetilde{\boldsymbol{x}}}^I}(\widetilde{\widetilde{\boldsymbol{x}}}^H),$$

where:

$$H^H\big|_{\widetilde{\widetilde{\boldsymbol{x}}}^I} = \Pi^H \circ b^H \circ R^H_{\mathrm{D,R}} \circ \hat{\phi}_{\mathrm{D}}^{\bar{T}_{\mathrm{D,R}}} \circ R^H_{\mathrm{F,D}} \circ \hat{\phi}_{\mathrm{F}}^{\bar{T}_{\mathrm{F,D}}} \circ \Sigma.$$

Finally, to aid in our search, we assume that the forward speed at the fixed point $\dot{\bar{x}}$ returns to the same value after the application of each mode map.

Consider:

$$\begin{aligned} &\hat{\phi}^{\bar{T}_{\mathrm{F,D}}} \circ \Sigma^H(\widetilde{\widetilde{\boldsymbol{x}}}^H) \\ &= \begin{pmatrix} e^{C_{\mathrm{F}}\bar{T}_{\mathrm{F,D}}} \begin{pmatrix} 0 \\ \dot{\bar{x}} \end{pmatrix} + \left(e^{C_{\mathrm{F}}\bar{T}_{\mathrm{F,D}}} - I\right) \begin{pmatrix} \Delta x^{\mathrm{Avg}} - \Delta\bar{x}^f \\ 0 \end{pmatrix} \\ \Delta\bar{x}^r \\ \Delta\bar{x}^f \end{pmatrix} \\ &= \begin{pmatrix} x_{\mathrm{F}} \\ \dot{\bar{x}} \\ \Delta\bar{x}^r \\ \Delta\bar{x}^f \end{pmatrix}, \end{aligned}$$

where x_{F} is the distance traveled horizontally by the mass center in mode F. The system

of equations given by the first two rows simplify to:

$$\left(e^{C_{\mathrm{F}}\bar{T}_{\mathrm{F,D}}} - I\right)\begin{pmatrix}\Delta x^{\mathrm{Avg}} - \bar{\Delta x}^{f} \\ \dot{\bar{x}}\end{pmatrix} = \begin{pmatrix} x_{\mathrm{F}} \\ 0\end{pmatrix},$$

allowing us to solve for x_{F} and $\bar{\Delta x}^{f}$:

$$x_{\mathrm{F}} = \begin{pmatrix}1 & 0\end{pmatrix}\left(e^{C_{\mathrm{F}}\bar{T}_{\mathrm{F,D}}} - I\right)\begin{pmatrix}\Delta x^{\mathrm{Avg}} - \bar{\Delta x}^{f} \\ \dot{\bar{x}}\end{pmatrix},$$

$$\bar{\Delta x}^{f} = \frac{\begin{pmatrix}0 & 1\end{pmatrix}\left(e^{C_{\mathrm{F}}\bar{T}_{\mathrm{F,D}}} - I\right)\begin{pmatrix}\Delta x^{\mathrm{Avg}} \\ \dot{\bar{x}}\end{pmatrix}}{\begin{pmatrix}0 & 1\end{pmatrix}\left(e^{C_{\mathrm{F}}\bar{T}_{\mathrm{F,D}}} - I\right)\begin{pmatrix}1 \\ 0\end{pmatrix}}.$$

Letting x_{D} denote the distance traveled horizontally by the mass center at the end of mode

D, we have that (successively adding on terms):

$$R_{\mathrm{F}}^{H} \circ \hat{\phi}^{\bar{T}_{\mathrm{F,D}}} \circ \Sigma^{H}(\widetilde{\boldsymbol{x}}^{H}) =$$
$$(x_{\mathrm{F}},\ \dot{\bar{x}},\ x_{\mathrm{F}} + \bar{\Delta x}^{r},\ \bar{\Delta x}^{f})^{T},$$

$$\hat{\phi}^{\bar{T}_{\mathrm{D,R}}} \circ R_{\mathrm{F}}^{H} \circ \hat{\phi}^{\bar{T}_{\mathrm{F,D}}} \circ \Sigma^{H}(\widetilde{\boldsymbol{x}}^{H}) =$$
$$(x_{\mathrm{D}},\ \dot{\bar{x}},\ x_{\mathrm{F}} + \bar{\Delta x}^{r},\ \bar{\Delta x}^{f})^{T},$$

$$R_{\mathrm{D}}^{H} \circ \hat{\phi}^{\bar{T}_{\mathrm{D,R}}} \circ R_{\mathrm{F}}^{H} \circ \hat{\phi}^{\bar{T}_{\mathrm{F,D}}} \circ \Sigma^{H}(\widetilde{\boldsymbol{x}}^{H}) =$$
$$(x_{\mathrm{D}},\ \dot{\bar{x}},\ x_{\mathrm{F}} + \bar{\Delta x}^{r},\ \Delta x^{\mathrm{Nom}})^{T},$$

$$b^{H} \circ R_{\mathrm{D}}^{H} \circ \hat{\phi}^{\bar{T}_{\mathrm{D,R}}} \circ R_{\mathrm{F}}^{H} \circ \hat{\phi}^{\bar{T}_{\mathrm{F,D}}} \circ \Sigma^{H}(\widetilde{\boldsymbol{x}}^{H}) =$$
$$(x_{\mathrm{D}},\ \dot{\bar{x}},\ \Delta x^{\mathrm{Nom}} - 2\Delta x^{\mathrm{Avg}},\ x_{\mathrm{F}} + \bar{\Delta x}^{r} + 2\Delta x^{\mathrm{Avg}})^{T},$$

$$\Pi^{H} \circ b^{H} \circ R_{\mathrm{D}}^{H} \circ \hat{\phi}^{\bar{T}_{\mathrm{D,R}}} \circ R_{\mathrm{F}}^{H} \circ \hat{\phi}^{\bar{T}_{\mathrm{F,D}}} \circ \Sigma^{H}(\widetilde{\boldsymbol{x}}^{H}) =$$
$$(\dot{\bar{x}},\ \Delta x^{\mathrm{Nom}} - 2\Delta x^{\mathrm{Avg}},\ x_{\mathrm{F}} + \bar{\Delta x}^{r} + 2\Delta x^{\mathrm{Avg}} - x_{\mathrm{D}})^{T},$$

and so:

$$H^{H} \begin{pmatrix} \dot{\bar{x}} \\ \bar{\Delta x}^{r} \\ \bar{\Delta x}^{f} \end{pmatrix} = \begin{pmatrix} \dot{\bar{x}} \\ \Delta x^{\mathrm{Nom}} - 2\Delta x^{\mathrm{Avg}} \\ x_{\mathrm{F}} + \bar{\Delta x}^{r} + 2\Delta x^{\mathrm{Avg}} - x_{\mathrm{D}} \end{pmatrix},$$

giving us $\Delta x^{\mathrm{Nom}} = \bar{\Delta x}^{r} + 2\Delta x^{\mathrm{Avg}}$ and $\bar{\Delta x}^{r} = \bar{\Delta x}^{f} - 2\Delta x^{\mathrm{Avg}} + (x_{\mathrm{D}} - x_{\mathrm{F}})$. As we already have the form of x_{F} and $\bar{\Delta x}^{f}$, all that remains is to calculate the form of x_{D} so as to obtain $\bar{\Delta x}^{r}$.

The first two rows of:

$$\hat{\phi}^{\bar{T}_{\mathrm{D,R}}} \circ R_{\mathrm{F}}^{H} \circ \hat{\phi}^{\bar{T}_{\mathrm{F,D}}} \circ \Sigma^{H}(\widetilde{\boldsymbol{x}}^{H}) = (x_{\mathrm{D}},\ \dot{\bar{x}},\ x_{\mathrm{F}} + \bar{\Delta x}^{r},\ \bar{\Delta x}^{f})^{T}$$

give us:

$$\begin{pmatrix} x_{\mathrm{D}} \\ \dot{\bar{x}} \end{pmatrix} = e^{C_{\mathrm{D}}\bar{T}_{\mathrm{D,R}}} \begin{pmatrix} x_{\mathrm{F}} \\ \dot{\bar{x}} \end{pmatrix} + \left(e^{C_{\mathrm{D}}\bar{T}_{\mathrm{D,R}}} - I\right) \begin{pmatrix} -\frac{1}{2}(x_{\mathrm{F}} + \Delta\bar{x}^r + \Delta\bar{x}^f) \\ 0 \end{pmatrix}.$$

Solving for x_{D} gives:

$$x_{\mathrm{D}} = 2(1,0)\left(e^{C_{\mathrm{D}}\bar{T}_{\mathrm{D,R}}} + I\right)^{-1} \left[e^{C_{\mathrm{D}}\bar{T}_{\mathrm{D,R}}} \begin{pmatrix} x_{\mathrm{F}} \\ 0 \end{pmatrix} + \left(e^{C_{\mathrm{D}}\bar{T}_{\mathrm{D,R}}} - I\right) \begin{pmatrix} \Delta x^{\mathrm{Avg}} - \Delta\bar{x}^f \\ \dot{\bar{x}} \end{pmatrix}\right].$$

Plugging the values of x_{D} and x_{F} into $\Delta\bar{x}^r = \Delta\bar{x}^f - 2\Delta x^{\mathrm{Avg}} + (x_{\mathrm{D}} - x_{\mathrm{F}})$ yields:

$$\Delta\bar{x}^r = \Delta\bar{x}^f - 2\Delta x^{\mathrm{Avg}} + \begin{pmatrix} 1 & 0 \end{pmatrix}\left(e^{C_{\mathrm{D}}\bar{T}_{\mathrm{D,R}}} + I\right)^{-1} \left(e^{C_{\mathrm{D}}\bar{T}_{\mathrm{D,R}}} - I\right)\left(e^{C_{\mathrm{F}}\bar{T}_{\mathrm{F,D}}} + I\right) \begin{pmatrix} \Delta x^{\mathrm{Avg}} - \Delta\bar{x}^f \\ \dot{\bar{x}} \end{pmatrix},$$

completing the proof.

Note that x_{F} and x_{D} simplify (in terms of $\Delta\bar{x}^r$ and $\Delta\bar{x}^r$ just derived) to:

$$x_{\mathrm{F}} = 2(\Delta\bar{x}^f - \Delta x^{\mathrm{Avg}}),$$
$$x_{\mathrm{D}} = \Delta\bar{x}^f + \Delta\bar{x}^r.$$

This allows us to conclude that on the periodic orbit at the end of D before the reset is

applied, the front and rear leg splays (used in (4.62)) are:

$$\begin{aligned}\bar{\Delta x}^r{}_{\mathrm{D}} &= \bar{\Delta x}^r - (x_{\mathrm{D}} - x_{\mathrm{F}}) = \bar{\Delta x}^f - 2\Delta x^{\mathrm{Avg}}, \\ \bar{\Delta x}^f{}_{\mathrm{D}} &= \bar{\Delta x}^f - x_{\mathrm{D}} \qquad\quad = -\bar{\Delta x}^r.\end{aligned} \tag{4.91}$$

□

4.11. Appendix to Chapter 4: Proof of Lemma 1

Proof. For brevity we only show the calculation of $\frac{\partial T^I_{\mathrm{F,D}}}{\partial \tilde{\boldsymbol{x}}^I}\Big|_{\tau=0}$, as the calculation of $\frac{\partial T^I_{\mathrm{D,R}}}{\partial \tilde{\boldsymbol{x}}^I}\Big|_{\tau=0}$ is nearly identical.

According to the definition of $T^I_{i,j}$ (4.39) and $G^I_{\mathrm{F,D}}$ (4.85), we have that:

$$\begin{aligned}T^I_{\mathrm{F,D}}(\boldsymbol{x}^I) &= \min\{t \in \mathbb{R}^+ | \phi^t_{\mathrm{F}}(\boldsymbol{x}^I) \in G^I_{\mathrm{F,D}}\} \\ &= \min\{t \in \mathbb{R}^+ | y^{r_{hip}} \circ \phi^t_{\mathrm{F}}(\boldsymbol{x}^I) = l_0 + g_{TD} \circ \phi^t_{\mathrm{F}}(\boldsymbol{x}^I) \\ &\qquad\qquad \wedge\ \dot{y}^{r_{hip}} \circ \phi^t_{\mathrm{F}}(\boldsymbol{x}^I) < 0\}.\end{aligned}$$

Differentiating the predicate's equality term yields:

$$\begin{aligned}&Dy^{r_{hip}}\Big|_{\phi^{T^I_{\mathrm{F,D}}(\boldsymbol{x}^I)}_{\mathrm{F}}(\boldsymbol{x}^I)} \cdot \left\{\frac{\partial \phi^t_{\mathrm{F}}(\boldsymbol{x}^I)}{\partial \boldsymbol{x}^I} + \frac{\partial \phi^t_{\mathrm{F}}(\boldsymbol{x}^I)}{\partial t}\frac{\partial T^I_{\mathrm{F,D}}}{\partial \boldsymbol{x}^I}\right\}\Big|_{\boldsymbol{x}^I, T^I_{\mathrm{F,D}}(\boldsymbol{x}^I)} \\ &= \\ &Dg_{TD}\Big|_{\phi^{T^I_{\mathrm{F,D}}(\boldsymbol{x}^I)}_{\mathrm{F}}(\boldsymbol{x}^I)} \cdot \left\{\frac{\partial \phi^t_{\mathrm{F}}(\boldsymbol{x}^I)}{\partial \boldsymbol{x}^I} + \frac{\partial \phi^t_{\mathrm{F}}(\boldsymbol{x}^I)}{\partial t}\frac{\partial T^I_{\mathrm{F,D}}}{\partial \boldsymbol{x}^I}\right\}\Big|_{\boldsymbol{x}^I, T^I_{\mathrm{F,D}}(\boldsymbol{x}^I)},\end{aligned}$$

and so:

$$\begin{aligned}\frac{\partial T^I_{\mathrm{F,D}}}{\partial \boldsymbol{x}^I} = -\frac{1}{s_{\mathrm{F}}} &\left\{Dy^{r_{hip}} - Dg_{TD}\right\}\Big|_{\phi_{\mathrm{F}}^{T^I_{\mathrm{F,D}}(\boldsymbol{x}^I)}(\boldsymbol{x}^I)} \\ &\frac{\partial \phi^t_{\mathrm{F}}(\boldsymbol{x}^I)}{\partial \boldsymbol{x}^I}\Big|_{\boldsymbol{x}^I, T^I_{\mathrm{F,D}}(\boldsymbol{x}^I)}, \\ s_{\mathrm{F}} = &\left\{Dy^{r_{hip}} - Dg_{TD}\right\}\Big|_{\phi_{\mathrm{F}}^{T^I_{\mathrm{F,D}}(\boldsymbol{x}^I)}(\boldsymbol{x}^I)} \\ &\frac{\partial \phi^t_{\mathrm{F}}(\boldsymbol{x}^I)}{\partial t}\Big|_{\boldsymbol{x}^I, T^I_{\mathrm{F,D}}(\boldsymbol{x}^I)}.\end{aligned}$$

Then:

$$\begin{aligned}\frac{\partial T^I_{\mathrm{F,D}}}{\partial \widetilde{\boldsymbol{x}}^I} = -\frac{1}{s_{\mathrm{F}}} &\left\{Dy^{r_{hip}} - Dg_{TD}\right\}\Big|_{\phi_{\mathrm{F}}^{T^I_{\mathrm{F,D}}(\boldsymbol{x}^I)}(\boldsymbol{x}^I)} \\ &\frac{\partial \phi^t_{\mathrm{F}}(\boldsymbol{x}^I)}{\partial \widetilde{\boldsymbol{x}}^I}\Big|_{\boldsymbol{x}^I, T^I_{\mathrm{F,D}}(\boldsymbol{x}^I)}, \\ s_{\mathrm{F}} = &\left\{Dy^{r_{hip}} - Dg_{TD}\right\}\Big|_{\phi_{\mathrm{F}}^{T^I_{\mathrm{F,D}}(\boldsymbol{x}^I)}(\boldsymbol{x}^I)} \\ &\frac{\partial \phi^t_{\mathrm{F}}(\boldsymbol{x}^I)}{\partial t}\Big|_{\boldsymbol{x}^I, T^I_{\mathrm{F,D}}(\boldsymbol{x}^I)}.\end{aligned} \tag{4.92}$$

The rest of the proof is concerned with evaluating each of the terms in (4.92) at $\tau = 0$.

As $y^{r_{hip}} : \boldsymbol{x}^I \mapsto y - \frac{d}{2}\varphi$ (4.28), we have that:

$$Dy^{r_{hip}} = \begin{pmatrix} 1, & -\frac{d}{2}, & 0, & 0, & 0 \end{pmatrix},$$

and (recalling the structure of the flow (4.34)):

$$\frac{\partial \phi_{\mathrm{F}}^{t}(\boldsymbol{x}^{I})}{\partial \widetilde{\boldsymbol{x}}^{I}}\Big|_{\boldsymbol{x}^{I},T_{\mathrm{F,D}}^{I}(\boldsymbol{x}^{I})} = \begin{pmatrix} I & T_{\mathrm{F,D}}^{I}(\boldsymbol{x}^{I})I \\ 0 & I \\ 0 & 0 \end{pmatrix},$$

$$\frac{\partial \phi_{\mathrm{F}}^{t}(\boldsymbol{x}^{I})}{\partial t}\Big|_{\boldsymbol{x}^{I},T_{\mathrm{F,D}}^{I}(\boldsymbol{x}^{I})} = \begin{pmatrix} \dot{\boldsymbol{q}}^{I} + \boldsymbol{c}_{\mathrm{F}} T_{\mathrm{F,D}}^{I}(\boldsymbol{x}^{I}) \\ \boldsymbol{c}_{\mathrm{F}} \\ 1 \end{pmatrix}.$$

The only remaining term in (4.92) is the quantity $Dg_{TD}\Big|_{\phi_{\mathrm{F}}^{T_{\mathrm{F,D}}^{I}(\boldsymbol{x}^{I})}(\boldsymbol{x}^{I})}$. Recall that g_{TD} (4.57) is given by:

$$g_{TD}(\boldsymbol{x}^{I}) = {\boldsymbol{k}^{I}}_{\mathrm{F}}{}^{T} \begin{pmatrix} y^{r_{hip}}{}_{\mathrm{F0}}(\boldsymbol{x}^{I}) - y^{r_{hip}}(\bar{\boldsymbol{x}}_{\mathrm{F0,D}}^{I}) \\ y^{f_{hip}}{}_{\mathrm{F0}}(\boldsymbol{x}^{I}) - y^{f_{hip}}(\bar{\boldsymbol{x}}_{\mathrm{F0,D}}^{I}) \\ \tau - \bar{T}_{\mathrm{F,D}} \end{pmatrix},$$

where $\bar{\boldsymbol{x}}_{\mathrm{F0,D}}^{I}$ and $\bar{T}_{\mathrm{F,D}}$ are constants, and the maps $y^{r_{hip}}{}_{\mathrm{F0}}, y^{f_{hip}}{}_{\mathrm{F0}}$ (4.58) are:

$$y^{r_{hip}}{}_{\mathrm{F0}}(\boldsymbol{x}^{I}) = y^{r_{hip}} \circ \phi_{\mathrm{F}}^{-\tau}(\boldsymbol{x}^{I}),$$
$$y^{f_{hip}}{}_{\mathrm{F0}}(\boldsymbol{x}^{I}) = y^{f_{hip}} \circ \phi_{\mathrm{F}}^{-\tau}(\boldsymbol{x}^{I}).$$

For clarity we introduce the following:

$$\phi_{i}^{-\tau}(\boldsymbol{x}^{I}) \equiv \widetilde{\phi}_{i}(\boldsymbol{x}^{I}),$$

Then:

$$Dg_{TD}\Big|_{\phi_{\mathrm{F}}^{T_{\mathrm{F,D}}^{I}(\boldsymbol{x}^{I})}(\boldsymbol{x}^{I})} = \left({k^{I}}_{\mathrm{F}1} Dy^{r_{hip}} + {k^{I}}_{\mathrm{F}2} Dy^{f_{hip}}\right), \frac{\partial \widetilde{\phi}_{\mathrm{F}}}{\partial \boldsymbol{x}^{I}}\Big|_{\phi_{\mathrm{F}}^{T_{\mathrm{F,D}}^{I}(\boldsymbol{x}^{I})}(\boldsymbol{x}^{I})} + {k^{I}}_{\mathrm{F}3} \frac{\partial \tau}{\partial \boldsymbol{x}^{I}},$$

where:

$$
\begin{aligned}
Dy^{r_{hip}} &= \begin{pmatrix} 1, & -\frac{d}{2}, & 0, & 0, & 0 \end{pmatrix}, \\
Dy^{f_{hip}} &= \begin{pmatrix} 1, & \frac{d}{2}, & 0, & 0, & 0 \end{pmatrix}, \\
\frac{\partial \widetilde{\phi}_{\mathrm{F}}}{\partial \boldsymbol{x}^I} &= \begin{pmatrix} I & -\tau I & \left(-\dot{\boldsymbol{q}}^I + \boldsymbol{c}_{\mathrm{F}}\tau\right) \\ 0 & I & -\boldsymbol{c}_{\mathrm{F}} \\ 0 & 0 & 0 \end{pmatrix},
\end{aligned}
$$

and so (simplifying terms):

$$
\begin{aligned}
&\frac{\partial \widetilde{\phi}_{\mathrm{F}}}{\partial \boldsymbol{x}^I}\Big|_{\phi_{\mathrm{F}}^{T^I_{\mathrm{F,D}}(\boldsymbol{x}^I)}(\boldsymbol{x}^I)} \\
&= \begin{pmatrix} I & \Big(-\big(T^I_{\mathrm{F,D}}(\boldsymbol{x}^I) + \tau\big) I \Big) & \left(-\dot{\boldsymbol{q}}^I + \boldsymbol{c}_{\mathrm{F}}\tau\right) \\ 0 & I & -\boldsymbol{c}_{\mathrm{F}} \\ 0 & 0 & 0 \end{pmatrix}.
\end{aligned}
$$

We have the form of all terms in (4.92), multiplying them together gives:

$$
\begin{aligned}
\frac{\partial T_{\mathrm{F,D}}}{\partial \widetilde{\boldsymbol{x}}^I}\Big|_{\tau=0} &= -\frac{1}{s_{\mathrm{F}}} \begin{pmatrix} 1 - k^I_{\mathrm{F},1} - k^I_{\mathrm{F},2} \\ (-1 + k^I_{\mathrm{F},1} - k^I_{\mathrm{F},2})\frac{d}{2} \\ \bar{T}_{\mathrm{F,D}} \\ -\frac{d}{2}\bar{T}_{\mathrm{F,D}} \end{pmatrix}^T, \\
s_{\mathrm{F}} &= \dot{y} - \frac{d}{2}\dot{\varphi} + \Big((1 - a^{-1})u_y - g\Big)\bar{T}_{\mathrm{F,D}} - k^I_{\mathrm{F},3}.
\end{aligned}
$$

□

4.12. Appendix to Chapter 4: Proof of Lemma 2

Proof. We aim to choose $\widetilde{\boldsymbol{k}}^I_{\mathrm{F}}$, $\widetilde{\boldsymbol{k}}^I_{\mathrm{D}}$ to make $DH^I\Big|_{\widetilde{\bar{\boldsymbol{x}}}^I}$ nilpotent.

Recall that $DH^I\Big|_{\widetilde{\bar{\boldsymbol{x}}}^I} = D\widetilde{b}^I \cdot D\widetilde{\Phi}^I_{\mathrm{D,R}}\Big|_{\Phi^I_{\mathrm{F,D}}(\bar{\boldsymbol{x}}^I)} \cdot D\widetilde{\Phi}^I_{\mathrm{F,D}}\Big|_{\bar{\boldsymbol{x}}^I}$ (4.71), where $D\widetilde{b}^I$ is a simple linear map (4.72) and:

$$D\widetilde{\Phi}^I_{\mathrm{D,R}}\Big|_{\Phi^I_{\mathrm{F,D}}(\bar{\boldsymbol{x}}^I)} = \begin{pmatrix} I & \bar{T}_{\mathrm{D,R}} I \\ 0 & I \end{pmatrix} + \begin{pmatrix} \dot{\bar{y}} \\ -\dot{\bar{\varphi}} \\ 2u_y - g \\ 0 \end{pmatrix} \widetilde{\boldsymbol{k}}_{\mathrm{D}}{}^{I\,T} M^I_{\mathrm{D}},$$

$$D\widetilde{\Phi}^I_{\mathrm{F,D}}\Big|_{\bar{\boldsymbol{x}}^I} = \begin{pmatrix} I & \bar{T}_{\mathrm{F,D}} I \\ 0 & I \end{pmatrix} + \begin{pmatrix} -\dot{\bar{y}} \\ -\dot{\bar{\varphi}} \\ u_y - g \\ -\frac{2u_y}{da} \end{pmatrix} \widetilde{\boldsymbol{k}}_{\mathrm{F}}{}^{I\,T} M^I_{\mathrm{F}}.$$

A necessary requirement for nilpotency of $DH^I\Big|_{\widetilde{\bar{\boldsymbol{x}}}^I}$ is that its determinant is zero, and so one of its factors must have a zero determinant. We find it algebraically convenient to zero

the determinant of $D\widetilde{\Phi}^I_{\mathrm{D,R}}\Big|_{\Phi^I_{\mathrm{F,D}}(\bar{\boldsymbol{x}}^I)}$:

$$
\begin{aligned}
&\det D\widetilde{\Phi}^I_{\mathrm{D,R}}\Big|_{\Phi^I_{\mathrm{F,D}}(\bar{\boldsymbol{x}}^I)} \\
&= \det\left(\begin{pmatrix} I & \bar{T}_{\mathrm{D,R}}I \\ 0 & I \end{pmatrix} + \begin{pmatrix} \dot{\bar{y}} \\ -\dot{\bar{\varphi}} \\ 2u_y - g \\ 0 \end{pmatrix} \widetilde{\boldsymbol{k}}_{\mathrm{D}}{}^{IT} M^I_{\mathrm{D}}\right) \\
&\overset{[73,\ \text{Lem. } 1.1]}{=} \det\begin{pmatrix} I & \bar{T}_{\mathrm{D,R}}I \\ 0 & I \end{pmatrix} \cdot \\
&\quad \left(1 + \widetilde{\boldsymbol{k}}_{\mathrm{D}}{}^{IT} M^I_{\mathrm{D}} \begin{pmatrix} I & -\bar{T}_{\mathrm{D,R}}I \\ 0 & I \end{pmatrix} \begin{pmatrix} \dot{\bar{y}} \\ -\dot{\bar{\varphi}} \\ 2u_y - g \\ 0 \end{pmatrix}\right) \\
&= 1 + \widetilde{\boldsymbol{k}}_{\mathrm{D}}{}^{IT} M^I_{\mathrm{D}} \begin{pmatrix} I & -\bar{T}_{\mathrm{D,R}}I \\ 0 & I \end{pmatrix} \begin{pmatrix} \dot{\bar{y}} \\ -\dot{\bar{\varphi}} \\ 2u_y - g \\ 0 \end{pmatrix} \\
&= 1 + \widetilde{\boldsymbol{k}}_{\mathrm{D}}{}^{IT} M^I_{\mathrm{D}} \begin{pmatrix} -\dot{\bar{y}} \\ -\dot{\bar{\varphi}} \\ 2u_y - g \\ 0 \end{pmatrix} \\
&= 1 + \widetilde{\boldsymbol{k}}_{\mathrm{D}}{}^{IT} \begin{pmatrix} -\dot{\bar{y}} \\ -\dot{\bar{\varphi}} \\ 2u_y - g \end{pmatrix} \\
&= 0 \iff \widetilde{\boldsymbol{k}}_{\mathrm{D}}{}^{IT} \begin{pmatrix} -\dot{\bar{y}} \\ -\dot{\bar{\varphi}} \\ 2u_y - g \end{pmatrix} = -1.
\end{aligned} \tag{4.93}
$$

The choice of $\widetilde{\boldsymbol{k}}_{\mathrm{D}}^{I}$ according to (4.93) results in the Jordan decomposition $D\widetilde{\Phi}^{I}_{\mathrm{D,R}}\Big|_{\Phi^{I}_{\mathrm{F,D}}(\bar{\boldsymbol{x}}^{I})} = V^{I}\Lambda^{I}{V^{I}}^{-1}$, where:

$$V^{I} = \begin{pmatrix} -\dot{\tilde{y}} & \dot{\tilde{y}} + {\widetilde{k}^{I}}^{-1}{}_{\mathrm{D},1} & -\frac{\widetilde{k}^{I}_{\mathrm{D},2}}{\widetilde{k}^{I}_{\mathrm{D},1}} & -\frac{\widetilde{k}^{I}_{\mathrm{D},3}(\widetilde{k}^{I}_{\mathrm{D},2} - \frac{d}{2}\widetilde{k}^{I}_{\mathrm{D},1})}{{\widetilde{k}^{I}}^{2}{}_{\mathrm{D},1}\bar{T}_{\mathrm{D,R}}} \\ -\dot{\tilde{\varphi}} & -\dot{\tilde{\varphi}} & 1 & 0 \\ 2u_y - g & 2u_y - g & 0 & -\frac{\widetilde{k}^{I}_{\mathrm{D},2}}{\widetilde{k}^{I}_{\mathrm{D},1}\bar{T}_{\mathrm{D,R}}} \\ 0 & 0 & 0 & \bar{T}^{-1}_{\mathrm{D,R}} \end{pmatrix}, \tag{4.94}$$

$$\Lambda^{I} = \begin{pmatrix} 0 & 0 & 0 & 0 \\ 0 & 1 + \widetilde{k}^{I}_{\mathrm{D},1}\bar{T}_{\mathrm{D,R}}(2u_y - g) & 0 & 0 \\ 0 & 0 & 1 & 1 \\ 0 & 0 & 0 & 1 \end{pmatrix}.$$

We have that $\det V^{I} = \frac{2u_y - g}{\widetilde{k}^{I}_{\mathrm{D},1}\bar{T}_{\mathrm{D,R}}}(1 + 2\dot{\tilde{y}}\widetilde{k}^{I}_{\mathrm{D},1})$, and so we will require that:

$$\widetilde{k}^{I}_{\mathrm{D},1} \neq -\frac{1}{2\dot{\tilde{y}}}, \quad \widetilde{k}^{I}_{\mathrm{D},1} \neq 0. \tag{4.95}$$

Nilpotency of a real matrix product is equivalent to nilpotency of the product of any cyclic permutation of its factors,[31] thus achieving our goal of a nilpotent:

$$\begin{aligned} DH^{I}\Big|_{\widetilde{\boldsymbol{x}}^{I}} &= D\widetilde{b}^{I} \cdot D\widetilde{\Phi}^{I}_{\mathrm{D,R}}\Big|_{\Phi^{I}_{\mathrm{F,D}}(\bar{\boldsymbol{x}}^{I})} \cdot D\widetilde{\Phi}^{I}_{\mathrm{F,D}}\Big|_{\bar{\boldsymbol{x}}^{I}} \\ &= D\widetilde{b}^{I} \cdot V^{I} \cdot \Lambda^{I} \cdot {V^{I}}^{-1} \cdot D\widetilde{\Phi}^{I}_{\mathrm{F,D}}\Big|_{\bar{\boldsymbol{x}}^{I}}, \end{aligned}$$

is equivalent to nilpotency of the cyclic permutation:

$$\Lambda^{I} \cdot {V^{I}}^{-1} \cdot D\widetilde{\Phi}^{I}_{\mathrm{F,D}}\Big|_{\bar{\boldsymbol{x}}^{I}} \cdot D\widetilde{b}^{I} \cdot V^{I}.$$

The block structure of the leading factor Λ^{I} guarantees both a zero eigenvalue and that the

[31] Proof: Let $M \in \mathbb{R}^{n\times n}, A \in \mathbb{R}^{n\times m}, B \in \mathbb{R}^{m\times n}$, $M = AB$. Assume there exists a $k \in \mathbb{N}$ such that $M^{k} = 0$ (M is nilpotent). Then $(AB)^{k} = 0$ and so $(BA)^{k+1} = B(AB)^{k}A = B(0)A = 0$. Then the cyclic permutation BA is nilpotent. Similarly, assume there exists a $k \in \mathbb{N}$ such that $(BA)^{k} = 0$ (the cyclic permutation BA is nilpotent). Then $M^{k+1} = (AB)^{k+1} = A(BA)^{k}B = A(0)B = 0$. Then M is nilpotent.

remaining three eigenvalues of the product can only be affected by the lower three-by-three block matrix of the product. This lower three-by-three block – which we represent by the matrix N – is given by:

$$N = T^I \cdot \Lambda^I \cdot {V^I}^{-1} \cdot D\widetilde{\Phi}^I_{\mathrm{F,D}}\Big|_{\bar{\boldsymbol{x}}^I} \cdot D\widetilde{b}^I \cdot V^I \cdot {T^I}^T,$$
$$T^I = \begin{pmatrix} 0 & 1 & 0 & 0 \\ 0 & 0 & 1 & 0 \\ 0 & 0 & 0 & 1 \end{pmatrix}.$$

Expanding $D\widetilde{\Phi}^I_{\mathrm{F,D}}\Big|_{\bar{\boldsymbol{x}}^I}$ results in:

$$N = A^I + \boldsymbol{d}^I {\widetilde{\boldsymbol{k}}_{\mathrm{F}}}^{I^T} M^I_{\mathrm{F}} D\widetilde{b}^I V^I {T^I}^T,$$
$$A^I = T^I \Lambda^I {V^I}^{-1} \begin{pmatrix} I & I\bar{T}_{\mathrm{F,D}} \\ 0 & I \end{pmatrix} D\widetilde{b}^I V^I {T^I}^T,$$
$$\boldsymbol{d}^I = T^I \Lambda^I {V^I}^{-1} \begin{pmatrix} -\dot{\bar{y}} \\ -\dot{\bar{\varphi}} \\ u_y - g \\ -\frac{2u_y}{da} \end{pmatrix}.$$

We place the eigenvalues of N at the origin using the standard Ackermann's formula [201, p. 611] via:

$${\widetilde{\boldsymbol{k}}_{\mathrm{F}}}^{I^T} M^I_{\mathrm{F}} D\widetilde{b}^I V^I {T^I}^T = -\begin{pmatrix} 0 & 0 & 1 \end{pmatrix} {R^I}^{-1} {A^I}^3,$$

where:

$$R^I = \begin{pmatrix} \boldsymbol{d}^I & A^I \boldsymbol{d}^I & {A^I}^2 \boldsymbol{d}^I \end{pmatrix}. \tag{4.96}$$

Equivalently:

$${\widetilde{\boldsymbol{k}}_{\mathrm{F}}}^{I^T} = -\begin{pmatrix} 0 & 0 & 1 \end{pmatrix} {R^I}^{-1} {A^I}^3 \left(M^I_{\mathrm{F}} D\widetilde{b}^I V^I {T^I}^T \right)^{-1},$$

where:

$$\det\left(M_{\mathrm{F}}^{I} D\widetilde{b}^{I} V^{I} T^{I^{T}}\right) =$$
$$\frac{\widetilde{k}_{\mathrm{D},2}^{I} - \frac{d}{2}\widetilde{k}_{\mathrm{D},1}^{I}}{\widetilde{k}^{I^{2}}{}_{\mathrm{D},1}\bar{T}_{\mathrm{D,R}}}\left(1 + \dot{\bar{y}}\widetilde{k}_{\mathrm{D},1}^{I} - \dot{\bar{\varphi}}\widetilde{k}_{\mathrm{D},2}^{I} + (2u_y - g)\widetilde{k}_{\mathrm{D},3}^{I}\right),$$

introducing the requirements that:

$$\begin{aligned} \widetilde{k}_{\mathrm{D},1}^{I} &\neq 0, \\ \widetilde{k}_{\mathrm{D},2}^{I} &\neq \frac{d}{2}\widetilde{k}_{\mathrm{D},1}^{I}, \\ \dot{\bar{y}}\widetilde{k}_{\mathrm{D},1}^{I} - \dot{\bar{\varphi}}\widetilde{k}_{\mathrm{D},2}^{I} + (2u_y - g)\widetilde{k}_{\mathrm{D},3}^{I} &\neq -1. \end{aligned} \tag{4.97}$$

The determinant of R^I is exceedingly complicated and so we leave as a conjecture that R^I is generically invertible. We verified invertibility numerically using the values from Table 5. □

4.13. Appendix to Chapter 4: Proof of Lemma 3

Proof. We desire a value of $\boldsymbol{k}^H = (k_{\mathrm{F}}^H, k_{\mathrm{D},1}^H, k_{\mathrm{D},2}^H)^T$ that makes $D_{\widetilde{\boldsymbol{x}}^H} H^H\big|_{\widetilde{\widetilde{\boldsymbol{x}}}^I}$ (4.70) nilpotent. Recall that $D_{\widetilde{\boldsymbol{x}}^H} H^H\big|_{\widetilde{\widetilde{\boldsymbol{x}}}^I}$ has the form:

$$\begin{aligned} D_{\widetilde{\boldsymbol{x}}^H} H^H\big|_{\widetilde{\widetilde{\boldsymbol{x}}}^I} =& D\Pi^H \cdot Db^H \cdot D_{\boldsymbol{x}^H} R_{\mathrm{D,R}}^H \cdot D_{\boldsymbol{x}^H} \hat{\phi}_{\mathrm{D}}^{\bar{T}_{\mathrm{D,R}}} \cdot \\ & D_{\boldsymbol{x}^H} R_{\mathrm{F,D}}^H \cdot D_{\boldsymbol{x}^H} \hat{\phi}_{\mathrm{F}}^{\bar{T}_{\mathrm{F,D}}} \cdot D\Sigma^H, \end{aligned}$$

where:

$$D\Pi^H = \begin{pmatrix} 0 & 1 & 0 & 0 \\ 0 & 0 & 1 & 0 \\ -1 & 0 & 0 & 1 \end{pmatrix}, \quad Db^H = \begin{pmatrix} 1 & 0 & 0 & 0 \\ 0 & 1 & 0 & 0 \\ 0 & 0 & 0 & 1 \\ 0 & 0 & 1 & 0 \end{pmatrix},$$

$$D\Sigma^H = \begin{pmatrix} 0 & 0 & 0 \\ 1 & 0 & 0 \\ 0 & 1 & 0 \\ 0 & 0 & 1 \end{pmatrix},$$

and:

$$D_{\boldsymbol{x}^H}\hat{\phi}_{\mathrm{F}}^{\bar{T}_{\mathrm{F,D}}} = \begin{pmatrix} e^{C_{\mathrm{F}}\bar{T}_{\mathrm{F,D}}} & (e^{C_{\mathrm{F}}\bar{T}_{\mathrm{F,D}}} - I)\begin{pmatrix} 0 & -1 \\ 0 & 0 \end{pmatrix} \\ 0 & I \end{pmatrix},$$

$$C_{\mathrm{F}} = \begin{pmatrix} 0 & 1 \\ \frac{u_y}{\bar{y}} & 0 \end{pmatrix},$$

$$D_{\boldsymbol{x}^H}\hat{\phi}_{\mathrm{D}}^{\bar{T}_{\mathrm{D,R}}} = \begin{pmatrix} e^{C_{\mathrm{D}}\bar{T}_{\mathrm{D,R}}} & \frac{1}{2}(e^{C_{\mathrm{D}}\bar{T}_{\mathrm{D,R}}} - I)\begin{pmatrix} -1 & -1 \\ 0 & 0 \end{pmatrix} \\ 0 & I \end{pmatrix},$$

$$C_{\mathrm{D}} = \begin{pmatrix} 0 & 1 \\ \frac{2u_y}{\bar{y}} & 0 \end{pmatrix},$$

$$D_{\boldsymbol{x}^H}R_{\mathrm{F,D}}^H = \begin{pmatrix} I & 0 \\ \begin{pmatrix} 1 & k_{\mathrm{F}}^H \\ 0 & 0 \end{pmatrix} & I \end{pmatrix},$$

$$D_{\boldsymbol{x}^H}R_{\mathrm{D,R}}^H = \begin{pmatrix} I & 0 \\ \begin{pmatrix} 0 & 0 \\ -(k_{\mathrm{D},1}^H + k_{\mathrm{D},2}^H) & 0 \end{pmatrix} & \begin{pmatrix} 1 & 0 \\ k_{\mathrm{D},1}^H & k_{\mathrm{D},2}^H \end{pmatrix} \end{pmatrix}.$$

Nilpotency of $D_{\widetilde{\boldsymbol{x}}^H}H^H\big|_{\widetilde{\widetilde{\boldsymbol{x}}}^I}$ is equivalent to nilpotency of the product of any cyclic permutation of the factors of $D_{\widetilde{\boldsymbol{x}}^H}H^H\big|_{\widetilde{\widetilde{\boldsymbol{x}}}^I}$. Consider the cyclic permutation:

$$D\Sigma^H \cdot D\Pi^H \cdot Db^H \cdot D_{\boldsymbol{x}^H}R_{\mathrm{D,R}}^H \cdot D_{\boldsymbol{x}^H}\hat{\phi}_{\mathrm{D}}^{\bar{T}_{\mathrm{D,R}}} \cdot D_{\boldsymbol{x}^H}R_{\mathrm{F,D}}^H \cdot D_{\boldsymbol{x}^H}\hat{\phi}_{\mathrm{F}}^{\bar{T}_{\mathrm{F,D}}}.$$

The product of the final four factors is equal to:

$$
\begin{aligned}
D_{\boldsymbol{x}^H}\hat{R}^H_{\mathrm{D,R}} :=& D\Sigma^H \cdot D\Pi^H \cdot Db^H \cdot D_{\boldsymbol{x}^H}R^H_{\mathrm{D,R}} \\
&= \begin{pmatrix} 0 & 0 & 0 & 0 \\ 0 & 1 & 0 & 0 \\ -(k^H_{\mathrm{D},1}+k^H_{\mathrm{D},2}) & 0 & k^H_{\mathrm{D},1} & k^H_{\mathrm{D},2} \\ -1 & 0 & 1 & 0 \end{pmatrix},
\end{aligned}
$$

which by inspection is generically rank three but drops to rank two when $k^H_{\mathrm{D},2} = 0$.

Let $k^H_{\mathrm{D},2} = 0$. Then:

$$
D_{\boldsymbol{x}^H}\hat{R}^H_{\mathrm{D,R}} = \begin{pmatrix} 0 & 0 & 0 & 0 \\ 0 & 1 & 0 & 0 \\ -k^H_{\mathrm{D},1} & 0 & k^H_{\mathrm{D},1} & 0 \\ -1 & 0 & 1 & 0 \end{pmatrix} = V\Lambda V^{-1},
$$

$$
V = \begin{pmatrix} 0 & 1 & 0 & 0 \\ 0 & 0 & 1 & 0 \\ 0 & 1 & 0 & k^H_{\mathrm{D},1} \\ 1 & 0 & 0 & 1 \end{pmatrix}, \quad \Lambda = \mathrm{diag}\{0, 0, 1, k^H_{\mathrm{D},1}\}
$$

$$
\text{s.t. } \Lambda V^{-1} = \begin{pmatrix} 0 & 0 & 0 & 0 \\ 0 & 0 & 0 & 0 \\ 0 & 1 & 0 & 0 \\ -1 & 0 & 1 & 0 \end{pmatrix}.
$$

We use these terms to simplify the previous cyclic permutation of $D_{\widetilde{\boldsymbol{x}}^H} H^H\big|_{\widetilde{\widetilde{\boldsymbol{x}}}^I}$:

$$
\begin{aligned}
&D\Sigma^H \cdot D\Pi^H \cdot Db^H \cdot D_{\boldsymbol{x}^H} R^H_{\mathrm{D,R}} \cdot \\
&\quad D_{\boldsymbol{x}^H} \hat{\phi}^{\bar{T}_{\mathrm{D,R}}}_{\mathrm{D}} \cdot D_{\boldsymbol{x}^H} R^H_{\mathrm{F,D}} \cdot D_{\boldsymbol{x}^H} \hat{\phi}^{\bar{T}_{\mathrm{F,D}}}_{\mathrm{F}} \\
&= D_{\boldsymbol{x}^H} \hat{R}^H_{\mathrm{D,R}} \cdot \left(D_{\boldsymbol{x}^H} \hat{\phi}^{\bar{T}_{\mathrm{D,R}}}_{\mathrm{D}} \cdot D_{\boldsymbol{x}^H} R^H_{\mathrm{F,D}} \cdot D_{\boldsymbol{x}^H} \hat{\phi}^{\bar{T}_{\mathrm{F,D}}}_{\mathrm{F}} \right) \\
&= V \cdot \Lambda \cdot V^{-1} \cdot \left(D_{\boldsymbol{x}^H} \hat{\phi}^{\bar{T}_{\mathrm{D,R}}}_{\mathrm{D}} \cdot D_{\boldsymbol{x}^H} R^H_{\mathrm{F,D}} \cdot D_{\boldsymbol{x}^H} \hat{\phi}^{\bar{T}_{\mathrm{F,D}}}_{\mathrm{F}} \right),
\end{aligned}
$$

and again cyclically permute it to:

$$
\Lambda \cdot V^{-1} \cdot D_{\boldsymbol{x}^H} \hat{\phi}^{\bar{T}_{\mathrm{D,R}}}_{\mathrm{D}} \cdot D_{\boldsymbol{x}^H} R^H_{\mathrm{F,D}} \cdot D_{\boldsymbol{x}^H} \hat{\phi}^{\bar{T}_{\mathrm{F,D}}}_{\mathrm{F}} \cdot V,
$$

which is four-by-four and, by virtue of Λ, has a block lower-triangular form with zeros in the upper-left two-by-two block. Then only the lower right two-by-two block can affect the remaining (possibly) non-zero eigenvalues, reducing our consideration to nilpotency of the two-by-two:

$$
\begin{aligned}
D_{\widetilde{\boldsymbol{x}}^H} \widetilde{H}^H\big|_{\widetilde{\widetilde{\boldsymbol{x}}}^I} := \begin{pmatrix} 0 & I \end{pmatrix} \cdot \Lambda \cdot V^{-1} \cdot D_{\boldsymbol{x}^H} \hat{\phi}^{\bar{T}_{\mathrm{D,R}}}_{\mathrm{D}} \cdot \\
D_{\boldsymbol{x}^H} R^H_{\mathrm{F,D}} \cdot D_{\boldsymbol{x}^H} \hat{\phi}^{\bar{T}_{\mathrm{F,D}}}_{\mathrm{F}} \cdot V \cdot \begin{pmatrix} 0 \\ I \end{pmatrix}.
\end{aligned}
$$

Expanding out $D_{\widetilde{\boldsymbol{x}}^H} \widetilde{H}^H\big|_{\widetilde{\widetilde{\boldsymbol{x}}}^I}$ and simplifying results in:

$$
\begin{aligned}
&D_{\widetilde{\boldsymbol{x}}^H} \widetilde{H}^H\big|_{\widetilde{\widetilde{\boldsymbol{x}}}^I} = \\
&\begin{pmatrix} 0 & 1 \\ -1 & 0 \end{pmatrix} e^{C_{\mathrm{D}} \bar{T}_{\mathrm{D,R}}} \left[e^{C_{\mathrm{F}} \bar{T}_{\mathrm{F,D}}} \begin{pmatrix} 0 & -1 \\ 1 & 0 \end{pmatrix} + \begin{pmatrix} 0 & 1 \\ 0 & 0 \end{pmatrix} \right] + \\
&\frac{1}{2} \left[\begin{pmatrix} 0 & 1 \\ -1 & 0 \end{pmatrix} e^{C_{\mathrm{D}} \bar{T}_{\mathrm{D,R}}} \begin{pmatrix} -1 & -1 \\ 0 & 0 \end{pmatrix} + \begin{pmatrix} 0 & 0 \\ 1 & -1 \end{pmatrix} \right] \cdot \\
&\begin{pmatrix} \tilde{k}^H_{\mathrm{F}} & \tilde{k}^H_{\mathrm{D},L} \\ 0 & 1 \end{pmatrix},
\end{aligned}
$$

where:

$$\begin{pmatrix} k_{\mathrm{F}}^{H} \\ k_{\mathrm{D},1}^{H} \end{pmatrix} = \begin{pmatrix} \cosh\left(\bar{T}_{\mathrm{F,D}}\sqrt{\frac{u_y}{\bar{y}}}\right) & 0 \\ -\sqrt{\frac{u_y}{\bar{y}}}\sinh\left(\bar{T}_{\mathrm{F,D}}\sqrt{\frac{u_y}{\bar{y}}}\right) & 1 \end{pmatrix}^{-1} \left\{ \begin{pmatrix} \tilde{k}_{\mathrm{F}}^{H} \\ \tilde{k}_{\mathrm{D},1}^{H} \end{pmatrix} - \begin{pmatrix} \sqrt{\frac{\bar{y}}{u_y}}\sinh\left(\bar{T}_{\mathrm{F,D}}\sqrt{\frac{u_y}{\bar{y}}}\right) \\ 1-\cosh\left(\bar{T}_{\mathrm{F,D}}\sqrt{\frac{u_y}{\bar{y}}}\right) \end{pmatrix} \right\},$$

and:

$$\det\begin{pmatrix} \cosh\left(\bar{T}_{\mathrm{F,D}}\sqrt{\frac{u_y}{\bar{y}}}\right) & 0 \\ -\sqrt{\frac{u_y}{\bar{y}}}\sinh\left(\bar{T}_{\mathrm{F,D}}\sqrt{\frac{u_y}{\bar{y}}}\right) & 1 \end{pmatrix} = \cosh\left(\bar{T}_{\mathrm{F,D}}\sqrt{\frac{u_y}{\bar{y}}}\right),$$

which never equals zero by virtue of $\bar{T}_{\mathrm{F,D}}, u_y \neq 0$.

Then $D_{\widetilde{\boldsymbol{x}}^H}\widetilde{H}^H\big|_{\widetilde{\widetilde{\boldsymbol{x}}}^I}$ simplifies to:

$$D_{\widetilde{\boldsymbol{x}}^H}\widetilde{H}^H\big|_{\widetilde{\widetilde{\boldsymbol{x}}}^I} = A^H + \boldsymbol{d}^H \begin{pmatrix} \tilde{k}_{\mathrm{F}}^{H} \\ \tilde{k}_{\mathrm{D},1}^{H} \end{pmatrix}^T,$$

where:

$$\begin{aligned} A^H &= \begin{pmatrix} 0 & 1 \\ -1 & 0 \end{pmatrix} e^{C_{\mathrm{D}}\bar{T}_{\mathrm{D,R}}}\Big(e^{C_{\mathrm{F}}\bar{T}_{\mathrm{F,D}}}\begin{pmatrix} 0 & -1 \\ 1 & 0 \end{pmatrix} + \begin{pmatrix} 0 & \frac{1}{2} \\ 0 & 0 \end{pmatrix}\Big) \\ &\quad - \begin{pmatrix} 0 & 0 \\ 0 & \frac{1}{2} \end{pmatrix}, \\ \boldsymbol{d}^H &= \begin{pmatrix} 0 & 1 \\ -1 & 0 \end{pmatrix} e^{C_{\mathrm{D}}\bar{T}_{\mathrm{D,R}}}\begin{pmatrix} -\frac{1}{2} \\ 0 \end{pmatrix} + \begin{pmatrix} 0 \\ \frac{1}{2} \end{pmatrix}. \end{aligned}$$

We place the eigenvalues of $D_{\widetilde{\boldsymbol{x}}^H}\widetilde{H}^H\big|_{\widetilde{\widetilde{\boldsymbol{x}}}^I}$ at the origin using the standard Ackermann's formula [201, p. 611] via:

$$\begin{pmatrix} \tilde{k}_{\mathrm{F}}^{H} \\ \tilde{k}_{\mathrm{D},1}^{H} \end{pmatrix} = -\left(R^{H^{-1}}A^{H^2}\right)^T \begin{pmatrix} 0 \\ 1 \end{pmatrix},$$

where:

$$R^H = \begin{pmatrix} \boldsymbol{d}^H & A^H \boldsymbol{d}^H \end{pmatrix},$$

and:

$$\begin{aligned} \det R^H =& \frac{1}{8}\sqrt{\frac{u_y}{\bar{y}}} e^{-\sqrt{\frac{u_y}{\bar{y}}}(\bar{T}_{\mathrm{F,D}}+\bar{T}_{\mathrm{D,R}})} \left(1 + e^{\sqrt{\frac{u_y}{\bar{y}}}\bar{T}_{\mathrm{D,R}}}\right)^2 \\ & \left(-1 + e^{2\sqrt{\frac{u_y}{\bar{y}}}(\bar{T}_{\mathrm{F,D}}+\bar{T}_{\mathrm{D,R}})}\right), \end{aligned}$$

thus R^H is invertible, as $u_y \neq 0$ and $2\sqrt{\frac{u_y}{\bar{y}}}(\bar{T}_{\mathrm{F,D}} + \bar{T}_{\mathrm{D,R}}) \neq 0$.

□

CHAPTER 5

Running with an unlocked back

This chapter provides empirical documentation of steady-state spined quadrupedal bounding at modest speeds utilizing sagittal-plane core actuation on a power-autonomous physical machine (the first such documentation in the literature to our knowledge) [79]. We compare this empirical steady-state behavior to the simulation of a simple reduced-order model of a spined quadruped presented in Chapter 5.1 and show (using the experimental setup of Chapter 5.2) a rough correspondence between the empirical and simulation results in Chapter 5.3, concluding that the proposed simplified model is sufficiently expressive to describe realistic bounding limit cycles utilizing core actuation and is thus of interest for robotic and biological applications, motivating a more formal data-driven and theoretical analysis for future work. Chapter 5.4 speculates about the relationship between the locked-back reduced-order model introduced in Chapter 4 and a spined machine.

The work of this chapter represents an experimental characterization of spined running and – at present – doesn't include a complete theoretical analysis as discussed in Chapter 5.4. For this reason, the model used to validate the experiments is simpler than the one used in Chapter 4. The results of this section motivate the use of an augmented version of the model presented in Chapter 4 – augmented by composing in a spine-bending degree-of-freedom – to obtain a formal understanding of the spine's role in running.

5.1. Sagittal-plane reduced-order model of a spined quadruped

Following [46,61,80,89,171], we propose a reduced-order sagittal-plane spined quadrupedal model consisting of two bipedal body segments connected by a massless pin joint[32] as shown in Figure 29. We take the state of the model to be given by $\mathbf{q} = (x, y, \phi, \psi)^T \in$

[32] While this is the most common class of robotic core actuation models in the literature, alternatives have been proposed such as [227].

$\mathscr{D} = \mathbb{R}^2 \times \mathbb{T}^2$ and its time derivative, where x and y respectively denote the horizontal and vertical displacement of the mass center from the origin, ϕ denotes the body pitch, and ψ denotes the angle of the spine (with zero occurring at full extension). Wrenches on the mass center can be applied by the legs – which are assumed to be massless – when in contact with the ground, and the spine can apply a torque at the pin joint. For generality we consider these wrenches to be external to the system even when due to compliance.[33]

To reduce the parameter space we make the following assumptions: the front and rear body segments possess identical parameters, each body segment's mass center is located at the leg hip, and the body segments individually possess no moment of inertia. The model can then be parametrized by $\mathbf{p} = (m, d)^T$, where $m \in \mathbb{R}^+$ denotes total mass and $d \in \mathbb{R}^+$ denotes extended body length. The distance between the front and rear masses $\bar{d}$ is given by $\bar{d} = d\cos(\psi/2)$, which we later use as a convenient surrogate for ψ.

The dynamics of the model are represented as

$$M\ddot{\mathbf{q}} + C\dot{\mathbf{q}} + N = \tau,$$

where

$$M(\mathbf{q}) = diag\{m, m, \frac{md^2}{8}\big(1+\cos(\psi)\big), \frac{md^2}{32}\big(1-\cos(\psi)\big)\}$$

is the diagonal inertial matrix,

$$C(\mathbf{q}, \dot{\mathbf{q}}) = \begin{pmatrix} 0 & 0 & 0 & 0 \\ 0 & 0 & 0 & 0 \\ 0 & 0 & 0 & -\frac{md^2}{8}\sin(\psi)\dot{\phi} \\ 0 & 0 & \frac{md^2}{16}\sin(\psi)\dot{\phi} & \frac{md^2}{64}\sin(\psi)\dot{\psi} \end{pmatrix}$$

[33] The advent of virtual compliance in legged drive-trains [114, 132] complicates considering compliance as part of the natural system dynamics.

gives the Coriolis terms, the effect of gravity is accounted for by

$$N(\mathbf{q}) = \begin{pmatrix} 0 & mg & 0 & 0 \end{pmatrix}^T,$$

and $\tau \in \mathbb{R}^4$ is the sum of the external wrenches on the mass center.

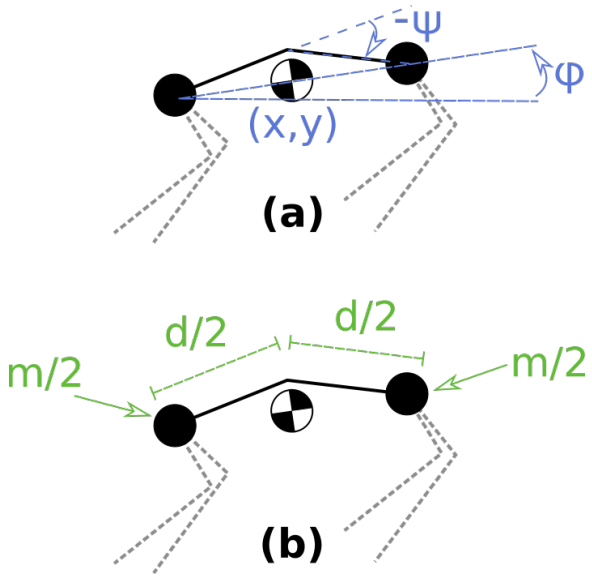

Figure 29: The reduced-order sagittal-plane spined quadrupedal model consists of two bipedal point masses connected by a massless pin joint. The state of the model shown in (a) is given by $\mathbf{q} = (x, y, \phi, \psi)^T \in \mathscr{Q} = \mathbb{R}^2 \times \mathbb{T}^2$ and its time derivative, where $\mathbf{q}$ respectively consists of the forward and vertical position of the mass center, the body pitch, and the spine angle with respect to full extension. The model is parametrized by the total mass m and extended body length d as shown in (b). The legs are assumed to be massless. The distance between the front and rear masses $\bar{d}$ is given by $\bar{d} = d\cos(\psi/2)$, which we use as a convenient surrogate for ψ.

One potential drawback with this modeling choice is that the inertial matrix loses rank when the spine is fully extended. We avoid numerical issues in simulation with little loss of fidelity by controlling the model to extend the spine short of this singularity instead of to the fully extended configuration.

5.2. Experimental setup

5.2.1. Bounding Control Strategy

The bounding control strategy used in the experiments builds upon ideas presented in [175] and [67], and is described below only in brief as the focus is on validating the correspondence of the spined model with the physical robot. The control algorithm consists of commanding the front and rear legs to act as modified sagittal-plane Raibert hoppers [175, p. 56] and actuating the spine according to which hopper is in stance. The front and rear body-segment controllers share no state information and are only coupled through the physical dynamics of the body, but this physical coupling is sufficient to give rise to a bounding gait (as described in [67]).

Specifically, the left and right legs of an individual body segment are commanded as one "virtual leg" [175, p. 92] to anchor the Spring Loaded Inverted Pendulum (SLIP) template [36, 185] so as to mimic a radial Hooke's law spring while in stance. A full description of the virtual compliance control scheme used to achieve the SLIP anchoring is given in [75]. The virtual legs are vertically energized by applying a radial piecewise-constant leg force to compress the radial virtual leg spring in the first half of stance and assist its extension in the second half of stance. Forward-speed control is achieved using Raibert's neutral-point technique [175, p. 40-47] to select a desired leg touchdown angle in flight. The forward speed is further energized by applying a leg torque in stance proportional to the difference between the actual leg angle and the desired liftoff angle of Raibert's neutral-point controller. The reason the controller of Chapter 4 wasn't used is because the work on bounding with an unlocked spine of this chapter was done first and motivated work on the analytically stable controller of the previous chapter. We expect that using an extended version of the previous chapter's controller would result in similar behavior to that presented here.

For a bounding gait to emerge from the physical coupling between the hopping front and rear body segments, we artificially limit the stance duration of the legs to be 190 ms or

less, after which the legs are retracted to force the body segment into flight. With longer stance durations, a pronking gait emerges. The causes of this gait bifurcation would be an interesting subject for future work.

The spine is controlled by commanding a spine retraction to a set angle if the front legs are the only legs in stance, commanding a full spine extension if the rear legs are the only legs in stance, and maintaining the spine's current angle otherwise.

5.2.2. Controller Implementation On-Board the Inu Robot

A stable bounding gait utilizing core actuation was achieved using the above controller on-board the Inu robot. Controller parameters such as the virtual spring stiffness were hand-tuned either on the robot or using the simulation described in Chapter 5.2.4 to search for a limit cycle. User input at runtime consisted of setting the desired speed via joystick. The only modification made to the algorithm presented in Chapter 5.2.1 was that the spine extension and retraction were commanded to occur gradually over the course of 100 ms because faster retraction and extension resulted in slippage of the spine belt over the driving sprocket.

5.2.3. Experiment Design

Two experiments were performed using the robot. In the first (Experiment 1), the robot was documented bounding with spine bending in steady-state at modest speeds so as to examine how well the reduced-order model could be fit to describe the empirical data. In the second (Experiment 2), the robot was recorded bounding at steady-state while keeping its spine rigid – by setting the spine retraction angle in the controller to be equal to the spine extension angle – and then transitioning into a bound utilizing core bending. The purpose of the second experiment is to both demonstrate the stability of the bound over a range of operating points and evaluate how well the model from Experiment 1 predicts bounding behavior at these different spine-bending operating points.

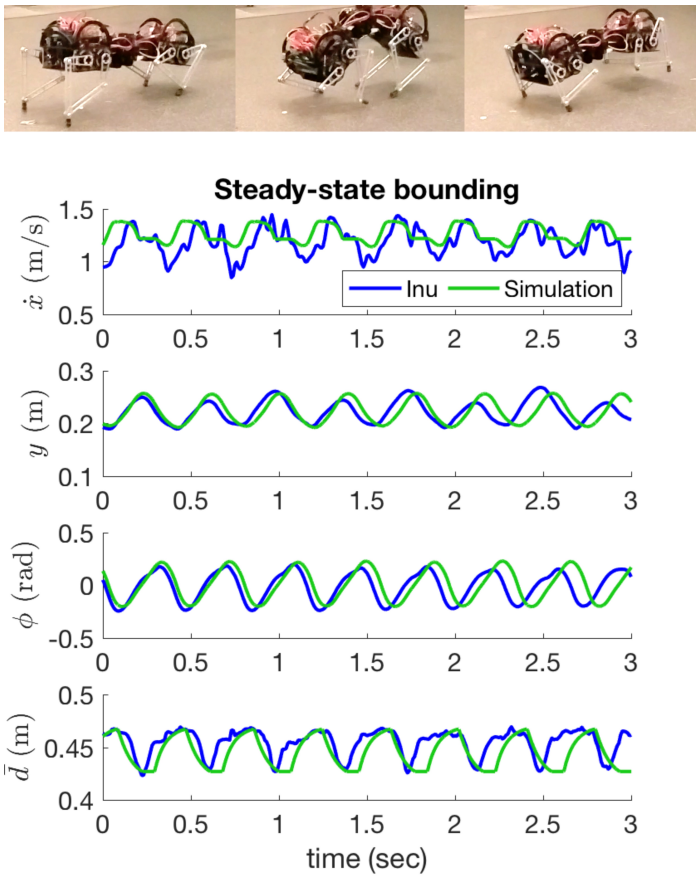

Figure 30: (Top) Three successive still shots taken of Inu bounding using core actuation. (Bottom) Empirical data of Inu bounding is plotted in blue over the course of 8 strides. Data of the reduced-order model utilizing a nearly identical controller as physically implemented is plotted in green. The data show a close agreement in stride frequency – 2.65 Hz for Inu versus 2.58 Hz for the simulation – as well as vertical height y and body pitch angle ϕ. The robot decelerates more in mid-stance than in the simulation and the spine bending trajectories are slightly different, the latter likely due to the modification of the spine controller when implemented on the robot to prevent belt slippage as described in Chapter 5.2.2.

Kinematic data of the bounding robot was collected using a Qualisys[34] motion capture system. The kinematic data was fit to the kinematics of the reduced-order model presented in Chapter 5.1 for comparison with the dynamical simulation of the reduced-order model described in Chapter 5.2.4.

[34] http://www.qualisys.com/

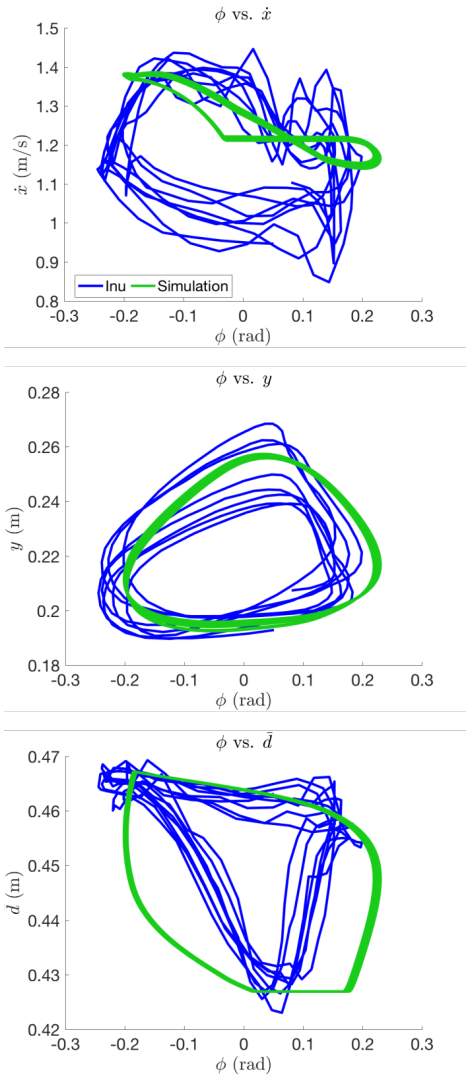

Figure 31: Projections of the robot state from Figure 30 – bounding in steady-state with core actuation over the course of 8 strides – are plotted in blue. Projections of the simulated robot state utilizing a nearly identical controller are plotted in green. These projections illustrate the close agreement between the robot and simulated model in vertical height y and body pitch angle ϕ (middle). It is unclear what is causing the Inu robot to slow down mid-stride (top) but it is likely due to an unmodeled phenomenon such as energetic losses from leg-ground impacts. The discrepancy in spine trajectory projections (bottom) is expected due to the the the modification of the spine controller when implemented on the robot to prevent belt slippage as described in Chapter 5.2.2.

5.2.4. Comparative Bounding Simulation Using the Reduced-Order Model

The reduced-order model presented in Chapter 5.1 was simulated in MATLAB using the controller introduced in Chapter 5.2.1 for comparison with the robot experimental behav-

iors described in Chapter 5.2.3. Several simplifications were made to reduce the system complexity in simulation with the goal of making any future analysis more tractable: linear damping was applied to the simulated legs in the radial and angular directions to coarsely account for the physical robot's motor torque limitations. The spine joint angle was directly actuated using a proportional derivative controller to achieve the desired spine extension, avoiding a complicated characterization of the physical spine mechanism. Aside from these differences, the controller used in simulation was identical to the controller used on the robot.

The four "free" parameters – the leg radial and angular damping, and the spine proportional and derivative gains – were used as inputs to hand-tune the simulation to correspond roughly to the data of Experiment 1 of Chapter 5.2.3. This set of parameters was then used to attempt to predict the robot gait transition of Experiment 2 so as to investigate the predictive ability of the controlled model at different desired speeds and spine deflections.

5.3. Experimental results

5.3.1. Experiment 1: Steady-State Inu Bounding Documentation and Model Correspondence

Steady state bounding was achieved using core actuation on the Inu robot as shown in Figure 30 at a modest average speed of 1.1 m/s, or 2.3 body-lengths per second, and a stride frequency of 2.65 Hz using a spine retraction distance of $d - \bar{d} = 5$ cm, roughly 10% of the robot's hip-to-hip length corresponding to a spine angle of $\psi = -0.9$ rad.

The controlled model shows good correspondence with the physical robot. Figure 30 shows that when the fitted model is simulated using a nearly identical controller, it has a stride frequency of 2.58 Hz, only a 3% difference. Projections of the state in Figure 31 illustrate a close match in the vertical height and pitching of the model with the robot. The spine trajectories have a different profile, but this is to be expected given the modification of the

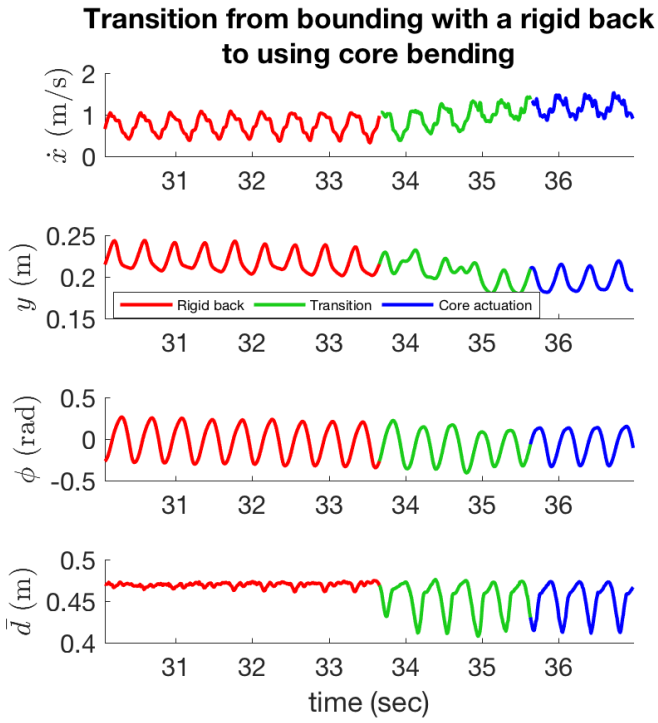

Figure 32: Documentation of the Inu robot transitioning from a bound with a rigid-back to a bound using core bending. The rigid-back bound was achieved by commanding the spine controller to prevent core bending, and the bound using core-bending was achieved using the controller described in Chapters 5.2.1 and 5.2.2. Engaging the core increased speed, decreased vertical height, and decreased the average pitch angle swept – as is more clearly illustrated in Figure 33. This data is used in Figure 34 to evaluate the predictive ability of the model.

spine controller when implemented on the robot to prevent belt slippage as described in Chapter 5.2.2. The main discrepancy between the simulation and robot is in forward speed. While the simulation forward speed fluctuates by only ± 0.1 m/s, the robot forward speed fluctuates by ± 0.3 m/s as the robot slows down significantly in mid-stride. It is unclear what exactly is causing this speed decrease but it is likely due to an unmodeled phenomenon such as energetic losses from leg-ground impacts that could be mitigated with further gait tuning.

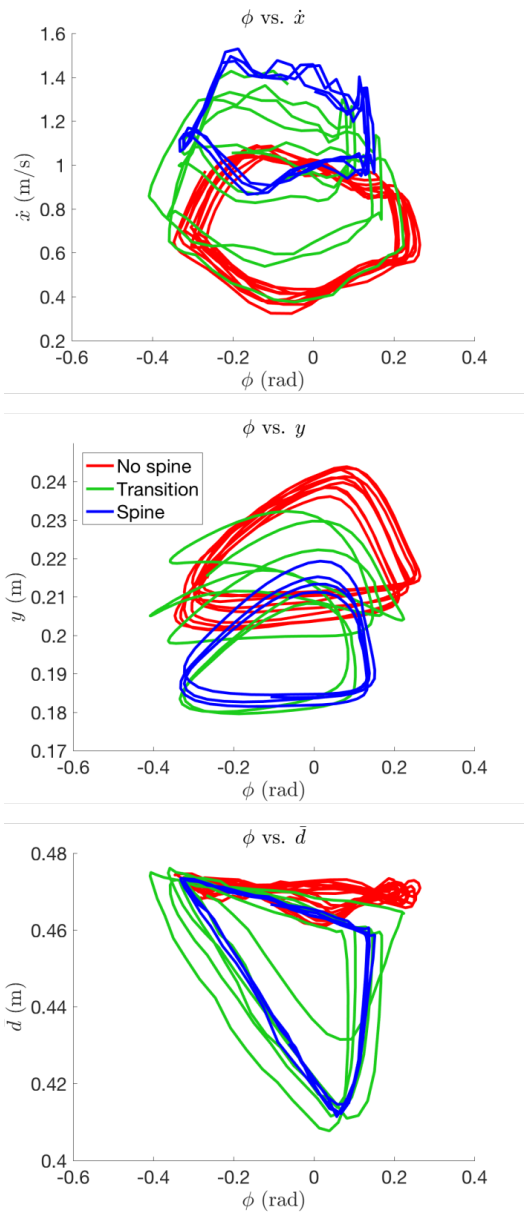

Figure 33: Projections of the state trajectories shown in Figure 32. When engaging the core, the robot's average speed increased by 0.4 m/s to 49% more than its original speed (top). The average pitch angle swept over the course of a stride decreased by 17% and vertical height decreased by approximately 3 cm (middle).

5.3.2. Experiment 2: Inu Gait Transition and Model Prediction

Inu is documented in Figure 32 successfully transitioning from a rigid-back bound to a core-bending bound while running, demonstrating stability of the control strategy over a

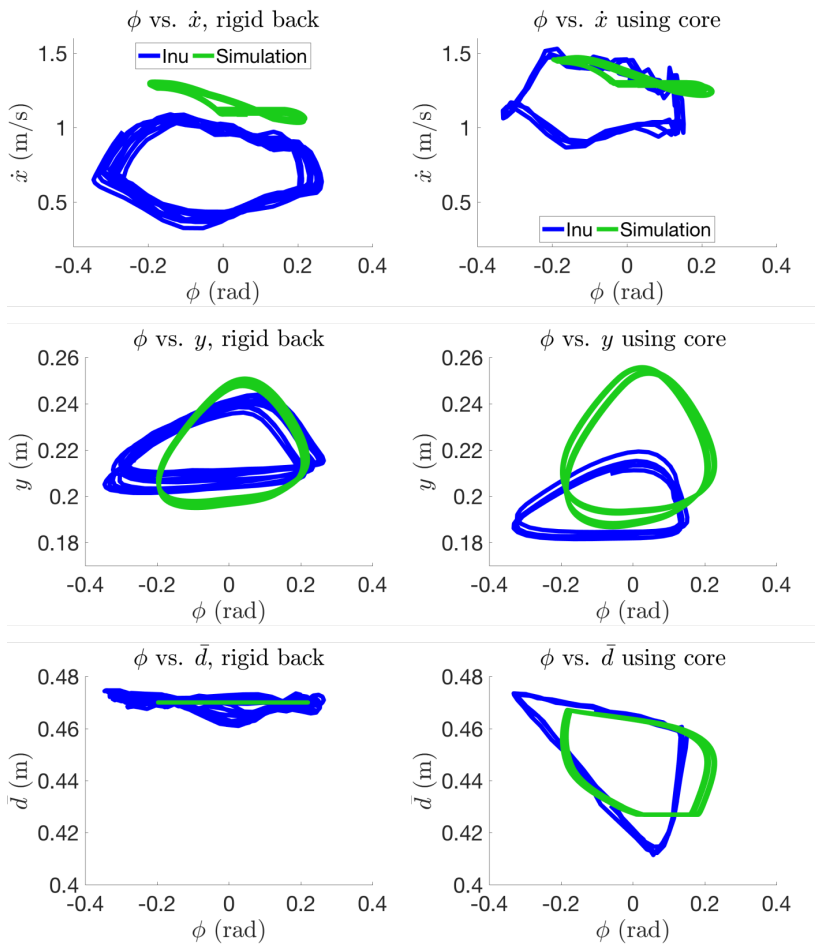

Figure 34: Model predictions (green) versus empirical data (blue) of the bounding Inu robot transitioning from a bound with a rigid back (left column) to a bound using core bending (right column). A larger speed increase was gained by using core actuation than was predicted by the simulation (top row). The predictions of the vertical height, pitch angle, and spine angle trajectories of the mass center offered by the simulation are relatively poor (middle and bottom rows). These discrepancies show that while the model appears to be descriptive enough to capture the limit cycle behavior shown in Figure 31, we are not yet able to use it predictively over a range of operating points.

range of spine-bending values. The projections of the state during the transition given in Figure 33 suggest a speed benefit conferred by the spine, as the average speed increased by 0.4 m/s (a 49% increase) when core bending was used. Using core bending also decreased the average pitch angle swept over the course of a stride by 17% and decreased the average vertical height by approximately 3 cm.

The results of Figure 34 show that using the model from Experiment 1 to predict bounding performance over the range of operating points in Experiment 2 had only limited success. A slightly larger speed increase was gained by using core actuation than was predicted by the simulation, and the predictions for the other states were relatively poor. These discrepancies show that while the model appears to be descriptive enough to capture the limit cycle behavior shown in Figure 31, we are not yet able to use it predictively over a range of operating points.

5.4. Beginnings of formal analytical results for spined running

As we discuss in Chapter 6, showing analytical stability for spined running remains an open problem. However, we can extend the locked-back model results of Chapter 4 to spined running under a very coarse decoupling approximation to show an increase in the speed limit (4.55).

Augment the state variables of the model in Chapter 4 to include the spine length $\bar{d}$, and denote the resulting dependence of the body's moment of inertia on $\bar{d}$ by $I(\bar{d})$. The spine generates internal forces on the body which must be transmitted through the toes in the form of ground reaction forces so as to apply a wrench on the mass-center state variables x, y, and φ. These state variables have the dynamics:

$$\begin{aligned} \ddot{x} &= u_x \\ \ddot{y} &= u_y \\ \frac{I(\bar{d})}{m}\ddot{\varphi} &= u_\varphi, \end{aligned}$$

which are coupled to the (unspecified) dynamics of $\bar{d}$ through the term $I(\bar{d})$, where u_x is the combined horizontal mass-specific force generated by the toes, u_y is the combined vertical mass-specific force generated by the toes, and u_φ is the combined mass-specific torque generated by the toes on the body.

We conjecture that there are parametric and operating regimes where variations of $\bar{d}$ have little effect on $\ddot{\varphi}$ and the resulting trajectories of φ, just as there are undoubtedly regimes where the trajectories of φ are highly conditioned to variations in $\bar{d}$. During operation in the conjectured well-conditioned regimes, we can approximate the functional form of the body's moment-of-inertia $I(\bar{d})$ by a constant I to decouple the states x, y, and φ from $\bar{d}$ and inherit the analytical results of Chapter 4 in these state components. In this case, the spine dynamics are cascaded with the rest of the system dynamics, but the spine can still kinematically augment the legs' workspace volume as discussed in Chapter 3.2. Assume that along a limit cycle, the spine is able to compress and extend such that – over the course of a half-stride – the mass-center moves a horizontal distance of $\delta\bar{d}$ with respect to the hip in stance. Then during the course of the stance event, the mass-center moves a distance of $\delta\bar{x}_{\text{Stance}} + \delta\bar{d}$ with respect to the stance toe, rather than a distance of $\delta\bar{x}_{\text{Stance}}$ in the case of a locked-back spine. Since $\delta\bar{x}_{\text{Stance}}$ is assumed to be kinematically limited to $\delta x^{\text{Max}}_{\text{Stance}}$, the added stride length provided by the spine increases the value of the approximated speed limit presented in Chapter 4. This speed limit, formerly of the form (4.55):

$$\dot{\bar{x}}^{\text{Max}} \approx \frac{\delta x^{\text{Max}}_{\text{Stance}}}{\bar{T}_{\text{Stance}}} = \delta x^{\text{Max}}_{\text{Stance}} \frac{2u_y - g}{g\bar{T}_{\text{F,D}}},$$

becomes:

$$\dot{\bar{x}}^{\text{Max}} \approx \frac{(\delta x^{\text{Max}}_{\text{Stance}} + \delta\bar{d})}{\bar{T}_{\text{Stance}}} = (\delta x^{\text{Max}}_{\text{Stance}} + \delta\bar{d}) \frac{2u_y - g}{g\bar{T}_{\text{F,D}}}, \tag{5.1}$$

an increase of $(100\frac{\delta\bar{d}}{\delta x^{\text{Max}}_{\text{Stance}}})\%$ in maximum running speed.

CHAPTER 6

Conclusions

The final chapter summarizes the contributions of the thesis in Chapter 6.1 and discusses concluding remarks with a nod to future work in Chapter 6.2.

6.1. Contributions summary

Broadly, the thesis presented insight into how a spine morphology can provide locomotion affordances for robotic quadrupeds using the Canid and Inu research platforms; providing designers with both quantifiable advantages afforded by this morphological design choice that can be evaluated against its added weight and complexity, and giving designers control strategies both to deal with the increase in degrees-of-freedom from the spine morphology and to leverage an increase in agility to reactively navigate irregular terrain.

For transitional tasks, the metric of "specific agility" was introduced to quantify how a spine can provides a reservoir of elastic energy storage that can be rapidly converted to kinetic energy, that a spine can augment the effective workspace of the legs without diminishing their force generation capability, and that – in cases of direct-drive or nearly direct-drive leg actuation – the spine motors can contribute more work in stance than the same actuator weight used in the legs, and can do so without diminishing the platform's proprioceptive capabilities. To put to use the agility provided by a suitably designed robotic platform, a formalism was introduced to approximate a set of transitional navigational tasks over irregular terrain, such as leaping over a gap, that lends itself to doubly reactive control synthesis.

For steady-state tasks, the increased complexity introduced by the spine joint was addressed with a modular compositional control framework. A locked-back, three mechanical degree-of-freedom version of bounding was shown to have nice local stability properties,

a well-understood hybrid periodic orbit, and well-approximate its instantiation in physical hardware – all necessary steps towards comparing performance with a four mechanical degrees-of-freedom simplified model of spined bounding so as to ascertain dynamic benefits and costs associated with utilizing an actuated spine. The model's compositional nature suggests that an extension to bounding with the spine unlocked may be possible. Even in its current form, the model indicates that unlocking the spine can increase the maximum achievable running speed associated with leg workspace limitations. Empirical data of Inu running with an unlocked spine was presented and correspondence in state trajectory was verified with a reduced-order model of spined running. A central theme to both the reactive navigation and the modular control frameworks is that analytical tractability is achieved by approximating the dynamics driving the environmental interactions to be constant acceleration.

6.2. Discussion and future work

Hybrid transition control

As discussed in Chapter 4.1, the inherently discontinuous nature of legged locomotion offers the opportunity for exerting control authority on the hybrid transitions of legged dynamics, which in our usage seemed to confer benefits in terms of actuator power expenditure. The notion that richer hybrid interactions present more opportunities for control may explain an advantage of galloping over bounding gaits. We also found that controlling on the hybrid transitions simplified the steady-state gait analysis in two ways. First, it allowed removing all control weights from the expression parameterizing the hybrid periodic orbit. Second, it constrained the locations of the control weights in the factors of the stride-map Jacobian. We found the control weights to be very transparent in their effect on the reset map Jacobian as they are not mixed into the flow expression of the continuous dynamics. The control weights from the guards do fold into the flow expression of the continuous dynamics, however they are by-design isolated to a single row vector in the mode-map Jacobian (for example

(4.67)) as they are contained in the time-to-impact map terms, tempering the analytical complexity of the mode-map Jacobian.

Work remains to evaluate the relative benefits of continuous control and hybrid transition control with application to legged locomotion. The advantages above come at the cost of control being applied inter-mode rather than intra-mode, decreasing the potential response time as compared to continuous control where perturbations can be corrected for immediately. Likely both styles of control would be most effective when used together. Principles motivating a canonical "division of labor" in their combined implementation to take advantage of their relative strengths would be an interesting subject for future work.

Dynamical analysis of a four degree-of-freedom spined running model

We would have liked for this thesis to contain a four degree-of-freedom stability analysis of spined running – the fourth being the addition of a spine joint – however this remains future work. This would be the first of its kind in the literature on spined machines, but analysis of four degree-of-freedom mechanisms is generally very difficult given the tools available to us today in hybrid dynamical systems theory. We hope that the three degree-of-freedom analysis of Chapter 4 represents useful progress towards the goal.

We anticipate a speed benefit will emerge from this analysis along the lines of (5.1) and possibly an accounting for mechanical work done by the spine with regards to energetic cost-of-transport. Especially useful would be if compliance could be modeled in the spine joint such that energy is recycled over the course of a stride, collecting energy as the spine collapses in front stance and expending it through spine extension in rear stance to propel the body forwards. However, it is likely that our hardware platforms from Chapter 2 – while very useful for the purposes they served as research platforms – are too inefficient to obtain a meaningfully impressive cost-of-transport result either with the spine locked or unlocked, and so any empirical illustration of this phenomenon would likely require a much more energy-efficient machine.

We also have a notion that the spine is a more efficient "engine" of legged locomotion than the legs, which we hope can be formalized by a four degree-of-freedom analysis. Specifically, the spine does work extending and contracting while the legs must use up half of their "stroke" recirculating with no work production.

The prospect of a "recipe" for compositional analysis

The analysis of Chapter 4 suggests there may be a "recipe" for this style of decoupling control and compositional synthesis. By using dynamics that have simple and explicit "closed-form" flow expressions to drive hybrid guard interactions, our parametrizations of the mode-times have a relatively clean form with which we used to derive a parametrization of the hybrid periodic orbit and a sufficiently simple stride-map Jacobian expression for a manageable stability analysis. Since the dynamics driving the hybrid transitions are simple, composing additional degrees-of-freedom seems to come at a more reduced cost than if the added states played a role in the transitions. Future work may be able to generalize this nebulous procedure to apply to other systems; building up complicated models by composing dynamical modules out from a "heartbeat" transition-driving module containing trivial dynamics, possibly with other compositions considered in addition to cascade compositions.

The future of spined robots

The best use-case for spined machines using currently available technology may be in direct-drive legged robots, where proprioceptive legs can be augmented by a powerful geared core – that is if the added complexity of the spine is acceptable. Direct-drive machines benefit from a very minimal mechanical complexity, and while an added spine may increase performance metrics, it may also violate the integrity of the design philosophy. The benefits of adding a spine in this use-case would be augmented if the spine designs of Chapter 2 were improved to be lighter weight, more robust, and mechanically simpler.

It remains to be seen whether spined robots in other use-cases will be leaving the laboratory in the near future. The future certainly holds promise for them, but it may be in these cases that spined robots are ahead of their time. This is due to both the lack of a full dynamical analysis to provide designers with further insight into the spine's role in steady-state running and because contemporary legged robots generally don't yet appear to have sufficiently advanced and robust controllers so as to reach the speed regimes where a spine would provide a speed benefit along the lines of (5.1). There is no doubt that the future will bring a decrease in actuator framing costs (Boston Dynamics [1] is leading the way through their impressive usage of scaled-down hydraulic actuation on their Atlas machines), increased speed regimes achieved by the application of formally understood control schemes, and more robust and simple mechanical designs – all of which will motivate the usage of spines in legged machines. But we believe this may still be five or more years away. Research in spined machines in Kodlab began in the year 2011 and eight years later in 2019 this area of research still seems as relevant as ever (especially given the ascendence of direct-drive machines) but work remains before spined robots will likely see widespread usage.

Bibliography

[1] "Boston dynamics," http://www.bostondynamics.com.

[2] J. Aguilar, T. Zhang, F. Qian, M. Kingsbury, B. McInroe, N. Mazouchova, C. Li, R. Maladen, C. Gong, M. Travers, R. L. Hatton, H. Choset, P. B. Umbanhowar, and D. I. Goldman, "A review on locomotion robophysics: The study of movement at the intersection of robotics, soft matter and dynamical systems," *Reports on Progress in Physics*, vol. 79, no. 11, p. 110001, 2016.

[3] A. Alessio and A. Bemporad, "A survey on explicit model predictive control," ser. Lecture Notes in Control and Information Sciences. Springer, 2009, vol. 384, pp. 345–369.

[4] R. M. Alexander, "Why mammals gallop," *Integrative and Comparative Biology*, vol. 28, no. 1, pp. 237–245, 1988.

[5] ——, "Modelling approaches in biomechanics," *Philosophical Transactions of the Royal Society B: Biological Sciences*, vol. 358, no. 1437, pp. 1429–1435, 2003.

[6] R. M. Alexander, N. J. Dimery, and R. F. Ker, "Elastic structures in the back and their rôle in galloping in some mammals," *Journal of zoology*, vol. 207, no. 4, pp. 467–482, 1985.

[7] R. M. Alexander, *Principles of animal locomotion*. Princeton University Press, 2003.

[8] R. Altendorfer, D. Koditschek, and P. Holmes, "Stability analysis of a clock-driven rigid-body slip model for rhex," *International Journal of Robotics Research*, vol. 23, no. 10–11, p. 1001–1012, 2004.

[9] R. Altendorfer, N. Moore, H. Komsuoglu, M. Buehler, H. B. Brown Jr., D. Mcmordie, U. Saranli, R. Full, and D. E. Koditschek, "Rhex: A biologically inspired hexapod runner," *Autonomous Robots*, vol. 11, no. 3, pp. 207–213, 2001.

[10] R. Altendorfer, U. Saranli, H. Komsuoglu, D. Koditschek, H. B. Brown, M. Buehler, N. Moore, D. McMordie, and R. Full, "Evidence for spring loaded inverted pendulum running in a hexapod robot," in *Experimental Robotics VII*, ser. Lecture Notes in Control and Information Sciences. Springer, 2001, vol. 271, pp. 291–302.

[11] A. Ananthanarayanan, M. Azadi, and S. Kim, "Towards a bio-inspired leg design for high-speed running," *Bioinspiration & Biomimetics*, vol. 7, no. 4, p. 046005, 2012.

[12] C. Argot, "Functional-adaptive anatomy of the axial skeleton of some extant marsupials and the paleobiology of the paleocene marsupials mayulestes ferox and pucadelphys andinus," *Journal of Morphology*, vol. 255, no. 3, pp. 279–300, 2003.

[13] S. J. Arnold, "Morphology, performance and fitness," *Integrative and Comparative Biology*, vol. 23, no. 2, pp. 347–361, 1983.

[14] V. I. Arnold, *Ordinary differential equations*. Springer Science & Business Media, 2006.

[15] ——, *Geometrical methods in the theory of ordinary differential equations*. Springer Science & Business Media, 2012, vol. 250.

[16] ——, *Mathematical methods of classical mechanics*. Springer Science & Business Media, 2013, vol. 60.

[17] J. P. Y. Arnould, D. R. Briggs, J. P. Croxall, P. A. Prince, and A. G. Wood, "The foraging behaviour and energetics of wandering albatrosses brooding chicks," *Antarctic Science*, vol. 8, no. 3, pp. 229–236, 1996.

[18] O. Arslan and U. Saranli, "Reactive planning and control of planar spring-mass running on rough terrain," *IEEE Transactions on Robotics*, vol. 28, no. 3, pp. 567–579, 2012.

[19] H. Asada and K. Youcef-Toumi, *Direct-drive robots: theory and practice*. MIT press, 1987.

[20] H. C. Astley and T. J. Roberts, "Evidence for a vertebrate catapult: Elastic energy storage in the plantaris tendon during frog jumping," *Biology Letters*, vol. 8, no. 3, pp. 386–389, 2012.

[21] K. Autumn, Y. A. Liang, S. T. Hsieh, W. Zesch, W. P. Chan, T. W. Kenny, R. Fearing, and R. J. Full, "Adhesive force of a single gecko foot-hair," *Nature*, vol. 405, no. 6787, pp. 681–685, 2000.

[22] K. Autumn, M. Sitti, Y. A. Liang, A. M. Peattie, W. R. Hansen, S. Sponberg, T. W. Kenny, R. Fearing, J. N. Israelachvili, and R. J. Full, "Evidence for van der waals adhesion in gecko setae," *Proceedings of the National Academy of Sciences of the United States of America*, vol. 99, no. 19, pp. 12 252–12 256, 2002.

[23] A. Back, J. Guckenheimer, and M. Myers, "A dynamical simulation facility for hybrid systems," in *Hybrid systems*, ser. Lecture Notes in Computer Science. Springer, 1992, vol. 736, pp. 255–267.

[24] L. W. Barsalou, "Grounded cognition," *Annual Review of Psychology*, vol. 59, no. 1, pp. 617–645, 2008.

[25] A. Bemporad, F. Borrelli, and M. Morari, "Model predictive control based on linear programming - the explicit solution," *IEEE Transactions on Automatic Control*, vol. 47, no. 12, pp. 1974–1985, 2002.

[26] H. C. Bennet Clark, "The energetics of the jump of the locust schistocerca gregaria," *Journal of Experimental Biology*, vol. 63, no. 1, pp. 53–83, 1975.

[27] H. C. Bennet-Clark and E. C. Lucey, "The jump of the flea: a study of the energetics and a model of the mechanism." *Journal of Experimental Biology*, vol. 47, no. 1, pp. 59–67, 1967.

[28] W. O. Bennett, R. S. Simons, and E. L. Brainerd, "Twisting and bending: The functional role of salamander lateral hypaxial musculature during locomotion," *Journal of Experimental Biology*, vol. 204, no. 11, pp. 1979–1989, 2001.

[29] K. Berns, W. Ilg, M. Deck, and R. Dillmann, "The mammalian-like quadrupedal walking machine bisam," in *AMC'98-Coimbra. 1998 5th International Workshop on Advanced Motion Control. Proceedings (Cat. No. 98TH8354)*. IEEE, 1998, pp. 429–433.

[30] J. E. A. Bertram and A. Gutmann, "Motions of the running horse and cheetah revisited: Fundamental mechanics of the transverse and rotary gallop," *Journal of the Royal Society Interface*, vol. 6, no. 35, pp. 549–559, 2009.

[31] D. P. Bertsekas and I. B. Rhodes, "On the minimax reachability of target sets and target tubes," *Automatica*, vol. 7, no. 2, pp. 233–247, 1971.

[32] P. A. Bhounsule, J. Cortell, and A. Ruina, "Design and control of ranger: An energy-efficient, dynamic walking robot," in *Adaptive Mobile Robotics - Proceedings of the 15th International Conference on Climbing and Walking Robots and the Support Technologies for Mobile Machines, CLAWAR*, 2012, pp. 441–448.

[33] A. A. Biewener, "Patterns of mechanical energy change in tetrapod gait: Pendula, springs and work," *Journal of Experimental Zoology Part A: Comparative Experimental Biology*, vol. 305, no. 11, pp. 899–911, 2006.

[34] A. A. Biewener and C. R. Taylor, "Bone strain: A determinant of gait and speed," *Journal of Experimental Biology*, vol. 123, no. 1, pp. 383–400, 1986.

[35] A. V. Birn-Jeffery and M. A. Daley, "Birds achieve high robustness in uneven terrain through active control of landing conditions," *Journal of Experimental Biology*, vol. 215, no. 12, pp. 2117–2127, 2012.

[36] R. Blickhan, "The spring-mass model for running and hopping," *Journal of Biomechanics*, vol. 22, no. 11, pp. 1217–1227, 1989.

[37] R. Blickhan and R. Full, "Similarity in multilegged locomotion: bouncing like a monopode," *Journal of Comparative Physiology A*, vol. 173, no. 5, pp. 509–517, 1993.

[38] Y. Blum, S. W. Lipfert, J. Rummel, and A. Seyfarth, "Swing leg control in human running," *Bioinspiration and Biomimetics*, vol. 5, no. 2, p. 026006, 2010.

[39] T. Boaventura, G. A. Medrano-Cerda, C. Semini, J. Buchli, and D. G. Caldwell, "Stability and performance of the compliance controller of the quadruped robot hyq," in *IEEE International Conference on Intelligent Robots and Systems*, 2013, pp. 1458–1464.

[40] A. P. Bowling, "Dynamic performance, mobility, and agility of multilegged robots," *Journal of Dynamic Systems, Measurement and Control, Transactions of the ASME*, vol. 128, no. 4, pp. 765–777, 2006.

[41] D. M. Bramble, "Axial-appendicular dynamics and the integration of breathing and gait in mammal," *Integrative and Comparative Biology*, vol. 29, no. 1, pp. 171–186, 1989.

[42] D. M. Bramble and D. R. Carrier, "Running and breathing in mammals," *Science*, vol. 219, no. 4582, pp. 251–256, 1983.

[43] R. Breithaupt, J. Dahnke, K. Zahedi, J. Hertzberg, and F. Pasemann, "Robo-salamander an approach for the benefit of both robotics and biology," in *Proceedings of the International Conference on Climbing and Walking Robots (CLAWAR'02)*, 2002, pp. 55–62.

[44] R. Burridge, A. Rizzi, and D. Koditschek, "Sequential composition of dynamically dexterous robot behaviors," *The International Journal of Robotics Research*, vol. 18, no. 6, pp. 534–555, 1999.

[45] J. . Cabelguen, A. Ijspeert, S. Lamarque, and D. Ryczko, "Axial dynamics during locomotion in vertebrates. lesson from the salamander," in *Breathe, Walk and Chew: The Neural Challenge: Part I*, ser. Progress in Brain Research. Elsevier, 2010, vol. 187, no. C, pp. 149–162.

[46] Q. Cao and I. Poulakakis, "Quadrupedal bounding with a segmented flexible torso: Passive stability and feedback control," *Bioinspiration and Biomimetics*, vol. 8, no. 4, p. 046007, 2013.

[47] H. Carlson, "Morphology and contraction properties of cat lumbar back muscles," *Acta Physiologica Scandinavica*, vol. 103, no. 2, pp. 180–197, 1978.

[48] S. G. Carver, N. J. Cowan, and J. M. Guckenheimer, "Lateral stability of the spring-mass hopper suggests a two-step control strategy for running," *Chaos*, vol. 19, no. 2, 2009.

[49] V. Chernyak, T. Flynn, J. O'Rourke, J. Morgan, A. Zalutsky, S. Chernova, S. S. Nestinger, and T. Padir, "The design and realization of a high mobility biomimetic quadrupedal robot," in *Proceedings of 2012 8th IEEE/ASME International Conference on Mechatronic and Embedded Systems and Applications, MESA*, 2012, pp. 93–98.

[50] C. Chevallereau, E. R. Westervelt, and J. W. Grizzle, "Asymptotically stable running for a five-link, four-actuator, planar bipedal robot," *International Journal of Robotics Research*, vol. 24, no. 6, pp. 431–464, 2005.

[51] H. J. Chiel and R. D. Beer, "The brain has a body: Adaptive behavior emerges from interactions of nervous system, body and environment," *Trends in neurosciences*, vol. 20, no. 12, pp. 553–557, 1997.

[52] H. J. Chiel, L. H. Ting, O. Ekeberg, and M. J. Z. Hartmann, "The brain in its body: Motor control and sensing in a biomechanical context," *Journal of Neuroscience*, vol. 29, no. 41, pp. 12 807–12 814, 2009.

[53] W. Cho, J. Choi, C. Kim, S. Choi, and K. Yi, "Unified chassis control for the improvement of agility, maneuverability, and lateral stability," *Vehicular Technology, IEEE Transactions on*, vol. 61, no. 3, pp. 1008–1020, 2012.

[54] S. Collins, A. Ruina, R. Tedrake, and M. Wisse, "Efficient bipedal robots based on passive-dynamic walkers," *Science*, vol. 307, no. 5712, pp. 1082–1085, 2005.

[55] A. Colombo and D. Del Vecchio, "Efficient algorithms for collision avoidance at intersections," in *HSCC'12 - Proceedings of the 15th ACM International Conference on Hybrid Systems: Computation and Control*, 2012, pp. 145–154.

[56] C. Conley, "The gradient structure of a flow: I," *Ergodic Theory and Dynamical Systems*, vol. 8, no. 8, pp. 11–26, 1988.

[57] D. C. Conner, H. Choset, and A. A. Rizzi, "Integrated planning and control for convex-bodied nonholonomic systems using local feedback control policies," in *Proceedings of 2007 Robotics: Science and Systems Conference*, vol. 2, 2007, pp. 57–64.

[58] D. C. Conner, A. A. Rizzi, and H. Choset, "Composition of local potential functions for global robot control and navigation," in *Proceedings of 2003 IEEE/RSJ International Conference on Intelligent Robots and Systems (IROS 2003)(Cat. No. 03CH37453)*, vol. 4. IEEE, 2003, pp. 3546–3551.

[59] G. Council, S. Yang, and S. Revzen, "Deadbeat control with (almost) no sensing in a hybrid model of legged locomotion," in *International Conference on Advanced Mechatronic Systems, ICAMechS*, 2014, pp. 475–480.

[60] N. J. Cowan, M. M. Ankarali, J. P. Dyhr, M. S. Madhav, E. Roth, S. Sefati, S. Sponberg, S. A. Stamper, E. S. Fortune, and T. L. Daniel, "Feedback control as a framework for understanding tradeoffs in biology," *Integrative and Comparative Biology*, vol. 54, no. 2, pp. 223–237, 2014.

[61] U. Culha and U. Saranli, "Quadrupedal bounding with an actuated spinal joint," in *Proceedings - IEEE International Conference on Robotics and Automation*, 2011, pp. 1392–1397.

[62] X. Da and J. Grizzle, "Combining trajectory optimization, supervised machine learning, and model structure for mitigating the curse of dimensionality in the control

of bipedal robots," *International Journal of Robotics Research*, vol. 38, no. 9, pp. 1063–1097, 2019.

[63] M. A. Daley and A. A. Biewener, "Running over rough terrain reveals limb control for intrinsic stability," *Proceedings of the National Academy of Sciences of the United States of America*, vol. 103, no. 42, pp. 15 681–15 686, 2006.

[64] M. A. Daley, J. R. Usherwood, G. Felix, and A. A. Biewener, "Running over rough terrain: Guinea fowl maintain dynamic stability despite a large unexpected change in substrate height," *Journal of Experimental Biology*, vol. 209, no. 1, pp. 171–187, 2006.

[65] W. T. d'Arcy, *On growth and form*. Cambridge Univ Press, 1963.

[66] A. De and D. E. Koditschek, "Parallel composition of templates for tail-energized planar hopping," in *Proceedings - IEEE International Conference on Robotics and Automation*, 2015, pp. 4562–4569.

[67] ——, "Vertical hopper compositions for preflexive and feedback-stabilized quadrupedal bounding, pacing, pronking, and trotting," *International Journal of Robotics Research*, vol. 37, no. 7, pp. 743–778, 2018.

[68] A. De, "Modular hopping and running via parallel composition," Ph.D. dissertation, The University of Pennsylvania, 2017.

[69] A. De, S. A. Burden, and D. E. Koditschek, "A hybrid dynamical extension of averaging and its application to the analysis of legged gait stability," *The International Journal of Robotics Research*, vol. 37, no. 2–3, p. 266–286, 2018.

[70] A. Degani, S. Feng, H. Brown, K. Lynch, H. Choset, and M. Mason, "The parkourbot-a dynamic bowleg climbing robot," in *Robotics and Automation (ICRA), 2011 IEEE International Conference on*, IEEE. IEEE, 2011, p. 795–801.

[71] M. H. Dickinson, C. T. Farley, R. J. Full, M. A. R. Koehl, R. Kram, and S. Lehman, "How animals move: An integrative view," *Science*, vol. 288, no. 5463, pp. 100–106, 2000.

[72] J. D. Dickson, J. Patel, and J. E. Clark, "Towards maneuverability in plane with a dynamic climbing platform," in *Robotics and Automation (ICRA), 2013 IEEE International Conference on*. IEEE, 2013, pp. 1355–1361.

[73] J. Ding and A. Zhou, "Eigenvalues of rank-one updated matrices with some applications," *Applied Mathematics Letters*, vol. 20, no. 12, pp. 1223–1226, 2007.

[74] J. M. Duperret, G. D. Kenneally, J. L. Pusey, and D. E. Koditschek, "Towards a comparative measure of legged agility," in *2014 International Symposium on Experimental Robotics (ISER)*, Marrakech/Essaouira, Morocco, June 2014, pp. 3–16.

[75] J. M. Duperret and D. E. Koditschek, "An empirical investigation of legged transitional maneuvers leveraging raibert's scissor algorithm," in *2015 IEEE International Conference on Robotics and Biomimetics (ROBIO)*, Zhuhai, China, Dec. 2015, pp. 2531–2538.

[76] ——, "Technical report on: Towards reactive control of simplified legged robotics maneuvers," Online: https://repository.upenn.edu/ese_reports/21/, University of Pennsylvania, Tech. Rep., 2017.

[77] ——, "Towards reactive control of transitional legged robot maneuvers," in *2017 International Symposium on Robotics Research (ISRR)*, Puerto Varas, Chile, Dec. 2017, in press. [Online]. Available: https://repository.upenn.edu/ese_papers/821/

[78] ——, "Extended version of simple sagittal running: Stability of a quadrupedal bound," Online: https://repository.upenn.edu/ese_reports/24/, University of Pennsylvania, Tech. Rep., 2019.

[79] ——, "Empirical validation of a spined sagittal-plane quadrupedal model," in *2017 IEEE International Conference on Robotics and Automation (ICRA)*, Singapore, June 2017, pp. 1058–1064.

[80] J. M. Duperret, B. Kramer, and D. E. Koditschek, "Core actuation promotes self-manipulability on a direct-drive quadrupedal robot," in *2016 International Symposium on Experimental Robotics (ISER)*, Tokyo, Japan, Oct. 2016, pp. 147–159.

[81] J. Eldering, M. Kvalheim, and S. Revzen, "Global linearization and fiber bundle structure of invariant manifolds," *Nonlinearity*, vol. 31, no. 9, pp. 4202–4245, 2018.

[82] A. W. English, "The functions of the lumbar spine during stepping in the cat," *Journal of Morphology*, vol. 165, no. 1, pp. 55–66, 1980.

[83] M. Erdmann, "Using backprojections for fine motion planning with uncertainty," *International Journal of Robotics Research*, vol. 5, no. 1, pp. 19–45, 1986.

[84] C. T. Farley, J. Glasheen, and T. A. McMahon, "Running springs: speed and animal size," *Journal of Experimental Biology*, vol. 185, no. 1, pp. 71–86, 1993.

[85] M. S. Fischer and R. Lehmann, "Application of cineradiography for the metric and kinematic study of in-phase gaits during locomotion of the pika (ochotona rufescens, mammalia: Lagomorpha)," *Zoology*, vol. 101, no. 3, pp. 148–173, 1998.

[86] M. S. Fischer, N. Schilling, M. Schmidt, D. Haarhaus, and H. Witte, "Basic limb kinematics of small therian mammals," *Journal of Experimental Biology*, vol. 205, no. 9, pp. 1315–1338, 2002.

[87] M. S. Fischer and H. Witte, "Legs evolved only at the end!" *Philosophical Transactions of the Royal Society A: Mathematical, Physical and Engineering Sciences*, vol. 365, no. 1850, pp. 185–198, 2007.

[88] D. A. Flores and M. M. Díaz, "Postcranial skeleton of glironia venusta (didelphimorphia, didelphidae, caluromyinae): Description and functional morphology," *Zoosystematics and Evolution*, vol. 85, no. 2, pp. 311–339, 2009.

[89] G. A. Folkertsma, S. Kim, and S. Stramigioli, "Parallel stiffness in a bounding quadruped with flexible spine," in *IEEE International Conference on Intelligent Robots and Systems*, 2012, pp. 2210–2215.

[90] R. J. Full and D. E. Koditschek, "Templates and anchors: Neuromechanical hypotheses of legged locomotion on land," *Journal of Experimental Biology*, vol. 202, no. 23, pp. 3325–3332, 1999.

[91] R. J. Full and M. S. Tu, "Mechanics of a rapid running insect: Two-, four- and six-legged locomotion," *Journal of Experimental Biology*, vol. 156, no. 1, pp. 215–231, 1991.

[92] F. Galis, D. R. Carrier, J. Van Alphen, S. D. Van Der Mije, T. J. M. Van Dooren, J. A. J. Metz, and C. M. A. Ten Broek, "Fast running restricts evolutionary change of the vertebral column in mammals," *Proceedings of the National Academy of Sciences of the United States of America*, vol. 111, no. 31, pp. 11 401–11 406, 2014.

[93] P. P. Gambaryan, "How mammals run," *Anatomical Adaptations*, 1974.

[94] R. M. Ghigliazza, R. Altendorfer, P. Holmes, and D. Koditschek, "A simply stabilized running model," *SIAM review*, vol. 47, no. 3, pp. 519–549, 2005.

[95] J. J. Gibson, *The ecological approach to visual perception: classic edition.* Psychology Press, 2014.

[96] D. I. Goldman, T. S. Chen, D. M. Dudek, and R. J. Full, "Dynamics of rapid vertical climbing in cockroaches reveals a template," *Journal of Experimental Biology*, vol. 209, no. 15, pp. 2990–3000, 2006.

[97] H. Goldstein, C. Poole, and J. Safko, *Classical mechanics.* AAPT, 2002.

[98] J. A. Grimes and J. W. Hurst, "The design of atrias 1.0 a unique monopod, hopping robot," in *Adaptive Mobile Robotics - Proceedings of the 15th International Conference on Climbing and Walking Robots and the Support Technologies for Mobile Machines, CLAWAR 2012*, 2012, pp. 548–554.

[99] S. Grimmer, M. Ernst, M. Günther, and R. Blickhan, "Running on uneven ground: Leg adjustment to vertical steps and self-stability," *Journal of Experimental Biology*, vol. 211, no. 18, pp. 2989–3000, 2008.

[100] J. Guckenheimer and P. J. Holmes, *Nonlinear oscillations, dynamical systems, and bifurcations of vector fields*. Springer Science & Business Media, 2013, vol. 42.

[101] J. M. Gál, "Mammalian spinal biomechanics. i. static and dynamic mechanical properties of intact intervertebral joints." *The Journal of experimental biology*, vol. 174, no. 1, pp. 247–280, 1993.

[102] ——, "Mammalian spinal biomechanics. ii. intervertebral lesion experiments and mechanisms of bending resistance." *The Journal of experimental biology*, vol. 174, no. 1, pp. 281–297, 1993.

[103] G. C. Haynes, J. Pusey, R. Knopf, A. M. Johnson, and D. E. Koditschek, "Laboratory on legs: an architecture for adjustable morphology with legged robots," in *Unmanned Systems Technology XIV*, vol. 8387. SPIE, 2012, p. 83870W, doi: 10.1117/12.920678.

[104] M. Hildebrand, "Motions of the running cheetah and horse," *Journal of Mammalogy*, vol. 40, no. 4, pp. 481–495, 1959.

[105] ——, "Further studies on locomotion of the cheetah," *Journal of mammalogy*, vol. 42, no. 1, pp. 84–91, 1961.

[106] A. V. Hill, "The heat of shortening and the dynamic constants of muscle," *Proceedings of the Royal Society of London. Series B-Biological Sciences*, vol. 126, no. 843, pp. 136–195, 1938.

[107] N. Hirose, "An ecological approach to embodiment and cognition," *Cognitive Systems Research*, vol. 3, no. 3, pp. 289–299, 2002.

[108] D. G. E. Hobbelen and M. Wisse, "Swing-leg retraction for limit cycle walkers improves disturbance rejection," *IEEE Transactions on Robotics*, vol. 24, no. 2, pp. 377–389, 2008.

[109] P. Holmes, R. J. Full, D. E. Koditschek, and J. Guckenheimer, "The dynamics of legged locomotion: Models, analyses, and challenges," *SIAM Review*, vol. 48, no. 2, pp. 207–304, 2006.

[110] A. M. Hoover, S. Burden, X. . Fu, S. S. Sastry, and R. S. Fearing, "Bio-inspired design and dynamic maneuverability of a minimally actuated six-legged robot," in *2010 3rd IEEE RAS and EMBS International Conference on Biomedical Robotics and Biomechatronics, BioRob 2010*, 2010, pp. 869–876.

[111] P. E. Hudson, S. A. Corr, and A. M. Wilson, "High speed galloping in the cheetah (acinonyx jubatus) and the racing greyhound (canis familiaris): Spatio-temporal and kinetic characteristics," *Journal of Experimental Biology*, vol. 215, no. 14, pp. 2425–2434, 2012.

[112] E. Huq, C. E. Wall, and A. B. Taylor, "Epaxial muscle fiber architecture favors enhanced excursion and power in the leaper galago senegalensis," *Journal of anatomy*, vol. 227, no. 4, pp. 524–540, 2015.

[113] J. Hwangbo, J. Lee, A. Dosovitskiy, D. Bellicoso, V. Tsounis, V. Koltun, and M. Hutter, "Learning agile and dynamic motor skills for legged robots," *Science Robotics*, vol. 4, no. 26, 2019. [Online]. Available: https://robotics.sciencemag.org/content/4/26/eaau5872

[114] D. J. Hyun, S. Seok, J. Lee, and S. Kim, "High speed trot-running: Implementation of a hierarchical controller using proprioceptive impedance control on the mit cheetah," *International Journal of Robotics Research*, vol. 33, no. 11, pp. 1417–1445, 2014.

[115] A. J. Ijspeert, A. Crespi, D. Ryczko, and J.-M. Cabelguen, "From swimming to walking with a salamander robot driven by a spinal cord model," *science*, vol. 315, no. 5817, pp. 1416–1420, 2007.

[116] D. J. Irschick and J. Garland T., "Intergrating function and ecology in studies of adaptation: Investigations of locomotor capacity as a model system," *Annual Review of Ecology and Systematics*, vol. 32, no. 1, pp. 367–396, 2001.

[117] K. Jayaram and R. J. Full, "Cockroaches traverse crevices, crawl rapidly in confined spaces, and inspire a soft, legged robot," *Proceedings of the National Academy of Sciences of the United States of America*, vol. 113, no. 8, pp. E950–E957, 2016.

[118] D. L. Jindrich, T. F. Besier, and D. G. Lloyd, "A hypothesis for the function of braking forces during running turns," *Journal of Biomechanics*, vol. 39, no. 9, pp. 1611–1620, 2006.

[119] D. L. Jindrich and R. J. Full, "Many-legged maneuverability: Dynamics of turning in hexapods," *Journal of Experimental Biology*, vol. 202, no. 12, pp. 1603–1623, 1999.

[120] D. L. Jindrich, N. C. Smith, K. Jespers, and A. M. Wilson, "Mechanics of cutting maneuvers by ostriches (struthio camelus)," *Journal of Experimental Biology*, vol. 210, no. 8, pp. 1378–1390, 2007.

[121] D. L. Jindrich and M. Qiao, "Maneuvers during legged locomotion," *Chaos: An Interdisciplinary Journal of Nonlinear Science*, vol. 19, no. 2, pp. 026 105–026 105, 2009.

[122] A. M. Johnson, S. A. Burden, and D. E. Koditschek, "A hybrid systems model for simple manipulation and self-manipulation systems," *International Journal of Robotics Research*, vol. 35, no. 11, pp. 1289–1327, 2016.

[123] A. M. Johnson and D. E. Koditschek, "Parametric jumping dataset on the rhex robot," Online: https://repository.upenn.edu/ese_reports/20/, University of Pennsylvania, Tech. Rep., 2012.

[124] ——, "Legged self-manipulation," *IEEE Access*, vol. 1, pp. 310–334, May 2013.

[125] ——, "Toward a vocabulary of legged leaping," in *Proceedings of the 2013 IEEE Intl. Conference on Robotics and Automation*, May 2013, pp. 2553–2560.

[126] S. E. Johnson and L. J. Shapiro, "Positional behavior and vertebral morphology in atelines and cebines," *American Journal of Physical Anthropology*, vol. 105, no. 3, pp. 333–354, 1998.

[127] C. K. Jones, "Geometric singular perturbation theory," in *Dynamical systems*, ser. Lecture Notes in Mathematics. Springer, 1995, vol. 1609, pp. 44–118.

[128] K. E. Jones, K. D. Angielczyk, P. D. Polly, J. J. Head, V. Fernandez, J. K. Lungmus, S. Tulga, and S. E. Pierce, "Fossils reveal the complex evolutionary history of the mammalian regionalized spine," *Science*, vol. 361, no. 6408, pp. 1249–1252, 2018.

[129] M. H. H. Kani, M. Derafshian, H. J. Bidgoly, and M. N. Ahmadabadi, "Effect of flexible spine on stability of a passive quadruped robot: Experimental results," in *2011 IEEE International Conference on Robotics and Biomimetics, ROBIO*, 2011, pp. 2793–2798.

[130] J. G. D. Karssen, M. Haberland, M. Wisse, and S. Kim, "The optimal swing-leg retraction rate for running," in *Proceedings - IEEE International Conference on Robotics and Automation*, 2011, pp. 4000–4006.

[131] S. S. Keerthi and E. G. Gilbert, "Computation of minimum-time feedback control laws for discrete-time systems with state-control constraints," *IEEE Transactions on Automatic Control*, vol. 32, no. 5, pp. 432–435, 1987.

[132] G. Kenneally, A. De, and D. E. Koditschek, "Design principles for a family of direct-drive legged robots," *IEEE Robotics and Automation Letters*, vol. 1, no. 2, p. 900–907, Jul 2016, doi: 10.1109/LRA.2016.2528294.

[133] M. Khoramshahi, A. Sprowitz, A. Tuleu, M. N. Ahmadabadi, and A. J. Ijspeert, "Benefits of an active spine supported bounding locomotion with a small compliant quadruped robot," in *Proceedings - IEEE International Conference on Robotics and Automation*, 2013, pp. 3329–3334.

[134] K.-H. Kim, S.-H. Park, and Y.-J. Lee, "Development of bio-mimetic quadruped walking robot with 2-dof waist joint," in *Proceedings of SPIE - The International Society for Optical Engineering*, vol. 6042. International Society for Optics and Photonics, 2005, p. 60423H.

[135] D. E. Koditschek, R. J. Full, and M. Buehler, "Mechanical aspects of legged locomotion control," *Arthropod Structure and Development*, vol. 33, no. 3, pp. 251–272, 2004.

[136] J. Koechling and M. Raibert, "How fast can a legged robot run," in *American Society of Mechanical Engineers, Dynamic Systems and Control Division (Publication) DSC*, vol. 11, 1988, pp. 241–249.

[137] M. A. R. Koehl, "When does morphology matter?" *Annual Review of Ecology and Systematics*, vol. 27, no. 1, pp. 501–542, 1996.

[138] S. Kuindersma, R. Deits, M. Fallon, A. Valenzuela, H. Dai, F. Permenter, T. Koolen, P. Marion, and R. Tedrake, "Optimization-based locomotion planning, estimation, and control design for the atlas humanoid robot," *Autonomous Robots*, vol. 40, no. 3, pp. 429–455, 2016.

[139] D. S. Laila and D. Nešić, "Changing supply rates for input-output to state stable discrete-time nonlinear systems with applications," *Automatica*, vol. 39, no. 5, pp. 821–835, 2003.

[140] J. H. Lee, "Model predictive control: Review of the three decades of development," *International Journal of Control, Automation and Systems*, vol. 9, no. 3, pp. 415–424, 2011.

[141] J. M. Lee, *Introduction to smooth manifolds*. Springer, 2001.

[142] K. F. Leeser, "Locomotion experiments on a planar quadruped robot with articulated spine," Ph.D. dissertation, Massachusetts Institute of Technology, Feb 1996.

[143] M. A. Lewis and G. A. Bekey, "Gait adaptation in a quadruped robot," *Autonomous robots*, vol. 12, no. 3, pp. 301–312, 2002.

[144] M. A. Lewis, "Self-organization of locomotory controllers in robots and animals," Ph.D. dissertation, University of Southern California, 1996.

[145] T. Libby, T. Y. Moore, E. Chang-Siu, D. Li, D. J. Cohen, A. Jusufi, and R. J. Full, "Tail-assisted pitch control in lizards, robots and dinosaurs," *Nature*, vol. 481, no. 7380, pp. 181–184, 2012.

[146] T. Lozano-Pérez, M. T. Mason, and R. H. Taylor, "Automatic synthesis of fine-motion strategies for robots," *The International Journal of Robotics Research*, vol. 3, no. 1, pp. 3–24, 1984.

[147] J. Lygeros, C. Tomlin, and S. Sastry, "Controllers for reachability specifications for hybrid systems," *Automatica*, vol. 35, no. 3, pp. 349–370, 1999.

[148] G. A. Lynch, J. E. Clark, P.-C. Lin, and D. E. Koditschek, "A bioinspired dynamical vertical climbing robot," *The International Journal of Robotics Research*, vol. 31, no. 8, pp. 974–996, 2012.

[149] A. Majumdar, A. A. Ahmadi, and R. Tedrake, "Control design along trajectories with sums of squares programming," in *Proceedings - IEEE International Conference on Robotics and Automation*, 2013, pp. 4054–4061.

[150] W. C. Martin, A. Wu, and H. Geyer, "Experimental evaluation of deadbeat running on the atrias biped," *IEEE Robotics and Automation Letters*, vol. 2, no. 2, pp. 1085–1092, 2017.

[151] M. Mason, "Automatic planning of fine motions: Correctness and completeness," in *Robotics and Automation. Proceedings. 1984 IEEE International Conference on*, vol. 1. IEEE, 1984, pp. 492–503.

[152] D. Q. Mayne, "Model predictive control: Recent developments and future promise," *Automatica*, vol. 50, no. 12, pp. 2967–2986, 2014.

[153] D. Q. Mayne and W. R. Schroeder, "Robust time-optimal control of constrained linear systems," *Automatica*, vol. 33, no. 12, pp. 2103–2118, 1997.

[154] T. Mcgeer, "Passive dynamic walking," *The International Journal of Robotics Research*, vol. 9, no. 2, pp. 62–82, 1990.

[155] C. P. McGowan, R. V. Baudinette, J. R. Usherwood, and A. A. Biewener, "The mechanics of jumping versus steady hopping in yellow-footed rock wallabies," *Journal of Experimental Biology*, vol. 208, no. 14, pp. 2741–2751, 2005.

[156] C. McGowan, *A practical guide to vertebrate mechanics*. Cambridge University Press, 1999.

[157] P. McLeod and Z. Dienes, "Do fielders know where to go to catch the ball or only how to get there?" *Journal of Experimental Psychology: Human Perception and Performance*, vol. 22, no. 3, pp. 531–543, 1996.

[158] D. Moore, N. Deuel, S. Drevemo, and A. Van den Bogert, "Kinematic analysis of world championship three-day event horses jumping a cross-country drop fence," *Journal of Equine Veterinary Science*, vol. 15, no. 12, pp. 527–531, 1995.

[159] R. M. Murray, Z. Li, S. S. Sastry, and S. S. Sastry, *A mathematical introduction to robotic manipulation*. CRC press, 1994.

[160] R. Müller and R. Blickhan, "Running on uneven ground: Leg adjustments to altered ground level," *Human Movement Science*, vol. 29, no. 4, pp. 578–589, 2010.

[161] K. Nishikawa, A. A. Biewener, P. Aerts, A. N. Ahn, H. J. Chiel, M. A. Daley, T. L. Daniel, R. J. Full, M. E. Hale, T. L. Hedrick, A. K. Lappin, T. R. Nichols, R. D. Quinn, R. A. Satterlie, and B. Szymik, "Neuromechanics: An integrative approach for understanding motor control," *Integrative and Comparative Biology*, vol. 47, no. 1, pp. 16–54, 2007.

[162] A. A. Paranjape and N. Ananthkrishnan, "Combat aircraft agility metrics-a review," *Journal of Aerospace Sciences and Technologies*, vol. 58, no. 2, pp. 143–154, 2006.

[163] H. . Park, P. M. Wensing, and S. Kim, "High-speed bounding with the mit cheetah 2: Control design and experiments," *International Journal of Robotics Research*, vol. 36, no. 2, pp. 167–192, 2017.

[164] H.-W. Park, P. M. Wensing, S. Kim *et al.*, "Online planning for autonomous running jumps over obstacles in high-speed quadrupeds," in *Proceedings of the Robotics: Science and System (RSS)*, Rome, Italy, July 2015, doi: 10.15607/RSS.2015.XI.047.

[165] S. Park and Y.-J. Lee, "Discontinuous zigzag gait planning of a quadruped walking robot with a waist-joint," *Advanced robotics*, vol. 21, no. 1-2, pp. 143–164, 2007.

[166] M. Pasupuleti, S. Nadubettu Yadukumar, and A. Ames, "Human-inspired underactuated bipedal robotic walking with amber on flat-ground, up-slope and uneven terrain," in *IEEE/RSJ International Conference on Intelligent Robots and Systems (IROS), Algarve, Portugal*, 2012, pp. 2478–2483.

[167] T. Pfau, A. Garland de Rivaz, S. Brighton, and R. Weller, "Kinetics of jump landing in agility dogs," *The Veterinary Journal*, vol. 190, no. 2, pp. 278–283, 2011.

[168] D. Polet and J. Bertram, "Rock me gently: the converse effects of pitch inertia on walking and running energetics," 2019, presented at Dynamic Walking 2019 conference.

[169] I. Poulakakis and J. W. Grizzle, "The spring loaded inverted pendulum as the hybrid zero dynamics of an asymmetric hopper," *IEEE Transactions on Automatic Control*, vol. 54, no. 8, pp. 1779–1793, 2009.

[170] I. Poulakakis, J. A. Smith, and M. Buehler, "Experimentally validated bounding models for the scout ii quadrupedal robot," in *Proceedings - IEEE International Conference on Robotics and Automation*, vol. 2004, 2004, pp. 2595–2600.

[171] S. Pouya, M. Khodabakhsh, A. Spröwitz, and A. Ijspeert, "Spinal joint compliance and actuation in a simulated bounding quadruped robot," *Autonomous Robots*, no. 2, pp. 437–452, 2017.

[172] P. A. Pridmore, "Trunk movements during locomotion in the marsupial monodelphis domestica (didelphidae)," *Journal of Morphology*, vol. 211, no. 2, pp. 137–146, 1992.

[173] J. L. Pusey, J. M. Duperret, G. C. Haynes, R. Knopf, and D. E. Koditschek, "Free-standing leaping experiments with a power-autonomous, elastic-spined quadruped," in *SPIE Defense, Security, and Sensing, vol. 8741. International Society for Optics and Photonics*, May 2013, pp. 87 410W–87 410W–15.

[174] R. A. Raff, *The Shape of Life: Genes, Development, and the Evolution of Animal Form*. University of Chicago Press Chicago, 1996.

[175] M. H. Raibert, *Legged Robots That Balance*. Cambridge: MIT Press, 1986.

[176] S. V. Raković, F. Blanchini, E. Crück, and M. Morari, "Robust obstacle avoidance for constrained linear discrete time systems: A set-theoretic approach," in *Proceedings of the IEEE Conference on Decision and Control*, 2007, pp. 188–193.

[177] S. V. Raković and D. Q. Mayne, "Robust time optimal obstacle avoidance problem for constrained discrete time systems," in *Proceedings of the 44th IEEE Conference on Decision and Control, and the European Control Conference, CDC-ECC*, 2005, pp. 981–986.

[178] S. Revzen, S. A. Burden, T. Y. Moore, J. . Mongeau, and R. J. Full, "Instantaneous kinematic phase reflects neuromechanical response to lateral perturbations of running cockroaches," *Biological cybernetics*, vol. 107, no. 2, pp. 179–200, 2013.

[179] D. Ritter, "Axial muscle function during lizard locomotion," *Journal of Experimental Biology*, vol. 199, no. 11, pp. 2499–2510, 1996.

[180] C. Robert, F. Audigié, J. Valette, P. Pourcelot, and J.-M. Denoix, "Effects of treadmill speed on the mechanics of the back in the trotting saddlehorse," *Equine veterinary journal*, vol. 33, no. S33, pp. 154–159, 2001.

[181] S. F. Roberts, D. E. Koditschek, and L. J. Miracchi, "Systematizing Gibsonian affordances in robotics: an empirical, generative approach derived from case studies in legged locomotion," poster presented at 2nd International Workshop on Computational Models of Affordances at ICRA, 2019, https://repository.upenn.edu/ese_papers/858/.

[182] T. J. Roberts and J. A. Scales, "Mechanical power output during running accelerations in wild turkeys," *Journal of Experimental Biology*, vol. 205, no. 10, pp. 1485–1494, 2002.

[183] T. J. Roberts, E. M. Abbott, and E. Azizi, "The weak link: do muscle properties determine locomotor performance in frogs?" *Philosophical Transactions of the Royal Society B: Biological Sciences*, vol. 366, no. 1570, pp. 1488–1495, 2011.

[184] H. Rockwell, F. G. Evans, and H. C. Pheasant, "The comparative morphology of the vertebrate spinal column. its form as related to function," *Journal of Morphology*, vol. 63, no. 1, pp. 87–117, 1938.

[185] U. Saranli, W. J. Schwind, and D. E. Koditschek, "Toward the control of a multi-jointed, monoped runner," in *Proceedings. 1998 IEEE International Conference on Robotics and Automation (Cat. No. 98CH36146)*, vol. 3. IEEE, 1998, pp. 2676–2682.

[186] E. J. Sargis, "A preliminary qualitative analysis of the axial skeleton of tupaiids (mammalia, scandentia): Functional morphology and phylogenetic implications," *Journal of zoology*, vol. 253, no. 4, pp. 473–483, 2001.

[187] J. Sastra, W. G. B. Heredia, J. Clark, and M. Yim, "A biologically-inspired dynamic legged locomotion with a modular reconfigurable robot," in *2008 Proceedings of the ASME Dynamic Systems and Control Conference, DSCC*, 2008, pp. 253–260.

[188] N. Schilling and M. S. Fischer, "Kinematic analysis of treadmill locomotion of tree shrews, tupaia glis (scandentia: Tupaiidae)," *Zeitschrift fur Saugetierkunde*, vol. 64, no. 3, pp. 129–153, 1999.

[189] N. Schilling, "Evolution of the axial system in craniates: morphology and function of the perivertebral musculature," *Frontiers in zoology*, vol. 8, no. 1, p. 4, 2011.

[190] N. Schilling and D. R. Carrier, "Function of the epaxial muscles in walking, trotting and galloping dogs: implications for the evolution of epaxial muscle function in tetrapods," *Journal of Experimental Biology*, vol. 213, no. 9, pp. 1490–1502, 2010.

[191] N. Schilling and R. Hackert, "Sagittal spine movements of small therian mammals during asymmetrical gaits," *Journal of Experimental Biology*, vol. 209, no. 19, pp. 3925–3939, 2006.

[192] K. Schmidt-Nielsen, *Scaling: why is animal size so important?* Cambridge University Press, 1984.

[193] J. Schmitt, "A simple stabilizing control for sagittal plane locomotion," *Journal of Computational and Nonlinear Dynamics*, vol. 1, no. 4, pp. 348–357, 2006.

[194] W. J. Schwind and D. E. Koditschek, "Approximating the stance map of a 2-dof monoped runner," *Journal of Nonlinear Science*, vol. 10, no. 5, pp. 533–568, 2000.

[195] W. J. Schwind, "Spring loaded inverted pendulum running: A plant model," Ph.D. dissertation, University of Michigan, 1999.

[196] S. Seok, A. Wang, M. Y. Chuah, D. J. Hyun, J. Lee, D. M. Otten, J. H. Lang, and S. Kim, "Design principles for energy-efficient legged locomotion and implementation on the mit cheetah robot," *IEEE/ASME Transactions on Mechatronics*, vol. 20, no. 3, pp. 1117–1129, 2014.

[197] S. Seok, A. Wang, D. Otten, and S. Kim, "Actuator design for high force proprioceptive control in fast legged locomotion," in *IEEE International Conference on Intelligent Robots and Systems*, 2012, pp. 1970–1975.

[198] A. Seyfarth, H. Geyer, and H. Herr, "Swing-leg retraction: A simple control model for stable running," *Journal of Experimental Biology*, vol. 206, no. 15, pp. 2547–2555, 2003.

[199] A. Seyfarth, H. Geyer, M. Günther, and R. Blickhan, "A movement criterion for running," *Journal of biomechanics*, vol. 35, no. 5, p. 649–655, 2002.

[200] E. L. C. Shepard, R. P. Wilson, W. G. Rees, E. Grundy, S. A. Lambertucci, and S. B. Vosper, "Energy landscapes shape animal movement ecology," *American Naturalist*, vol. 182, no. 3, pp. 298–312, 2013.

[201] S. M. Shinners, *Modern control system theory and design*, 2nd ed. John Wiley & Sons, 1998.

[202] E. D. Sontag, "Further facts about input to state stabilization," *IEEE Transactions on Automatic Control*, vol. 35, no. 4, pp. 473–476, 1990.

[203] S. Sponberg and R. J. Full, "Neuromechanical response of musculo-skeletal structures in cockroaches during rapid running on rough terrain," *Journal of Experimental Biology*, vol. 211, no. 3, pp. 433–446, 2008.

[204] K. Sreenath, H. . Park, I. Poulakakis, and J. W. Grizzle, "A compliant hybrid zero dynamics controller for stable, efficient and fast bipedal walking on mabel," *International Journal of Robotics Research*, vol. 30, no. 9, pp. 1170–1193, 2011.

[205] T. Takuma, M. Ikeda, and T. Masuda, "Facilitating multi-modal locomotion in a quadruped robot utilizing passive oscillation of the spine structure," in *2010 IEEE/RSJ International Conference on Intelligent Robots and Systems*. IEEE, 2010, pp. 4940–4945.

[206] R. Tedrake, I. R. Manchester, M. Tobenkin, and J. W. Roberts, "Lqr-trees: Feedback motion planning via sums-of-squares verification," *International Journal of Robotics Research*, vol. 29, no. 8, pp. 1038–1052, 2010.

[207] L. H. Ting and J. L. McKay, "Neuromechanics of muscle synergies for posture and movement," *Current opinion in neurobiology*, vol. 17, no. 6, pp. 622–628, 2007.

[208] T. T. Topping, V. Vasilopoulos, A. De, and E. Koditschek, Daniel, "Composition of templates for transitional pedipulation behaviors," in *International Symposium on Robotics Research (ISRR)*, 2019, (in press).

[209] K. Tsujita, T. Kobayashi, T. Inoura, and T. Masuda, "Gait transition by tuning muscle tones using pneumatic actuators in quadruped locomotion," in *2008 IEEE/RSJ International Conference on Intelligent Robots and Systems, IROS*, 2008, pp. 2453–2458.

[210] J. Urata, Y. Nakanishi, K. Okada, and M. Inaba, "Design of high torque and high speed leg module for high power humanoid," in *Intelligent Robots and Systems (IROS), 2010 IEEE/RSJ International Conference on*. IEEE, 2010, pp. 4497–4502.

[211] M. Vidyasagar, "Decomposition techniques for large-scale systems with nonadditive interactions: Stability and stabilizability," *IEEE Transactions on Automatic Control*, vol. 25, no. 4, pp. 773–779, 1980.

[212] P. C. Wainwright, "Functional versus morphological diversity in macroevolution," ser. Annual Review of Ecology, Evolution, and Systematics, 2007, vol. 38, pp. 381–401.

[213] P. C. Wainwright, M. E. Alfaro, D. I. Bolnick, and C. D. Hulsey, "Many-to-one mapping of form to function: A general principle in organismal design?" *Integrative and Comparative Biology*, vol. 45, no. 2, pp. 256–262, 2005.

[214] J. A. Walker, "Does a rigid body limit maneuverability?" *Journal of Experimental Biology*, vol. 203, no. 22, pp. 3391–3396, 2000.

[215] B. Webb, "What does robotics offer animal behaviour?" *Animal Behaviour*, vol. 60, no. 5, pp. 545–558, 2000.

[216] P. W. Webb, "Maneuverability-general issues," *Oceanic Engineering, IEEE Journal of*, vol. 29, no. 3, pp. 547–555, 2004.

[217] E. L. Webster, P. E. Hudson, and S. B. Channon, "Comparative functional anatomy of the epaxial musculature of dogs (canis familiaris) bred for sprinting vs. fighting," *Journal of anatomy*, vol. 225, no. 3, pp. 317–327, 2014.

[218] E. R. Westervelt, J. W. Grizzle, and D. E. Koditschek, "Hybrid zero dynamics of planar biped walkers," *IEEE Transactions on Automatic Control*, vol. 48, no. 1, pp. 42–56, 2003.

[219] C. D. Williams and N. C. Holt, "Spatial scale and structural heterogeneity in skeletal muscle performance," *Integrative and Comparative Biology*, vol. 58, no. 2, pp. 163–173, 2018.

[220] S. B. Williams, H. Tan, J. R. Usherwood, and A. M. Wilson, "Pitch then power: Limitations to acceleration in quadrupeds," *Biology Letters*, vol. 5, no. 5, pp. 610–613, 2009.

[221] M. Wilson, "Six views of embodied cognition," *Psychonomic Bulletin and Review*, vol. 9, no. 4, pp. 625–636, 2002.

[222] A. Wu and H. Geyer, "The 3-d spring-mass model reveals a time-based deadbeat control for highly robust running and steering in uncertain environments," *IEEE Transactions on Robotics*, vol. 29, no. 5, pp. 1114–1124, 2013.

[223] Y. Yesilevskiy, W. Yang, and C. D. Remy, "Spine morphology and energetics: How principles from nature apply to robotics," *Bioinspiration and Biomimetics*, vol. 13, no. 3, p. 036002, 2018.

[224] J. K. Yim and R. S. Fearing, "Precision jumping limits from flight-phase control in salto-1p," in *IEEE International Conference on Intelligent Robots and Systems*, 2018, pp. 2229–2236.

[225] I. S. Young, R. Alexander, A. J. Woakes, P. J. Butler, and L. Anderson, "The synchronization of ventilation and locomotion in horses (equus caballus)," *The Journal of experimental biology*, vol. 166, no. 1, pp. 19–31, 1992.

[226] Q. Zhao, K. Nakajima, H. Sumioka, X. Yu, and R. Pfeifer, "Embodiment enables the spinal engine in quadruped robot locomotion," in *IEEE International Conference on Intelligent Robots and Systems*, 2012, pp. 2449–2456.

[227] Q. Zhao, H. Sumioka, K. Nakajima, X. Yu, and R. Pfeifer, "Spine as an engine: Effect of spine morphology on spine-driven quadruped locomotion," *Advanced Robotics*, vol. 28, no. 6, pp. 367–378, 2014.

[228] X. Zhou and S. Bi, "A survey of bio-inspired compliant legged robot designs," *Bioinspiration & biomimetics*, vol. 7, no. 4, p. 041001, 2012.